UNIVERSITÀ DEGLI STUDI DI MILANO-BICOCCA
SCUOLA DI DOTTORATO DI SCIENZE
CORSO DI DOTTORATO DI RICERCA IN FISICA E ASTRONOMIA

Ph.D. Thesis

Characterization of Atmospheric Pressure Plasmas for Aerodynamic Applications

Ilaria Biganzoli

Supervisor:
Prof. Claudia Riccardi

School Coordinator:
Prof. Giberto Chirico

Ciclo XXVI, A.A. 2011 - 2013

Contents

CHAPTER 1

Introduction

The use of plasmas in aerodynamics has recently become a hot topic of interest. In particular, over the last ten years, plasma actuation has received much attention as a promising active method for airflow control. Flow control consists of manipulating the properties of a generic moving fluid with the aim of achieving a desired change, but flow dynamics in proximity of a solid object is usually considered, being a consistent and significant issue in many engineering applications, such as engine, automobile or airplane design. Plasma control of airflows along surfaces has been the subject of several experimental studies whose aim was to reduce turbulence, to decrease drag, to enhance airfoil lift or to prevent flow detachment. The fast temporal

response and the absence of moving parts are the most promising features from which plasma actuators could benefit. Different types of plasma sources are currently studied as good candidates for these kinds of applications, but Dielectric Barrier Discharges (DBDs) are usually preferred, being characterized by the presence of an insulating barrier between the electrodes. This allows the generation of a non-thermal plasma at atmospheric pressure and prevents the discharge from collapsing into an arc. Surface Dielectric Barrier Discharges (SDBDs) are particularly suitable since plasma is created by ionizing a thin portion of air nearby the dielectric barrier, and this can effectively influence the local properties of the boundary layer associated to an external flow.

This thesis deals with SDBDs in an asymmetric configuration where one electrode is glued into an insulating material and the other one is exposed to air, so that plasma is created in correspondence of just one side of the dielectric barrier. The buried electrode is connected to the ground, whereas a sinusoidal high-voltage is applied to the exposed one. It is known that, when these discharges are operated in quiescent air, an airflow of several metres per second is observed above the dielectric sheet and near the plasma region. This is usually called *electric wind*, or *ionic wind* because the main mechanism responsible for its generation is believed to be momentum transfer from the ions drifting in the discharge electric field to the surrounding fluid, by particle-particle collisions. When the voltage difference between the electrodes is sufficiently high, plasma is created and electrical charges are transported through the gap and accumulated on the insulating surface. This charge accumulation generates an electric field that locally weakens the external one. When the total electric field falls below the threshold necessary for plasma ignition, the discharge extinguishes. If the voltage imposed to the fed electrode is increased, the discharge can be locally initiated again, and

that is the reason why a sinusoidal high-voltage supply is adopted instead of a continuous one. Consequently, the presence of the insulating barrier usually leads to a regime where charge is mainly transported in sub-millimetre regions consisting of current filaments with temporal duration limited to a few tens of nanoseconds. These *plasma microdischarges* are concentrated into two phase intervals of the voltage supply, when the modulus of the applied voltage difference is high enough and is increasing in time. These two phases of plasma activity are often called *Backward Stroke* (BD) and *Forward Stroke* (FD), depending if the high-voltage signal is rising from its minimum to its maximum or decreasing from its maximum to its minimum.

This thesis is motivated by the fact new studies focusing on plasma properties and dynamics are required in order to get better and better aerodynamic results, to understand which parameters mainly affect the actuator performances and to validate numerical models trying to forecast the aerodynamic effects induced by the discharge. This has brought to a scientific collaboration between the Centre of Excellence PlasmaPrometeo of University of Milano-Bicocca and the Aerodynamics and Wind Tunnel Department of the aerospace company Alenia Aermacchi. The interest of this italian leader in aeronautics for this topic was born some years ago, after that several papers (published mainly in the American Institute of Aeronautics and Astronautics Journal) presented the potentialities of these discharges. Plasma actuators are appealing because they are free of moving parts, can be installed directly on the aerodynamic surface of interest and guarantees a fast response. Alenia Aermacchi thus began to study and test this method for active flow control with both quiescent air and wind tunnel experimental campaigns. Interesting results dealing with lift enhancement, drag reduction and stall delay were found. Despite that, it is more and more evident that, even though several optimizations have been done by the worldwide scientific and aero-

nautics community in terms of driving voltage and geometrical configuration (for both single and multiple actuators), there still remain some basic characteristics of these discharges that are not well understood and that limit the present usefulness of these devices to low speed applications, being the velocity of the electric wind generally of a few metres per second. Experiments performed during this Ph.D. project thus focused on a basic plasma actuator configuration, because the aim was to gain a deeper knowledge of the peculiarities of these discharges.

In Chapter 2 the fundamental physics of non-thermal discharges at atmospheric pressure are presented, whereas Chapter 3 introduces the concepts of flow control and plasma actuation. During these years I have studied the properties of these discharges by means of electrical and optical diagnostics (mainly Rogowski coils, capacitive probes, a photomultiplier tube and a thermal camera), which are described in Chapter 4 together with the experimental layout. With some of these diagnostic tools a temporal resolution high enough for studying several characteristics of plasma microdischarges has been achieved. This is important because these strokes manifest as series of current and light pulses, lasting tens of nanoseconds and a few nanoseconds respectively. I have first of all carried out a detailed investigation of the typical properties of these events and of their evolution in space and time in the course of the BD and FD, which is presented in Section 5. The exact mechanisms of interaction between the weakly ionized gas and neutral air are still debated. It is nevertheless commonly believed that collisional processes involving plasma species and neutral molecules of the background air are responsible for momentum transfer and for the consequent airflow induced by the discharge. In the following experiments I have thus focused mainly on the properties of current microdicharges, which are related to the movement of charge particles inside the air gap. Several SDBDs with different

geometrical configurations and operating parameters have been considered, and their aerodynamic potentialities have been evaluated in terms of local velocity of the electric wind, which has been measured by means of a Pitot probe. These results are presented in Chapter 6 together with the energy consumed by plasma actuators in the course of a voltage cycle. The power required by a flow control actuator is in fact a quantity that has to be taken into account when practical applications are considered. In several cases a sort of saturation of the induced airflow has been observed, meaning that its velocity can't exceed a certain level, despite an increase of the applied voltage or consumed power. In Chapter 7 experiments aiming to understand the origin of this evidence are discussed. An analysis method of current pulses performed at this purpose turned out to be also interesting for the determination of the system capacitance by means of Lissajous figures, as described at the end of the same chapter. Eventually, during my Ph.D. thesis I proposed to adopt the Background Oriented Schlieren (BOS) technique for the visualization and characterization of the airflow induced by the discharge, and thus for future investigations concerning the interaction between plasma and background air. BOS is a completely non-intrusive optical diagnostics that is sensitive to gradients of the refractive index as the conventional Schlieren method, with the advantage of a simpler and more versatile setup. The main features of this technique are presented in Chapter 8, together with the description of how it has been implemented and adopted at University of Milano-Bicocca.

CHAPTER 2

Non-Thermal Atmospheric Pressure Discharges

2.1 Introduction

A simple way to produce a plasma consists in applying a sufficiently high electric field to a neutral gas. Both laboratory and natural plasmas can be divided into thermal and non-thermal plasmas. A plasma contains electrons, ions and neutral species, and the average kinetic energy of these components can be different, so that these species can be characterized by their own temperatures. In particular, in many conditions the electron temperature

is higher than the heavy particle ones because of their considerably smaller mass, whereas thermal equilibrium requires the same temperature for all species. For low-temperature laboratory plasmas, this subdivision is mainly related to gas pressure and discharge gap: high pressures and long gaps imply many collisions and mean free paths short compared to the discharge length, thus favouring thermal equilibrium [1]. In thermal plasmas (such as torches and electric arcs) the gas temperature is very high (from 5000 to 20000 K) [2]. Non-thermal plasmas are instead characterised by an electron temperature (in the range of 1-10 eV) much higher than the ion and macroscopic gas temperatures (not exceeding ambient temperature significantly), since the applied electrical energy primarily produces energetic electrons instead of heating the gas [3]. These electrons collide with the background gas, thus producing additional electrons and ions as well as excited species and free radicals. Several chemical reactions forbidden in similar environmental conditions can thus be initiated: a great advantage of non-thermal plasmas is that they offer high energy efficiency and selectivity of plasma chemical reactions. Just to mention a couple of examples, in the surface modification field these plasmas can efficiently initiate several advantageous physical and chemical processes, while in pollution control applications excited and reactive species of non-thermal discharges reduce, decompose or oxidise pollutants (differently from thermal incineration processes in which the entire gas stream is heated) [4]. Moreover, the cold or non-thermal discharges can be used for treatment of temperature sensitive materials, allowing o extend their range of applications beyond traditional uses.

Among non thermal-plasmas, atmospheric pressure cold plasma discharges are increasingly taken into consideration as an interesting alternative to low pressure plasmas, since the possibility of avoiding the use of vacuum systems favours the technological transfer of promising plasma processes, which are appealing for several applied physics sectors, such as surface modification,

medicine and gas treatment [5–9]. Non-thermal plasmas can be produced by a variety of sources. Dielectric barrier discharges (DBDs) are often chosen because of their simplicity and versatility [8]. Most of this chapter is dedicated to the description of the properties of DBDs.

2.2 Dynamics of Charged Particles and Electrical Breakdown

Let's consider for simplicity a plane gap of length d that separates two electrodes maintained at a voltage difference V. If a free electron is present inside the gap its motion is influenced by the presence of the homogeneous electric field $E = V/d$, which accelerates it along the field lines and towards the anode. Elastic collisions with molecules of the background gas randomize the electron motion in the three directions. In these events the direction of the electron velocity is modified but just a small change of the electron velocity modulus and kinetic energy occurs, being the electron mass (m_e) much smaller than heavier background gas particles (M_g) [10, 11]. The fraction of electron energy loss is in fact of the order of $\delta = 2m_e/M_g$ (approximatively $4 \cdot 10^{-5}$ for a nitrogen molecule). Averaging over several collisions and scattering angles, one finds that the memory of the initial velocity is lost in few events. Along the field direction, electron velocity is reduced in a collision and then increased again by the field, and the average electron moves with a terminal steady velocity parallel and opposite to the electric field, known as *drift velocity* v_d and equal to

$$\mathbf{v_d} = -\frac{e}{m_e \nu_m}\mathbf{E}, \tag{2.1}$$

where e stands for the electron charge and ν_m is the frequency of collision for electron momentum transfer through elastic collisions (see Figure 2.1) [12]. The mobility μ_e is defined as the proportionality coefficient between the electron drift velocity and the electric field. The effective collision frequency

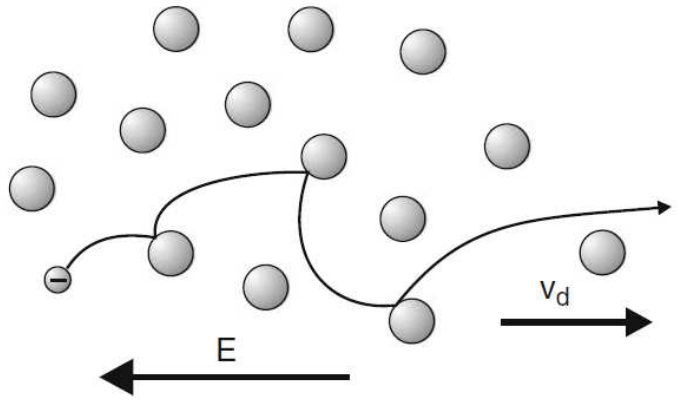

Figure 2.1: Motion of an electron in an homogeneous electric field E. Elastic collisions with neutral atoms interrupt its trajectory, and on average the electron moves at the drift velocity v_d along the E-field direction [12].

and consequently the mobility depend on the electron energy, but simple models treat them as constant. For air a reasonable effective value for $\mu_e p$ is $0.45 \cdot 10^6\,\mathrm{cm}^2 \cdot \mathrm{Torr/V \cdot s}$ in the range $E/p = 4 \div 50\,\mathrm{V/cm \cdot Torr}$, corresponding, at atmospheric pressure, to $\mu_e \approx 6 \cdot 10^2\,\mathrm{cm}^2/\mathrm{V \cdot s}$ in the range $E = 3 \div 38\,\mathrm{kV/cm}$ [13]. This value corresponds to a velocity drifts equal to $1.8 \cdot 10^6\,\mathrm{cm/s}$, $5.9 \cdot 10^6\,\mathrm{cm/s}$ and $1.8 \cdot 10^7\,\mathrm{cm/s}$ at $3\,\mathrm{kV/cm}$, $10\,\mathrm{kV/cm}$ and $30\,\mathrm{kV/cm}$ respectively. The latter is the electric field necessary for breakdown in air at atmospheric pressure. The dynamics of electrons is determined not only by the directed average motion known as drift but also by their random thermal motion. At $300\,\mathrm{K}$ the average thermal velocity for electron is about $1 \cdot 10^5\,\mathrm{m/s} = 1 \cdot 10^7\,\mathrm{cm/s}$, higher than v_d for moderately electric fields. Similar consideration can be done for ions, but in this case the energy exchange with neutrals in elastic collisions is very efficient, because of their similar masses. The mobilities of ions is defined in a way analogous to that of electrons, but it is considerably lower than the electron one. For air at atmospheric pressure $\mu_i \approx 2\,\mathrm{cm}^2/\mathrm{V \cdot s}$ and $v_d \approx 7 \cdot 10^2\,\mathrm{m/s} = 7 \cdot 10^4\,\mathrm{cm/s}$ at $30\,\mathrm{kV/cm}$ [14, 15], whereas the average thermal velocity at $300\,\mathrm{K}$ is equal to about $450\,\mathrm{m/s} = 4.5 \cdot 10^4\,\mathrm{cm/s}$. The contribution of ions to electric current

density j and conductivity σ is small and the current is carried by electrons:

$$j \approx -en_e v_d = en_e \mu_e E = \sigma E. \tag{2.2}$$

Both j and σ depend on the degree of ionization of the weakly ionized gas.

If their density is spatially non uniform, electrons and ions undergo diffusion too [13]. In the presented description electron-ion interactions have been neglected because encounters of charged particles are rare in weakly ionized plasmas, and the motion of electrons and ions is governed by the applied electric field and collisions with the atoms of the background gas. Thus, elastic and inelastic collisions (excitation and ionization) dominate over Coulomb interactions among charged particles. Since most of the electron collisions are elastic, therefore, inelastic collisions (in which electrons lose a large fraction of their energy) have been neglected in the calculation of the drift velocity. However, considerable inelastic losses become important at electron energies higher than 10 eV [11]. These energetic electrons can arise from their motion in high-strength electric fields or can belong to the high energy tail of a Maxwellian group of electrons.

The dynamics of electrons and their interaction with neutral particles is the basis for the creation of a non-thermal laboratory plasma. Electric breakdown happens when an initially insulating material (a gas in our case) begins to conduct current as consequence of the application of a sufficiently strong electric field [5]. Even though the breakdown is a rather complicate process strongly depending on the system conditions, it always begins with an electron avalanche, which consists in the multiplication (in cascade ionization) of some primary seed electrons moving under the influence of an external electric field. As a matter of fact, we can imagine the occasional formation of some primary electrons near the cathode, either by the action of cosmic rays or as a consequence of field emission from asperities on the surface, close

to which the electric field is enhanced [11]. In the course of their drift to the anode, if their energy is sufficiently high, these electrons can undergo ionizing collisions with atoms, producing electron-ion pairs (Figure 2.2). These new electrons start moving towards the anode and can contribute to the production of new charges. In each ionizing collision a new electron is formed, and the result is a cloud of electrons travelling toward the anode, known as electron avalanche, and a cloud of ions, remaining behind it, almost stationary in the time scale of motion of the electron avalanche. The avalanche

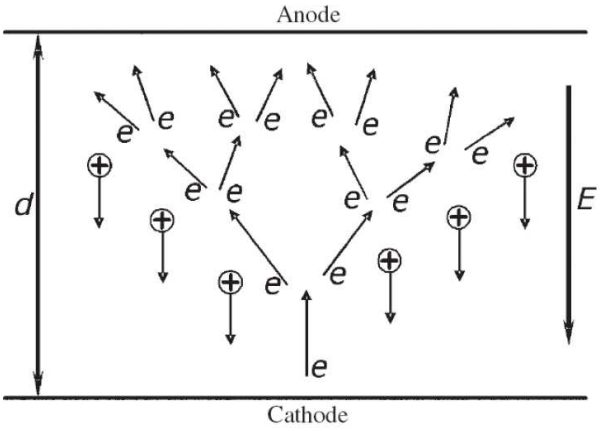

Figure 2.2: Illustration of an electron avalanche initiated by a primary electron moving from the cathode to the anode [5].

develops both in time and in space, because the multiplication of electrons proceeds with their drift from the cathode to anode. The rate of ionization can thus be conveniently characterized by the probability per unit length that a new electron is created. This is the first Townsend's coefficient α [13]. In electronegative gases (like air) we must take into consideration also the second Townsend's coefficient β, defined as the probability per unit length that an electron of the avalanche is lost in an attachment process, that is a binary collision in which an electron is captured to form a stable negative ion. In this case we can define an effective ionization coefficient $\alpha_{eff} = \alpha - \beta$. The following equations describe the variations in the number of electrons

(dN_e), positive ions (dN_+) and negative ions (dN_-) as the avalanche moves forward a distance dx [13]:

$$dN_e = N_e(\alpha - \beta)dx = N_e \cdot \alpha_{eff} \cdot dx, \tag{2.3}$$

$$dN_+ = N_e \cdot \alpha \cdot dx, \tag{2.4}$$

$$dN_- = N_e \cdot \beta \cdot dx, \tag{2.5}$$

where N is the number of particles of the considered species before the avalanche goes through dx. Electron-ion recombination can be neglected because the ionization degree is very low during the breakdown phase. If the x axis points from the cathode (placed in $x = x_0 = 0$) to the anode and if $N_{e0} = 1$, the following integrated equations give the spatial evolution of charges in an avalanche produced by a primary seed electron:

$$N_e(x) = N_{e0} \cdot e^{(\alpha-\beta)(x-x_0)} = e^{(\alpha-\beta)x} = e^{\alpha_{ff} \cdot x}, \tag{2.6}$$

$$N_+ = \frac{\alpha}{\alpha-\beta}(N_e - 1) = \frac{\alpha}{\alpha-\beta}(e^{(\alpha-\beta)x} - 1) = \frac{\alpha}{\alpha_{eff}}(e^{\alpha_{eff} \cdot x} - 1), \tag{2.7}$$

$$N_- = \frac{\beta}{\alpha-\beta}(N_e - 1) = \frac{\beta}{\alpha-\beta}(e^{(\alpha-\beta)x} - 1) = \frac{\beta}{\alpha_{eff}}(e^{\alpha_{eff} \cdot x} - 1). \tag{2.8}$$

All the produced electrons move along the non-disturbed electric field lines at the drift velocity, but at the same time diffusion makes them spread radially around the centre of the avalanche. The result is that the electron density radially decreases as a gauss function. The radius of the avalanche increases in time and with the spatial propagation of the avalanche. When the number of negative charges created in the avalanche is high (without attachment this means $N_e = exp(\alpha x) \approx 10^6$ and thus $\alpha x \approx 14$), the electrostatic repulsion among electrons dominates over their diffusional spreading, and the avalanche head broadens abruptly. Once the electron cloud size becomes comparable to one ionization length α^{-1} the distance among charges

of opposite signs is comparable with that among charges of the same sign and the attractive force due to the positive ions avoids any further repulsive spreading of electrons. The maximum transverse size of the avalanche head is thus of the order of $\alpha^{-1} \approx 1\,\mathrm{mm}$, since the first Townsend's coefficient for atmospheric pressure breakdown fields in air ($30\,\mathrm{kV/cm}$) is typically $\alpha = 10\,\mathrm{cm}^{-1}$. When the avalanche reaches the anode, the spatial distribution of ions has a nearly conical shape with a summit of maximum density at the anode (Figure 2.3). Most electrons will be drawn to the anode except for some few that are bound by the positive ion column.

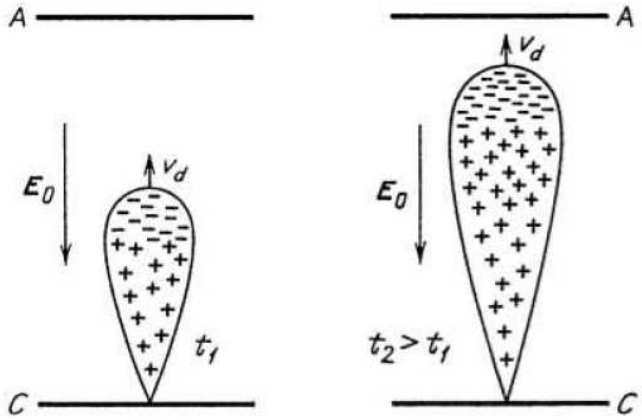

Figure 2.3: Shape and charge distribution of an electron avalanche at two moments t_1 and $t_2 > t_1$. During their drift from the cathode (C) to the anode (A) electrons leave behind a cloud of positive ions [13].

After this initial stage the following development of the discharge depends on several parameters as gas composition, pressure, distance between electrodes, frequency of the applied field and geometry of the system. For electrical breakdown to occur, however, a secondary mechanism is necessary for regeneration of the avalanche [16]. At relative low values of the product between pressure and gap length (pd) the initial avalanche proceeds until the anode and the plasma fills the whole discharge region. After a long series of successive avalanches sustained by secondary electron emission at the

cathode, a conducting path is established between the electrodes. This is the Townsend breakdown mechanism, described in Section 2.2.1. For higher *pd* values, the avalanche ionization can generate a great number of electrons giving rise to a localized space charge which strengthen the external electric field and favours photoionization as secondary emission mechanism. The electron avalanche is enhanced and luminous fronts propagating towards the electrodes, known as *streamers*, are created. A conducting path is established between the anode and the cathode in a time comparable to the electron transit time, so the so-called streamer breakdown, described in Section 2.2.2 requires much less time than the Townsend one. If no means are taken to limit the current in the system, this is only the initial stage of an arc discharge, in which high temperatures of the gas are reached.

2.2.1 Townsend Breakdown Mechanism

The Townsend breakdown mechanism is sustained by secondary electron emission caused by positive ions that hit the cathode at the end of their drift inside the gap. Since the kinetic energy of incoming particles is usually not high enough for an effective knocking out of electrons from the cathode surface, this process is possible because of field distortion provoked by an ion approaching the cathode within a distance of atomic dimensions. If we consider a gap of length d, each primary electron coming from the cathode produces an avalanche with

$$N_+ = \frac{\alpha}{\alpha_{eff}}(e^{\alpha_{eff} \cdot d} - 1) \tag{2.9}$$

positive ions in the gap (see Equation 2.7), each one moving back to the cathode. If we define the third Townsend's coefficient γ as the probability that a secondary electron is generated from an ion impact against the cathode [5], the number of secondary electrons produced by the ions of the primary

avalanche is $\gamma \cdot N_+$. In order to have a self-sustained discharge, positive ions generated by a single electron avalanche must produce at least one electron to start a new avalanche [11]. Consequently, the simplest Townsend breakdown condition can be expressed as

$$\gamma \frac{\alpha}{\alpha_{eff}} (e^{\alpha_{eff} \cdot d} - 1) = 1 \tag{2.10}$$

The secondary electron emission coefficient γ depends on the cathode material, on the state of the surface, on type of gas and on the ion energy; its typical value in electric discharges is $0.01 \div 0.2$ [5, 11].

2.2.2 Streamer Breakdown Mechanism

The already discussed Townsend mechanism of breakdown, which is relatively homogeneous and includes the development of independent avalanches that evolve via secondary cathode emission, is predominant at low pressure. In larger gaps, at higher pressures and considerable overvoltages, the avalanches essentially disturb the electric field and they are no longer independent, leading to the streamer and spark mechanism of breakdown. In this case the breakdown of the discharge is achieved much faster than predicted by the multiplication of avalanches through secondary electron emission at the cathode. This process can be ignored because ions don't have time (about $10\,\mu$s at atmospheric pressure for $d = 1\,$cm and $E = 30\,$kV/cm) to cross the gap, since the formative time lags of sparks at atmospheric pressure have been measured to be about $10^{-7}\,$s or less. This is comparable with the time of flight of an electron from the cathode to anode (about $100\,$ns at atmospheric pressure for $d = 1\,$cm and $E = 30\,$kV/cm), or even faster. Moreover, at atmospheric pressure the sparking potential has been found to be largely independent of the cathode material, whereas the Townsend's theory, even though somewhat insensitive to the value of gamma at higher

pressures, requires a definite dependence of the order of 10 percent on the value of γ [17].

Even though the precise boundary values of pd at which the breakdown mechanisms replace each other is not completely understood (in the range $200 \div 5000\,\mathrm{Torr} \cdot \mathrm{cm}$) [13], it is clear that the mechanism of the breakdown at low values of pd essentially differs from that at higher pd. The latter, as well as the Townsend one, is primarily related to the avalanches, but they cannot be considered as independent and stimulated by electron emission from the cathode. A qualitative picture of the process was evolved by Loeb and has been placed on a quantitative basis by Meek [18, 19]. The theory is based on the concept of the growth of a thin ionized channel (a *streamer*) between the electrodes. Streamers are produced by an intensive primary avalanche if the space charge inside it is large enough to create an electric field with a strength comparable to the applied electric field. This condition for streamer formation is also known as the Meek condition. If the distance between electrodes is more than a metre (or even kilometres long, such as in lightnings), individual streamers are not sufficient to provide breakdown on such a large-scale, and the so-called *leader* is moving from one electrode to another. The latter is like a much more conductive streamer, including streamers as its elements [13].

Space charge effects are due to the difference in the drift velocity of ions and electrons. Electrons run at the head of the avalanche, leaving ions behind. This spatial separation is of the order of the ionization length α^{-1}, that is the distance that an electron covers on average before producing a new pair of charges. This creates a sort of electric dipole with length α^{-1} and charge $N_e \cdot exp(\alpha x)$ [13]. The electric field related to this dipole (E') adds up vectorially with the external electric field E_0 (see Figure 2.4). The dipole formation provokes the appearance of the external electric field

distortion. The total electric field is maximum in front of the avalanche negative head and behind the positive tail. On the contrary, between the centres of space charges E_0 and E' point in opposite directions and the resulting filed is weaker than the external one. The total field also develops a radial component.

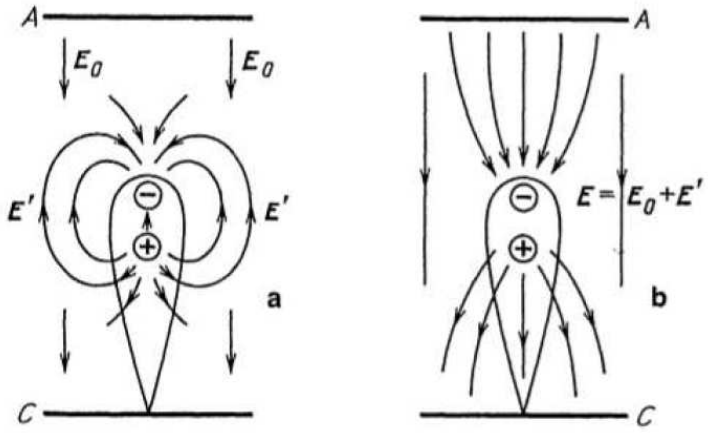

Figure 2.4: Distorsion of the external electric field E_0 in presence of a significant electric field E' due to spatial separation of electrons and positive ions inside an avalanche. On the left (a) the lines of forces associated to E_0 and E' are shown separately, whereas on the right (b) the resulting field is depicted [13].

Ionization processes are favoured and accelerated where the field is enhanced. The streamer formation is possible because of photoelectric ionization: electron impacts on neutrals in an avalanche produce not only a cumulative ionization but also many excited atoms and molecules. Some of them emit ultraviolet radiation in some 10^{-8} s which can be absorbed in the gas causing ionization. Consequently, part of these photons are responsible for photoionization in the vicinity of the avalanche. The field enhancement due to space-charge effects exerts a directive action on charged particles produced by photoemission, drawing them toward the negative or positive side of the dipole. Photoelectrons thus initiates secondary avalanches that intermix with the primary avalanche.

Cathode-directed streamer The qualitative change in avalanche behaviour takes place when the charge amplification $exp(\alpha x)$ is high, and the production of a space charge with its own significant electric field takes place. This effect becomes strong as charge multiplication continues and influences the subsequent process of ionization. At relatively small discharge gaps, the transformation occurs only when the avalanche reaches the anode. In this case the electrons sink into the electrode leaving the ions to occupy the discharge gap. At this point the total electric field is due to the external field, to the ionic trail and to the ionic charge image in the anode. The total electric field reaches the maximum value at the axial distance from the anode of the order of the characteristic ionization length α^{-1}. Electrons of numerous secondary photoelectron avalanches are pulled into the positive primary trail by the enhanced field, and create now photons that continue the process. They mix with the primary positive charges, thus creating a neutral plasma region. The positive ions left behind in secondary avalanches extend the positive space charge towards the cathode. As shown in Figure 2.5, this enhanced positive charge attracts the electrons from the next generation of avalanches and develops from the anode to the cathode as a *cathode-directed streamer* (or *positive spaced charge streamer*, or *streamer with a positive head*). It operates as a thin conductive needle growing from the anode, and at its tip the electric field is very high, stimulating the fast streamer propagation in the direction of the cathode. The velocity of propagation is extremely rapid, undoubtedly more rapid than the velocity of $2 \cdot 10^7$ cm/s of the initial electron avalanche. This is because it depends on photon propagation and photoionization and on the motion of electrons in high fields near the space charge (the electric field there is so high that it provides electron drift with a velocity of about 10^8 cm/s) [13]. Usually, the source of photons and seed electrons for secondary avalanches is sufficiently great and the streamer propagation is limited by the rate of neutralization of the positive space charge near the

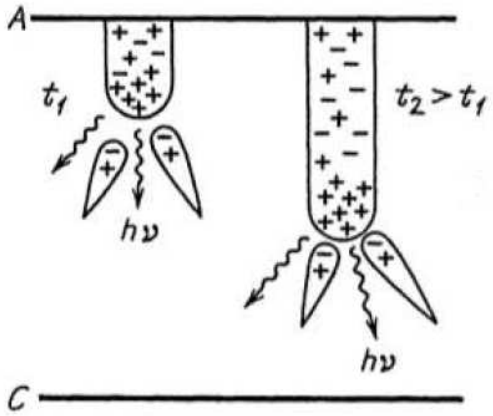

Figure 2.5: Cathode-directed streamer at two different moments $t_2 > t_1$, with secondary avalanches moving towards the positive streamer head [13].

tip of the needle. The velocity of propagation (growth) of the streamer is greater the longer it is and the stronger the external field is. To an order of magnitude, the measured velocities are about 10^8 cm/s, while the drift velocities in the external field are about 10^7 cm/s. The streamer channel diameter is comparable with the avalanche head diameter at the stage of maximum expansion, $10^{-2} \div 10^{-1}$ cm. At any rate, the charge density is not less than the maximum density in the avalanche, presumably, $10^{12}\ cm^{-3}$ [13].

Anode-directed streamer If the discharge gap and voltage are large enough, the avalanche-to-streamer transformation can take place quite far from the anode, because the electric field produced by the primary avalanche becomes comparable to the external one well before the electron drift towards the electrode is completed. In this case, the streamer is able to grow towards both the electrodes, mostly toward the anode if the avalanche has not yet gone far from the cathode (Figure 2.6. It is then called *anode-directed streamer* (or *negative streamer*, or *streamer with a negative head*). The mechanism of growth towards the cathode remains almost the same. In the direction of the anode it is also similar, but here electrons drift in the same direction as

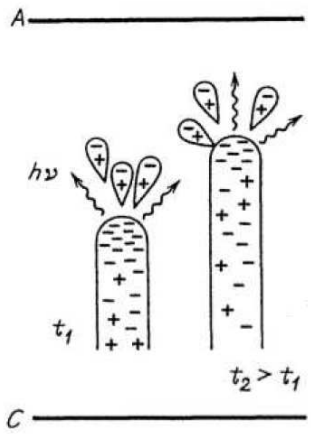

Figure 2.6: Anode-directed streamer at two different moments $t_2 > t_1$, with secondary avalanches moving towards the negative streamer head [13].

the front of the plasma streamer. The electrons of the head, moving rapidly in a strong total electric field, join the ionic trails of secondary avalanches and together form the plasma. Secondary avalanches can be initiated here not only by photons, but also by some electrons moving in front of the primary avalanche. Presumably, in this case a propagation mechanism without photons is also possible.

So, in the streamer breakdown mechanism, a strong primary avalanche amplifies the external electric field, leading to the formation of a thin weakly ionized plasma channel, the so-called streamer. A streamer is a conductor, so that electrostatically it acts as a metallic needle protruding from the surface of the anode (a perfectly conducting needle would be exactly at the anode potential). Since photons are emitted and absorbed in a random manner, situations are possible in which a new predominant direction appears for the propagation of a great number of secondary avalanches. This is a likely mechanism of generation of experimentally observed zigzag streamers and spark channels [17]. Electric field non-uniformities have a strong influence on breakdown conditions and the avalanche transformation into a streamer,

reducing the breakdown voltage for a given distance between the electrodes.

Once the conducting streamer channel connects the electrodes, the current can significantly rise and the streamer can convert to a spark: if no means are used to limit the current, the temperature of the gas will rise rapidly due to Joule heating. A simple solution to the problem is to place a dielectric barrier between the electrodes which prevents the electrons to reach the electrodes [8]. At this point, after the streamer channel is created, only a limited current for a short time can flow and the temperature of the gas remains quite low . This solution establishes a transient discharge which must be reactivate by the external circuit using an alternating or pulsed current power supply. These non-thermal plasma sources are called Dielectric Barrier Discharges (DBDs) and are described in Section 2.3.

2.3 Dielectric Barrier Discharges

A dielectric barrier discharge (DBD) is an electrical discharge between two electrodes separated by at least one insulating dielectric barrier [20]. This peculiarity allows to obtain a streamer discharge in which the current is restricted by charging of the dielectric layer. The electrodes are separated from the discharge volume, and this can be advantageous, for instance when highly aggressive gases are considered. In contrast to most other non-equilibrium discharges the dielectric barrier discharges are non-equilibrium gas discharges that can be operated at elevated pressures ($0.1 \div 10$ atm) [21]. One of the first reports of a dielectric barrier discharge was published in 1857 by Siemens, who observed a glow between two coaxial glass tubes with external electrodes while generating ozone [21].

When the external electric field is sufficiently high, a free electron in the gap produces secondary electrons by direct ionization and starts an electron avalanche. In certain cases, if the Meek condition is satisfied (see Section 2.2.2), the avalanche develops into a streamer discharge. After several

nanoseconds, the streamer filament reaches the dielectric barrier and builds up charges on the surfaces exposed to the plasma region. The discharge ceases as soon as the electric field associated to these surface charges and to the positive ions still in the gap is high enough to locally decrease the externally applied electric field to a level below breakdown voltage. The short duration of these *microdischarges* (dozens of nanoseconds [22]) leads to very low overheating of the streamer channel, and the DBD plasma remains strongly non-thermal. The presence of the dielectric barrier precludes dc operation: DBDs are usually driven by sinusoidal voltages (with frequency generally between 500 Hz and 500 kHz), but for some applications high-voltage pulses lasting some nanoseconds or a few tens of nanoseconds are also adopted. In the first case the increase or reversal of the applied voltage difference can lead to successive mircrodischarges even though charge accumulation on the dielectric barrier, whereas in the second case breakdown occurs in correspondence of each pulse.

It is important to clarify the terms streamer and microdischarge. An initial electron coming from some point in the discharge gap (or from the dielectric that covers the cathode) produces secondary electrons by direct ionization and develops an electron avalanche, followed by a streamer (or *ionizing wave*) that bridges the gap and forms a conducting channel of weakly ionized plasma. The group of local processes in the discharge gap initiated by the avalanche and developed until that current terminates because of local electric field collapse is usually called microdischarge. The principal microdischarge properties depend on the gas composition, pressure and electrode configuration. After the microdicharge current termination there is no more electron-ion plasma in the main part of microdischarge channel, but high level of vibrational and electronic excitation in the channel as well as charges deposited on the surface and ionic charges in the volume allow us to separate this region from the rest of the volume and call it *mi-*

crodischarge remnant. Interesting phenomena can occur due to the mutual influence of microdischarges. These are in fact related to the interaction of a microdischarge with residual charge left on the dielectric barrier and with the changes and excited species present in the gap. As a matter of fact, the self-termination of the discharge leaves a cloud of electrons and ions. In atmospheric pressure air it takes about 10 nanoseconds for the electrons to attach to molecular oxygen forming negative ions [13], and the electrons in the conducting plasma channel established by the streamers dissipate from the gap in dozens of nanoseconds. The residual ion cloud decays in microseconds due to recombination processes and drift or diffusion to the walls. If the next breakdown happens while the ions are still present or before the local heating has dissipated it will most likely follow the same path. That is why in many cases it is possible to see a stable pattern of the microdischarges in DBDs, even though each of them is short. Moreover, if a sinusoidal voltage is applied, when the voltage polarity reverses, the deposited charges can facilitate the formation of new avalanches and streamers in the same spot. As a result, a family of streamers is formed, which is macroscopically observable as a spatially localized bright filament. Sometimes the plasma decays and thermalizes completely before the next breakdown occurs so the streamers start at random locations each time. In this case the discharge appears uniform. The non fully dissipation of microdischarge remnant before the formation of next microdischarge is called memory effect.

In DBDs plasma is highly non-equilibrium with hot electron and cold heavy particles. This characterizes most applications, where energetic electron efficiently transfer energy through ionization, electron excitation, and electron impact dissociation, but not significantly through direct heating. Strong thermodynamic non-equilibrium and simple design are distinctive properties of these plasmas. Moreover, the possibility of operating at atmospheric pressure makes these discharges appealing for industrial applications.

Among them, which are comprehensively summarized by Kogelschatz [8] we cite ozone generation, high-power CO2 lasers, excimer lamps (as an UV-source) and plasma display panels [20, 23, 24]. In addition, DBDs in air are commonly adopted to treat polymer surfaces in order to promote wettability, printability and adhesion [8, 25, 26]. Another promising application is pollution control, to remove dust, CO, NOx and volatile organic compounds [27]. Among recent applications there are plasma medicine and sterilization, plasma assisted ignition and combustion, and plasma aerodynamics [28–32].

Several geometric arrangements are possible, both as volume and surface discharges, depending if the breakdown occurs across a gas gap or in proximity of the dielectric surface. As a matter of fact, Surface Dielectric Barrier Discharges (SBDs) are special types of configurations where the barrier fills the entire gap between the electrodes [33]. In this case, the gas discharge occurs at the electrode edges above and close to the surface of the dielectric material. SDBDs have a simple discharge design and the complete electrode arrangement can be incorporated in a single component in many possible geometries (tubular or plate-like). Due to these facts, this configuration can be advantageous for some of the already cited DBD applications,

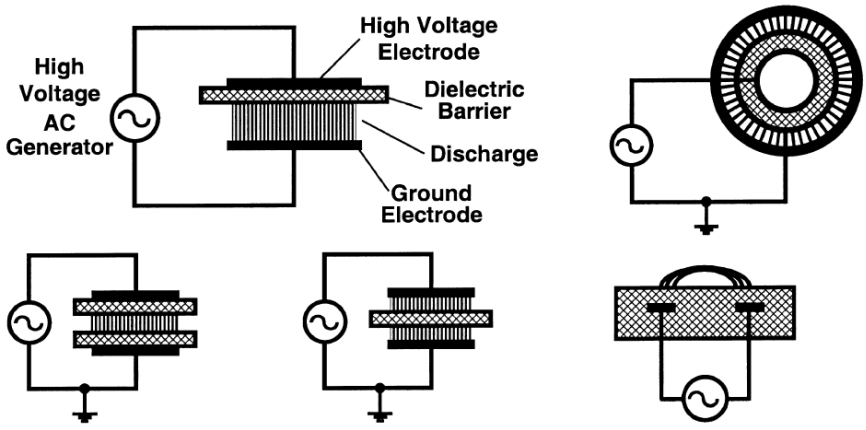

Figure 2.7: Examples of common dielectric barrier discharge configurations [34].

such as pollution control of exhaust gases [35], skin or wound treatment [29], and actuators for gas flow control [31]. Examples of planar and cylindrical configurations with one or two dielectric barriers are shown in Figure 2.7 [8].

2.4 DBD Discharge Modes

Usually dielectric barrier discharges work in a filamentary regime, in which the streamer breakdown leads to the formation of narrow microdischarges and memory effects (Section 2.3). However, in 1968 Bartnikas found that helium ac discharges between closely spaced plane parallel electrodes can exhibit diffuse glow discharge characteristics [36]. After this first observation, many research groups studied this particular regime finding, that stable diffuse discharges could be obtained in several gases including helium, neon, argon, nitrogen, oxygen, and air [37–39]. However, this diffuse regime remains extremely unstable and tends to convert to the more stable streamer regime.

Streamers can be avoided by using an applied electric field sufficiently low to prevent the achievement of the Meek's degeneration condition for primary avalanches (Section 2.2.2). As an alternative, the requirement for establishing a stable diffuse discharge is that the number of seed electrons is large enough to cause appreciable overlap and merging of the primary avalanches. This results in a smoothing of the field gradients due to space-charge at the stage when streamer formation would otherwise occur. The fundamental mechanism that ensures the presence of enough seed electrons is the so called Penning ionization [40]. A Penning mixture usually consists of a primary gas with a small admixture of impurities. If the components of an impurity B have a ionization potential lower than a metastable potential of the gas A, then the metastable atoms of the main gas can ionize the molecules of B according to $A^* + B \rightarrow A + B^+ + e^-$ (usually, the probability of this process is so high that very small admixtures may have considerable

influence on the discharge development). For example, in helium, which possess highly energetic metastable levels, the background nitrogen impurities may be enough for the creation of a Penning mixture. However, in presence of a sinusoidal excitation voltage, the amplitude and frequency that allow to obtain a diffuse discharge are limited, because if the slope of the voltage versus time is too high instabilities are induced.

The mechanism of the diffuse BD in nitrogen has not been completely understood yet. As already stated, the decisive criterion for the generation of a diffuse BD is the presence of charge carriers at a low electric field, i.e. a memory effect responsible for the production of primary electrons below the usual breakdown voltage [41]. The processes discussed in the literature for nitrogen are Penning ionization due to collisions with nitrogen metastable $N_2(A^3\Sigma_u^+)$ and electron emission from the dielectric surface because of desorption or secondary electron emission by nitrogen metastables [41,42]. This discharge regime is also called *atmospheric pressure glow discharge*,*glow silent discharge*, or *homogeneous barrier discharge* [34, 41, 43].

Molecular oxygen is an effective quencher of the metastable states ($O_2 + N_2(A^3\Sigma_u^+) \rightarrow N_2(X^1\Sigma_g^+) + O + O$ [42]. Another negative effect can be caused by electronegativity of molecular oxygen. Due to electron attachment ($O_2 + e^- \rightarrow O^- + O$), free electrons are removed from the discharge zone. Collisional quenching as well as electron attachment finally results in a reduction of seed electrons and thus in a qualitative change of the discharge mechanism (the transition from the diffuse to the filamentary mode). That's why breakdown in oxygen as well as in air usually consists of a number of microdischarges lasting tens of nanosecond, and randomly but uniformly distributed over the dielectric surface [8]. Discharges operating in the diffuse mode have been found for N_2/O_2 mixtures with very low O_2 content [42]

2.5 Radiative Properties of Atmospheric Pressure Air Plasmas

Plasma light emission is associated to de-excitation of electronic energy levels of atoms, molecules, ions and radicals. The brightest feature in the spectra of an air discharge is the Second Positive System (SPS) of molecular nitrogen. This emission is related to the de-excitation transitions of molecular nitrogen from the $C^3\Pi_u$ excited electronic state to the lower $B^3\Pi_g$ excited state according to

$$C^3\Pi_u \rightarrow B^3\Pi_g + h\nu \tag{2.11}$$

These states lie 11.0 eV and 7.4 ev above the ground state respectively. In a filamentary dielectric barrier discharge at atmospheric pressure, usually the First Negative System (FNS) of N_2^+ is generally observable, corresponding to the following transition:

$$B^2\Sigma_u^+ \rightarrow X^2\Sigma_g^+ + h\nu. \tag{2.12}$$

Figure 2.8 shows the wavelength collocation of the brightest bands of the SPS and FNS, whereas a partial energy level diagram of N_2 transitions is depicted in Figure 2.9 [44].

Filamentary and diffuse modes of DBD can be distinguished using current oscillography (current spikes in the case of a filamentary mode and long-lasting humps in the current signal in the case of a diffuse mode) or by optical emission spectroscopy [42]. For example, for discharges operating in the filamentary mode in air and binary N_2/O_2 mixtures, emission spectra were found to consist of several bands of the Second Positive System of molecular nitrogen, and of one band of the First Negative System of N_2^+, whereas in the case of the diffuse mode, no emission from the FNS was found in the spectrum, but peaks corresponding to NO and N_2O were found [42]. We will focus on optical properties of air at amospheric pressure. The following six elementary processes should be taken into account to describe the radiation

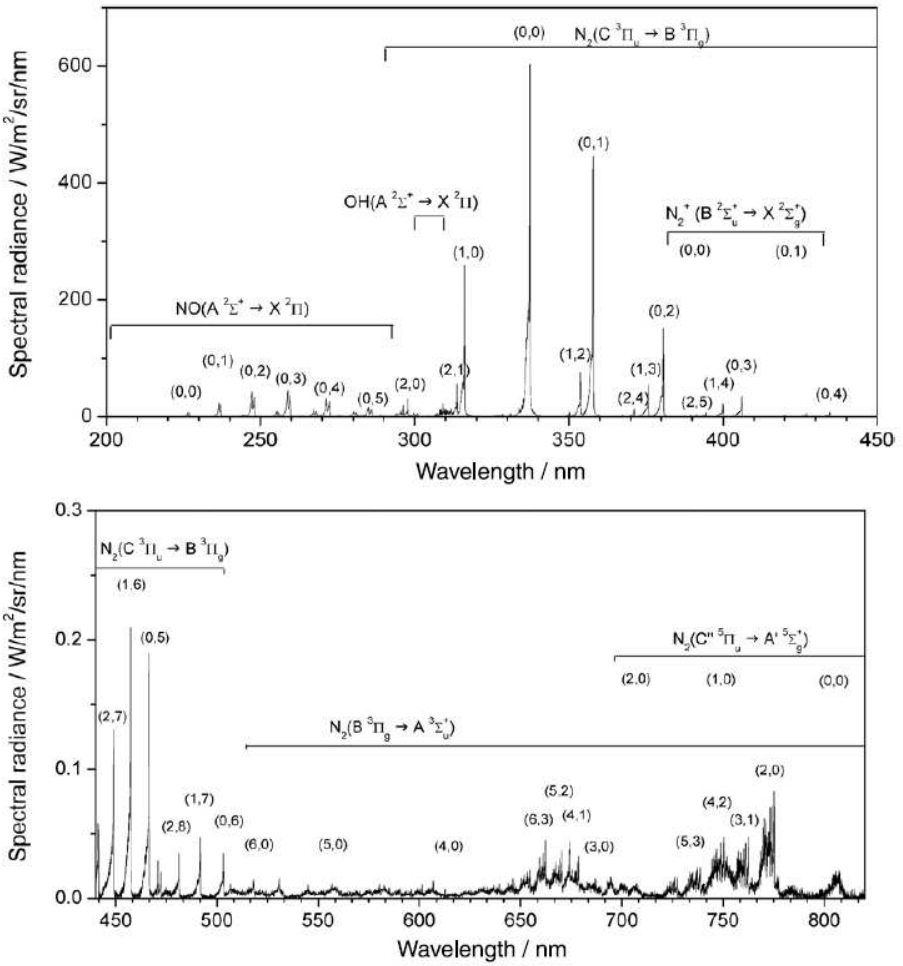

Figure 2.8: Typical spectrum.

kinetics for the 0-0 transitions of SPS and FNS at atmospheric pressure [42].

- Excitation of molecular nitrogen in the ground state by electron impact:

$$e + N_2\left(X^1\Sigma_g^+\right)_{\nu=0} \longrightarrow N_2\left(C^3\Pi_u\right)_{\nu'=0} + e \qquad \Delta E = 11.0\,\text{eV} \quad (2.13)$$

$$e + N_2\left(X^1\Sigma_g^+\right)_{\nu=0} \longrightarrow N_2^+\left(B^2\Sigma_u^+\right)_{\nu'=0} + 2e \qquad \Delta E = 18.7\,\text{eV} \quad (2.14)$$

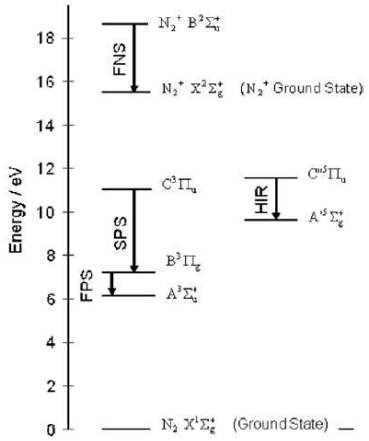

Figure 2.9: Energy level diagram.

- Spontaneous radiation of thus formed excited species:

$$N_2\left(C^3\Pi_u\right)_{\nu'=0} \longrightarrow N_2\left(B^3\Pi_g\right)_{\nu''=0} + h\nu \qquad \lambda = 337.1\,\mathrm{nm} \tag{2.15}$$

$$N_2^+\left(B^2\Sigma_u^+\right)_{\nu'=0} \longrightarrow N_2^+\left(X^2\Sigma_u^+\right)_{\nu''=0} + h\nu \qquad \lambda = 391.5\,\mathrm{nm} \tag{2.16}$$

- Collisional quenching of the excited species by the molecules of nitrogen and oxygen:

$$N_2\left(C^3\Pi_u\right)_{\nu'=0} + N_2 \longrightarrow \text{Products} \tag{2.17}$$

$$N_2\left(C^3\Pi_u\right)_{\nu'=0} + O_2 \longrightarrow \text{Products} \tag{2.18}$$

$$N_2^+\left(B^2\Sigma_u^+\right)_{\nu'=0} + N_2 \longrightarrow \text{Products} \tag{2.19}$$

$$N_2^+\left(B^2\Sigma_u^+\right)_{\nu'=0} + O_2 \longrightarrow \text{Products} \tag{2.20}$$

This model should be completed by including the vibrational kinetics of excited nitrogen, and in particular the processes

$$e + N_2\left(X^1\Sigma_g^+\right) \longrightarrow N_2\left(C^3\Pi_u\right)_{\nu'\geq 1} + e \tag{2.21}$$

$$N_2\left(C^3\Pi_u\right)_{\nu'\geq 1} + N_2 \longrightarrow N_2\left(B^3\Pi_g\right)_{\nu'-1} + N_2 \tag{2.22}$$

providing additional sources of the radiating species being considered. In air at atmospheric pressure, a stepwise excitation of molecular and ionized nitrogen is hardly possible because of very effective collisional quenching of excited states by molecular oxygen, so only direct electron impact has been taken into account [45, 46].

Since the radiative lifetimes of the excited species $N_2\left(C^3\Pi_u\right)_{\nu'=0}$ and $N_2^+\left(B^2\Sigma_u^+\right)_{\nu'=0}$ (44.5 ns and 65.8 ns, respectively) are considerably greater than their effective lifetimes (0.51 ns and 0.14 ns, respectively) because of the dominant collisional quenching [47], the observed spatio-temporal distributions of the luminosities for the FNS and SPS follow the reaction rates of the direct excitation reactions, with a time lag less than 1 ns. These reaction rates are directly proportional to electron density, while the rate constants are strongly dependent on electric field. Furthermore, under the conditions of non-equilibrium weakly ionized plasmas in air at atmospheric pressure, the mean electron energy is within the range of a few eV. Hence, it is only a very small fraction of electrons in the tail of the energy distribution that possess the energies exceeding the threshold values of the reactions 2.13 and 2.14. In such a case, the higher the threshold energy, the stronger is the dependence of the corresponding rate constant on the electric field [2]. Thus, the spatio-temporal distribution of the FNS signal represents approximately the development of the electric field E/n, while the SPS signal can be attributed to the convolution of the electric field and the electron density [47].

Results from Cross-Correlation Spectroscopy Recent results obtained with cross-correlation spectroscopy provide useful information for understanding micordischarge properties in dielectric barrier discharges at atmospheric pressure. This technique consists in replacing the measurement of the light pulse emitted from a single microdischarge with the statistically averaged determination of the correlation function between two optical signals, both originat-

ing from the same source [42]. The first of these signals is used as synchronizing signal, whereas the second one is the main signal. If the repetitive light sources reproduce each other sufficiently exactly and if the synchronizing signal occurs always at the same moment, the measured time delay between these two signals is a probability density function for the evolution of the light pulse intensity. In reference [47] results concerning three different types of DBDs have been presented (Figure 2.10). Two configurations

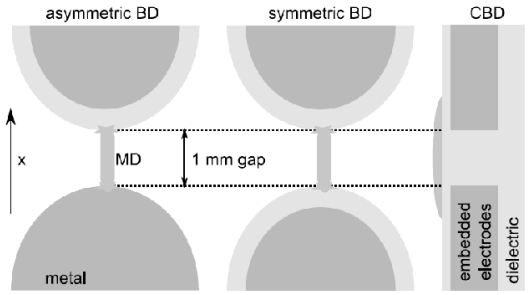

Figure 2.10: Electrode arrangements for the dielectric barrier discharge configurations studied in reference [47].

consist in two semi-spherical electrodes, separated by an air gap and one or two insulating layers. The last arrangement consists in a coplanar barrier discharge with both electrodes embedded into the dielectric. The evolution of the weak FNS emission was interpreted as the electric field E/n, whereas the SPS signal was attributed to the convolution of the electric field and the electron density. For all the electrode configurations they distinguished the following consequent phases of the MD development: a Townsend prebreakdown phase, a phase of ionizing wave propagation and a decay phase. They focused on the bands (0-0) of both the second positive and first negative systems. We report in Figure 2.11 these signals for barrier configurations with one insulated electrode.

The Townsend phase manifests itself as a weak but continuously growing glow in front of the anode, visible in the SPS signal (chosen as an indicator of the presence of the electrons) for $t < 15$ ns. The electric field in the

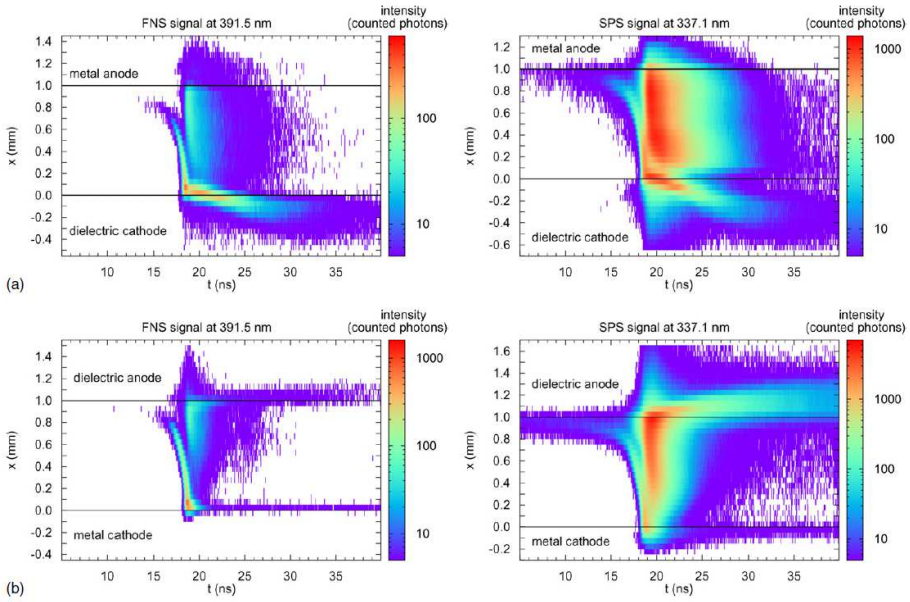

Figure 2.11: Spatio-temporal distributions of the discharge luminosity of the molecular nitrogen FNS and SPS [47].

discharge gap is quasi-stationary within the Townsend phase [48], whereas the electron density (and consequently the observed light intensity) grows exponentially in time due to the consecutive electron avalanches. The accumulation of electric space charge leads to the distortion of the electric field and to the formation of the cathode-directed ionizing wave (CDIW). Being waves of electric field, they are clearly seen on the plots for the FNS. In the case of CBD, the CDIW is accompanied by another ionizing wave (second wave) propagating over the anode surface in the opposite direction. The maximal velocity of the CDIW is reached at the moment before the CDIW impacts onto the surface of the cathode, and all maximal values are of the order of magnitude $10^6\,\mathrm{m}\cdot\mathrm{s}^{-1}$. The maximal velocity is obtained with the metal cathode, since positive ions (coming from avalanches of the Townsend phase) that have already been deposited on dielectric cathodes repulse the positive head of the ionizing wave. The impact of the CDIW onto the cathode surface results in a very fast rearrangement of the electric field within the

gap between the electrodes. This process is accompanied with the appearance of a radiating area within the MD channel. A first intensity maximum near the cathode is followed by a second intensity maximum near the anode. The long tail of luminosity on the cathode observed for the first negative system of nitrogen may be considered as an indication of the relatively high electric field remaining on the dielectric surface after the breakdown: the electric field near the cathode is higher than near the anode, and electron density, in contrast, is considerably lower. When the anode is metallic, the decay rate is slower: the MD development during this phase is determined by the properties of the anode since the absence of the accumulation of negative surface charge (electrons predominantly) on the metal anode (shortly after the CDIW crosses the gap) is responsible for no effective creation of electric field with opposite polarity. Eventually, when a metal cathode is considered, the authors describe the creation of the transient cathode layer similar to that in a glow discharge (with thickness of $30\,\mu$m and the radius $120\,\mu$m) after the impact of the CDIW onto the metal cathode surface; the electric field in this region stays enhanced for up to 150 ns. When nitrogen/oxygen mixtures are considered (with a percentage of oxygen sufficient for having a filamentary discharge) no noticeable influence of oxygen content upon the propagation of the cathode-directed ionizing waves can be observed, whereas the decay phase is the shorter the greater the oxygen content is: during this phase most of the electrons are in the region with a low and slowly decreasing electric field [45], so electrons disappear from the MD channel not only because of their drift and transition onto the anode surface, but due to electron attachment as well. Obviously, the greater the oxygen concentration, the higher the electron attachment rate is. Moreover, when a cathode-directed streamer propagates through a media enriched by negative ions, a lower field is necessary to produce seed electrons before the streamer, because of effective detachment processes, and the velocity of the streamer

is expected to be higher.

In a more recent work [49], the authors considered a surface dielectric barrier discharge with two needle electrodes placed at the opposite sides of a dielectric barrier, their tips facing each other with a gap of about 1 mm. The configuration is asymmetric because one electrode is exposed and the other is embedded into the dielectric and grounded. For the semi-cycle in which the voltage is positive, they found a discharge development similar for the configurations already discussed: a Townsend phase is followed by the formation of a cathode-directed ionizing wave. Its velocity is somewhat smaller that in the other arrangements (about $3 \cdot 10^5\,\mathrm{m} \cdot \mathrm{s}^{-1}$ at 0.2 mm from the anode) and decreases during propagation. The MD is driven forward in an external electric field decreasing in the cathode region, which might be a reason for the decreasing streamer velocity. Furthermore, surface processes could have a significant influence on the microdischarge development [50]. The results for both SPS and FNS and both semi-cycles are shown in Figures 2.12 and 2.13.

For the negative half period, instead, they observed a really faint FNS signal, appreciable mainly at the tip of the cathode, and a discharge spreading from the cathode to the anode. Their results suggest that seed electrons for electron avalanches are created in the high field region at the tip of the exposed electrode, similar as in negative corona discharges, and that the resulting avalanches develop along the decreasing electric field on the dielectric surface. On their way, no positive streamer could be detected. They consider this mechanisms similar to simulation results by Boeuf [51], where the discharge is proposed to be a glow corona-like discharge. The electrical measurements showed that the current pulses in the negative half period are significantly lower in amplitude. For volume arrangements they found a MD development inside the gap independent on the phase of the sinusoidal voltage. On the contrary, the propagation over the dielectric surface is influenced

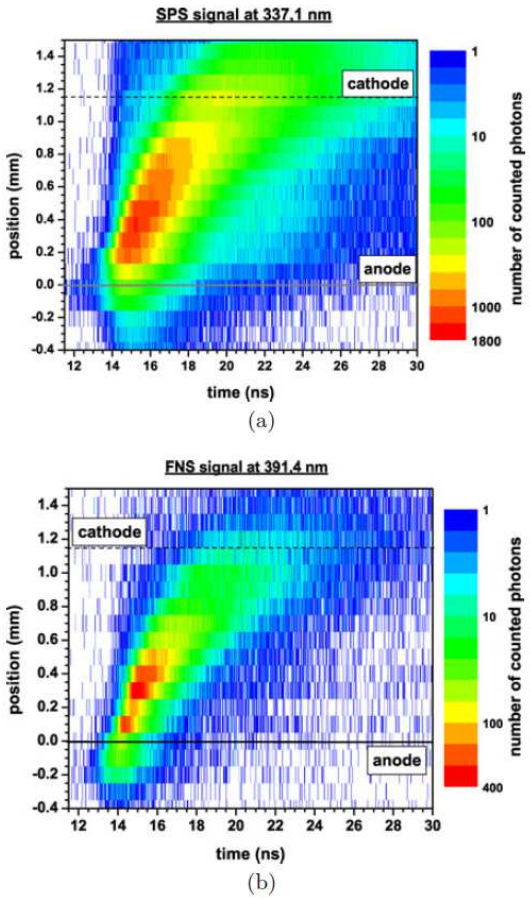

Figure 2.12: Spatio-temporal distributions of the discharge luminosity of the molecular nitroge FNS and SPS for the positive half-period of a surface dielectric barrier discharge.

by residual charges. They investigated this point for the positive half-period of the surface barrier [52]. They found that microdischarges of the same cycle chose the shortest paths available avoiding those already followed by previous microdischarges. These *forbidden zones* probably arise because of charging of the dielectric, which locally weakens the electric field. At these voltages (higher than the minimum voltage burning), behind the ionization front a second maximum of light emission is observable at the anode tip. For the following microdischarges both the velocity of the streamer and the anode light emission intensity increases. Behind the cathode directed ion-

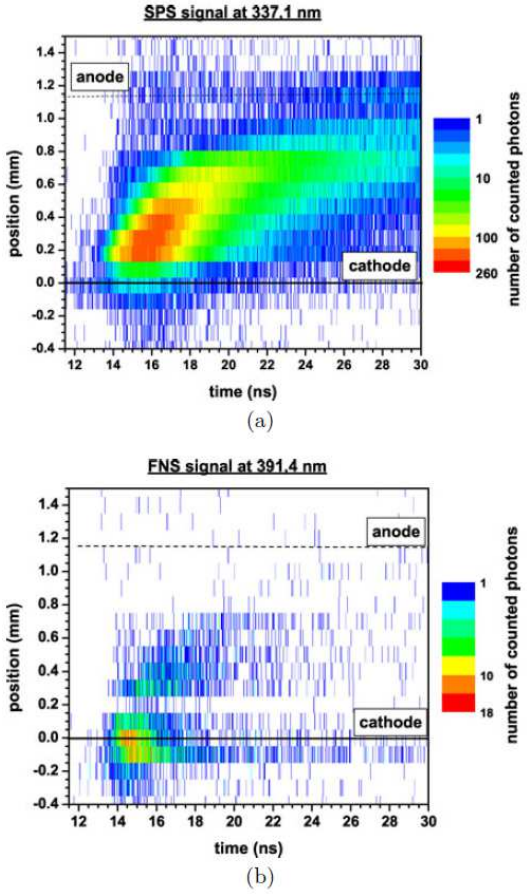

Figure 2.13: Spatio-temporal distributions of the discharge luminosity of the molecular nitroge FNS and SPS for the negative half-period of a surface dielectric barrier discharge.

ization front, electrons are drifting towards the anode. In this region the electric field increases again and electrons can gain further energy on their way to the anode. At higher voltage amplitude the electric field in front of the needle electrode reaches a value high enough for sufficient excitation of nitrogen molecules.

CHAPTER 3

Plasma Actuators

3.1 Boundary Layer Flow Control

Flow control consists of manipulating the properties of a generic moving fluid with the aim of achieving a desired change, but flow dynamics in proximity of a solid object is usually considered [53]. As a matter of fact, fluid flow over solid surfaces is a consistent and significant issue in many engineering applications. For example, it comes into play in pipe flow, engine design, and aerodynamics of automobiles and airplanes. In general, the fluid far from the body is relatively unperturbed by the existence of the object. In the simplest situation, this so-called *freestream* is characterized by a velocity steady in both modulus and direction (U_∞). On the contrary, the fluid near the body

is forced to flow around it, and its way is somehow altered compared to the rest of the flow. Moreover, the fluid directly touching the body experiences a frictional force from the surface that considerably reduces its speed, and an infinitesimally thin layer in which the fluid is stationary with regard to the body exists. This is the *no-slip condition*, meaning that the flow at the surface has the velocity of the surface. There must logically be a transitional region between this stationary layer and the freestream fluid, the so called *boundary layer*. By convention, the external frontier of the boundary layer is reached when $u = 0.99\,U_\infty$ [54]. The flow field around an object can thus be separated in two regions: an external zone in which the effects of viscosity are negligible compared to inertial effects (and the Navier-Stokes equations are reduced to Euler equations), and a region close to the body where viscosity and inertial effects are comparable. As a matter of fact, the concept of boundary layer has been introduced by Prandtl in 1904 in order to obtain approximated solutions to the Navier-Stokes equations describing the behaviour of a viscous fluid around a moving body [54]. The frictional force influences not only the fluid motion but the surface too: the latter feels a *shear stress* τ (Figure 3.1), defined as a force per unit area, tangential to the surface and directed as the flow.

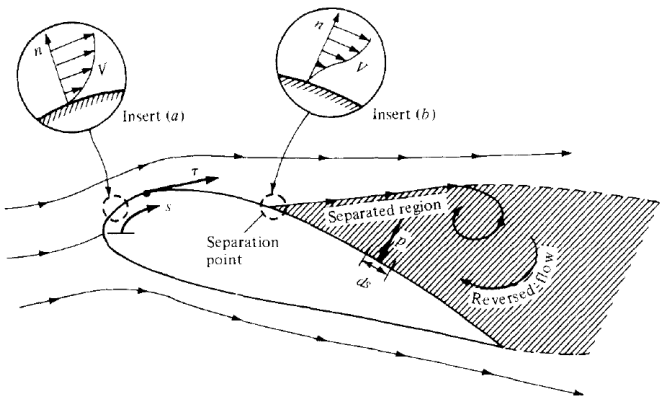

Figure 3.1: Effect of viscosity on a body in a moving fluid: shear stress and separated flow [54].

The field of *boundary layer flow control* includes any process through which a boundary layer is caused to behave differently than it normally would. Particularly, a broad and widely studied topic is the control of *flow separation*, occurring when the boundary layer peels away from the solid surface as the result of an adverse pressure gradient. This is commonly encountered in flows around the back of blunt obstacle. Let's thus consider the inviscid region (outside the boundary layer) of flow around the cylinder shown in Figure 3.2. Due to the space restriction imposed by the object,

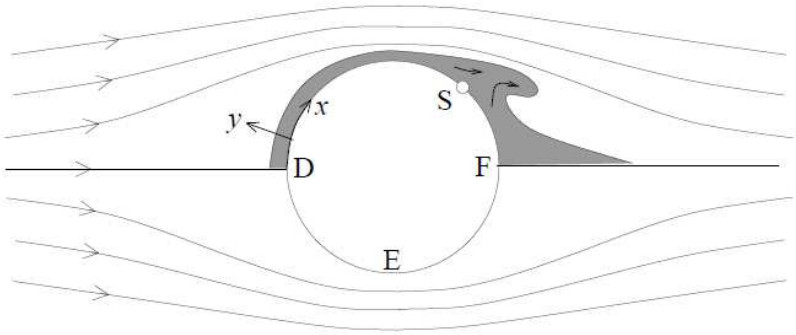

Figure 3.2: Flow around a blunt body: fluid elements are accelerated from the leading edge D to the point E (where the body thickness is maximum), and decelerated from E to the trailing edge F. The boundary layer (show in gray) detaches from the body surface downstream the separation point S.

the streamlines become more closely packed between points D and E, then space out again at the tail F. To maintain a constant throughput, therefore, the flow must speed up from D to E then slow down from E to F. The only impetus for acceleration and deceleration in inviscid flows are pressure gradients. So there must exist a pressure gradient $\delta p/\delta x < 0$ to accelerate the fluid along the surface x from D to E, and a gradient $\delta p/\delta x > 0$ to decelerate it again between E and F. For this inviscid part of the flow the fluid arrives at F with the same velocity it had in D. These increases and decreases of pressure are impressed on the boundary layer from the outside. The characteristics of the boundary layer thus depend on the amplitude and sign of

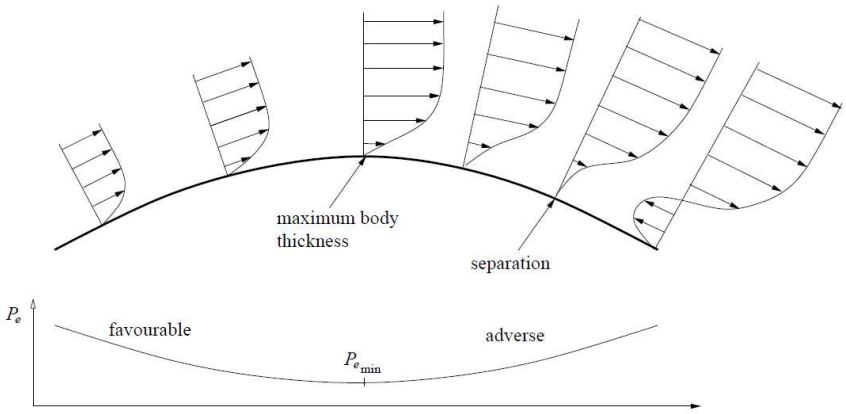

Figure 3.3: Pressure gradients and boundary layer separation.

these longitudinal pressure gradients. Negative pressure gradients have a favourable influence because they counteract the deceleration due to viscous effects on the surface, limiting the thickness of the boundary layer. On the contrary, when the external flow is slowed down by a positive pressure gradient, the particles in the boundary layer can have a low kinetic energy and thus difficulties in entering zones with higher pressures. The boundary layer then thickens and, if sufficiently high, the positive gradient can generate a detachment zone where the fluid flows in the inverse direction respect to the external flow, under the action of the adverse pressure gradient. The thickness of the detachment zone can be substantially higher than the thickness of the original boundary layer. This phenomenon is described schematically in Figure 3.1 and Figure 3.3: the separation point can be defined as the limit separating the direct flow from the reversed flow [54]. Therefore, in addition to the generation of shear stress, the influence of friction can cause the flow over a body to separate from the surface. Once separation has occurred, downstream the separation point a wake of recirculating flow typically appears, which differs drastically from the predictions of inviscid theory. In this region, the primary flow sees an altered body shape, and the net effect is the creation of a pressure distribution over the actual body surface that

results in an integrated force in the flow direction, a "suction drag" on the body, which is typically much larger than any viscous drag exerted by the boundary layer itself. The occurrence of separated flow over an aerodynamic body not only increases the drag but also results in a substantial loss of lift.

Boundary layers are typically described as laminar or turbulent, depending if path lines of various fluid elements are smooth and regular or if the motion of a fluid element is very irregular and tortuous. Because of the agitated motion of a turbulent flow, the high-energy fluid elements in the outer regions of the boundary layer are pumped close to the surface. Hence, the average flow velocity near a solid surface is larger for a turbulent flow rather than for a laminar one. Moreover, near the object surface, the velocity gradient in the direction perpendicular to the surface ($\delta U/\delta y$) are much larger for turbulent boundary layers. Because of this difference, drag and other frictional effects can be considerably less severe for laminar flows. Control over laminar-to-turbulent transition can be very beneficial: for aircrafts and cars this means better fuel efficiency, longer ranges, and higher speeds [53]. Moreover, turbulence suppression can play a fundamental role in acoustic noise reduction. An increase in turbulence can instead lead to better flow mixing, in the case of mixing layers for example. Moreover, because of the higher energy of the fluid elements close to the surface, a turbulent flow is less likely to separate from the body surface, and if separation occurs, the involved region will be smaller. As a result, the pressure drag due to flow separation will be smaller for turbulent flow. Thus, turbulent boundary layers are often preferred if there is a risk of separation, as the increased drag initially induced by the turbulent layer is still much less than the drag caused by separation. The lift at a given angle of attack can be increased by increasing the chamber, but the maximum achievable lift is limited by the ability of a flow to follow the curvature of the airfoil. The maximum lift and stall characteristics of a wing affect many performance aspects of aircraft

(including take-off and landing distances), as well as the range of operational conditions for a wind turbine and the manoeuvrability of a fighter jet. For these reasons, suppression of boundary layer separation is one of the main opportunities for flow control, and boundary layer control is of great practical importance in many fields, such as automotive industry, commercial and military aviation, as well as energy systems.

Flow separation control techniques can be categorized as active or passive methods, depending if energy is brought into the systems or not. Passive methods are mainly based on mixing high and low momentum fluid areas, by means of geometric changes such as vortex generators and slotted flaps or slats. A vortex generator is a small vertical plate positioned at a certain angle with respect to the local freestream flow. It creates eddies that mix the fluid inside the boundary layer and increase the near wall flow velocity. This approach of boundary layer manipulation is simple, does not require any power source to operate and is always operative. The freedom to choose the shapes and positions of the vortex generators on an airplane wing or turbine blade leaves many opportunities for optimization. On the other hand, vortex generators cannot adapt to changing flight conditions. A similar method, which is used to trigger the laminar-to-turbulent transition, is boundary layer turbulizers, consisting in the use of rough surfaces to trip the boundary layer and create vortices. Airfoils typically employ trailing edge flaps and leading edge slats that can be deflected during take-off or landing and stowed during cruise. Such devices enhance lift by increasing the camber of the wing, so that higher angles of attack, which are more subjected to stall, can be avoided. Traditional methods of preventing flow separation on high-lift airfoils utilize multi-element flaps that allow mixing of fluid between the upper and lower surfaces (called pressure and suction sides). The disadvantage is that these systems can create significant increases in mechanical complexity and weight of the aircraft, together with additional drag in

the cruise configuration. The replacement of conventional multi-element flap systems with a simple flap utilizing active flow control technology is a viable alternative. Passive control techniques are thus effective if the aircraft is operating in a flight regime that is in its design envelope, but in off-design conditions they can have detrimental effects that are often manifested in the form of increased drag. Active separation control has gained popularity in recent years due to its potential for maintaining or enhancing the benefits of passive control techniques without this penalty. The main difference is that active control can be turned on and off more easily, allowing additional flexibility. Moreover, active control strategies also have the potential to be implemented in a feedback system that, coupled with adequate sensors and controller, could create great benefits in flight efficiency [55]. These flow control techniques can be classified into three main solutions: fluidic, acoustic excitations or periodic forcing, and plasma. The most commonly used fluidic actuators are synthetic jets and boundary layer suction or blowing [56, 57]. The former are based on alternately ingesting and expelling fluid into the flow, in order to create vortices and a higher momentum boundary layer. Another method for increasing the boundary layer momentum is blowing, whereas suction consists in the removal of the flow moving at low speed. Methods belonging to acoustic excitation and periodic forcing are based on periodic disturbances of the boundary layer by means of acoustic waves or by moving bodies (such as ribbons, wires and small flaps) inducing local fluid motion [58]. These methods achieve the maximum efficiency at specific frequencies: the perturbation should be introduced with a period similar to the time necessary for the freestream flow to propagate over the separated region. The final class is plasma actuators, which have gained popularity in recent years and are the subject of next section.

3.2 Plasma Flow Control

Plasma actuators come in different discharge forms, such as direct current, radio-frequency, dielectric barrier and arc discharges [59–62]. Moreau has provided a review of plasma actuators working principles and research, focusing on two configurations that are mostly used because of their relatively simple geometry and operation, the surface corona discharge and the single dielectric barrier discharge [31]. The simplest corona discharge consists in two wires (flush-mounted on a dielectric surface) between which a dc high-voltage is applied. The DBD plasma actuator for aerodynamic flow control is instead usually composed of two electrodes (one insulated and one exposed to air) that are separated by a dielectric material and arranged in an asymmetric fashion as shown in Figure 3.4. Application of a sufficiently high-voltage signal between the electrodes weakly ionizes the air over the dielectric surface. The DBD plasma actuator generates a non-thermal self-limiting plasma in which the accumulation of charged particles onto the dielectric surface opposes the external electric field. Consequently, AC or pulsed high-voltages are required. In the perspective of using plasmas for airflow control, these types of discharges have the advantages that they can operate at atmospheric pressure and they do not require an electrode sticking out of the object to ionize the gas surrounding it. DBDs are often preferred over coronas because

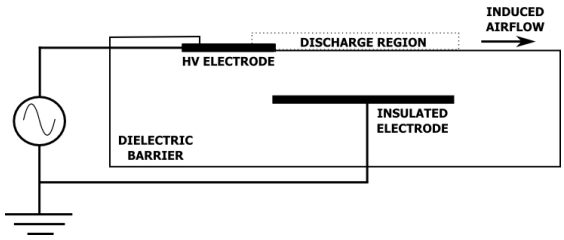

Figure 3.4: Schematic side view of a DBD plasma actuator. The electrodes are separated by a dielectric barrier, and the ground electrode is encapsulated so that plasma is created only at one side of the barrier. The arrow indicate the direction of the wind induced by the discharge.

are more stable at atmospheric pressure [63]. As a matter of fact, the dielectric barrier allows the generation of a non-thermal plasma by preventing the discharge from collapsing into an arc, which consume high power and induce high temperatures in the gas and electrodes.

For arc discharges and for DBDs sustained by high-voltage short pulses, an intense, localized and rapid heating produced by the discharge produces shock waves that interact with the flow surrounding the actuator [62,64,65]. The principle of operation of corona and dielectric barrier actuators is instead believed to be different, and is known as *induced wind*, *electric wind*, *wall jet* or *ionic wind* [31,32]. This indicate a directional flow, from the exposed electrode to the buried one for an asymmetric SDBD (as indicated in Figure 3.4) and from the anode to the cathode for a DC corona discharge with a thin anode [31, 66]. The believed working principle is momentum transfer from the accelerated ions to the surrounding fluid by particle-particle collisions. Despite their high drift velocities, the contribution of electrons is negligible due to their considerably smaller mass compared to the mass of neutrals. The typical spatial and temporal scales of gas-discharge processes are shorter than those of the resulting airflow scenario, so at spatial and temporal scales relevant for aerodynamic flow-control in first approximation a quasi-steady momentum is imparted to the surrounding airflow. As a result, the flow field changes such that a quasi-steady wall jet is developed under quiescent air conditions or an existing velocity profile is steadily manipulated. Other mechanisms like alterations of the physical properties of the gas (density, viscosity, etc) may eventually contribute to the coupling of the discharge with the airflow [67]. However it seems that this effect is negligible in the case of velocities below $30\,\mathrm{ms}^{-1}$. Indeed, only the effect of the electric wind in generally considered, excepted for high velocities.

Since DBD plasma actuators are operated with AC voltages, the underlying electrical field periodically changes its sign. This has led to ongoing

debates concerning momentum transfer details and about the temporal nature of the actuation. The community has still not reached an agreement about whether the plasma strongly pushes (accelerates) the flow downstream during one half cycle and weakly pulls (decelerates) it upstream in the other half cycle (the so-called *push-pull* mechanism) [68,69], or whether the plasma pushes the flow downstream in both half cycles (*push-push* theory) [70, 71].

Before the end of the nineties just a few papers about plasma flow control were published [72–76]. Then two groups started to work more continuously on this subject. The first one included people from the University of Poitiers (France) and the University of Buenos Aires (Argentina), focusing on the study of dc coronas for airflow applications [77, 78]. The second group was directed by J.R. Roth, from the University of Tennessee, who developed, in 1992, a surface discharge dedicated to decontamination, called One Atmosphere Uniform Glow Discharge Plasma (OAUGDP) [79]. In 1994 they proposed to use it for flow control, after having realized that this discharge could induce a secondary airflow of several ms^{-1} [80, 81]. We can say that airflow control by plasma actuators was born in 2000. The number of paper published on this subject has been increasing with years since that moment and, if one considers the works presented at the AIAA meetings, it becomes clear that the simplicity of these types of plasma actuators allowed many researchers in aerodynamics to work on this subject without necessarily being a specialist in plasma generation, and that's why this topic has considerably influenced research on airflow control.

Plasma-based control devices become especially attractive when moving parts have to be avoided and a fast time response is required. As a matter of fact, despite their effectiveness, mechanical devices have some drawbacks: they are complicated, add weight, have volume and are sources of noise and vibration. The main advantage of plasma actuators is that they directly convert electric energy into kinetic energy without involving moving mechanical

parts. Secondly, their response time is very short and enables a real-time control: the time needed for a surface barrier discharge to begin working at regime depends on the power supply characteristics, and generally it is in the order of tens of milliseconds [67], considerably smaller than the several seconds required for the aperture of flaps. It is thus clear that the contribution of plasma devices to flow can be essential in situations where actuation should intervene as soon as possible. The possibility of combining these actuators with sensors for the implementation of a feedback control system makes them even more attractive [55]. As a matter of fact, real aerodynamic flows are subjected to non-stationary perturbations that appear at different temporal scales. For instance, during a flight, the take-off and landing phases involve predefined changes in the lift and drag force occurring over large time scales (in the absence of safety manoeuvres). Conversely, atmospheric turbulence is sudden and intermittent, resulting in small time scale perturbations: in these cases, an efficient and robust control system has to consider these transient phenomena over a broad range of flow conditions, and the control system has to react autonomously. Other advantages are their simple construction, implementation and installation on models [55], whereas the main disadvantage is that high voltages are required and induced velocities of only about $10\,\mathrm{ms}^{-1}$ are usually obtained for an actuator constituted of a single DBD or corona device [31].

The use of surface plasmas in low-speed airflows has become a recent topic of interest in the field of airflow control. As a matter of fact, the induced flow has the characteristics of a jet with maximum velocity located at a few millimetres from the wall and this is often amenable for influencing boundary layers [82]. Despite the low induced velocity, the actuation can achieve the control objective at specific aerodynamic conditions. In fact, this directional flow has been demonstrated to be effective in boundary layer separation control [83–87], laminar-turbulent boundary layer transition delay [88],

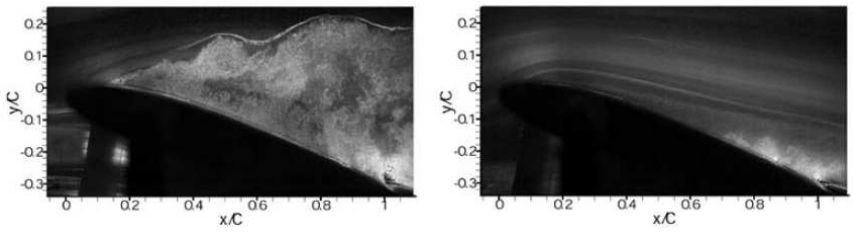

Figure 3.5: Flow visualization for a natural airflow (left) and for the same flow controlled by the plasma actuator ($U_{inf} = 20\,\mathrm{m/s}$, $\mathrm{Re} = 2.6 \cdot 10^5$, angle of attack equal to 16°). The actuator is a DBD driven with a sinusoidal voltage with frequency equal to 1 kHz and amplitude equal to 18 kV [104].

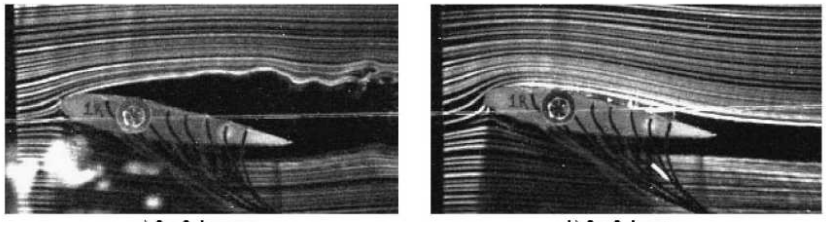

Figure 3.6: Flow visualization for a natural airflow (left) and for the same flow controlled by the plasma actuator ($U_{inf} = 2.85\,\mathrm{m/s}$, angle of attack equal to 8○). The actuator is composed of several DBDs driven with a sinusoidal voltage with frequency equal to 4.2 kHz and energized at 4.2 kV rms [105].

turbulent boundary layer manipulation [89], and vortex generation [90,91]. The mechanism responsible for separation control by DBD plasma is generally associated with the wall jet generation, but whether this results in boundary layer tripping, energizing or amplification of instabilities is still in debate and depends on the flow system under consideration. The exact location at which the plasma actuator accomplishes control is not immediately obvious, but actuators placed at or slightly upstream of the separation location give favourable results [85,92,93]. Studies have reported that actuators placed near the trailing edge of airfoils can produce lift-enhancement similar to plain flaps with deflections of a few degrees [94]. It is evident that the subjects of these studies are often wings or airfoils for flow separation control [84,93,95–98] as well as flat panels for a stabilization of boundary layers or for skin friction reduction [99,100], but flow separation behind other bluff

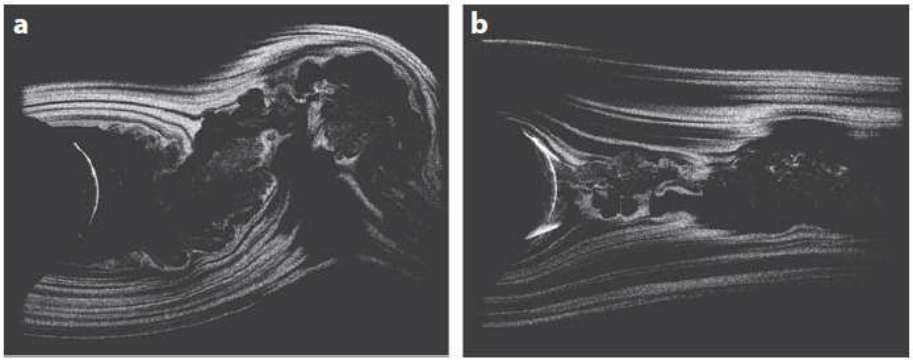

Figure 3.7: Particle-image-velocimetry images of the flow behind a circular cylinder at Re = 33000 without (a) and with (b) plasma actuators [32,106].

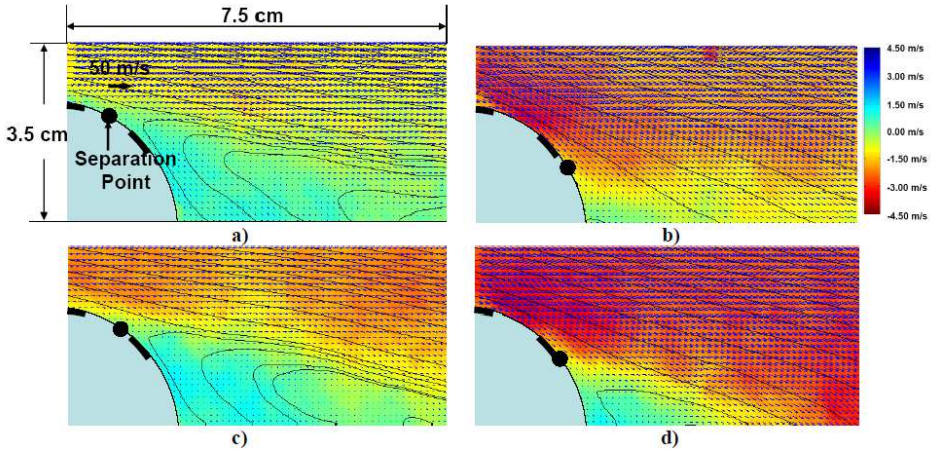

Figure 3.8: Mean flow field obtained from particle-image-velocimetry images without DBD at 15 m/s (a), with DBD at 15 m/s (b), without DBD at 20 m/s (c), and with DBD at 20 m/s (d). The DBD was operated with a sinusoidal voltage, with frequency and amplitude equal to 25 kHz and 12 kV respectively. Black curves are mean streamlines and the color map illustrates the vertical velocity. The separation points indicated by black dots are moved downstream by the actuator [83].

bodies such as cylinders has been studied too [83,86,101–103]. Examples of such experimental studies are shown in Figures 3.5 and 3.6 for airfoil models and in Figures 3.7 and 3.8 for cylinders. The velocity range investigated in most of these prior studies is from 0 to 15 m/s, but higher velocity ranges have been investigated, for examples for flow actuation on a cylinder or at the leading edge of a wing [84, 96, 107]. Initially dedicated to the control of

boundary layer and separated airflow, new applications have recently gained popularity, such as jet mixing [108, 109], noise control [110], and cavity flow manipulation [111, 112].

Like synthetics jets, in order to get the most effective performances of DBD actuators some excitation frequencies are preferable [113–115]: the actuator should be excited with a sufficiently high carrier frequency to produce the plasma ($1 \div 10\,\mathrm{kHz}$) and modulated at a lower frequency to excite the long wavelength instabilities associated with most separated flow dynamics. Many studies of separation control with DBD plasma actuators assume that the flow does not feel perturbations created by the high-frequency carrier signal. For the majority of low speed applications, this is true because the instabilities involved are not receptive to high-frequency perturbations and instead feel their effect as a quasi-steady phenomenon. However, it has been confirmed that the movement of charged species in the plasma does in fact create a perturbation at the frequency of plasma generation, giving possibility of using of DBD plasma actuators for high-frequency forcing applications if sufficient amplitude can be produced [116].

It has been shown that the force production of AC driven DBD plasma actuators is dependent on pressure and oxygen content of the environment [117, 118]. This has opened studies concerning the application of such devices at cruising altitudes in working flight environments questionable at this time. The variety of investigated flow control applications ranges from velocities of a few meters per second to supersonic conditions: plasma actuators have shown their good efficiency for airflow control at velocities up to $30\,\mathrm{m/s}$ and Reynolds numbers typically lower than a few 10^5 [31, 119], but some significant results have been obtained up to $110\,\mathrm{m/s}$ [31, 114]. The potentialities of dielectric barrier discharges concerning turbulent boundary layer suppression in a supersonic flow have been demonstrated, paving the way for plasma flow control actuators in scramjet engine applications [120].

However, significant work still remains to make these devices suitable for realistic flight applications. Namely, the performance of DBD plasma in harsh environments has not been fully explored, and the penalties associated with transporting power supplies capable of producing the high voltages necessary for plasma generation may prove costly. Nevertheless, the possible gains of an actuator that is simple to construction, lacks moving parts, exhibits no additional drag and is capable of high bandwidth excitation are too tempting to resist at this point in its maturation.

For supersonic and hypersonic flows other types of plasmas are generally tested, such as volume plasmas, spark jets, or dc discharges [121–124], but we recall in particular DBDs fed with nanosecond pulses [125–129]: these discharges seem to accomplish control based on thermal effects alone similar to arc filament-based plasma actuators [130].

CHAPTER 4

Experimental Setup and Diagnostics

4.1 SDBD Configuration

As already said in Section 2.3, DBDs are plasma sources whose main feature consists in the insertion of a dielectric layer within the discharge gap in order to prevent a direct current flowing between the electrodes. All plasma actuators presented in this work are surface dielectric barrier discharges, since the air above the dielectric panel is ionized by a sufficiently high electric field, and a thin plasma sheet glowing over the panel surface is generated (Figure 4.1). Its vertical extension does not exceed a few millimetres, based on visual inspection. Two different setup types were adopted in these experiments. The first one (setup A) was used for experiments concerning the

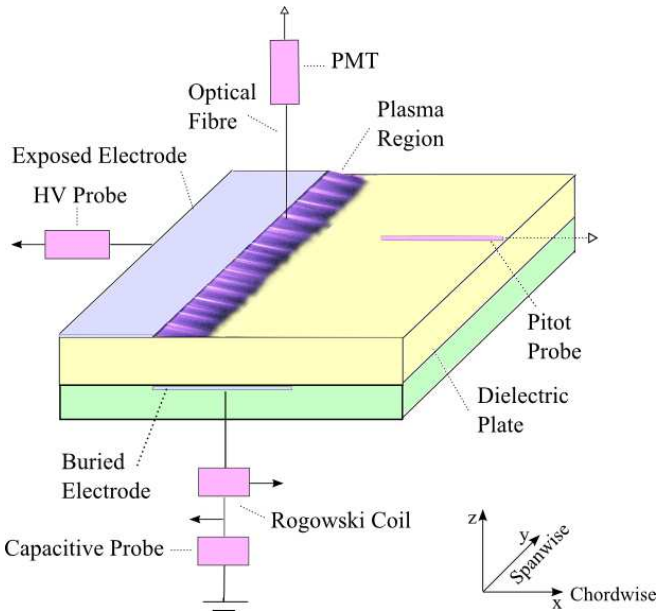

Figure 4.1: Experimental layout. The yellow and green regions indicate the insulating materials. The former is used as dielectric barrier, the latter prevents plasma to create on the buried electrode side. Light blue objects represent the discharge electrodes, whereas pink rectangles sketch the positions of the adopted diagnostics. Arrows mean that the probe outputs are connected to the oscilloscope.

optical and electrical characterization of plasma microdischarges (Section 5). The device (shown in Figure 4.2) consists of a pair of electrodes placed at the opposite sides of a square dielectric panel (3 mm thick, 200 mm side) and overlapping for 25 mm along the chordwise x-coordinate, so that the SDBD impedance matches fairly well the output impedance of the adopted power generation system (50 pF). We have used plexiglass as dielectric material, being one of the most common choices for aerodynamic applications [31]. The lower electrode (aluminum, 10 mm thick, 40 mm wide, 175 mm long) is grounded and buried in a plexiglass frame, preventing plasma formation on the lower side of the dielectric material. The upper electrode (aluminium adhesive tapes, 80 μm thick, 95 mm wide, 175 mm long) is glued onto the top of the dielectric panel and connected to the power supply. The somewhat overextended chordwise size, with respect to those usually employed in aerodynamic applications [32], as well as the buried electrode thickness,

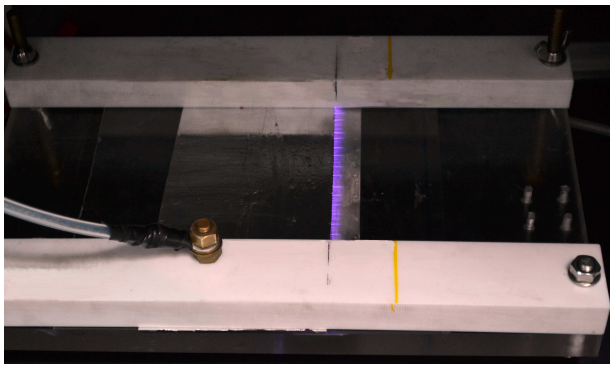

Figure 4.2: Picture of the first setup, in which a plexiglas sheet and the electrodes are embedded in a plexiglas and teflon scaffold, which is used to avoid unwanted discharges at the buried electrode side and allows the electrode connection to the HV and ground cables.

were chosen to provide a better separation between the HV supply line and the ground return cables.

In setup B, instead, the electrodes are tin clad copper adhesive tapes (60 μm thick and 200 mm long) placed at the opposite sides of a flat dielectric panel without overlap in the chordwise x-direction. The insulated electrode is 10 mm wide, whereas the air exposed one is just 5 mm wide. An insulating polyisobutylene self-amalgamating tape is used for avoiding discharges at the lower electrode side, but also upstream of the exposed electrode and at the spanwise electrode ends (Figure 4.3). Different voltages (up to about 30 kV peak amplitude), frequencies (in the range $10 \div 20$ kHz) and dielectric materials (teflon, plexiglass, mica, peek, delrin, etc) with various thickness were studied. However, this choice was not completely free, as the generator's ability to deliver a signal with a certain amplitude and frequency depends on the load capacitance.

The first configuration has the advantage of having a more separation and insulation of the HV and ground cables, allowing to run experiments for a longer time without undesired arc discharges at the electrode ends or near the cable-electrode junctions. The second configuration has instead been chosen because it is the one adopted for flow control experiments at Alenia

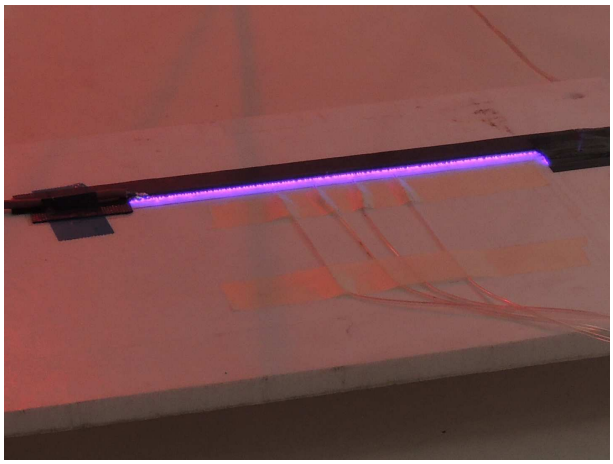

Figure 4.3: Picture of the second setup, in which both the electrodes are tin clad adhesive tapes, and a black polyisobutylene tape is used for avoiding discharges at the lower electrode side, upstream of the exposed electrode and at the spanwise electrode ends. The dielectric barrier in this case is teflon 12 mm thick.

Aermacchi. As a matter of fact, the absence of an insulating scaffold, the reduced electrode chordwise width and the use of adhesive electrode is suitable for experiments in wind tunnel, in which combinations of several actuators are often used. This second setup has been adopted at both University of Milano-Bicocca and Alenia Aermacchi Laboratories. Setup A has instead been used only at University of Milano-Bicocca.

4.2 Electric Power Supply

At University of Milano-Bicocca, the voltage difference between the electrodes is imposed by a resonant power generator (Tigres power supply V20 and voltage transformer ATV-20). The power output occurs in a power-controlled manner through variation of the frequency via an automatic impedance matching in the range between 3 kHz and 100 kHz. The exposed electrode is connected through a HV cable to the secondary coil of a transformer, whose primary circuit is linked to a tunable power generator [26,131]. The whole system constitutes a double resonant circuit: the frequency of

the signal is regulated in order to match the resonant frequency of the primary circuit (which depends on the selected power level) with the resonant frequency of the secondary circuit (which is given by the inductance of the secondary coil and by the capacitance of the SDBD). Consequently, the sinusoidal voltage amplitude and period are not independent. The power supply is composed by a current rectifier which brings the line current from 230 V AC to a 310 V DC. A transistor switching system create the AC current that is transferred to the primary winding of the high voltage transformer. For the powers and impedances generally utilized, the frequency of the signal is within 35 kHz and 45 kHz.

At Alenia Aermacchi the high-voltage power supply used was the MiniPuls 6 by GBS Elektronik GmbH. It consists out of a transistor bridge followed by a transformer cascade. The former is connected to a GW Instek SFG-2004 signal generator that delivers a - 5 V rectangle signal with modulation frequency equal to the voltage frequency desired for the high-voltage. The input voltage for the bridge of the MiniPuls is produced by a 30 V DC laboratory power supply unit. Within the bridge, this voltage becomes modulated with the signal-generator frequency through an oscillating circuit made out of several capacitors and coils. Thus the signal is alternating with the frequency given by the signal generators when leaving the bridge. It is of low voltage and high current. The voltage on the exit of the bridge is fed into the transformer cascade, consisting out of multiple coils (from a minimum of 6 to a maximum of 8). Each one increases the signal voltage by maximally 8.5 kV while hereby decreasing the current. The voltage at the generator exit can thus ideally reach up to 68 kV. The frequency range for the high-voltage signal is about $10 \div 30$ kHz. The impedance of the plasma actuator and the voltage supply have to be somewhat matched, otherwise no clean sinusoidal signal can be produced and the achievable voltage amplitude is decreased. This adjustment of the resonance frequency can be done by adding

or removing coils from the system.

4.3 Diagnostics

Plasma microdischarges have been experimentally studied with a sufficient high temporal resolution by means of a photosensor module, based on a photomultiplier tube (PMT) and a home-made Rogowski coil. These probes allow measuring the light emitted by the plasma sheet and the electric current flowing into the circuit. A capacitive probe was placed between the buried grounded electrode and the earth as a diagnostics for measuring power consumption and for visualizing the shapes of the Lissajous figures, which are obtained when the measured operating charge and voltage values are plotted against each other in Q-V cyclograms [20]. A commercial HV probe (Tektronix P6015A, granted for a bandwidth of 75 MHz) was instead employed for evaluating the voltage at the exposed electrode. The outputs of all these probes were connected to different channels of a large bandwidth digital oscilloscope (Agilent MSO8104A with sampling rate equal to $2\,GSa\,s^{-1}$, or Tektronix TDS-5104 with sampling rate equal to $1.25\,GSa\,s^{-1}$). The temporal series associated to different probes were acquired simultaneously, so that the HV probe could be used to set the time and phase references of the sinusoidal signal driving the discharge. At this purpose, the HV signal was fitted with a sinusoidal function, whose best fit parameters were also used as the effective values of the SDBD voltage amplitude and repetition frequency. During the discharge active phases, even at the highest power level, the voltage signal does not show any ripple or higher harmonic excitation, as sometimes happens in the existing literature [132]. This is quite important, and often overlooked, since it would make difficult to compare different results, because a perturbation of the sinusoidal voltage supply often gives rise to pauses within plasma activity or even to inversions in the sign of the discharge current. As discussed in Section 7.1, the presence of absence of

discharge disuniformities in the spanwise direction was verified with a thermal infrared camera FLIR ThermaCAM SC640. Finally, the average fluid dynamic effects induced by the plasma actuator were investigated using a Pitot tube connected to an LPM-9381 Druck transducer that records the differential pressure from which the flow velocity was derived.

In the following sections these diagnostics are presented in more detail, together with a description of the processing of the temporal series that has been implemented for electrical measurements.

4.3.1 PMT

A PMT by Hamamatsu (H10721-210) was chosen for its fast temporal response and high sensitivity. It provides an electric signal whose amplitude is proportional to its gain (which can be varied by adjusting the PMT high voltage supply, usually by means of a low voltage control) and to the intensity of the light collected by its photocathode. In order to avoid the introduction of corrections for the gain and to ensure the overall stability of our measurements, we paid attention to keep the same voltage control during experiments. In practice, a steady dc voltage supply providing a control voltage of 1 V (gain $2 \cdot 10^6$) was used. The PMT declared rise time is 0.57 ns. Its ultra bialkali photocathode is sensitive to light with wavelength in the range $230 \div 700$ nm and the radiant sensitivity curve is almost flat between 300 and 500 nm, closely matching the air DBD spectra. It is known that emission spectra of DBD in air are dominated by the emission lines of the second positive system (SPS) of nitrogen molecules (see Section 2.5) [47,133], and these emission lines completely fall into this wavelength range. Light is collected and brought to the PMT photocathode by means of an optical fibre (100 μm core diameter) appended above the dielectric surface. Stray light signal was checked to be negligible during experiments. The PMT output signal was sent directly on the low impedance (50Ω) input channel of

the scope. It has already been observed in literature that, when the voltage is high enough for plasma generation, the temporal resolved signal of the emitted light usually appears as a series of pulses concentrated in the phase intervals of plasma activity (one for each voltage semi-cycle) [32]. The typical single event registrable by the PMT appears as a peak in the scope signal with a triangular shape lasting 3 ± 1 ns (see Figure 4.4). This duration, together with some ripple noises, somewhat sets the minimum time length of detected events. During experiments light signals longer than these single events were also recorded (Figure 4.4). The peak amplitude obviously depends on the collected light intensity.

The recorded signals are treated as follows. A threshold is used for the identification of a light event, which, in order to cut noise fluctuations, is taken into consideration only if at least a couple of consecutive points lie above this value. Many thresholds can be used, provided that they are smaller than the amplitude of the weakest single events but sufficiently higher

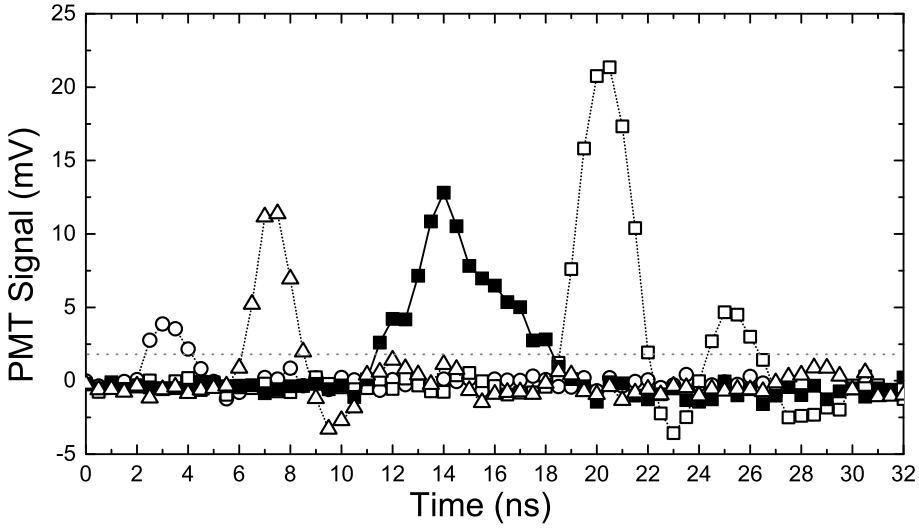

Figure 4.4: A few examples of photomultiplier outputs in presence of a light event. The three continuous lines with blank symbols show single events (whose shape is due to the PMT response) whereas full squares refers to a longer light emission. The PMT voltage taken as threshold is marked with the dotted line.

than the noise on the input channel. During all our experiments we opted for a threshold value equal to 1.7 mV, just 3σ above the measured noise. The beginning and the end of an event are found by moving back and forth along the time series until the signal crosses the zero level. The peak duration and temporal position are defined, respectively, as the difference and the mean value between the end and the beginning of the peak. The falling time is the temporal interval separating the time at which the event reaches its maximum value from its end. If the delay between two events is shorter than 5 ns and the falling time of the first one is lower than 3 ns, the second peak is rejected, because it is considered as one of the ripple noises mentioned above. The peak maximum value (peak amplitude) and the area lying below it (peak subtended area) were registered too.

In order to have a number of light events high enough for a statistical analysis, a certain amount of temporal series of about $2 \cdot 10^6$ samples were recorded by the scope, at the maximum sampling rate, for a total number of available voltage cycles equal to about 200. We have checked that the statistical dataset was stable over the different series. Two kinds of measurements have been performed: temporally resolved and spatio-temporally resolved light measurements. In the first case the optical fibre was placed a few centimetres above the discharge and was tilted 45 degrees, so that the field of view of the fibre was a couple of centimetres both in the spanwise and chordwise directions. In the second case, the optical fibre acceptance cone was reduced by placing the fibre connector inside a thin non reflective alumina tube which was situated just 1 mm above the dielectric material and perpendicular to its surface (Figure 4.1). In this way the collected light lies inside a circle with diameter lower than 0.5 mm and chordwise maps were obtained by moving the optical fibre in steps of 0.5 mm; at this purpose a translation stage with precision up to 50 μm was used. It is also possible to add up all the light events collected at different spatial positions to obtain a

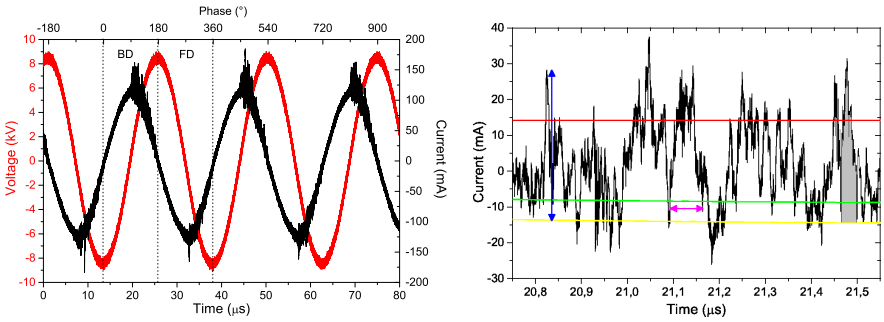

(a) (b)

Figure 4.5: (a) An example of voltage and current signals. The top axis reports the phase of reference, useful for defining the BD and FD semi-cycles. (b) A few backward current microdischarges are shown together with the threshold value (the red line in the highest position), the lowest baseline, and an intermediate green one useful for distinguishing between two consecutive current peaks and for defining the peak beginning and end. The pink horizontal arrow, the blue vertical one and the shaded area are examples of a peak temporal duration, amplitude and area, respectively.

large dataset that can be compared with the temporally resolved light measurements taken with the extended field of view. We have performed both these two temporal resolved measurements and we have checked that they provide similar results.

4.3.2 Rogowski Coils

In a DBD, the electric current flowing into the circuit can be viewed as the superimposition of a low-frequency sinusoidal capacitive current, which is almost independent of plasma presence in the gap, and a discharge current, which is associated to plasma microdischarges and appears as a series of fast current pulses (Figure 4.5). A current transducer like a Rogowski coil can provide the high sensitivity and the wide bandwidth necessary for studying the electrical behaviour of SDBDs.

A Rogowski coil is a conducting wire that is wound in spiral around a magnetic or non magnetic core and then returns to the original point. The coil is placed around the cable connecting the buried electrode to the ground

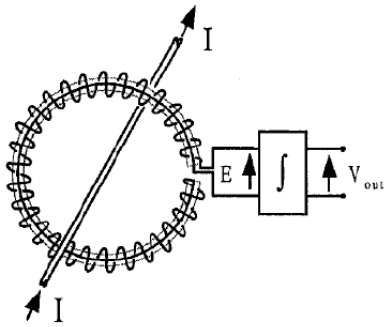

Figure 4.6: Schematic representation of a Rogowski coil. The current I flowing in a cable generate a emf E at the output of the coil which is proportional to $\delta I/\delta t$ and must be integrated with a passive or active circuit.

(Figure 4.1). The operating principle was formulated by Rogowski and Steinhaus in 1912 [134]. A schematic representation of a Rogowski coil is shown in Figure 4.6. The current I flowing in the cable generates an electromotive force emf at the output of the coil which is proportional (following the Faraday's law) to the rate of change of the current $\delta I/\delta t$ [135]. Consequently, the emf must be integrated with an integrating circuit, that can be reduced to a simple resistance [136,137]. By a proper choice of the coil geometrical characteristics and by tuning the electrical parameters of its measuring circuitry, we used a few home-made probes with suitable bandwidth [137, 138]. The use of a small resistance as integrating system allows the probe to operate in the self-integrating mode in a large frequency range, thus producing a voltage signal directly proportional to the instantaneous current [131]. Anyway, the probe can be used also outside this self-integrating bandwidth, provided that the frequency dependent attenuation and phase-shift are taken into account. This requires a calibration that will be discussed in a short while [139]. In the original design, Rogowski coils were air cored to avoid saturation of magnetic core when measuring high currents. In the present measurements, however, currents are constantly far below saturation (the capacitive and microdischarge current are a few hundreds of mA at most), and a magnetic core is preferable in order to have a higher sensitivity [137]. We also notice

that all toroidal inductors are highly self-shielding, with most of the flux lines contained within the core: flux density is essentially uniform over its entire magnetic path and the actual shape of the winding circuitry causes little changes in the probe response. Moreover stray magnetic fields have very little, if any, effects on toroids. This allows their use also in operating conditions where electrical discharges are around. The use of high bandwidth ferrite coils allows to push the probe response up to 100 MHz or more, which is suitable for microdischarge investigation [140]. On the other side, ferrite cores with higher magnetic permeability enhance the Rogowski coil sensitivity down to the typical frequencies adopted for discharge generation, in the range of tens of kHz.

In the simplest measurement setup, Rogowski coils can be used merely by connecting their integrating resistance, bridging the winding endings, to the high impedance input of a digital scope with sufficiently large bandwidth. We used a 1 m long RG-59 BNC coaxial cable, which was calibrated with the probe and used always together. The Rogowski coils were calibrated over the spectral range $10 \div 100$ MHz with two tunable frequency waveform generators, specifically a NF-1940 Synthesizer and a Kenwood SG-7130, depending on the frequency range considered (bandwidths are $0 \div 20$ MHz and $0.1 \div 1300$ MHz). The generator 50Ω BNC output impedance was used. Voltage signals of different amplitudes and frequencies were used to fed a high power and high linearity coaxial 50Ω resistor (Bird Electronic Co. 8135, maximum power 150 W) through a matched line, assuring that the same current will be measured at different points of the line. The instantaneous current was thus derived from the voltage drop over the resistor (measured with the voltage probe of a Agilent MSO8104A scope), and the signal revealed by the Rogowski coil was simultaneously recorded. In order to best match the line, 50Ω BNC cables and connections were used everywhere and the line was made as short as possible. The Rogowski coil was inserted us-

ing two BNC breakouts to banana plugs, as close as possible to the resistor for reducing any systematic calibration error due to a small line mismatch. As an example of this versatility, amplitude and phase-shift frequency response of three different Rogowski coils are shown in Figure 4.7, where two MnZn ferrite toroids (Epcos N30, outer diameter/inner diameter/height = $40\times24\times16$ mm) are compared with a NiZn core (Anra, outer diameter/inner diameter/height = $30 \times 20 \times 6$ mm). The maximum current measurable by these probes (in order to avoid magnetic core saturation) exceeds several A, whereas, using our scope, the minimum current detectable was about 1 mA. From the values of amplitude attenuation and phase-shift obtained at different frequencies, we have interpolated a calibration curve (shown in a case in Figure 4.7), with the aim of taking into consideration the behavior of the probe in the whole spectral range considered.

Once the SDBD current signals have been recorded, they are processed as follows. The voltage output of the probe is transformed into a discharge current measure by processing the signal with a fast Fourier transform (FFT)

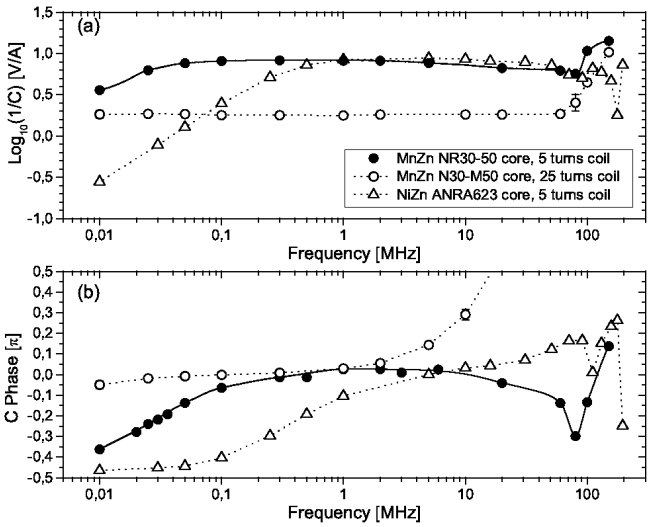

Figure 4.7: Rogowski coil amplitude and phase-shift responsivity. C is the multiplicative correction factor applied at each frequency of the FFT component of the measured voltage to obtain the electric current.

algorithm, which uses the calibration coefficients evaluated from the calibration curve values at the different frequencies for correcting the corresponding FFT components. Eventually, the revised signal is returned through the inverse FFT. Since we are mainly interested to the current signal associated with plasma microdischarges, we must separate this current component from the displacement one. Two approaches are possible for this purpose. The first one consists in the detection of the capacitive contribution by means of a sinusoidal fit, which is afterwards subtracted from the total electric current signal. The second method makes use of the fast Fourier transforms for the implementation of band pass filters. The latter is computationally easier and faster, especially for large datasets, and was thus chosen as the preferred solution. After displacement current subtraction, the fast current events due to plasma microdischarges appear as pulses emerging from a noisy base line. Usually, the sinusoidal fit and the FFT signal processing provide similar results. In some circumstances, however, the former results are more accurate, because with the band pass filter the base line is not completely flat but it is slightly curved in correspondence of time intervals when plasma current MDs arise. In these cases the problem can be easily fixed by considering a curved base line. The base line is useful for detecting current pulses, which can be easily identified by setting a threshold value sufficiently higher than noise spikes. Figure 4.5 shows a few current peaks together with the three lines introduced for the analysis: a threshold adopted for the identification of discharge current pulses, a baseline used to evaluate the intensity of peaks, and a baseline eventually introduced in order to evaluate the beginning and the end of current pulses, and thus to distinguish between two different consecutive current peaks. So, using this baseline we can evaluate current microdischarge properties such as their duration and temporal position, while with the other one we calculate amplitude and area, this last being the charge delivered by the current pulse. In order to study the MD

evolution within a sinusoidal cycle, the voltage signal can be fitted and used to provide the reference phase. Within each half-cycle, a statistical analysis could be performed on the set of current pulses. During the experiments, in order to have a number of current events high enough for a statistical analysis, a temporal series of $2 \cdot 10^6$ samples was recorded, for a total number of available voltage cycles equal to 25 at a frequency of 16 kHz.

4.3.3 Capacitive Probe

Two methods are usually adopted for power measurement: the electric current method and the electric charge method [132, 141–143]. In the first case the time-series of the current $I(t)$ is recorded (by means of a shunt resistor or of a Rogowski coil) in combination with the applied voltage $V(t)$, and the power dissipated during a voltage cycle is obtained by averaging the instantaneous power $I(t) \cdot V(t)$ over one period. This method is the most direct one but can suffer from large uncertainties. As a matter of fact, in a DBD, the electric current flowing into the circuit can be viewed as the superimposition of a low-frequency sinusoidal current and a discharge current associated with plasma micodischarges. When averaging over the period, the power associated with the sinusoidal capacitive current should be zero, but the cancellation of this contribution could affect the precision of the measurement. For this reason the charge method was chosen for these experiments [142]. An integrating capacitor, usually called capacitive probe, is placed in series between the low voltage covered actuator electrode and ground. The capacitance C_{probe} is known and must be sufficiently large so that the voltage difference ΔV between the DBD electrodes is almost equal to the voltage V applied to the powered electrode. Since the capacitance of actuators usually lies in the range $1 \div 100$ pF, typical capacitive probes are selected with a value between 10 nF and 330 nF. This assures that the probe is not intrusive and that the voltage drop across the capacitor (ΔV_{probe}) is

small enough to be measured without necessarily using a high-voltage probe. In our experiments 10, 46 and 100 nF have been used, depending on the maximum ΔV_{probe} and thus on both the plasma actuator geometry and on the voltage applied to the exposed electrode. Before experiments each capacitive probe was calibrated and the phase shift was checked to be equal to zero as expected [141].

The capacitor-based charge method for power measurement was firstly introduced by Manley for discharges between parallel plates [144], whereas Pons was the first to use it in the context of SDBDs for aeronautical application [145]. The instantaneous charge Q is given by $Q = C_{probe} \cdot \Delta V_{probe}$. In Figure 4.8 two examples of voltage and charge signals in presence of plasma are shown. Two different capacitive probes have been adopted, and in one case in the Q signal it is clearly visible a series of pulses, which are associated to the plasma presence.

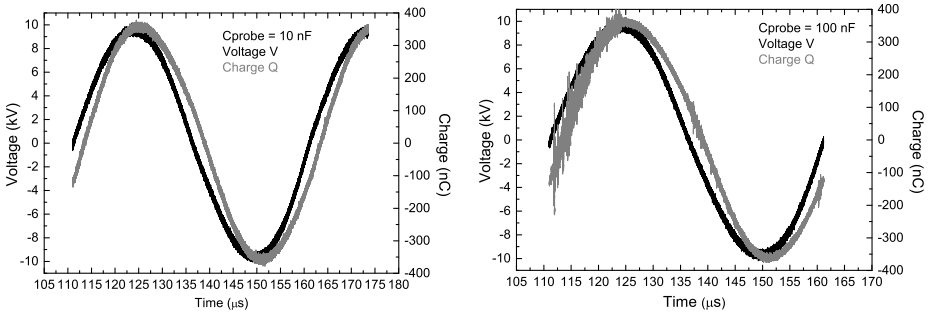

Figure 4.8: Two examples of voltage (in black) and charge (in gray) signals in presence of plasma. Two difference C_{probe} were used: 10 nF (a) and 100 nF (b).

A Lissajous figure is obtained plotting the instantaneous charge Q versus the instantaneous voltage V. The area of this curve gives the energy dissipated per cycle, and then the power P_{dis} is obtained after dividing by the period [141,144]. Figure 4.9 shows that the area is independent of the value of C_{probe}, despite the different high-frequency response of the two probes. When the voltage applied to the exposed electrode is too short for plasma generation,

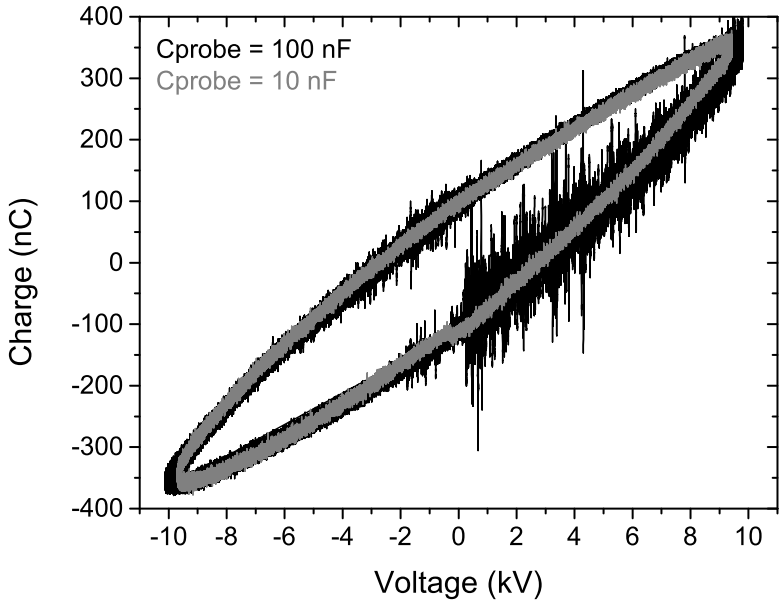

Figure 4.9: Lissajous figures obtained with two different capacitive probes.

the system is purely capacitive and Q and V are in phase, so the Lissajous figure is a straight line and the enclosed area is equal to zero.

4.3.4 Pitot Probe

The Pitot tube was invented in 1732 by F.H. Pitot during his attempts to measure the flow velocity of the Seine River in Paris [54]. Nowadays, it is commonly used for fluid velocity measurements when the Bernoulli's equation for incompressible flow is valid, stating that if the fluid is flowing horizontally (no elevation variations) the total pressure (p_t), given by the static and dynamic pressures (p_s and p_d), keeps constant throughout the flow:

$$p_t = p_s + p_d = p_s + \frac{1}{2}\rho v^2 = const, \tag{4.1}$$

where v is the local flow velocity and ρ is the density, which is taken as constant, so only gases flowing at low speed (Mach number $M < 0.3$) and liquids are considered [54]. The Pitot tube is inserted into the flow, with an

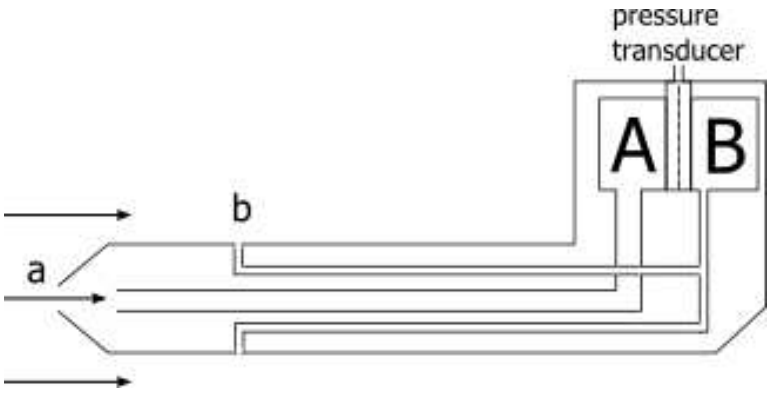

Figure 4.10: Pitot tube, schematic representation.

open end facing directly into the flow, meaning that the plane of the opening of the tube is perpendicular to the flow at point a, as shown in Figure 4.10. The other end A of the Pitot tube is connected to a pressure gauge. The Pitot tube is closed in A, so the fluid elements along streamline $a - A$ slow down and finally have velocity equal to zero at point A (which is called *stagnation point*). The pressure in point B is instead equal to the static pressure (which is associated to the purely random motion of molecules) measured at point b. But the static pressures in a and b are equal, so $p_a = p_B$. It follows that

$$p_A = p_a + \frac{1}{2}\rho v_a^2 = p_B + \frac{1}{2}\rho v_a^2, \tag{4.2}$$

$$v_a = \sqrt{\frac{2(p_A - p_B)}{\rho}}. \tag{4.3}$$

In our experiments the Pitot tubes were small glass tubes with outer and inner diameters usually equal to 1.4 mm and 1.0 mm respectively, and the pressure difference $(p_A - p_B)$ was measured by a LPM-9381 Druck transducer. The Pitot inlet was placed in contact with the electrode surface, and generally the chordwise position was kept equal to 10 mm downstream the exposed electrode edge, in correspondence of the end of the buried electrode for Setup B (Section 4.1). The single Pitot tube was often replaced by a series of three or more connected capillaries, in order to take a measurement

of the flow velocity averaged in the spanwise direction.

4.3.5 Infrared Camera

A thermal camera by FLIR (model ThermalCAM SC640 and spectral range $7.5 \div 13\,\mu$m) has been used for plasma visualization [146], in order to monitor the plasma spanwise uniformity for different high-voltage amplitudes and frequencies. The camera records the infrared emission of the dielectric surface, which is a function of its temperature. The camera was placed about 50 cm above the discharge, and the temperature measured by the thermal camera before the discharge ignition was compared with the room temperature. Six frames per second were acquired, and the camera was switched on a few seconds before the ignition of the discharge, directly at the desired voltage amplitude and frequency. Before every measurement we waited until the actuator cooled down to room temperature again.

CHAPTER 5

Plasma Microdischarges

In this chapter results concerning plasma microdischarges are presented. These experiments have been conducted at University of Milano-Bicocca and with setup A (already decribed in Section 4.1), with the aim of better understanding the properties of these asymmetric dielectric barrier discharges.

It has already been observed in literature that, when the voltage is high enough for plasma generation, the PMT temporal resolved signal describing the emitted light usually looks like a series of pulses emerging from a noisy baseline [32], similarly to the one shown in Figure 5.1, which has been obtained with our experimental configuration. As already stated in Section 4.3.2, once the sinusoidal capacitive component has been separated from the

plasma contribution to the curent signal, the latter is composed of current pulses emerging from a noisy baseline too. The sign of current pulses proves that electrons move towards the dielectric during the FD and towards the exposed electrode during the BD. Both light and current events are not

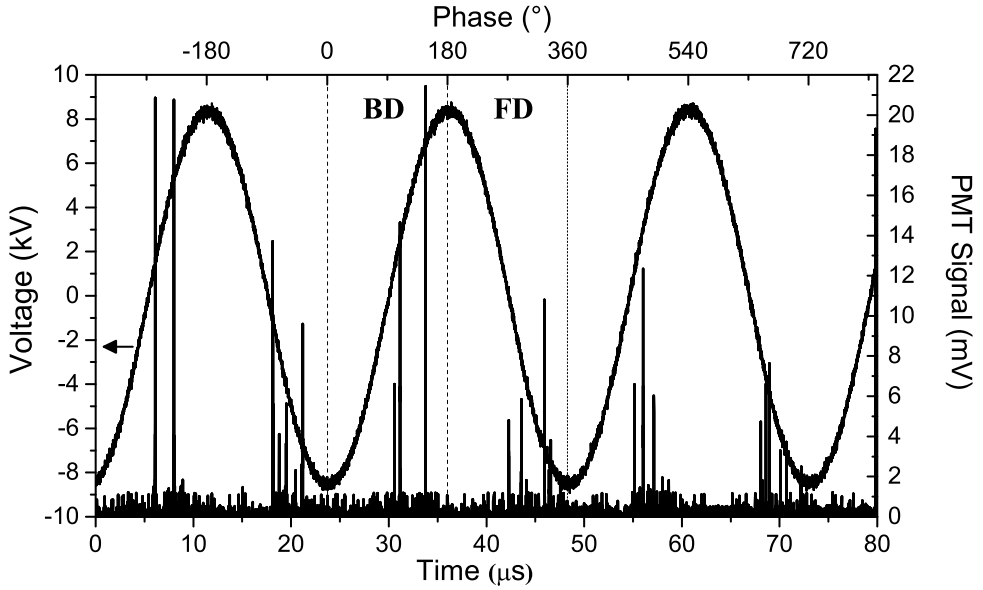

Figure 5.1: An example of voltage and PMT signals. The top axis reports the phase of reference (with the zero set in correspondence to the voltage minimum), useful for defining the BD and FD semi-cycles.

uniformly distributed into the sinusoidal voltage period, but they are concentrated inside two disjointed phases of plasma activity that occupy only a fraction of the two voltage semi-cycles. Consequently, plasma microdischarges will be classified as belonging to the *Backward Discharge* (BD) or to the *Forward Discharge* (FD), depending on which time interval these spikes fall into. These two terms have already been introduced in the plasma actuator research field for indicating the semi-cycles during which the voltage is rising and falling, respectively [147]. We talk of microdischarges because these pulses are detected during both half-cycles and, as it will be discussed in a short while, their temporal duration are quite similar. As already discussed in Section 2.3 the term microdishcarge indicates the group of local

processes in the discharge gap, lasting dozens of nanoseconds, that begin with an electron avalanche and end with electric field collapse due to charge accumulation. In DBDs these events usually include the development of a streamer (or ionizing wave), but for these plasma actuator configurations it is still an open question if both the BD and FD operates in a streamer regime or not. For instance, cross-correlation spectroscopy reveals that a cathode-directed ionizing wave generates between a dielectric and a metal semi-spherical electrode independently of the voltage polarity (see Section 2.5). However, for a surface point-to-point DBD the ionizing wave could be detected only when the exposed electrode plays the role of the anode.

Since the greatest pulses generally seem to appear in the backward discharge rather than in the forward one and since several groups studying aerodynamic applications of SDBDs believe that the induced airflow effects are principally due to the BD contribution, we chose as the zero phase of reference the condition corresponding to the minimum value of the voltage, as shown in Figure 5.1, with the aim of considering the backward discharge at first [32].

In Section 5.1 spatio-temporally resolved light measurements are presented, paying attention to the differences and analogies between the two strokes. When the light pulses detected at different spatial positions are considered altogether, one gets temporally resolved and spatially integrated optical measurements, which can be compared to results coming from the temporal analysis of the discharge current, for which we recorded only spatially integrated signals up to now. This is discussed in Section 5.2. Eventually, we have tried to follow the light signal propagation along the dielectric surface, in order to verify the existence of a propagating ionizing wave, as described in the last part of the chapter (Section 5.3).

5.1 Spatio-Temporally Resolved Light Measurements

Temporally and spatially resolved measurements of the light emitted by the plasma have been performed with the aims of understanding the discharge evolution and making comparisons between the backward and forward stokes. Before performing these experiments we have recorded a few optical spectra of the emitted light by means of a spectrometer (AvaSpec-2048 by Avantes) with resolution of about 0.8 nm and a spectral band extending from 180 to 1150 nm, averaging over several voltage cycles. A typical spectrum is shown in Figure 5.2. As expected (see Section 2.5), the spectrum of a DBD is dominated by the second positive system of molecular nitrogen, but lines belonging to the first negative system of N_2^+, whose most intense emission is at 391 nm [133], and to the first positive system of N_2 are also visible. No monochromators nor filters have been placed in front of the photomultiplier tube, so the whole spectrum contributes to the temporal resolved PMT signal.

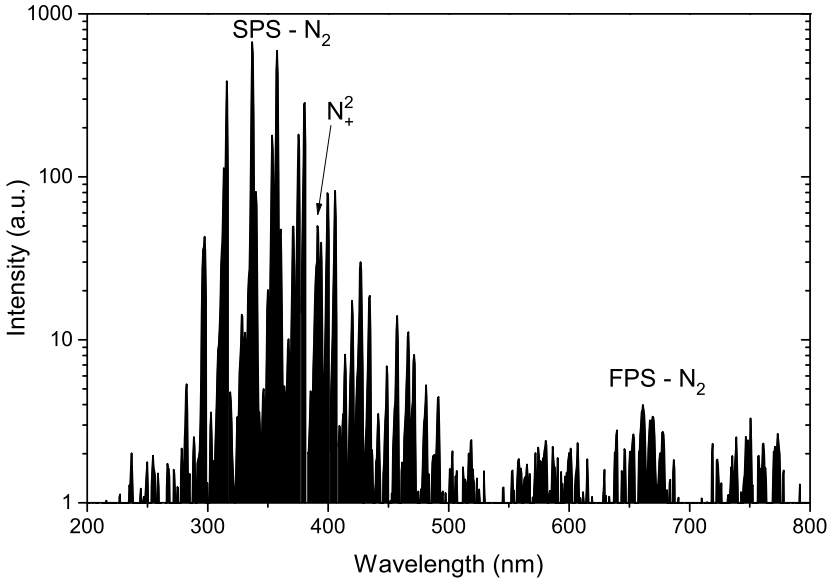

Figure 5.2: A typical emission spectrum of these surface dielectric barrier discharges.

Spatio-temporally resolved measurements have been performed as discussed in Section 4.3.1. They are temporally resolved because single pulses are detected and analysed. However, since the number of light pulses within each stroke is small with such a small field of view, events registered during different voltage cycles have been gathered in order to collect enough pulses for a statistical analysis, and phase intervals equals to 2° have been considered (corresponding to about 140 ns at our frequency). The discharge dynamics is thus phase resolved. The number of light pulses counted in each bin is plotted in Figure 5.3 as a function of the phase and chordwise x position. This figure thus depicts the distribution of plasma microdischarges in space and time. Figure 5.3a shows the region across the electrode edge ($x = 0$ mm) where almost all events happen (between -2 mm and 5.5 mm), whereas Figure 5.3b is a magnification of the furthest region. Much information can be obtained from these temporally and spatially resolved measurements. First of all, these maps give insights about the different temporal length of the active phases of the two semi-cycles: only 40° for the backward discharge (corresponding to about $2.8\,\mu s$) and 80° in the forward case. As a matter of fact, with the voltage amplitude equal to 8.5 kV applied in the presented case, the BD breakdown is recorded about 10° after the voltage change of polarity, at $98° \pm 6°$), and the active phase ends at $135° \pm 20°$. The forward stroke begins some degrees after the voltage reversal too (at $281° \pm 4°$), but it extinguishes nearer to the voltage minimum, around $354° \pm 8°$. We point out that these phases have been estimated by recording the temporal positions of the first and last light pulses detected in every single voltage half-cycle. Due to the small field of view of the optical fibre, some of them could have been lost, so the breakdown and ending phases could have been shifted and could show a somewhat larger spread than in reality. This difference between the FD and BD active phases indicates that at the end of the BD semi-cycle the electric field in which electrons move cannot energize them

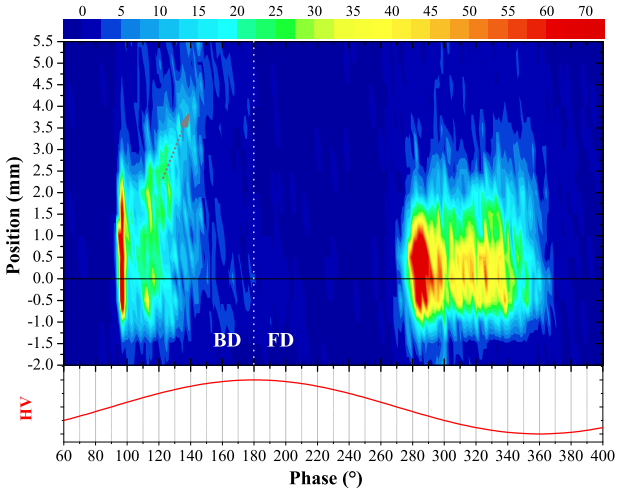

(a)

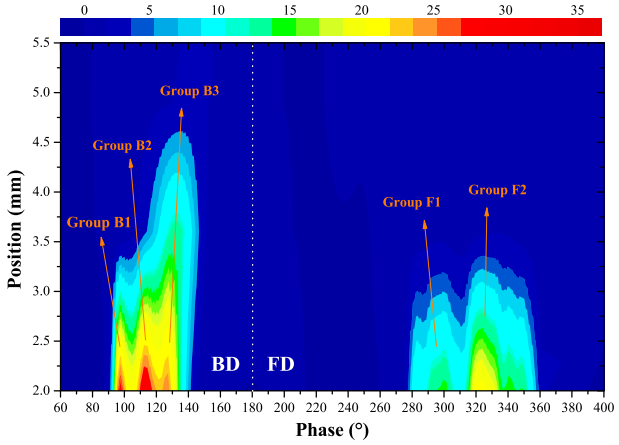

(b)

Figure 5.3: Number of light events detected as a function of the reference phase and of the chordwise distance from the exposed electrode edge. The black line (electrode edge) separates the region of the dielectric surface (positive chrodwise values) from the exposed electrode region. Subfigure (b) shows the furthest dielectric region where light could be detected.

enough for exciting nitrogen molecules [47, 148, 149]. One could guess that they could even be unable to generate new plasma microdischarges, but we will see from electric current measurements that it is not the case. Another asymmetry concerns the number of detected light pulses, which is larger for

the forward discharge (65% of the total), especially in the region straddling the exposed electrode edge or at the beginning of the strokes (Figure 5.3a). Eventually, we found that the spatial extent of the region where most of the emitted light comes from is approximately 4.5 mm and 3.5 mm during the BD and FD, respectively. This difference has already been noticed in previous experimental works [32]. With our setup, light microdischarges have been observed above the exposed electrode too, but from a somewhat smaller region (within 2 mm from the edge) because of the chordwise asymmetry in the electric field. Moreover, in both semi-cycles the maximum plasma extension over the exposed electrode is recorded immediately after the stroke breakdown (at about 100° and at 280° ÷ 310°, see Figure 5.3a), whereas that over the dielectric material is reached later (at about 135° and at 330°, see Figure 5.3b). A higher voltage at the exposed electrode is thus required for activating the furthest dielectric regions.

Concerning the backward discharge internal structure, we can distinguish three categories of microdischarges (highlighted in Figure 5.3b), which are generated during three consecutive phase intervals. The first two groups (named *Group B1* and *Group B2*, at 93° ÷ 99° and at 110° ÷ 120° respectively) are made up of microdischarges with a similar spatial extent. The last group (beyond 120°, *Group B3*) is instead formed by a set of microdischarges that seem to shift away from the exposed electrode edge (see the contour plot of Figure 5.3b). This can be thought as an expansion of the discharge region over the dielectric surface. In fact, a plasma propagation has already been noticed in the literature [98], but authors could not distinguish among different groups of microdischarges. We have estimated a spreading velocity of approximately 1 kms^{-1} (see the grey arrow in Figure 5.3a), somewhat larger than previously reported. The physical interpretation of this phenomenon will be discussed later. Referring to the FD stroke, we can instead distinguish a group of breakdown microdischarges (*Group*

F1), lasting for a phase interval ($280° \div 300°$) quite longer than the one associated with the backward breakdown Group B1. During the rest of the semi-cycle (gathered in *Group F2*) light intensity appears quite uniform and plasma does not spread significantly on the dielectric surface (Figure 5.3a).

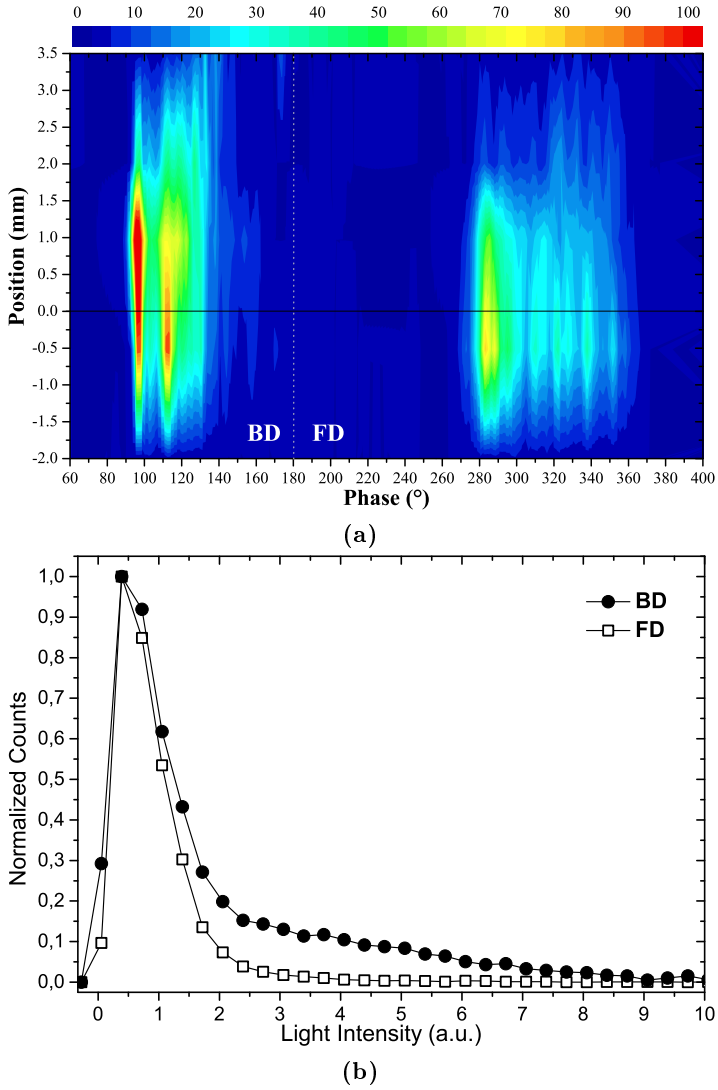

Figure 5.4: (a) Spatio-temporal distribution of the light intensity, that is the total peak subtended area, expressed in arbitrary units and obtained by taking into consideration the contribution of all detected light peaks. (b) Distribution of the light intensity of all single light pulses detected during the backward (full circles) and forward (blank squares) discharges. Each distribution is normalized to its maximum, which, by the way, is three times higher for the forward stroke.

The larger number of microdischarges and the longer active phase could induce thinking that light is mainly emitted in the forward semi-cycle. Nevertheless, the spatio-temporal map of the light intensity shown in Figure 5.4a (that is obtained by adding up the area subtended below every light peak, already defined in Section 4.3.1) reveals that 54% of the emitted light is associated with the backward discharge. The reason is that there are several brighter microdischarges during the backward stroke, as demonstrated by the tail of the microdischarge intensity distribution of Figure 5.4b. These highly emitting BD microdischarges are quite uniformly distributed with phase and were detected mainly near the electrode edge ($-1\,\text{mm} < x < 2$ mm). This suggests that in each of these BD microdischarges there are more energetic electrons, probably because they move in a stronger electric field. This is consistent with the results of a recent experimental work, showing that in a SDBD the mean reduced electric field is higher for the backward semi-cycle rather than for the forward one [150]. Looking at the phase distribution of Figure 5.4a, we note that the maximum in the FD emitted light is recorded near the exposed electrode and at the stroke breakdown. For instance, almost 60% of the total FD light is due to Group F1. Focusing on the BD, the light intensity map allows us to see more clearly the first two categories of microdischarges, whereas the third one becomes less discernible. Despite the higher peak intensity of Group B1, its contribution to the total BD light is slightly less than the one associated with Group B2 (26% versus 32%). The remaining is emitted during Group B3 (33%) and during the phases separating Group B1 from Group B2. So, the three categories of backward microdischarges provide a comparable contribution to the total backward light, since they distribute it in phase intervals with different lengths, as well as in different spatial regions. For example, the light emitted from Group B1 is quite uniform along the x direction, whereas during Group B2 more light is emitted on the electrode rather than over the dielectric material (Figure

5.4a). Similar information can be inferred by considering the spatio-temporal map and the distribution of peak amplitudes instead of their subtended area.

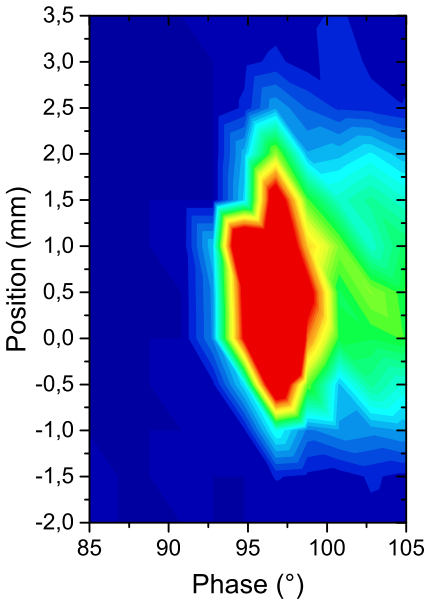

Figure 5.5: Spatio-temporal distribution of the light intensity (total peak subtended area) associated to Group B1, expressed in arbitrary units.

Some more considerations about Group B1 are helpful for understanding the physical mechanisms involved during the discharge evolution. A closer look at the light intensity map shows that microdischarges belonging to Group B1 are all triggered within a few hundred nanoseconds after the backward breakdown. At first they emit light mainly above the dielectric surface, within the first millimetre from the electrode edge (Figure 5.5). Light emission then spreads towards the electrode region, as well as towards slightly further dielectric zones. This spatial profile remains almost untouched during the phase interval $100° \div 110°$ separating Group B1 from Group B2. When Group B2 begins, light is predominantly concentrated above the electrode surface. The total BD light intensity as a function of phase is obtained by integrating the map of Figure 5.4a, and is shown in Figure 5.6a. The considerable signal associated with microdischarges of Group B1 is clearly visible as a peak just at the stroke beginning. This light signal has been fitted with a Gaussian function, which is shown in the same graph. This is interesting because we observed that, when the operating conditions are changed, the breakdown phase varies and this signal associated with Group B1 is always evident immediately after it, so we can really think to Group

B1 as the breakdown group. In particular, the curves representing Group B1 at different HV amplitudes demonstrate that the breakdown phase decreases as the voltage increases (Figure 5.6b). This reduction is not linear, being more accentuated at the lowest HV amplitudes. Moreover, it is interesting to notice that for sufficiently high voltages the backward stroke begins before 90°, that is to say that the voltage at the exposed electrode has not become positive yet. This demonstrates that there is a negative charge accumulation (on the dielectric surface or into the gap) sufficient for reversing the electric field direction, at least in part of the gap. We expect that this negative charge is mainly ascribable to electrons. So, we can conclude that Group B1 is probably made up of microdischarges initiated, at the stroke breakdown, by the electrons that have been left by the previous forward semi-cycle. Since we have seen that the first microdischarges emit light mainly within 1 mm from the electrode edge, we can think that at least part of them are accumulated on the dielectric surface. After some hundreds of nanoseconds Group B1 is finished and the backward discharge is partially quenched (Figure 5.6a, phase interval $100° \div 110°$). This could be due to the fact that many electrons have been removed and the electric field in the gap is no more enhanced by the presence of many negatively charged particles on the dielectric surface. A higher voltage at the exposed electrode is thus needed for generating a new significant group of light microdischarges without the possibility of exploiting a great surface charging. When this condition is satisfied, Group B2 is initiated. With this description we can suppose that Group B3 begins when the region near the exposed electrode has been covered enough with positive particles, so that the electric field is weakened in the range $0 \text{ mm} < x < 1 \text{ mm}$. Moreover, at these phases the voltage has become high enough for activating the zone $2 \text{ mm} < x < 4$ mm. The discharge region thus spreads away from the exposed electrode, as we have previously noticed (Figure 5.4). This peculiarity of Group B3 is

interesting, because charged particles belonging to these microdischarges can transfer momentum to neutrals in further spatial regions, thus increasing the effectively volume where plasma actuation works. Such a discharge dynamics

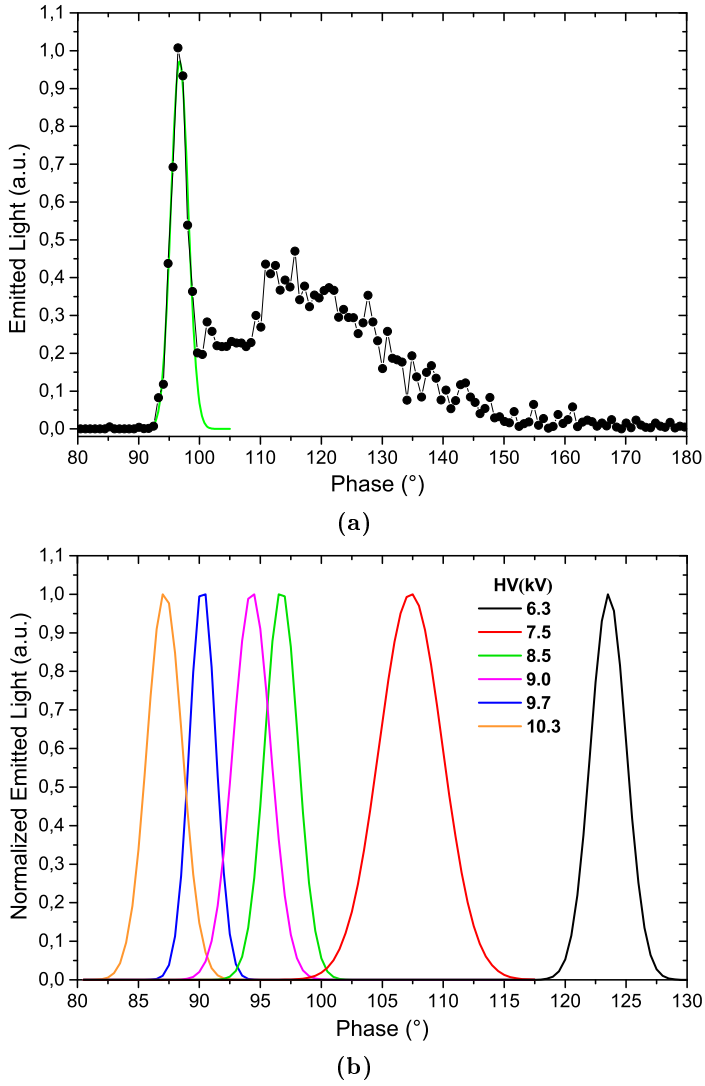

Figure 5.6: (a) Total light intensity of the backward discharge as a function of the reference phase. The intensity peak corresponding to microdischarges of Group B1 has been fitted with a Gaussian function (continuous green line). Since this light signal is made up of many light events and since it occupies a short phase interval, we have exploited our whole phase resolution (that is 0.8°, corresponding to about 55 ns). (b) Phase position of the intensity peak corresponding to Group B1 at different voltage amplitudes.

would be consistent with experimental evidence of surface charging and discharging observed in [151], suggesting that at the beginning of the BD there is a negative charge accumulated on the dielectric material, especially near the electrode edge, and that this charge accumulation changes sign during the BD stroke. In such a scenario, we can also guess that microdischages of Group F1 are created by the positive charges left by the previous backward discharge. Afterwards, electrons are progressively accumulated on the dielectric surface, as suggested by the slightly longer extension of microdischarges detected in correspondence to 325°.

Finally, it is worth spending a few words on the temporal duration of light pulses we have talked about. A few experimental works using the cross-correlation spectroscopy technique [47, 52] have suggested that in a dielectric barrier discharge a microdischarge develops as a cathode-directed ionizing wave followed by a decay phase during which a light signal lasting for few nanoseconds appears in the microdischarge channel (Section 2.5). This is consistent with our measurements, because the temporal duration of light pulses seldom exceeds 10 ns. Most of the light pulses detected during both the BD and FD last 3 ± 1 ns and have the triangular shape due to the PMT response (Section 4.3.1). However, there is a fraction of the stroke events characterized by a longer temporal duration, especially during the backward semi-cycle (almost 40% in the BD and only 10% in the FD). We can suppose that these microdischarges are due to a cathode-directed ionizing wave moving slower because of a weaker electric field. Moreover, some of these events show a multi-peak shape instead of a triangular one (see Figure 5.7a), maybe because of a partial superimposition of light signals coming from different localized spatial zones of a single microdischarge, presumably associated with a discharge branching. In the FD, these long lasting peaks are quite uniformly distributed and they do not last for more than about 8 ns. This is not the case of the BD. In Figure 5.7b we have plotted the

mean temporal duration of light peaks longer than 4 ns, as a function of the phase and chordwise position. It is evident that the mean value is higher for microdischarges created during Group B3 and in the furthest dielectric regions, suggesting again that these microdischarges are created in a weaker

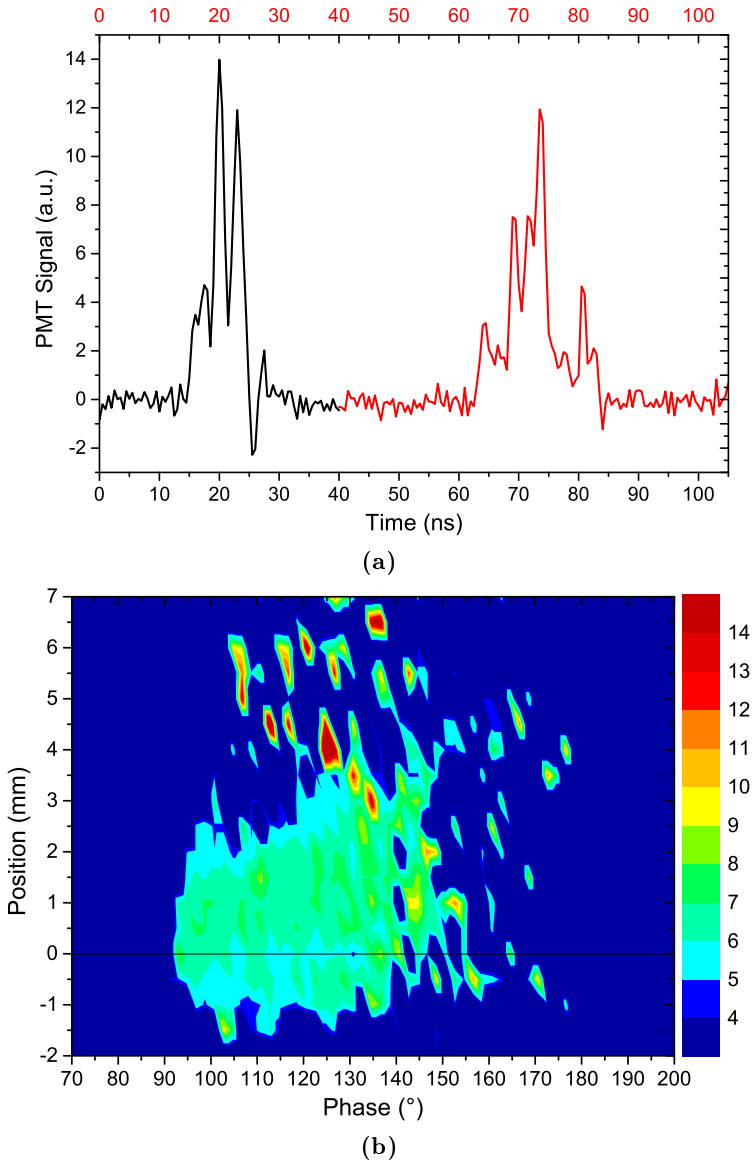

Figure 5.7: (a) A couple of examples of events lasting several nanoseconds and showing a multi-peaked temporal structure. (b) Mean light peak temporal duration as a function of the reference phase and of the distance from the end of the exposed electrode. Only light pulses longer than four nanoseconds are considered.

electric field.

5.2 Temporally Resolved Light and Current Measurements

Spatially integrated and temporally resolved light measurements can be obtained by adding up all the light events collected at different spatial positions that have been presented in the previous section. Current measurements allow us to obtain, with a diagnostics which is independent of the optical one, both similar and complementary information concerning the discharge breakdown and quenching phases, the presence of groups of microdischarges or the asymmetry between the two semi-cycles. Concerning this last point, it is worth comparing the optical and electrical signals associated with the two strokes, as depicted in Figure 5.8. Full circles represent the total emit-

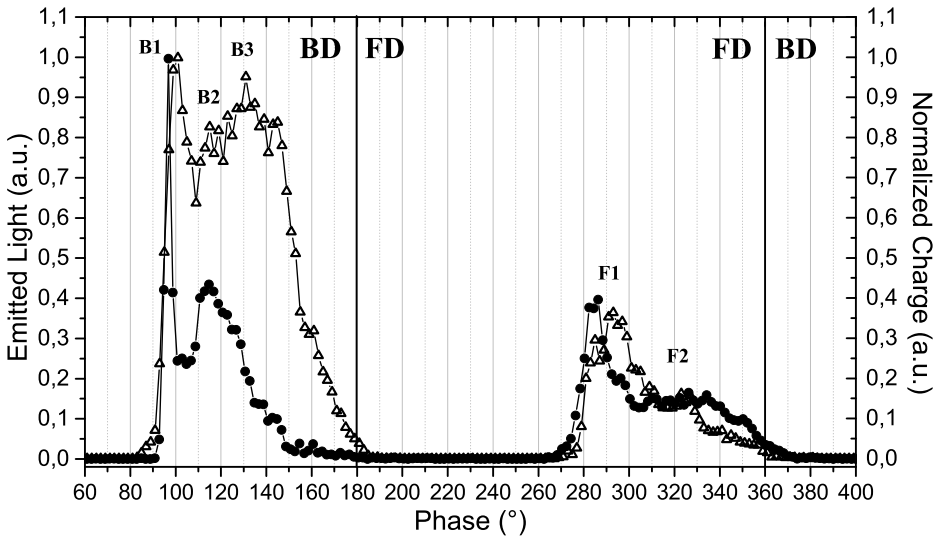

Figure 5.8: Total emitted light (full circles) and total transported charge (blank squares) as a function of the reference phase.

ted light, obtained by integrating the map of Figure 5.4a along the chordwise x direction. For the electrical measurements, we have chosen the total transported charge, obtained by adding up the contribution of each cur-

rent microdischarge. As discussed in Section 4.3.2, the latter is the integral of the current pulse, between its beginning and ending times. The total transported charge is interesting because charge particles moving in plasma microdischarges collide with neutral air particles, transferring their momentum and thus directly inducing the airflow exploited in plasma actuation applications. As previously noticed, a slightly higher fraction of the total light is emitted during the backward semi-cycle (54%) rather than in the course of the forward one. However, the asymmetry between the BD and FD is much more pronounced if one considers the charge transported by current microdischarges: the backward contribution is 80% (Figure 5.8, blank squares). This highlights the importance of using electric current diagnostics for getting new information about the discharge properties. With this setup and at 8.5 kV, the charge transported during a voltage cycle is of the order of 40 nC for the BD and almost 10 nC for the FD. This large asymmetry is due to both the number of current pulses detected during a stroke and to the different mean charge transported by a single microdischarge. In fact, the number of microdischarges is usually greater for the backward semi-cycle, even though this asymmetry reduces with the voltage amplitude, as shown in Figure 5.9. In contrast, the mean charge associated with a single microdischarge is quite independent of the voltage amplitude and differs in the two semi-cycles (about 1.4 nC for the BD microdischarges and 0.8 nC for the FD ones). As shown in Figure 5.8, the phase distributions of light and charge signals are quite different in the BD. In fact, light intensity is high mainly at the stroke breakdown and, in less measure, during Group B2. The light signal then progressively decreases, and goes to zero at 150°, well before the voltage maximum is reached. In contrast, the charge signal intensity begins to reduce only after 160°, and goes to zero only around 180°. So, in terms of the transported charge, the backward discharge finishes only in correspondence to the voltage maximum. As suggested in the literature, the

backward and forward strokes cannot continue after the voltage maximum and minimum (180° and 360°) because the build-up of charged particles on the dielectric surface tends to quench the discharge, so that an increase in the voltage magnitude is needed for the discharge sustainment. Using data shown in Figure 5.8 we can assess that a substantial fraction of the total BD charge is transported by Group B3 (60%, compared with 21% of Group B1 and 19% of Group B2), which is thus made of microdischarges that move a considerable amount of charged particles even though they do not emit light. A similar asymmetry between the light and charge signals is visible during Group B1 too. As a matter of fact, we can easily notice from the charge signal that Group B1 finishes at almost 110°, and not at 99° as it seemed from the light signal. So, we can think that plasma microdischarges that are created immediately after the BD breakdown (up to 99°) always emit light, because they generate an intense peak in the light signal. After a few hundred nanoseconds there is instead a great fraction of non-emitting microdischarges, because the light signal reduces but not the transported charge ($99° \div 110°$). During the forward semi-cycle, the trends of light and

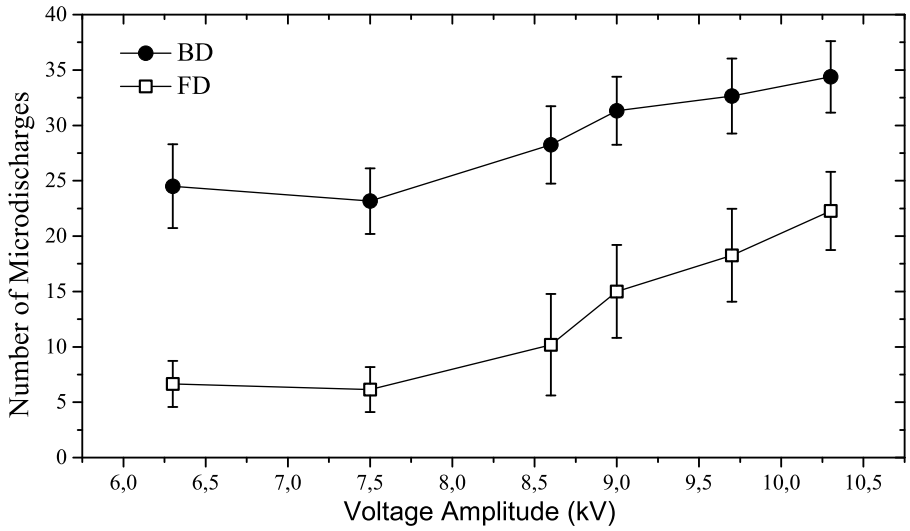

Figure 5.9: Number of current microdischarges during the BD (full circles) and FD (blank squares) semi-cycles as a function of the voltage amplitude.

charge signals with phase instead appear quite similar. The only relevant difference is that light associated to Group F1 is emitted mainly at the beginning, whereas charge is transported also in the second part of Group F1. It is also interesting to observe that the small peak visible in the charge signal at 325° well corresponds to the longest FD spatial extent we have noticed from the spatio-temporal map of light microdischarges (Figure 5.3b).

The differences emerged in the evolution of charge and light signals with phase suggest that electrical and optical diagnostics give insights about different aspects of the SDBD dynamics. Light presumably reflects what happens at the microdischarge formation. As a matter of fact, we expect that the radiative de-excitation of the SPS excited states occurs only for a few nanoseconds, because in air at atmospheric pressure the collisional quenching of these states is particularly rapid [47]. Moreover, about 11 eV are required for exciting the SPS electronic states, and thus only the most energetic electrons created during the microdischarge formation can induce the emission of light [47]. Consequently, the percentage of microdischarges that contributes to the light signal intensity depends on the electric field strength that brings to the creation of a microdischarge and on the density of electrons that can gain energy from this electric field. At the BD breakdown, we can think that the light signal is particularly high because there are many free electrons on the dielectric surface: they enhance both the electric field in the discharge gap and the electron density during the microdischarge formation. In our experiments we found that the temporal duration of a current pulse varies between 10 and 100 ns, whereas we have seen that light pulses generally last just few ns. Then, the current signal is presumably determined by the microdischarge temporal evolution that follows the microdischarge formation. In particular, it is natural thinking that a current pulse is mainly related to the transport of charged particles into the microdischarge channel and that this process requires a longer time.

5.3 Ionizing Wave Propagation Measurements

Results presented in previous sections of this chapter let think that a plasma microdischarge is initiated by a ionizing wave that propagates across the gap and leaves back a channel of weakly ionized plasma. We have thus tried to detect it and to measure the direction and velocity of propagation by contemporary collecting light from different parts of the gap. For these experiments the two electrodes lie parallel with the edges just corresponding in order to avoid any overlap. As a matter of fact, we expect that microdischarges could be longer with a zero superposition instead of a negative overlap. In order to increase the light collected, $200\,\mu m$ core optical fibres (FC-UV200-2 by Avantes) were used instead of the $100\,\mu m$ ones, and we imaged the discharge onto the fibre inlets by means of a commercial objective lens. A discharge pattern of a few millimetres can be anticipated from Figure 5.3. The field of view of the fibres was adjusted to look at this part of the dielectric region by back illuminating the fibres with a torch. A four-furcated optical fibre (FCB-UV200-2 by Avantes) was used to merge signals arriving from the different view lines and was connected to the photomultiplier tube. In order to better separate events coming from different points of the discharge we have introduced fixed delays using optical fibres of different length for the two channels. The fibre material refractive index leads to a prediction of the signal propagation velocity inside the fibre equal to $(1.972 \pm 0.013)10^8$ m/s ($n = 1.52 \pm 0.01$ at 400 nm), which means that each 2 m long fibre provides an expected delay of 10.14 ± 0.07 ns. So, if a different number of fibres is used, photons passing through the channel with a longer total optical path reach later the PMT. The short duration of light pulses associated to the discharges allows to check the theoretical delay caused by the optical fibres: the view lines of two optical fibres were adjusted so that they observed the same spot on the dielectric plate and multiple fibres were connected so that the total fibre length was different for the two channels. As shown in Figure

5.10a, histograms of the relative frequencies of the difference between measured and theoretical delays between signals show a nice sharp peak at about zero nanoseconds. This was obtained for any two couple of channels and various fibre length differences, as could be grasped by the examples displayed

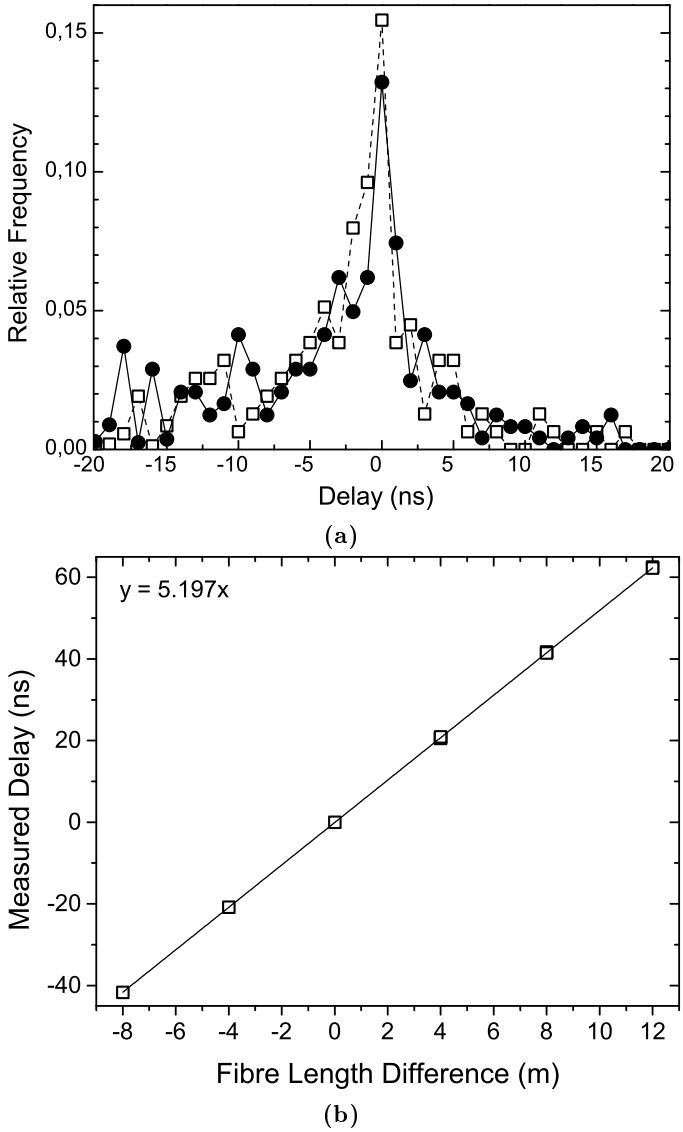

Figure 5.10: (a) Relative frequency histogram of the differences between theoretical and measured delays for first and second channels (full circles, total length difference 8 m) and first and third (blank squares, total length difference 12 m). (b) Measured delay as a function of the fibre length difference, with a linear fit to data.

in Figure 5.10a. As reported in Figure 5.10b, a nice linearity was obtained by increasing the difference in the optical path between two channels. A linear fit to the reported delays versus length difference was used to measure the effective speed of light travelling along our fibres. The delay introduced by the optical fibre material is 5.197 ± 0.007 ns/m, corresponding to a velocity $v = (1.924 \pm 0.003)10^8$ m/s and to a refractive index $n = 1.558 \pm 0.002$. By inverting the lengths of the two optical paths we could also confirm that no bias in the delay was introduced. Indeed the linear fit yields an intercept of -0.07 ± 0.11 ns, consistent with absence of asymmetries.

At this point, experiments were carried out with the first channel pointing directly at the exposed electrode edge ($x = 0$), while the second channel looked at the dielectric surface. The distance between the points of observation is 2.7 ± 0.2 mm. The other two channels were more downstream along the dielectric surface and could not collect light in the present setup. They could be used in future experimental campaigns. In Figure 5.11 the delays measured between two twin PMT peaks is shown as a function of the expected lag due to the difference introduced in the optical path through the optical fibres. In order to achieve the maximal time resolution, multiple peaks like those reported in Figures 4.4 and 5.7 were discarded. This greatly reduce the spread in the measured delays. When only one channel is connected to the photomultiplier tube, about 450.000 events/s were recorded in the case of the first channel, with a mean duration of 2.6 ns. The second channel count rate was smaller, about 80.000 events/s, with a slightly larger duration of 3.2 ns. When we recorded both channels simultaneously, we selected pulses belonging to the backward discharge. This corresponds to events where the voltage of the exposed electrode is positive and rising. In a typical dataset we collected about 300 events, whose relative delay is less than 500 ns. The histogram of the delays between these twin light pulses was calculated and fitted with a Gaussian function, in order to obtain

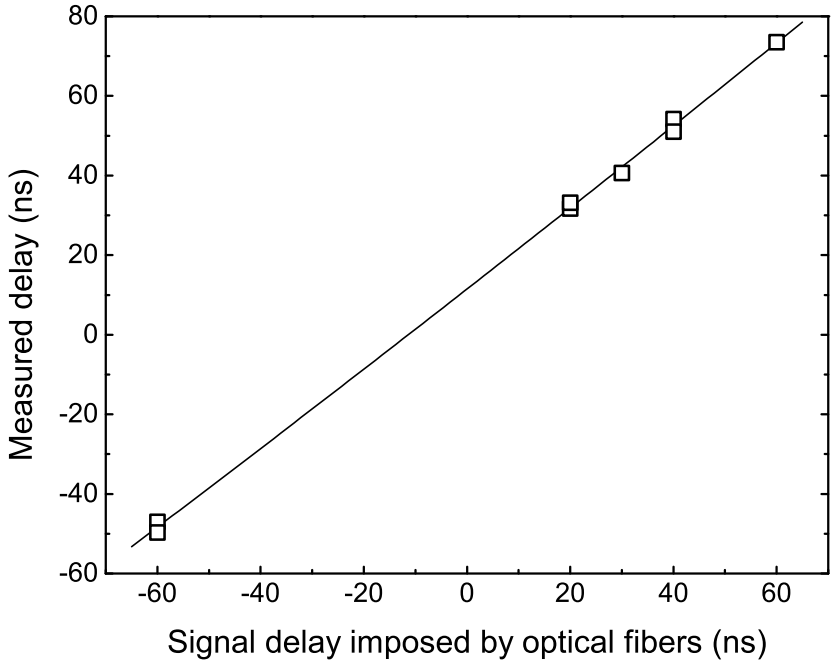

Figure 5.11: The measured delay peak as a function of the calculated delay imposed by the fibre length mismatch for backward discharge events.

data shown in Figure 5.11. A definite time lag is present between the two channels, independently from the preset delay. The nice linearity allows to estimate a time lag of 12.1 ± 0.6 ns. This corresponds to a propagation velocity of 223 ± 17 km/s directed from the electrode edge to the dielectric surface. This direction is opposite to that of the drifting electrons of the backward discharge, and it is thus associated to a cathode-directed ionizing wave.

Then we analysed also events belonging to the forward discharge. Unfortunately, while the count rate in the first channel was high enough, actually even larger than that of the backward events (as expected from Figure 5.3a, the same does not hold for the second channel. Here only the 15% of the events happens in the forward stroke. We tried to reconstruct a delay histogram without finding any definite peak, at least for delays shorter than 500 ns. Due to the limited statistics we can neither estimate nor exclude

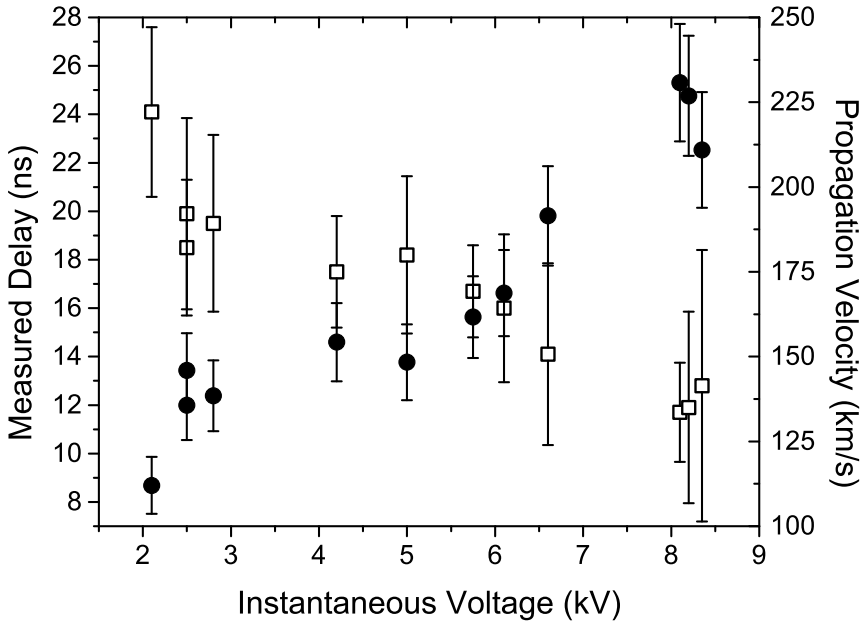

Figure 5.12: Time lag between the two channels and corresponding propagation velocity as a function of HV instantaneous value.

a propagation, although it is confirmed that most of the FD events develops near the edge of the exposed electrode and do not spread much on the dielectric surface.

Finally, using the segmented acquisition function of the scope, we accumulated statistics of events happening in a definite and limited range of values of the instantaneous voltage. A clear, albeit somewhat noisy, dependence can be appreciated from the data reported in Figure 5.12. The time lag decreases with voltage and the corresponding propagation velocity, always directed from the electrode edge towards the dielectric, increases from 110 km/s up to 250 km/s. These results are consistent with the ones obtained by means of cross-correlation spectroscopy [52].

CHAPTER 6

Plasma Actuator Performances

When the possibility of using these asymmetric SDBDs for aerodynamic applications is considered, it is important to evaluate the discharge ability to work as a flow control actuator as well as the energy required for obtaining these fluid dynamic benefits. The operating parameters (such as voltage and frequency) and the geometrical arrangement should be optimized in order to achieve the best efficiency, defined as the ability of transferring the injected electrical power to the fluid surrounding the actuator [152]. As a matter of fact, for in-flight flow control applications, control of weight and power consumption is of utmost importance [153]. With the aim of evaluating the potentialities of a single SDBD as a plasma actuator for flow control, we

have measured the velocity of the electric wind by means of a Pitot tube, and results are presented in Section 6.1. Electric power measurements have instead been performed by means of a capacitive probe, and are discussed in Section 6.2.

6.1 Induced Wind Speed

The x-component U of the airflow induced by the discharge in absence of a free external airflow has been measured as described in Section 4.3.4, providing an indication of the region where the plasma couples momentum into the background still air [154]. A velocity profile is obtained by measuring U at different distances z from the dielectric surface. Figure 6.1 shows three profiles obtained at three different distances x from the exposed electrode

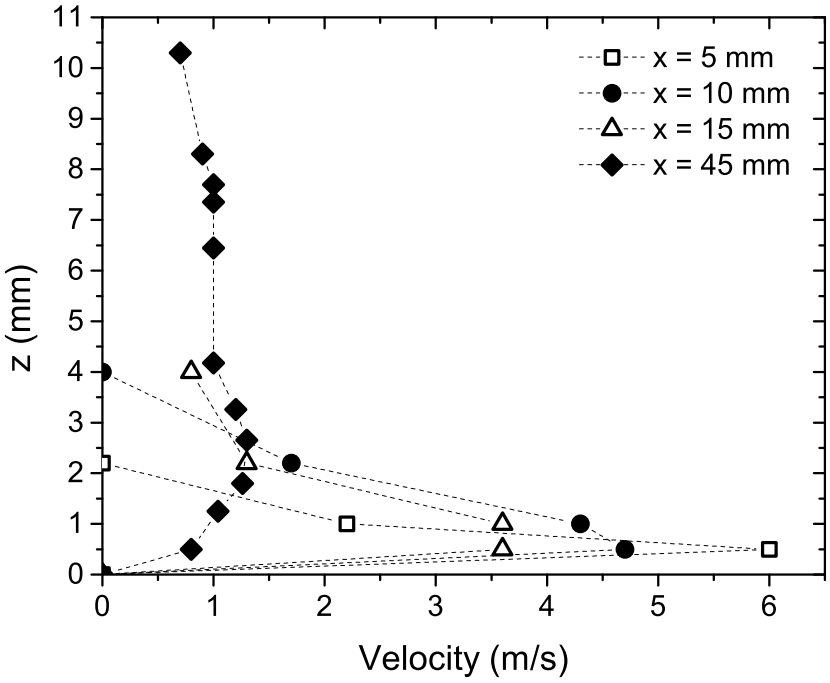

Figure 6.1: Velocity profiles at four chordwise distances x from the exposed electrode edge, for a SDBD with a 1.5 mm thick teflon barrier. The widths of the exposed and buried electrodes are 5 mm and 10 mm. The driving frequency and the voltage amplitude are 7 kV and 45 kHz respectively.

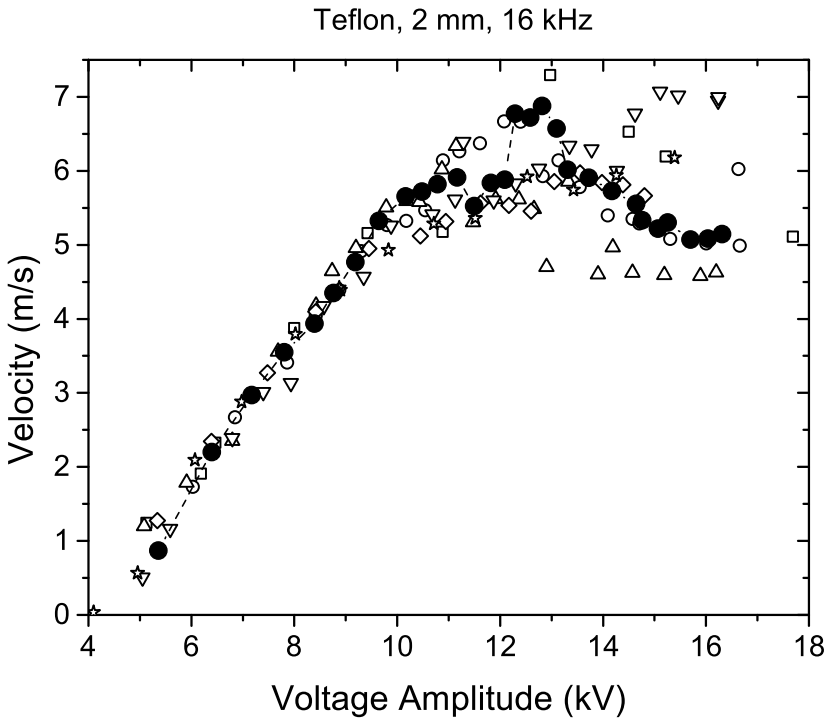

Figure 6.2: Velocity of the airflow induced by the SDBD for different amplitudes of the applied sine voltage. A 2 mm teflon plate is used as insulating barrier. The driving frequency is equal to 16 kHz.

edge, for a plasma actuator with a 1.5 mm thick teflon sheet as insulator, fed with a sinusoidal voltage with amplitude equal to 7 kV and frequency 45 kHz. The plasma chordwise extension has been measured by imaging the light emitted by the discharge with a digital camera and is equal to about 5 mm. Given x, the maximum velocity of the profile is usually located within the first millimetre above the dielectric surface [31, 155]. This is true until the induced airflow detaches from the wall. In Figure 6.1, before flow detachment the vertical extension of the wall jet is limited to a few millimetres and the profile has a well defined maximum velocity near the surface. If x is varied, the maximum velocity of the induced jet is located in correspondence of the spatial end of the discharge in the chordwise direction and gradually decreases when moving downstream (Figure 6.1) [31, 156]. At $x = 45$ mm the velocity is quite uniform along the z direction for several millimetres,

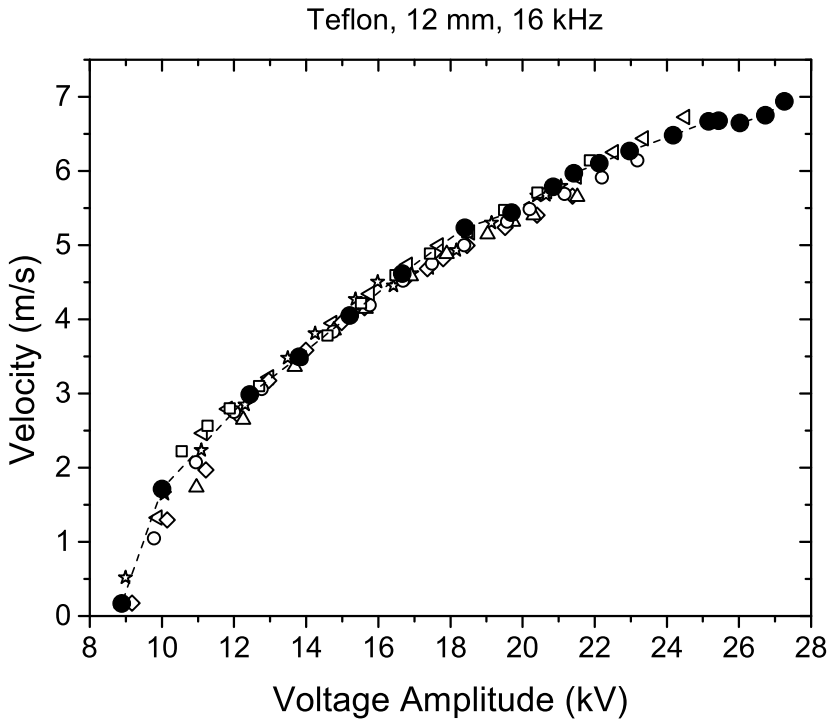

Figure 6.3: Velocity of the airflow induced by the SDBD for different amplitudes of the applied sine voltage. A 12 mm teflon plate is used as insulating barrier. The driving frequency is equal to 16 kHz.

with a small maximum located at $z = 2.5$ mm. The exposed and buried electrode chordwise widths are 5 mm and 10 mm respectively. This is our typical setup so, in order to compare plasma actuators differing for the dielectric barrier or the sinusoidal voltage adopted, we have chosen to measure the induced velocity at the end of the buried electrode, that is at $x = 10$ mm. All the measures presented in the following graphs are wall velocity, meaning that the pitot tube was located in contact with the plasma actuator surface.

Given a insulating barrier, we have fixed the frequency and measured the velocity of the wall jet as a function of the voltage amplitude, as shown in black circles for two teflon sheets with different thickness in Figures 6.2 and 6.3. We have made these measurements several times, for repeatability and uncertainty evaluation. In these figures a different symbol is adopted for each

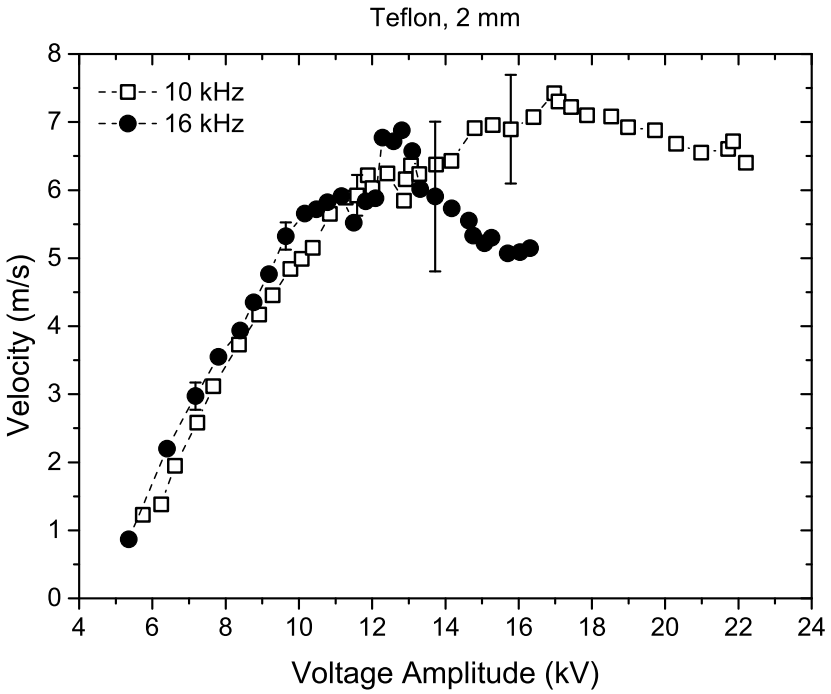

Figure 6.4: Velocity of the airflow induced by the SDBD for different amplitudes of the applied sine voltage. The insulating barrier is a teflon plate with thickness equal to 2 mm. Results for two different frequencies of the applied voltage are shown.

velocity versus voltage curve. Error bars have thus been associated to the velocity values. Below a voltage threshold the induced wind speed is equal to zero because the electric field generated inside the air gap is not sufficient for ionization and plasma generation. When the voltage amplitude is increased enough, the discharge breakdown is obtained and an electric wind with non-zero velocity is generated. This voltage threshold depends on the dielectric barrier choice because the more the thickness the more is the voltage drop on the insulating sheet. As a matter of fact, in absence of plasma, we can think to the actuator as a series of two capacitances C_{air} and C_{die}. The former is associated to the air gap between the exposed electrode and the dielectric surface, the latter to the insulating barrier. Given a voltage V_1 applied to the exposed electrode, the voltage drop across the air gap is $(V_1 - V_2)$ and V_2 is the one across the dielectric plate. The system behaves like a voltage

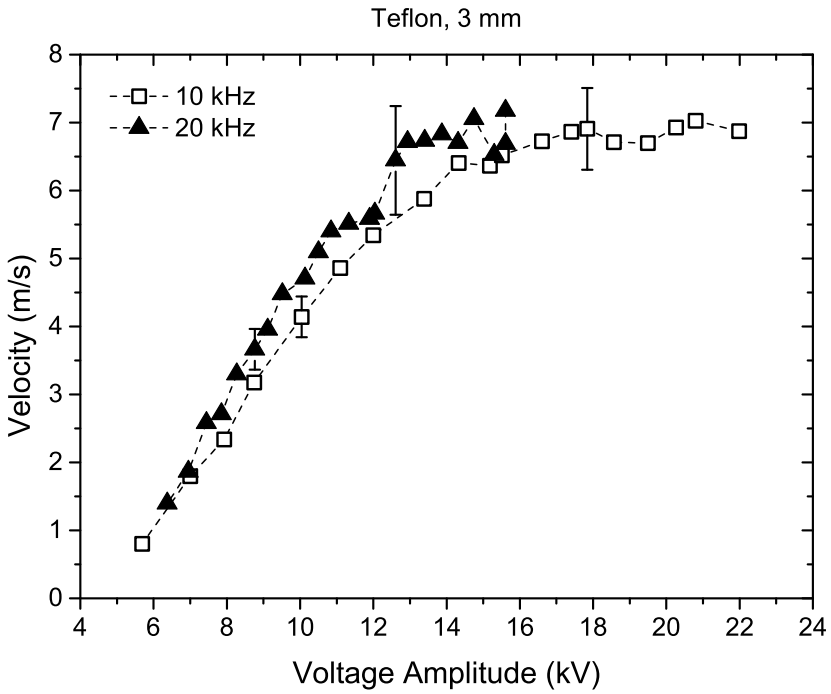

Figure 6.5: Velocity of the airflow induced by the SDBD for different amplitudes of the applied sine voltage. The insulating barrier is a teflon plate with thickness equal to 3 mm. Results for two different frequencies of the applied voltage are shown.

divider with

$$V_2 = \frac{C_1}{C_1 + C_2} V_1, \tag{6.1}$$

so V_2 rises if C_2 decreases and thus if the thickness of the insulating barrier increases. Clearly this is a first approximation, and since the set up electrode configuration is not planar the value of V_2 on the dielectric barrier depends on the chordwise position x.

The electric wind velocity at first increases with the voltage amplitude for both the cases presented in Figures 6.2 and 6.3. However, for the thin teflon plate, a saturation of the induced airflow velocity is evident for voltages higher than $10 \div 11$ kV. It is evident that the uncertainty associated to the wall jet velocity becomes considerably larger when saturation occurs: $\pm(0.8 \div 1.2)$ m/s against $\pm(0.2 \div 0.3)$ m/s. Some measurements show that above a

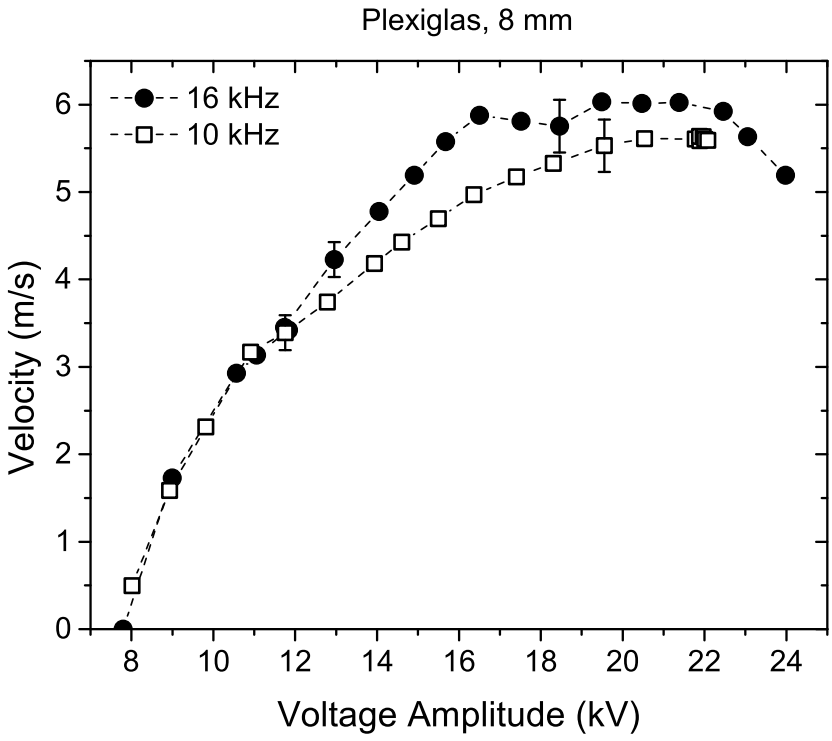

Figure 6.6: Velocity of the airflow induced by the SDBD for different amplitudes of the applied sine voltage. The insulating barrier is a plexiglas plate with thickness equal to 8 mm. Results for two different frequencies of the applied voltage are shown.

certain threshold the speed can even decrease with the applied voltage (see for example full or blank circles in Figure 6.2). For the 12 mm thick teflon it is not clear if the velocity curve is going to flatten above 25 kV. Voltage amplitudes higher than the ones accessible with our power supply should be necessary to investigate this point. In Figures 6.4 - 6.9 different materials and frequencies have been considered.

Basing on these velocity versus voltage plots, at least for sufficiently thin dielectric panels, we can distinguish a range of voltages in correspondence of which the velocity increases (*growth region*, between a *breakdown voltage* and up to a *saturation voltage*) from a *saturation region* where the velocity fluctuations are larger and the speed of the wind induced by the discharge seems to remain constant or even decrease with the voltage amplitude. This

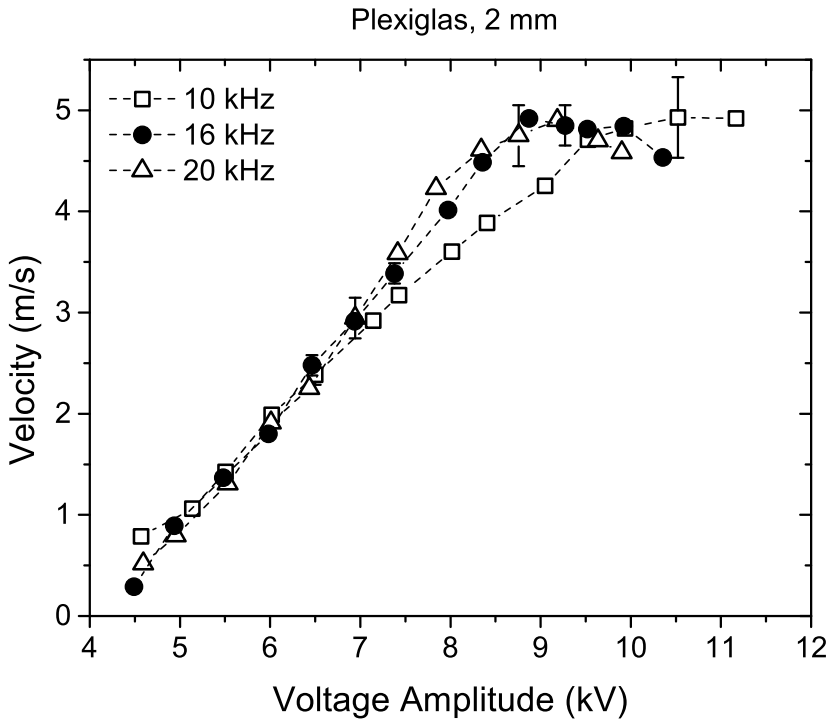

Figure 6.7: Velocity of the airflow induced by the SDBD for different amplitudes of the applied sine voltage. The insulating barrier is a plexiglas plate with thickness equal to 2 mm. Results for three different frequencies of the applied voltage are shown.

saturation has sometimes already been observed in literature, as a flattening of the induced velocity or thrust with the voltage amplitude or the consumed power [31, 155, 157, 158]. As a matter of fact, thrust is another quantity used to describe the wall jet, and is usually interpreted as a measure of the reaction force on the dielectric plate resulting from the plasma induced body force and shearing effects [159].

These plots reveal that in the growth zone a higher frequency generally corresponds to slightly higher velocities. However saturation occurs at lower voltages so the maximum velocity (*saturation velocity*) is quite independent on frequency or even decreases with a frequency increase. For example, when a 2 mm thick plate in teflon or peek is used (Figures 6.4 and 6.8), the saturation velocity seems higher at 10 kHz rather than at 16 kHz. What

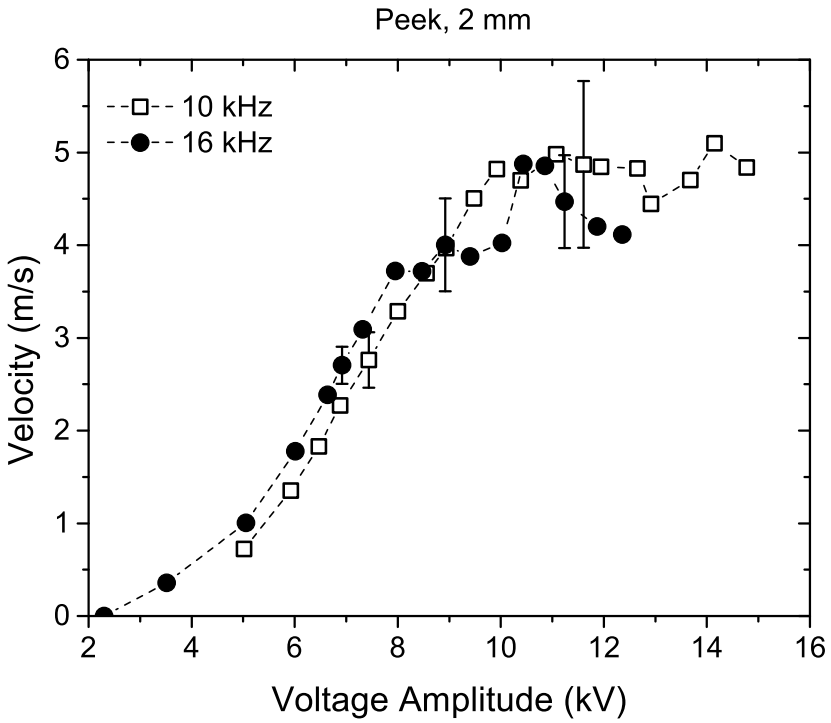

Figure 6.8: Velocity of the airflow induced by the SDBD for different amplitudes of the applied sine voltage. The insulating barrier is a peek plate with thickness equal to 2 mm. Results for two different frequencies of the applied voltage are shown.

appears quite clearly from our measurements is that the breakdown voltage for electric wind generation is quite independent from frequency, and that a few kV after breakdown the induced wind velocity increases faster for higher frequencies. Nevertheless, when larger frequencies are adopted, saturation occurs at lower voltage amplitudes and the transition from the growth regime to the saturation one is more defined and abrupt. For instance, for the plexiglas panel with thickness equal to 8 mm (Figure 6.6) the velocity saturation is visible 9 kV after the voltage breakdown at 16 kHz and 13 kV at 10 kHz, and for the teflon panel with thickness equal to 3 mm (Figure 6.5) the voltages of the growth region cover a interval of $6 \div 7$ kV at 20 kHz and of $9 \div 10$ kV at 10 kHz. These results are consistent with the ones presented in reference [157], in which authors found that below saturation a given thrust

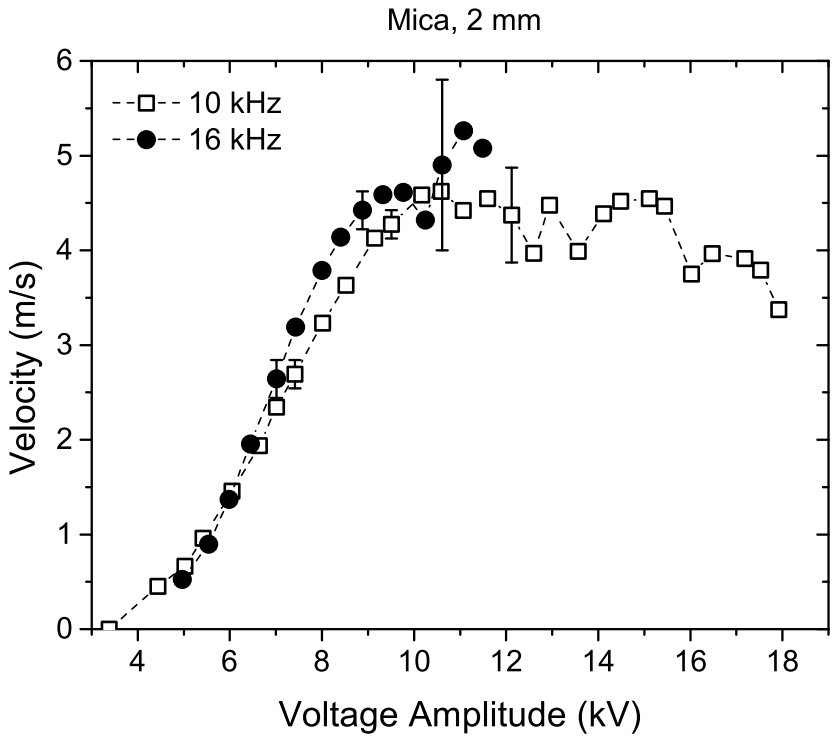

Figure 6.9: Velocity of the airflow induced by the SDBD for different amplitudes of the applied sine voltage. The insulating barrier is a mica plate with thickness equal to 2 mm. Results for two different frequencies of the applied voltage are shown.

can be obtained at lower voltages if higher frequencies are used, and that saturation can be delayed by lowering the frequency of the sinusoidal high voltage.

Both growth and saturation regions have been observed for every material and thickness presented in these figures, except for the thickest teflon plate (12 mm), but results suggest that saturation may occur with this dielectric barrier too, if higher voltage amplitudes could be achieved. When thin dielectric barriers are used in the growth region the velocity increases linearly with voltage. For an insulating barrier with thickness equal to 2 mm the slope is $(8.1 \pm 0.4) \cdot 10^{-1}$ m/skV at 10 kHz and $(9.7 \pm 0.4) \cdot 10^{-1}$ m/skV at 16 kHz. For thicker panels (8 and 12 mm) it is evident that velocity does not follow a linear growth.

The influence of the dielectric material can be analysed by comparing plasma actuators with the same thickness of the insulating barrier and working at the same frequency (Figures 6.11 and 6.12). Teflon, plexiglas, peek and mica have been adopted, with nominal relative permittivity ε_r equal to (2.0÷2.1), (2.2÷3.4), (3.0÷3.2) and (4÷9). We thus expect that ε_r increases if teflon, plexiglas, peek and mica are considered in this order. For checking it we have applied two circular disks of aluminium tape (diameter 45±1 mm) at the opposite surfaces of the insulating plate, thus obtaining a capacitor with a planar configuration. One electrode was connected to the high-voltage power supply and the high-voltage probe, whereas a capacitive probe (see Section 4.3.3) was interposed between the other electrode and the ground.

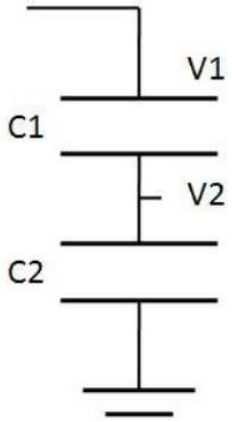

Figure 6.10: Sketch of the capacitive voltage divider.

If V_1 is the applied high-voltage, the voltage drop across the insulating plate (with capacitance $C1$) is $(V_1 - V_2)$, where V_2 is the one across the capacitive probe with capacitance equal to C_2 (Figure 6.10). The system behaves like a voltage divider and Equation 6.1 holds. This allows to indirectly measure C_1, and then ε_r can be obtained by considering the expression for a parallel plane disk capacitor $C_{pl} = \varepsilon_0 \varepsilon_r \pi R^2/d$, where R is the disk radius, d the separation between the electrodes and ε_0 the vacuum permittivity. However, for taking into consideration edge effects we have corrected the value of C_{pl} by multiplying it for the following expression that depends on the aspect ratio $b = d/R$ [160]:

$$\tilde{C}_{pl} = C_{pl}(1 + 1.298 b^{0.867}), \tag{6.2}$$

and we have then imposed $C_1 = \tilde{C}_{pl}$. We used a few panels with different

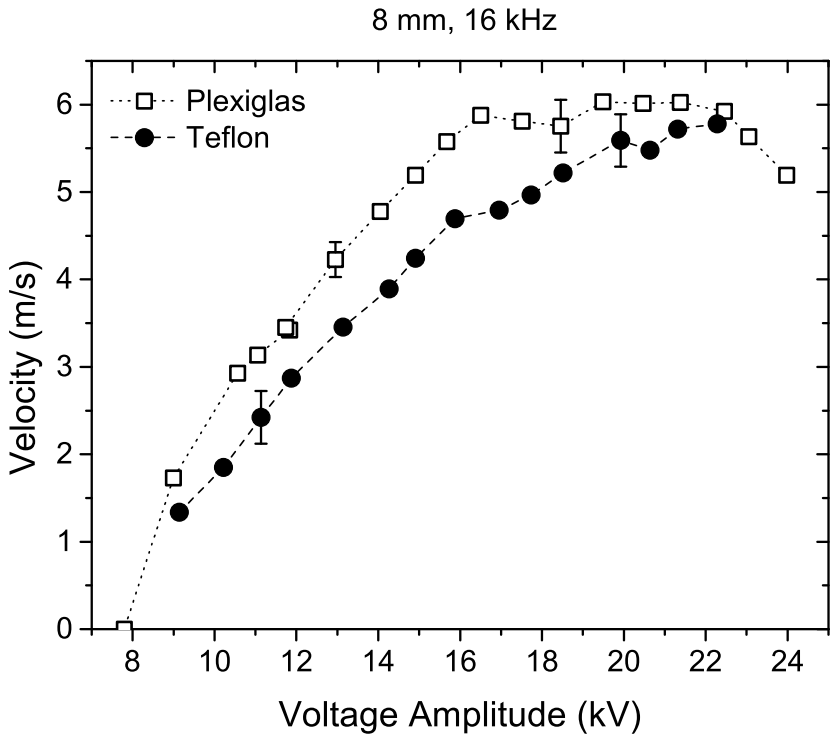

Figure 6.11: Velocity of the airflow induced by the SDBD for different amplitudes of the applied sine voltage. The insulating barrier is made of teflon or plexiglas and is 8 mm thick. The frequency of the high voltage signal is 16 kHz.

thickness for teflon (1.5 mm, 2 mm, 3 mm and 12 mm) and plexiglas (2 mm, 3 mm and 8 mm), and we found $\varepsilon_r = 2.07 \pm 0.14$ and $\varepsilon_r = 3.1 \pm 0.2$ respectively. These uncertainties are dominated by differences found among panels. Concerning peek and mica, we had just 2 mm thick plates and we found $\varepsilon_r = 3.8$ and $\varepsilon_r = 4.2$ respectively. Assuming an uncertainty equal to 0.2 for these dielectric permittivity too, we can think teflon has the lowest relative dielectric constant, followed by plexiglas, peek and eventually mica.

Figure 6.11 shows that an increase of ε_r has the same effect of using of a higher frequency: the electric wind has a faster speed in the growth zone, but its trend with voltage flattens at lower amplitudes and more abruptly. This is again consistent with results showing that the maximum thrust achievable before saturation can be increased by choosing materials with a low relative

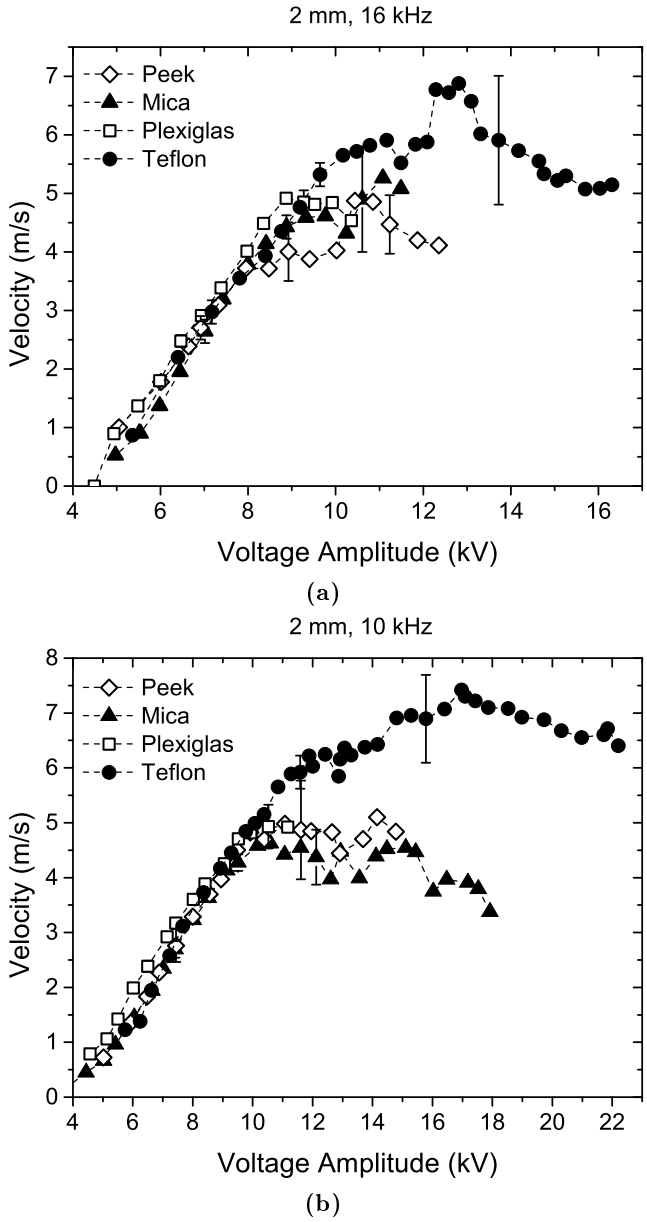

Figure 6.12: Velocity of the airflow induced by the SDBD for different amplitudes of the applied sine voltage. The insulating barrier is made of teflon, plexiglas, peek or mica and is 2 mm thick. The frequency of the high voltage signal is 16 kHz (a) or 10 kHz (b).

permittivity [157]. Such a dependence from ε_r is less clear when a thinner insulating barrier (2 mm) is adopted (Figure 6.12), even though the greatest velocities are still obtained with teflon. The choice of the insulating mate-

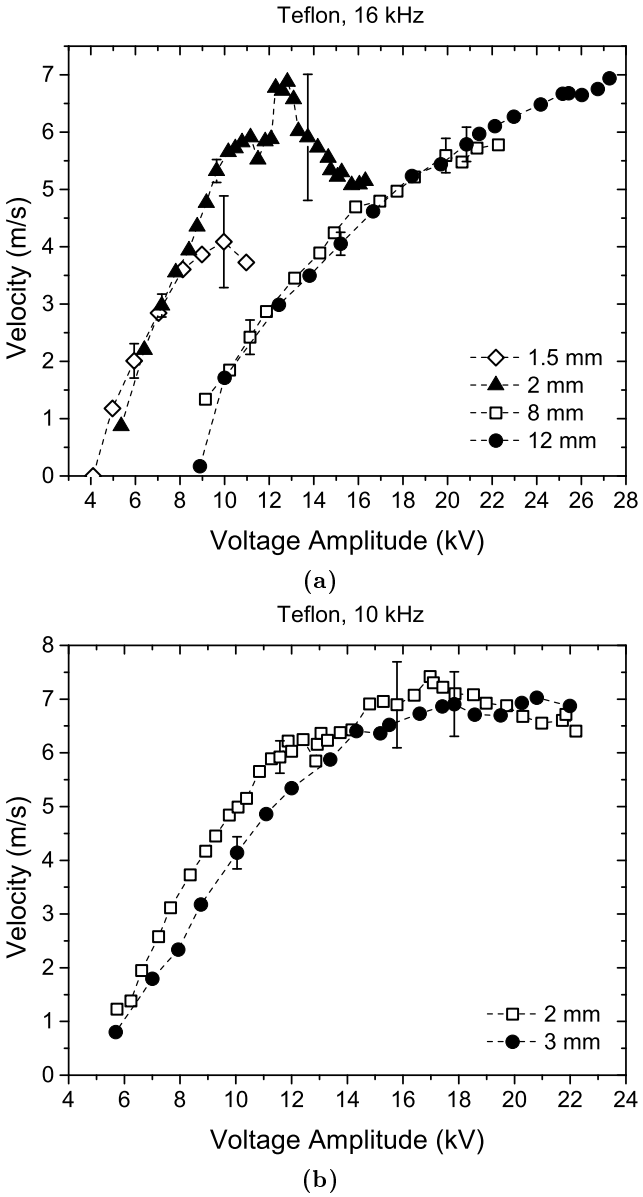

Figure 6.13: Velocity of the airflow induced by the SDBD for different amplitudes of the applied sine voltage. The insulating barrier is made of teflon and is 1.5, 2, 3, 8 or 12 mm thick. The frequency of the high voltage signal is 16 kHz (a) or 10 kHz (b).

rial does not influence significantly the breakdown voltage amplitude above which the electric wind is produced by the surface discharge.

In Figures 6.13 and 6.14 the velocity of the wall jet is displayed for

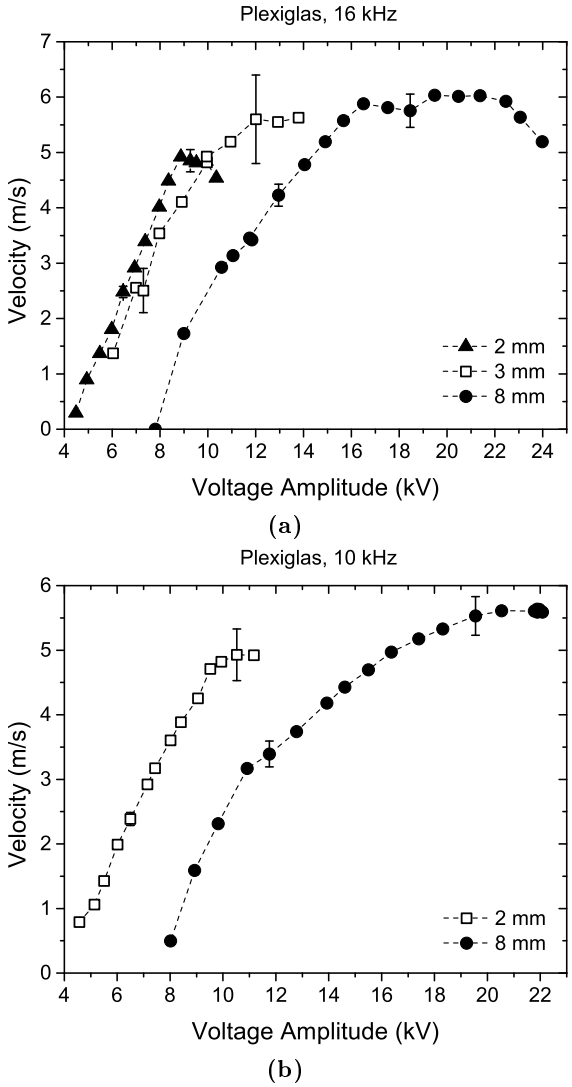

Figure 6.14: Velocity of the airflow induced by the SDBD for different amplitudes of the applied sine voltage. The insulating barrier is made of plexiglas and is 2, 3 or 8 mm thick. The frequency of the high voltage signal is 16 kHz (a) or 10 kHz (b).

different values of the thickness d of a same insulating material. It is clear that if d increases from 2 or 3 mm to 8 or 12 mm considerably higher voltages are needed for obtaining the same airflow velocity. As a matter of fact, a larger dielectric thickness causes a greater voltage drop across the insulating barrier and thus a smaller electric field inside the gap. If the

system capacitance scaled with ε_r/d as in a planar configuration, the effect of doubling ε_r or of halving d would be the same. In our experiments the influence of d is more evident rather than the one of ε_r, first of all because of the ranges of d and ε_r considered. If we consider teflon and plexiglas the dielectric constant ratio is equal to about 1.5, and an equal value is obtained changing d from 8 to 12 mm or from 2 to 3 mm. Figure 6.11 shows that for having a velocity equal to 3.5 m/s with a 8 mm thick panel in teflon or plexiglas a voltage difference of about 1.5 kV is necessary. Almost the same happens if two teflon panels with different thicknesses are used (2 mm $\rightarrow$ 3 mm in Figure 6.13b, and 8 mm $\rightarrow$ 12 mm in Figure 6.13a). However, a lower voltage difference (0.5 kV or less) is found when thin plexiglas sheets are used (2 mm and 3 mm, Figure 6.14a) or if a 2 mm plate in teflon or plexiglas is adopted (Figure 6.12). In this last case it is noticeable that no significant differences can be noticed even between teflon and mica, although ε_r doubles.

We can thus conclude that higher voltages are required when the insulating barrier thickness is increased, especially if changes of some millimetres are involved. The dependence on the value of relative permittivity is instead

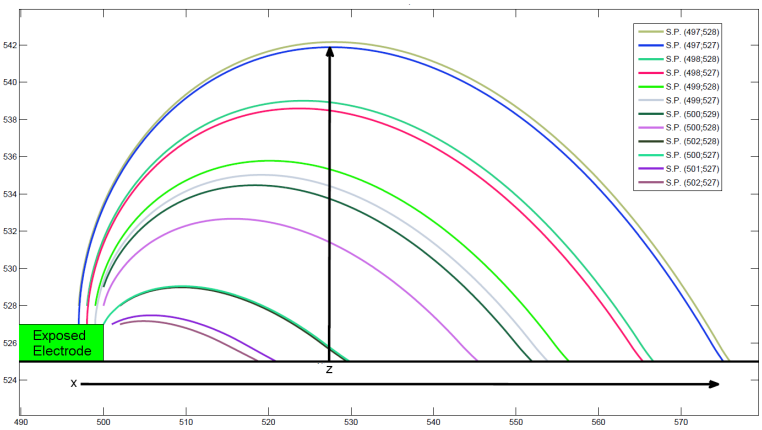

Figure 6.15: Representation of the electric field lines. Axis are in arbitrary units. The longest field line (marked as $(497-528)$) has a spatial extension equal to 3 mm along x and to 0.7 mm along z.

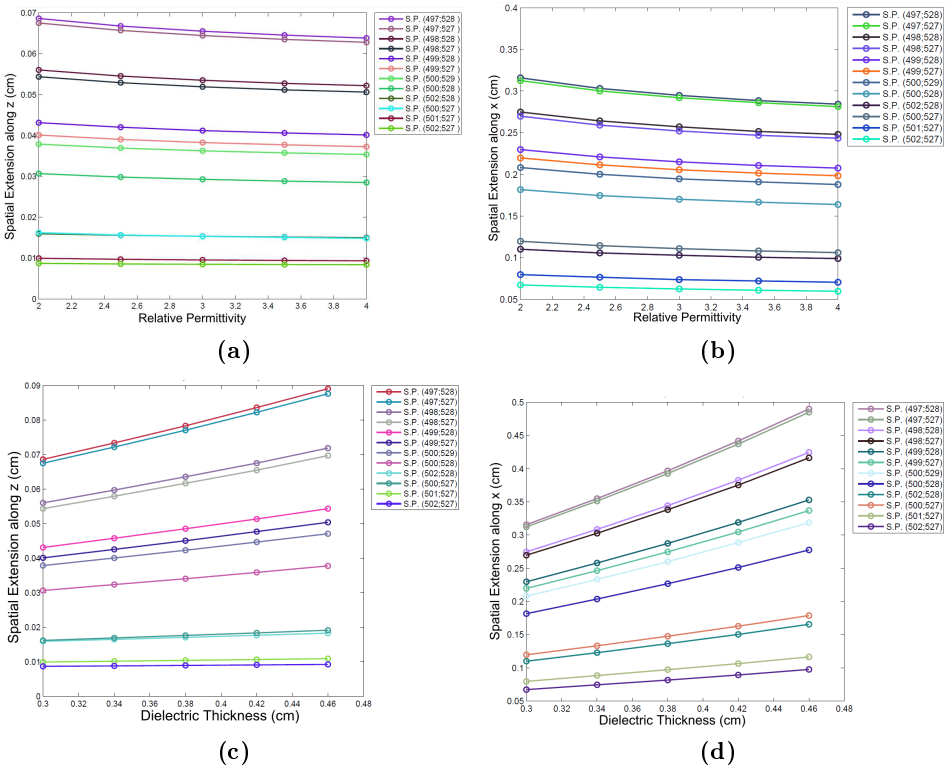

Figure 6.16: The spatial extensions of the field lines depicted in Figure 6.15 as a function of the relative permittivity ε_r and of the dielectric thickness d [161].

less clear. Simulations of the Laplacian field filling the space between two electrodes with chordwise extension equal to 5 and 10 mm and zero overlap, like in our setup, show that the influence on the shape of the electric field lines of d is greater than the one of ε_r [161]. Figures 6.15 and 6.16 show how their maximum extensions above the dielectric surface and in the chordwise direction depend on these two parameters. For example, if we consider the line marked as (497-527), a change of the dielectric constant from 2 to 3 (ratio equal to 1.5) provokes a percentage decrease equal to 10% along x and to 4% along z. This means that the region of high electric field is more concentrated near the exposed electrode edge and the dielectric surface [162]. For the same line, a variation of d from 4.5 mm to 3 mm (ratio equal to 1.5 again) instead involves a percentage variation of 40% and 25% respectively.

We have also tried to change the surface properties of the insulating barrier by placing a self-adhesive tape (in teflon, kapton and other materials) on the dielectric barrier side where air is ionized. As Figure 6.17 reveals, no

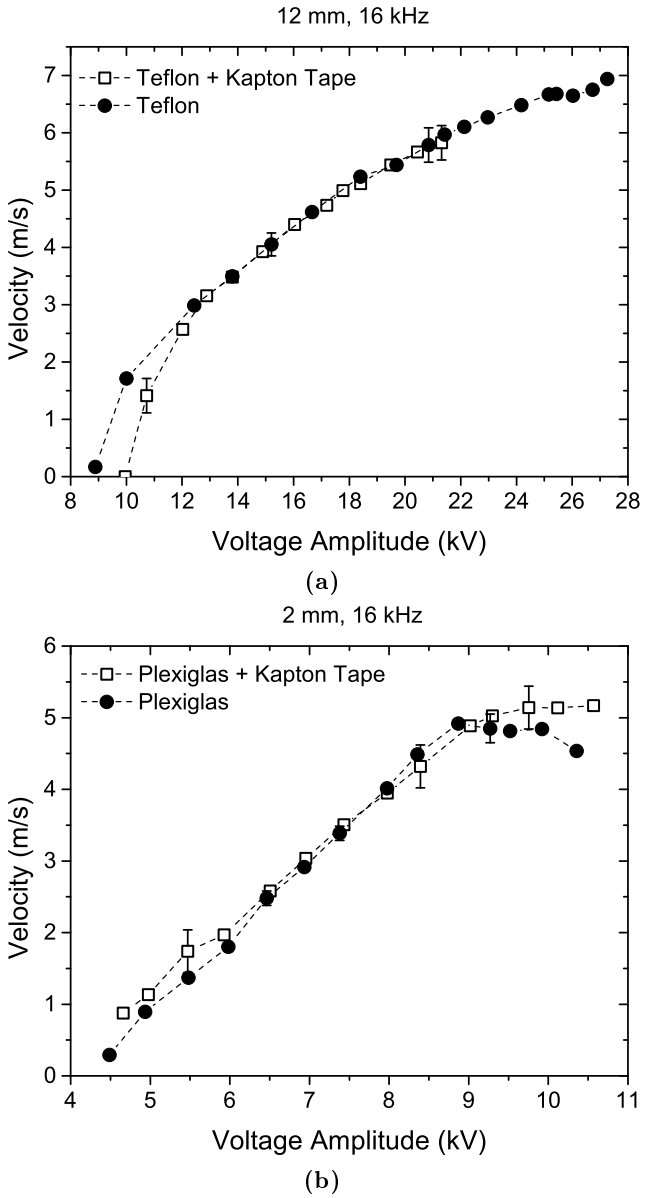

Figure 6.17: Velocity of the airflow induced by the SDBD for different amplitudes of the applied sine voltage, with and without the presence of a kapton tape ($65\mu m$ thick) placed on a 12 mm teflon barrier (a) or on a 2 mm plexiglas sheet (b). The frequency of the high voltage signal is 16 kHz.

appreciable differences in the electric wind velocity could be found, so we did not investigate further this point. Even though the submillimetric characteristics of the surface could influence the microdischarge generation and evolution, before focusing on this topic a deeper knowledge of the properties of these discharges would be helpful.

The arrangement of the electrodes used in this experimental campaign has been chosen because it is a configuration typically adopted at Alenia Aermacchi Wind Tunnel Gallery and Plasma Laboratories. As a matter of fact, the electrode chordwise widths (5 mm and 10 mm) are quite limited and guarantee a good versatility for experiments using multi-actuator configurations covering a non-rectangular surface such as a wing. The zero overlap between the electrodes is not optimized because it is known that the fastest wind speed is obtained for a positive x separation between the end of the exposed electrode and the beginning of the buried one [145, 155]. However, this x_{best} value depend on the dielectric thickness and material and should thus be optimized for every plasma actuator, whereas the zero overlap assures quite good performances independently from the plasma actuator characteristics. This ground electrode width is usually larger than the plasma chordwise extension. It has been already observed that a too narrow buried electrode can be responsible for the saturation of the electric wind we have talked about [158]. In Figure 6.18 two examples demonstrating that the velocity is not limited by the electrode width are shown. In particular, in Figure 6.18a, saturation is well visible also when the electrode extension is doubled.

As a final remark it's worth pointing out that the velocity at $x = 10$ mm can be smaller than the maximum speed U_{max} of the wall jet, especially at low voltages, when plasma covers just a small portion of the electrode. As a matter of fact, the electric wind velocity rises up to the end of the discharge region and then usually decreases with x. However, if x is not

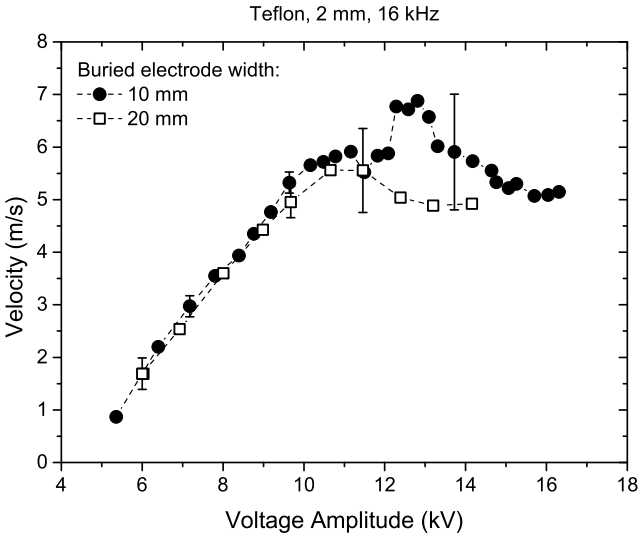

(a)

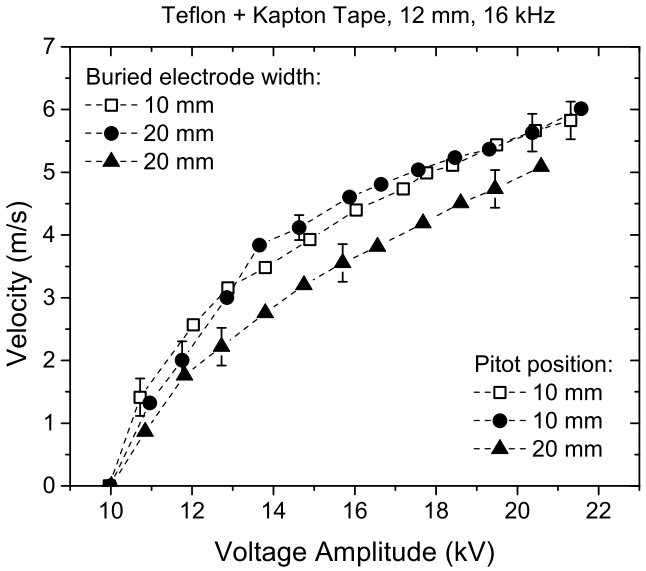

(b)

Figure 6.18: Velocity of the airflow induced by the SDBD for different amplitudes of the applied sine voltage for a teflon barrier with tickness equal to 2 mm (a) or 12 mm (b). The buried electrode chordwise width is 10 mm or 20 mm. In subfigure (a) the Pitot tube chordowise position is $x = 10$ mm, whereas in subfigure (b) it is $x = 10$ mm or $x = 20$ mm. The frequency of the high voltage signal is 16 kHz.

too large compared to plasma extension, the trend of the velocity measured in x is similar to the behaviour of U_{max} with the applied voltage [159]. The end of the buried electrode ($x = 10$ mm) generally corresponds to

a few millimetres beyond the plasma propagation length. An advantage of measuring the velocity at a fixed x (instead of U_{max}) is that knowing the actuator behaviour in correspondence of a certain position allows to foresee its aerodynamics potentialities, such as the ability of preventing flow detachment at that point. In any case, results similar to the ones shown in this section have been found by considering U_{max} [31, 163].

This experimental campaign let think that the speed of the airflow induced by a surface DBD initially grows with the applied voltage, but can not be increased as much as desired, since above a certain threshold a larger voltage amplitude does not correspond to a faster electric wind. The results presented here, together with the ones already published in literature, show that the typical velocity of the wind induced by the discharge is few metres per second. For flow separation control, such velocities are sufficient for moving the separation point of external airflows with speed up to 20 m/s, but for the practical usage of actuators this velocity should increase up to 100 m/s [164]. Further investigations about the properties of these discharges and about the growth and saturation regimes of the electric wind are thus required.

6.2 Power Consumption

As described in Section 4.3.3, an accurate method for the determination of power consumption is to integrate the current passing through the actuator in time using a capacitive probe [88, 165]. The trend of the power P_{dis} as a function of the applied voltage has been investigated for insulating barriers with different thickness and composition. The electrode arrangement is the one of setup B, already described in Section 4.1 and already adopted for electric wind speed measurements. In Figure 6.19 results for teflon and plexiglas barriers and a same frequency of the voltage signal are shown. It is evident that, given a voltage amplitude and frequency, the thinner the

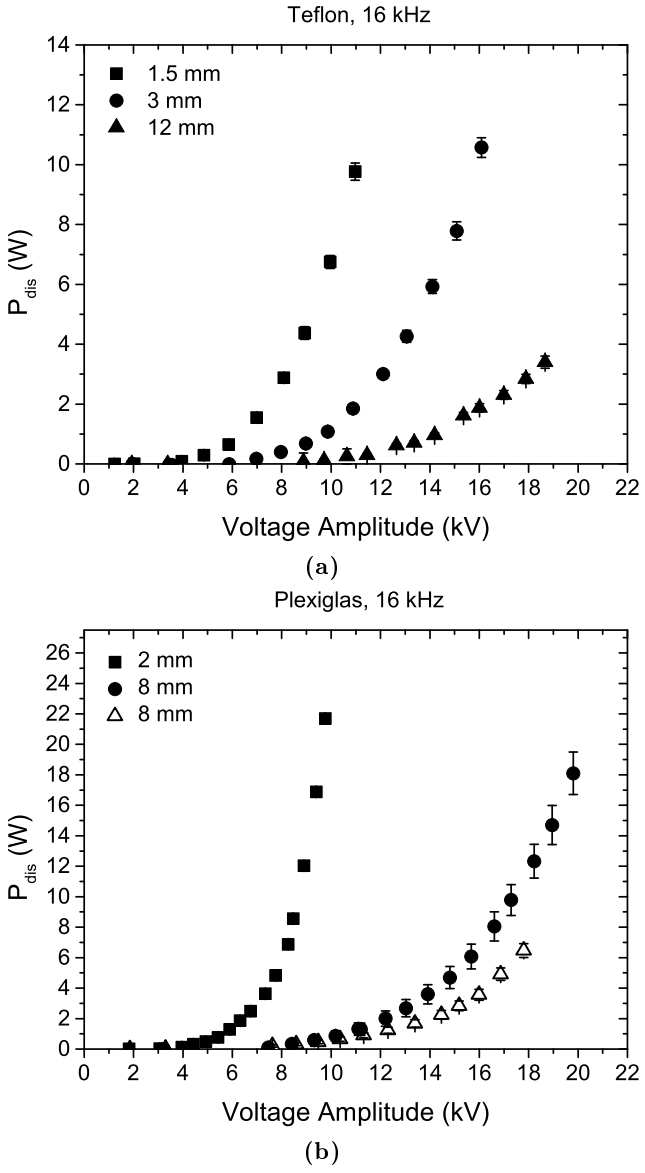

Figure 6.19: Consumed power at 16 kV for different amplitudes of the applied sine voltage for teflon (a) and plexiglas (b) barriers. The plate thickness varies in the range $1.5 \div 12$ mm and it is indicated in the label. For plexiglas, blank triangles refer to a plasma actuator with electrode length equal to 10 cm instead of the usual 20 cm.

dielectric plate the larger is the dissipated power. This is in agreement with results presented in literature [145], and it is first of all an effect of the difference in the voltage necessary for electrical breakdown. In Figure 6.19b

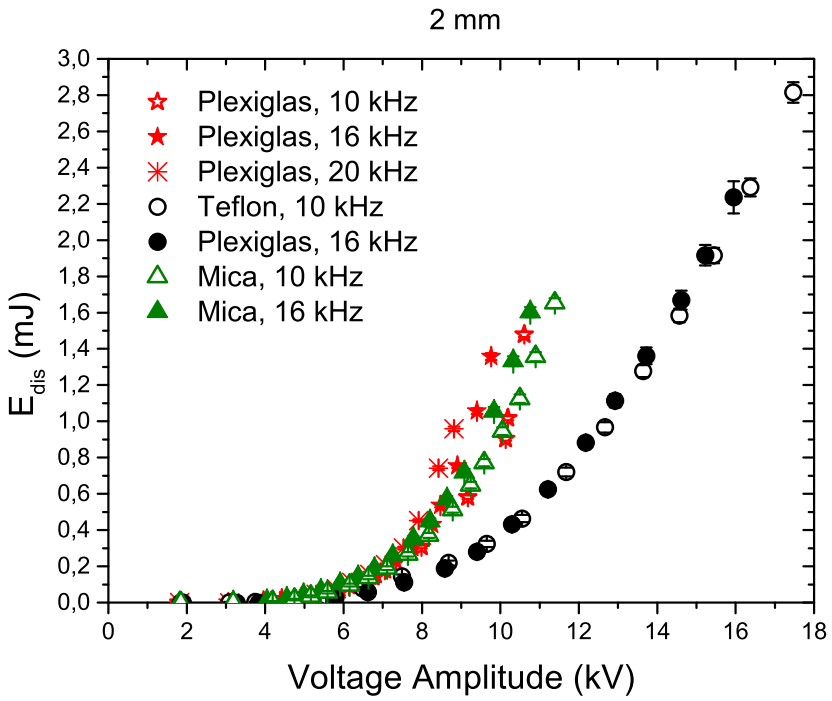

Figure 6.20: Consumed energy at different frequencies and voltage amplitudes for 2 mm thick dielectric barriers made of different materials.

it is also shown that if the spanwise y extension of the plasma actuator is reduced the power decreases. The power values presented in these graphs have been obtained at the same frequency because it is known that this quantity is not independent from the period of the applied voltage. Several authors claim that the consumed power increases linearly with frequency [155, 158, 166, 167], whereas in few cases a power-law dependence with an exponent higher than one has been proposed [152]. Our results agree quite well with the linear dependence, as suggested by Figure 6.20, in which the power divided the frequency has been plotted, corresponding to the energy lost per cycle E_{dis}.

Results relative to different dielectric materials are presented, for a same plate thickness equal to 2 mm. First of all, it is evident that, given a voltage amplitude, the power dissipated when mica and plexiglas are chosen as insulating barriers is higher compared to the teflon case, which has a

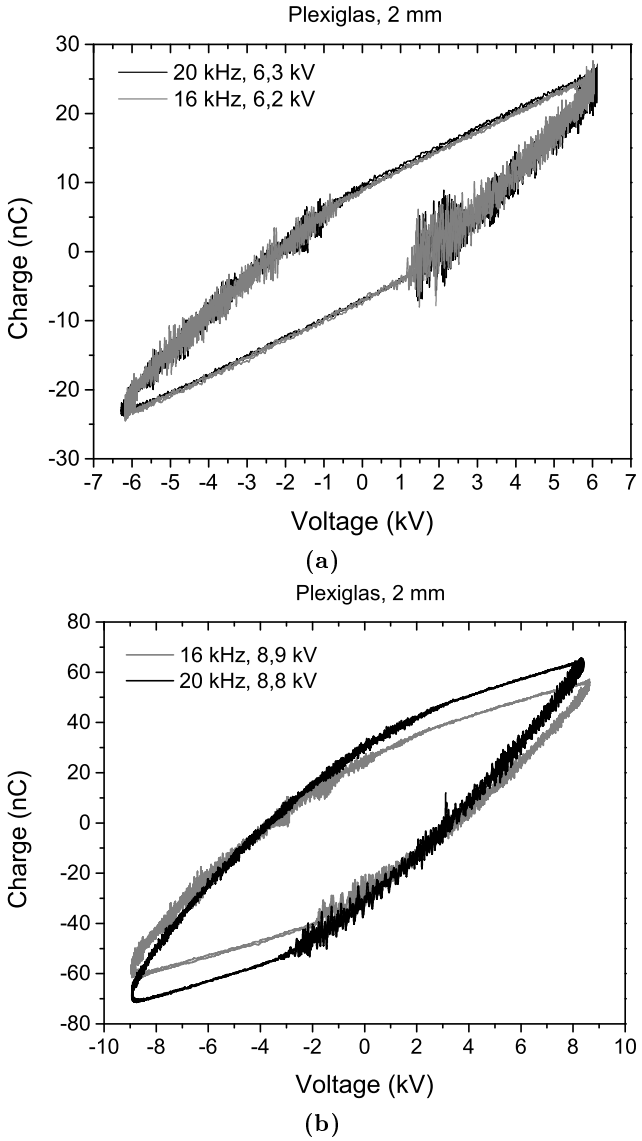

Figure 6.21: Lissajous figures obtained at 16 kHz and 20 kHz and different voltage amplitudes with a 2 mm thick plexiglas barrier.

lower relative dielectric permittivity ε_r [145]. The overlap between the curves obtained at different frequencies is quite good, except when voltages greater than 8 kV are used and the dielectric is plexiglas or, in less measure, mica. In this circumstances the higher the frequency the more energy is dissipated. This reminds the dependence of the induced wind speed from frequency found for these barriers (Figures 6.7 and 6.9). As discussed in Section 4.3.3,

the energy dissipated in the course of a cycle corresponds to the area enclosed inside the corresponding Lissajous figure. If energy does not depend on frequency it is expected that the shape of the Lissajous figure is the same. This is true, as shown in Figure 6.21a for plexiglas 2 mmthick at 6 kV, when there are no significant differences among frequencies. On the contrary, when a higher voltage is considered (9 kV), the higher power values found at higher frequencies correspond to larger areas inside the Lissajous curve. It is clear from Figure 6.21b that this difference is mainly due to the larger slope of the portions of the curve corresponding to the forward and backward discharges.

We have thus seen that for a given voltage amplitude the consumed power and energy decrease with the barrier thickness and increase with the dielectric constant and the spanwise length of the electrodes. This suggests that P_{dis} and E_{dis} rise with the plasma actuator capacitance. Thus, instead of considering the consumed power (or energy) per spanwise length (as it is often used when dealing with plasma actuators) or to multiply the power (or energy) for the ratio d/ε_r of the barrier thickness d and the relative permittivity ε_r, we decided to divide the value of P_{dis} (or E_{dis}) for the capacitance C. The latter has been measured by applying a voltage V_1 at the exposed electrode not sufficient for plasma creation (usually lower than 2 kV) and measuring the voltage drop V_2 across the capacitive probe. In this way the relationship between V_1 and V_2 is $V_2 = CV_1/(C + C_{probe})$, where C_{probe} is known, being the capacitance of the probe. If the power depends on the plasma actuator capacitance this method takes into account the spanwise and chordwise extensions of the electrodes, as well as their overlap. Moreover, accurate measured or nominal values for ε_r are not required. In Figure 6.22 the values of $(E/C)_{dis}$ for different actuators with the same thickness are shown, whereas in Figure 6.23 results referring to teflon or plexiglass plates with various d are presented. As shown in Figure 6.22a, the values

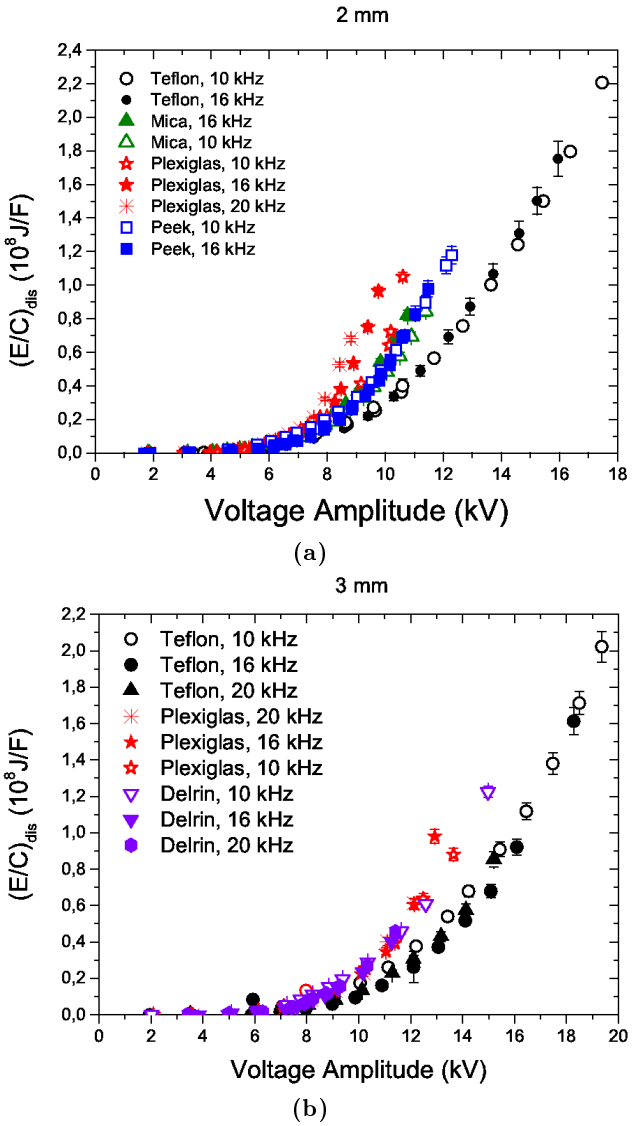

Figure 6.22: Consumed energy divided by the panel capacitance at different frequencies and voltage amplitudes for various dielectric barriers with thickness equal to 2 mm (a) and 3 mm (b).

of energy normalized to the capacitance of plexiglas at 10 kHz are similar to the ones of mica and peek at both the frequencies considered. A good overlap with data relative to plexiglas at 16 kHz and 20 kHz and to teflon is visible just up to 8 kV. Above this voltage amplitude, $(E/C)_{dis}$ increases slower for teflon than for the other materials. Similar considerations can be

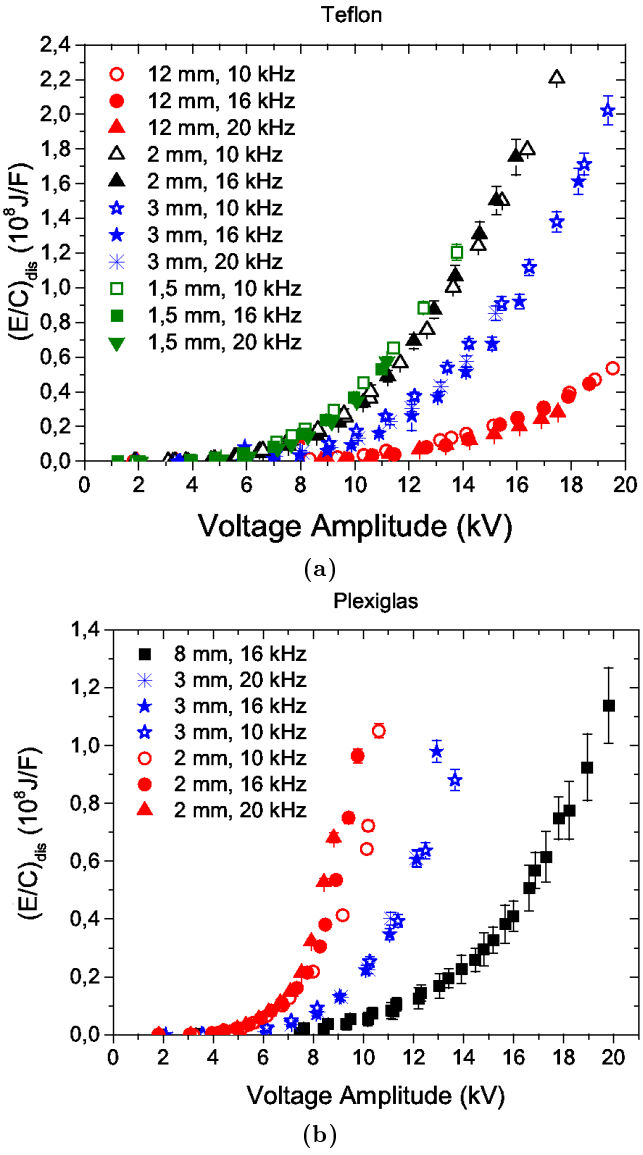

Figure 6.23: Consumed energy divided by the panel capacitance at different frequencies and voltage amplitudes for teflon (a) and plexiglas (b) dielectric barriers with thickness in the range $1.5 \div 12$ mm.

done when a barrier thickness equal to 3 mm is considered (Figure 6.22b). In Figure 6.23 the dependence on the dielectric thickness d is shown. A dependence for P_{dis} from V_A with the form of power-law has already been proposed, with exponent equal to 2, included between 2 and 3, between 3 and 5 or equal to 3.5 [92, 97, 132, 142, 154, 158, 168]. The trend of $(E/C)_{dis}$

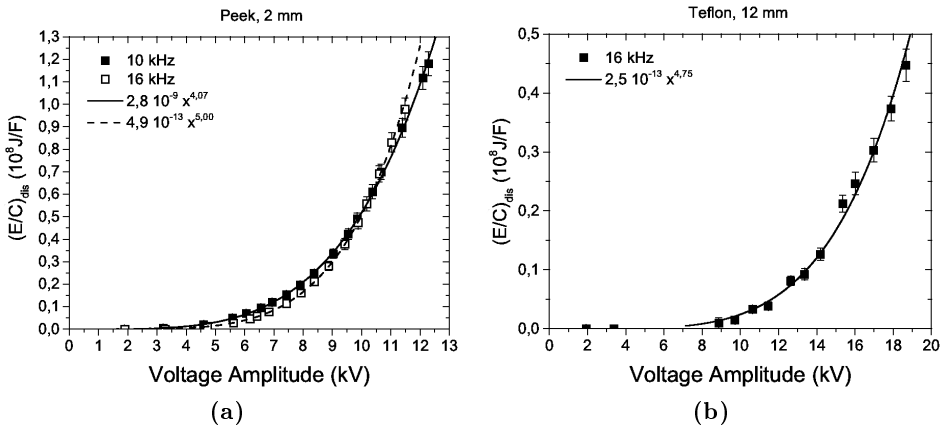

Figure 6.24: Examples of interpolation of $(E/C)_{dis}$ with a power-law function on the whole range of voltage amplitudes.

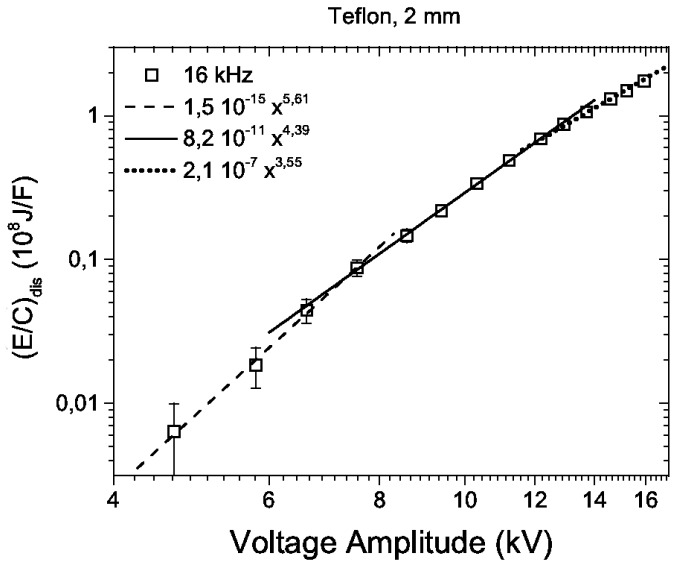

Figure 6.25: Example of interpolations of $(E/C)_{dis}$ with a power-law function, obtained by considering three disjoint ranges of voltage amplitudes.

with the voltage amplitude has thus been interpolated with a power-law $a \cdot V_A^b$ for the different dielectric barriers. Looking carefully at these curves, it can be noticed that $(E/C)_{dis}$ in reality slightly depends on the adopter frequency, since this quantity seems to rise faster with V_A when a higher frequency f is adopted. Consequently, data relative to different frequencies have been treated independently. An example is shown in Figure 6.24a,

demonstrating that a power-law is often adequate for describing these trends over the whole voltage range and that the parameters a and b slightly depend on f. However, in some cases, it appears clear that data slightly scatter from the power-law trend, as shown in Figure 6.24b. A logarithmic scale reveals that in such circumstances it is much better to divide the range of voltage amplitudes into two or three subintervals, corresponding to interpolating functions with different parameters a and b. An example is shown in Figure 6.25. Indeed, the dependence of $(E/C)_{dis}$ on V_A can be different for the growth and saturation regions of the electric wind speed described in Section

Material	f (mm)	f (kHz)	Growth Part1 (kV)	Growth Part2 (kV)	Saturation (kV)
Teflon	1.5	10	$3 \div 7$	$7 \div 10$	$10 \div 14$
Teflon	1.5	16		$4 \div 7$	$7 \div 11$
Teflon	1.5	20		$4 \div 7$	$7 \div 12$
Teflon	2	10	$6 \div 8$	$8 \div 12$	$12 \div 18$
Teflon	2	16	$4 \div 8$	$8 \div 12$	$12 \div 16$
Teflon	3	10		$6 \div 10$	$10 \div 20$
Teflon	3	16		$7 \div 11$	$11 \div 19$
Teflon	3	20	$6 \div 8$	$9 \div 11$	$11 \div 15$
Teflon	12	16	$8 \div 11$	$11 \div 18$	
Teflon	12	20	$8 \div 12$	$12 \div 19$	
Plexiglas	2	10	$4 \div 6$	$6 \div 10$	
Plexiglas	2	16		$4 \div 8$	$8 \div 10$
Plexiglas	2	20	$4 \div 6$	$6 \div 8$	
Plexiglas	3	10		$6 \div 10$	$10 \div 14$
Plexiglas	3	16		$6 \div 10$	$10 \div 14$
Plexiglas	3	20		$6 \div 9$	$9 \div 14$
Plexiglas	8	16		$9 \div 15$	$15 \div 20$
Mica	2	10	$4 \div 6$	$6 \div 9$	$9 \div 11$
Mica	2	16	$4 \div 6$	$6 \div 9$	$9 \div 11$
Peek	2	10	$3 \div 6$	$6 \div 10$	$10 \div 13$
Peek	2	16		$5 \div 8$	$8 \div 12$
Delrin	3	10		$5 \div 9$	$9 \div 15$
Delrin	3	16		$6 \div 9$	$9 \div 11$
Delrin	3	20		$6 \div 9$	$9 \div 11$

Table 6.1

6.1. Moreover, sometimes voltages immediately higher than the breakdown value behave differently from the remaining part of the growth region, so in these cases two interpolations have been performed (in the so called *Part 1* and *Part 2* of the *Growth* region). This is not surprising, since for example in Figure 6.3 the velocity of the wind induced by the discharge seems to increase faster with the voltage amplitude in the range 8 kV $\div$11 kV rather than for higher applied voltages. In Table 6.1 the voltage subintervals are listed for the different barriers, whereas the estimated values for b are given in Table 6.2.

Material	f (mm)	f (kHz)	Whole Range	Growth Part 1	Growth Part 2	Saturation
Teflon	1.5	10	3.77 ± 0.07	4.44 ± 0.10	3.76 ± 0.01	3.38 ± 0.05
Teflon	1.5	16	4.28 ± 0.08		4.82 ± 0.16	3.98 ± 0.05
Teflon	1.5	20	4.72 ± 0.16		5.58 ± 0.02	4.57 ± 0.06
Teflon	2	10	4.33 ± 0.10	4.6 ± 0.3	4.07 ± 0.10	3.36 ± 0.08
Teflon	2	16	4.23 ± 0.13	5.6 ± 0.2	4.39 ± 0.13	3.55 ± 0.08
Teflon	3	10	3.77 ± 0.05		3.9 ± 0.3	3.64 ± 0.04
Teflon	3	16	4.5 ± 0.4		5.13 ± 0.16	4.40 ± 0.04
Teflon	3	20	4.46 ± 0.06	4.7 ± 0.2	4.81 ± 0.10	4.5 ± 0.2
Teflon	12	16	4.75 ± 0.16	5.8 ± 0.2	4.49 ± 0.18	
Teflon	12	20	5.1 ± 0.5	13.6 ± 0.5	4.14 ± 0.01	
Plexiglas	2	10	5.01 ± 0.15	6.4 ± 0.4	4.65 ± 0.07	
Plexiglas	2	16	5.75 ± 0.15		4.92 ± 0.10	6.63 ± 0.14
Plexiglas	2	20	6.4 ± 0.2	7.70 ± 0.01	5.29 ± 0.10	7.3 ± 0.4
Plexiglas	3	10	4.48 ± 0.08		4.50 ± 0.07	4.4 ± 0.2
Plexiglas	3	16	5.5 ± 0.2		4.92 ± 0.11	6.1 ± 0.4
Plexiglas	3	20	5.6 ± 0.3		6.4 ± 0.5	5.4 ± 0.2
Plexiglas	8	16			4.53 ± 0.04	4.62 ± 0.04
Mica	2	10	4.79 ± 0.10	7.6 ± 0.7	4.69 ± 0.02	4.46 ± 0.06
Mica	2	16	4.77 ± 0.06	6.4 ± 0.5	4.57 ± 0.03	4.73 ± 0.04
Peek	2	10	4.07 ± 0.03	4.56 ± 0.07	4.03 ± 0.04	3.82 ± 0.09
Peek	2	16	5.00 ± 0.07		5.03 ± 0.07	4.93 ± 0.05
Delrin	3	10	4.21 ± 0.11		5.12 ± 0.16	3.92 ± 0.03
Delrin	3	16	5.5 ± 0.2		6.0 ± 0.3	5.04 ± 0.05
Delrin	3	20	5.43 ± 0.15		7.4 ± 0.6	5.10 ± 0.08

Table 6.2

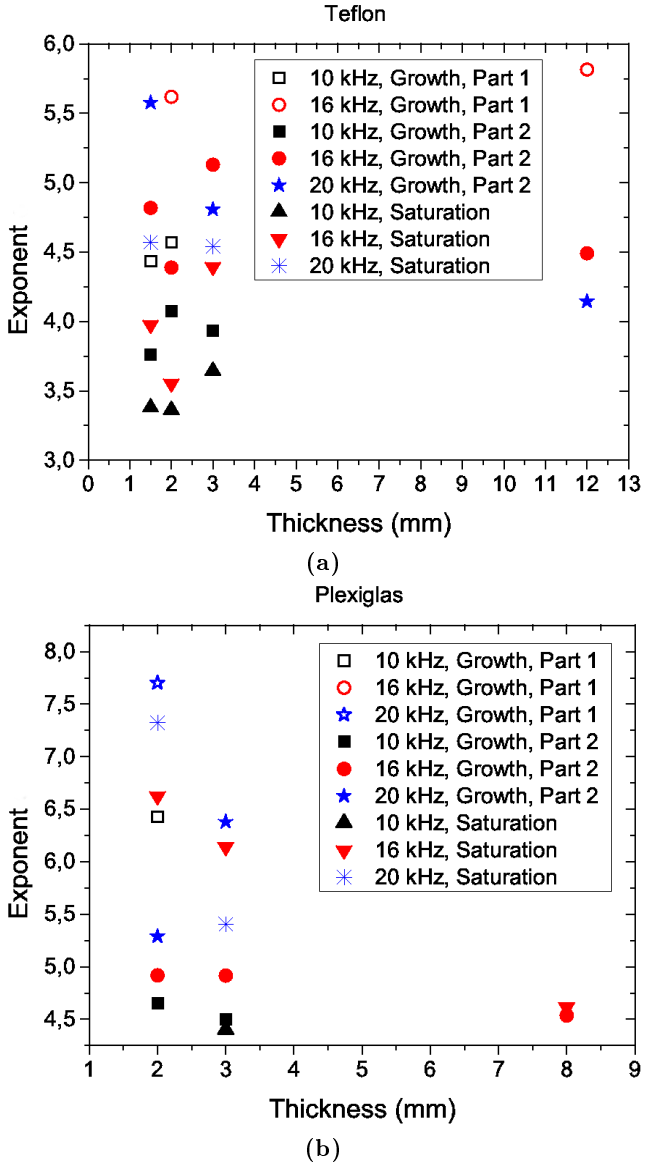

Figure 6.26: Exponent b of the power-law aV_A^b obtained for teflon (a) and plexiglas (b) with dielectric barriers of various thickness. Colours refer to different frequencies (10 kHz in black, 16 kHz in red, and 20 kHz in blue), whereas symbols indicate the ranges of voltages (Growth Part 1, Growth Part 2 and Saturation) considered for the interpolations.

Values for b relative to teflon and plexiglas are also shown in Figure 6.26. First of all it is evident that they are higher for plexiglas rather than for teflon. For the saturation region this is probably due to the accentuate

power increase we have already pointed out for thin plexiglas sheets, presumably associated to heating and burning of the insulating barrier surface. However, apart from that, we can notice from Table 6.2 that, given a dielectric thickness, b for teflon is generally lower compared to other materials. Moreover, b often increases with frequency and tends to decrease with the thickness d for plexiglas, whereas it is more independent from d for teflon (Figure 6.26). Values of b are mainly in the range $3.7 \div 5.0$ for the growth region and $3.3 \div 5.0$ for the saturation region.

Finally, it's worth pointing out that the saturation of the electric wind with the voltage amplitude discussed in Section 6.1 could also be observed by considering the wind velocity as a function of the dissipated power, as sometimes done in literature [155, 158], since P_{dis} is a rising functions of the applied voltage.

CHAPTER 7

Discharge Regimes and Induced Wind

While running the experiments concerning electric wind velocity and power consumption described in Chapter 6, we noticed that for sufficiently high voltages and thin dielectric panels the discharge does not appear uniform but several *plasma filaments* become evident. An example is shown in Figure 7.1, which refers to a teflon panel with thickness $d = 2$ mm and two different voltage amplitudes. This change in the plasma appearance could not be observed with the thickest dielectric barriers, at least for the voltages achievable with the adopted power supplies. We can't exclude the same

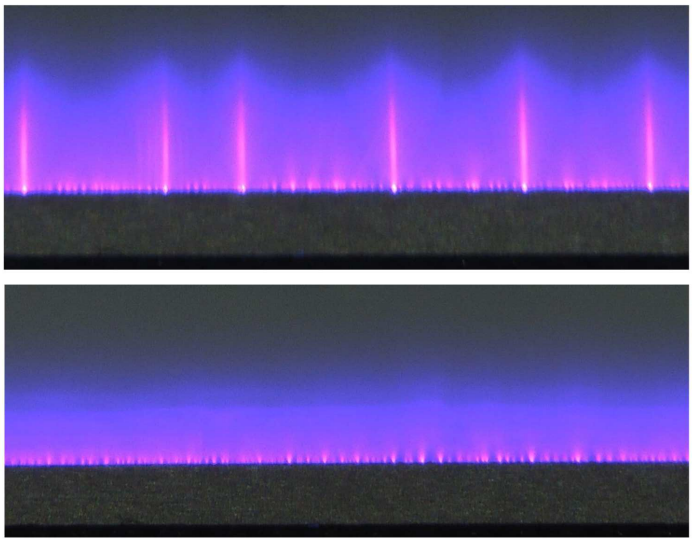

Figure 7.1: Examples of a SDBD working in non-filamentary (bottom) and filamentary (top) regimes. These pictures were taken from above the discharge, with a commercial digital camera, and refer to a a teflon panel with thickness d equal to 2 mm and to different voltage amplitudes (9 kV and 11 kV).

thing would happen if higher potential differences would be employed. Since a saturation of the velocity of the wind induced by the discharge has been clearly observed for insulating plates with $d < 8$ mm (see Section 6.1), we decided to investigate if electric wind saturation is related to this plasma behaviour. The studies conduced at this purpose are presented in Section 7.1. It is worth pointing out that the expression plasma filaments is adopted in order to avoid the terms streamers or microdischarges, sometimes used in literature [169], that we instead refer to precesses which are certainly not visible with unaided eye or with commercial digital cameras (see Chapter 2). Similarly, we will improperly employ the expression *plasma regimes* just to distinguish between these two discharge appearances.

A method of analysis of current pulses performed during these investigations turned out to be also interesting for the determination of the system capacitance by means of Lissajous figures, as described in Section 7.2.

7.1 Filamentary and Non-Filamentary Regimes

A dielectric barrier of teflon with thickness equal to 2 mm and a frequency equal to 16 kHz have been chosen. A couple of measurements of the induced wind speed as a function of the voltage amplitude are shown in Figure 7.2, having the characteristics already discussed in Section 6.1. The thermal camera presented in Chapter 4 was used to visualize the voltages at which plasma filaments become visible. Images were captured about one second af-

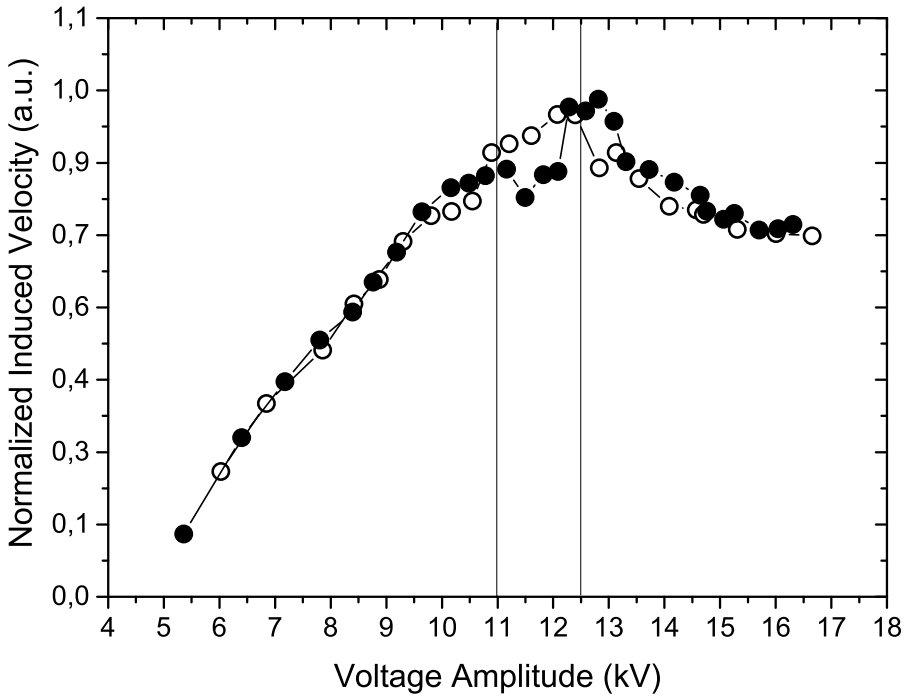

Figure 7.2: Speed of the induced flow as a function of the applied voltage. Values are normalized to the maximum speed obtained. Full and empty circles are two set of measures, showing a good repeatability and stability of the induced airflow, except in the transition from small to well developed plasma filaments ($11.0 \div 12.5$ kV).

ter the discharge ignition, for voltage amplitudes in the range 6.5 kV $\div$17.0 kV, at steps of 1.5 kV. We found that at 6.5 kV (Figure 7.3a) and 8.0 kV the discharge appears quite uniform along electrode length (the so-called spanwise direction). At 9.5 kV the plasma regime changes because some

small filaments become evident (Figure 7.3b). At 11.0 kV they cover the whole electrode length and are more or less uniformly spaced (Figure 7.3c). Above 12.5 kV the plasma state changes again because there are longer filaments, which are separated one from the other by a larger spanwise distance (Figure 7.3d). Eventually, at the highest voltages (Figures 7.3e and 7.3f) these plasma filaments become more numerous. The three Pitot tubes used

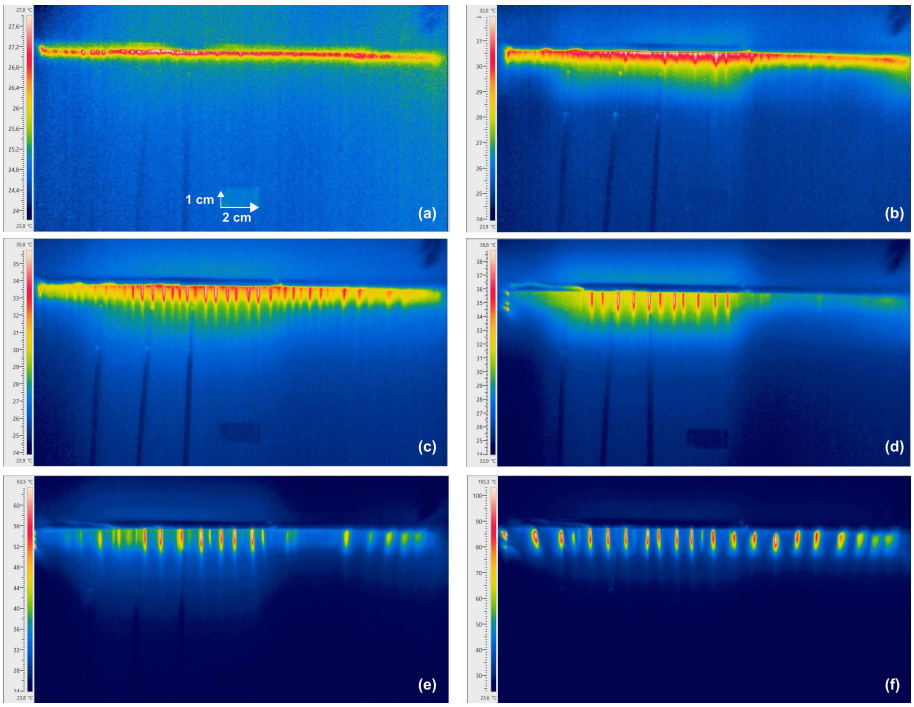

Figure 7.3: Thermal camera images taken approximately one second after plasma ignition, for different voltage amplitudes: 6.5 kV (a), 9.5 kV (b), 11.0 kV (c), 12.5 kV (d), 14 kV (e), and 17 kV (f).

for measuring the average speed of the induced airflow are visible in Figure 7.3. It is evident that in subfigures (c), (d) and (e) the plasma filaments are not uniformly distributed along the spanwise direction, but are more concentrated on the left half of the picture. This is not due to the presence of the Pitot tubes. As a matter of fact, plasma filaments generally change position (moving a few millimetres along the electrode) every some minutes, and we noticed that, if we try to keep a Pitot tube too close to a filament and

perfectly in front of it for minutes, this filament motion can be enhanced by the probe presence, because filaments tend to go away from the Pitot tube. In this case this discharge non-uniformity is instead ascribable to differences in the local dielectric panel temperature before plasma ignition, which in the left portion of the panel was about three degrees higher than the room temperature. For voltages larger than the ones associated to the discharge regime transition, this temperature difference did not influence the spanwise position of filaments, which immediately appeared uniformly distributed as in Figure 7.3f. However, for lower voltage amplitudes, we noticed that the creation of plasma filaments along the whole the electrode length could take some seconds and began from hotter region [159]. These thermal images have been recorded within the first second of plasma actuator operation, and this is the origin of this discharge disuniformity.

The two velocity curves of Figure 7.2 overlap well, except in the range $11.0 \div 12.5$ kV, which corresponds to the transition from small filaments to well developed plasma filaments. These curves of the induced wind speed show that these transitions in the discharge regime can influence the induced flow speed, and thus the potentialities of plasma actuator. A few similar observations can be found in literature for thrust and velocity measurements. It is evident that the the velocity of the induced airflow increases quite linearly until small filaments appear (in the range $9.5 \div 11$ kV). Since the electric wind saturation thus seems to be related to the onset of this filamentary behaviour, we have positioned a single glass Pitot tube in front of a plasma filament or in correspondence of the uniform plasma between two filaments, with the aim of detecting possible differences. We firstly tried to draw a curve representing the electric wind speed versus the spanwise distance. A micrometer movement system was thus used. This method required too much time and thus turned out not to be particularly effective, since we have already said that a Pitot probe can favour the movement of plasma

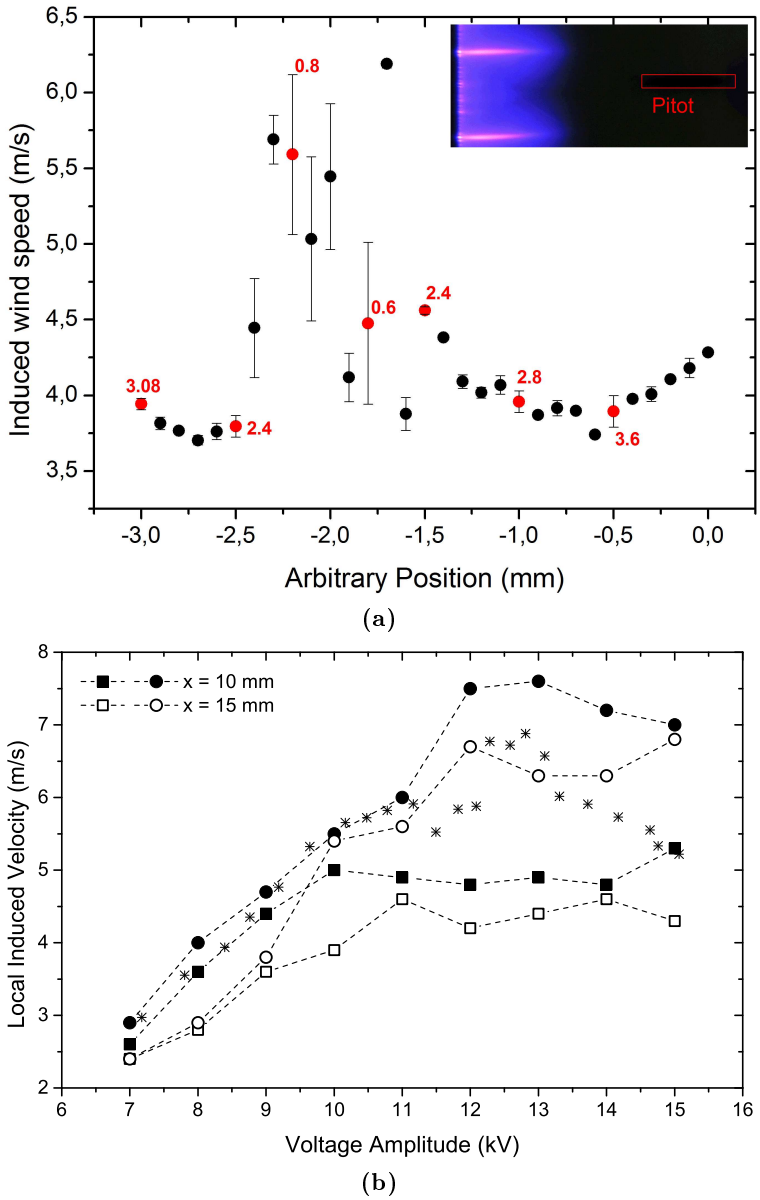

Figure 7.4: (a): Induced airflow speed as a function of a the spanwise position of the Pitot probe. In red the relative distance from the plasma filament is indicated for some points. This distance has been calculated by means of digital images contemporary acquired. (b): maximum (circles) and minimum (squares) velocity as a function of the voltage amplitude, measured at the chordwise distances $x = 10$ mm (full symbols) and $x = 15$ mm (blank symbols).

filaments in the spanwise direction, if it is kept too close to a filament and perfectly in front of it for minutes. However, we succeeded in making some

measurements at some randomly occurring relative positions between the Pitot tube and the filament. These distances have been calculated thanks to some digital images contemporary acquired, such as the one shown in Figure 7.4a [159]. Results are presented in Figure 7.4a and are enough to understand that velocities detected in proximity of a discharge filament are higher but also more variable in time. It is thus clear the reason why the velocities presented in Figure 7.2 and in Section 6.1 are subjected to higher uncertainties when filaments appear.

At this point, since we found that the wind speed reduces with the spanwise distance from a filament and with the aim of understanding the origin of the velocity saturation, we have varied the voltage amplitude and measured the maximum and minimum speed. Again we found that the former is obtained when a filament passes by the Pitot probe and the latter between two filaments. Results are shown in Figure 7.4b and were obtained by positioning the Pitot probe in two different chordwise positions ($x = 10$ mm and $x = 15$ mm). The conclusion that we can draw from these experiments is that, when the voltage amplitude is increased enough, the plasma regime changes from homogeneous to filamentary, and there is a transitional range of voltages in which filaments are smaller than the well developed plasma filaments. During this transition the velocity of the wind produced by plasma filaments is higher compared to the one associated to uniform plasma regions. Moreover, a saturation if the electric wind is observed in correspondence of the latter. At the highest voltages, instead, also the the wind speed associated to filaments saturates, and sometimes even decreases. We can thus think that the formation of filaments is not the only change involved in the plasma regime transition, because saturation in the induced wind speed is observed where the plasma appears homogeneous but also in front of filaments.

Evidences indicating changes in the plasma state or the appearance of plasma filaments have been looked for through an analysis of the current mi-

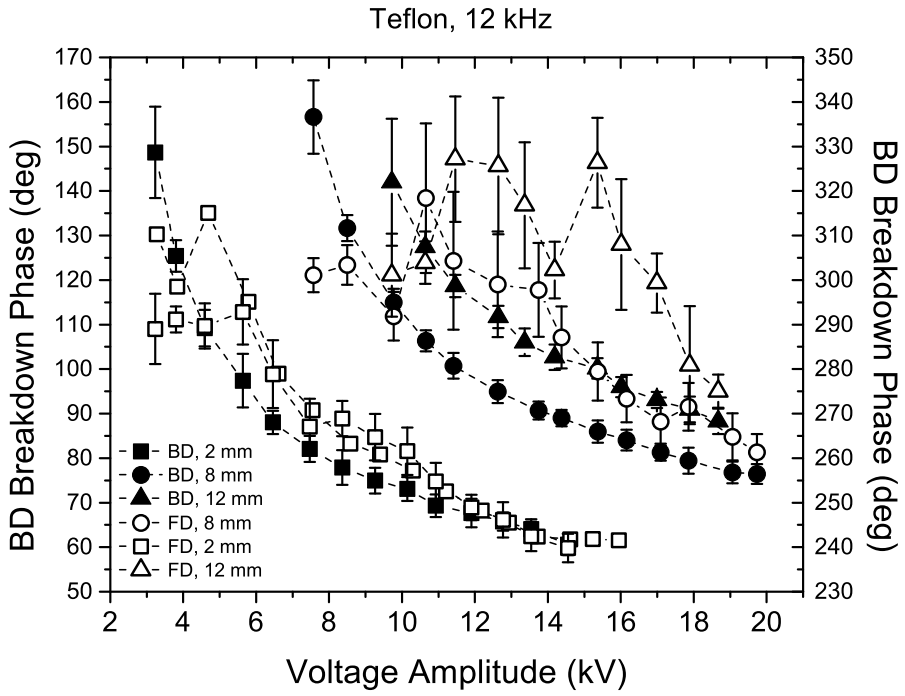

Figure 7.5: Breakdown phase associated to the backward discharge (full symbols) and forward discharge (blank symbols) as a function of the applied voltage for teflon barriers with different thickness.

crodischarge signals (see Section 4.3.2). This diagnostics was chosen because it has a temporal resolution sufficient for following the discharge dynamics without integrating over voltage cycle periods, and because we have seen in Section 5.2 that some phases of the backward evolution could be detected with current measurements but not with light ones. For the moment we focus on changes in the global behaviour of the forward and backward strokes. In Section 5.1 we observed that the light signal associated to breakdown microdischarges of the backward stroke appears at lower phases as the voltage amplitude increases, but that this phase reduction is more accentuated for low voltages (see Figure 5.6). We thus analysed the behaviour of the breakdown phases associated to both the backward and forward discharges. This quantity was calculated as the phase (averaged over several half-cycles) at which the first current pulse of the BD or FD stroke appears. Results rela-

tive to teflon plates with different thickness are presented in Figure 7.5. No evident or sudden saturation points can be guessed. For the thickest plates the trend relative to the forward discharge is not clear but just because the number of FD current pulses becomes considerable only at voltages well above the minimum voltage required for discharge breakdown. The higher the voltage amplitude the more the two half-cycles behave similarly. This let think that the main difference between low and high voltages, as well as between thin and thick dielectric panels, lies in the degree of asymmetry between the backward and forward strokes, that could thus be responsible for the saturation observed for thin panels and high applied voltages. It is still an open question whether the forward and backward semi-cycles both contribute in generating the induced wind (the so called *push-push mechanism*) or if they energize the air in partially opposite directions so that the result is an average airflow with a weaker velocity (*push-pull mechanism*) [32].

At this point we considered the total charge (Q_{tot}) transported by current microdischarges within a semi-cycle, which is shown in Figure 7.6. As a matter of fact, from the investigations presented in Section 5.2, this quantity seemed to be the more representative for the asymmetry between the BD and FD, as well as for the amount of charged particles moved inside microdischarge channels during a whole backward of forward stroke. In this graph, the ordinate scale used for the 2 mm teflon sheet is different from the one adopted for thick panels, since we found that thin panels transport more charge through current pulses. For all the three cases, it is evident that the minimum voltage amplitude at which current microdischarges could be detected is lower for the backward half-cycle rather than for the forward one. For the thinnest panel these voltages are about 4.0 kV and 5.5 kV respectively. For thick plates this difference between the BD and FD is much more accentuated, since at 8.5 kV backward microdischarges already transport charge inside the gap, whereas the contribution of the forward stroke

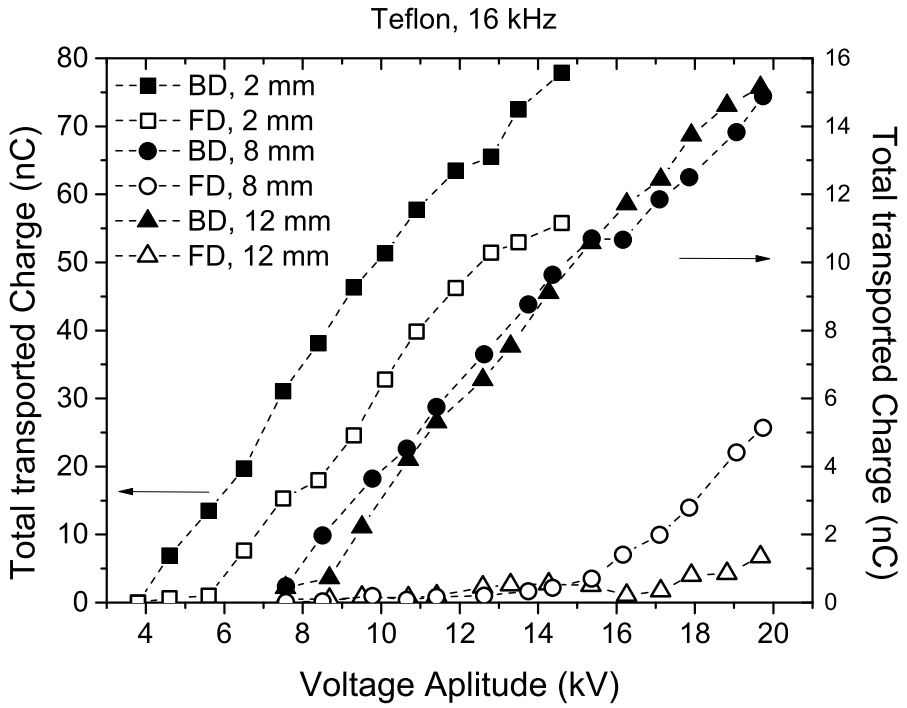

Figure 7.6: Total charge Q_{tot} transported in the course of a BD (full symbols) or FD (blank symbols) as a function of the voltage amplitude, for teflon panels with different thickness d in the range 2 mm $\div$12 mm. The ordinate scale on the left is referred to $d = 2$ mm, whereas the one on the right to the other insulating barriers.

becomes appreciable only at 16.0 kV for the 8 mm thick sheet and at even higher voltages for the 12 mm thick one. This fact that for the thickest panels there is a wide range of voltages during which the forward microdischarges are almost absent means that the BD alone can be responsible for the electric wind production and also let think to a push-pull mechanism. It's worth to pointing out that these results refer to the charge moved in the form of current microdischarges, not considering eventual current components varying slower with time.

The breakdown phase as well as the total transported charge are quantities that refer to the backward and forward discharge rather than to the single microdischarges they are made of. We have thus analysed the mean properties of these current pulses. In Figure 7.7 the distributions of their am-

plitudes for different dielectric barriers and applied voltages are presented. A logarithmic ordinate scale has been used for a better visualization of the right tail of each distribution, which is normalized to its maximum value. As already observed in Chapter 5, current pulses have amplitudes of a some

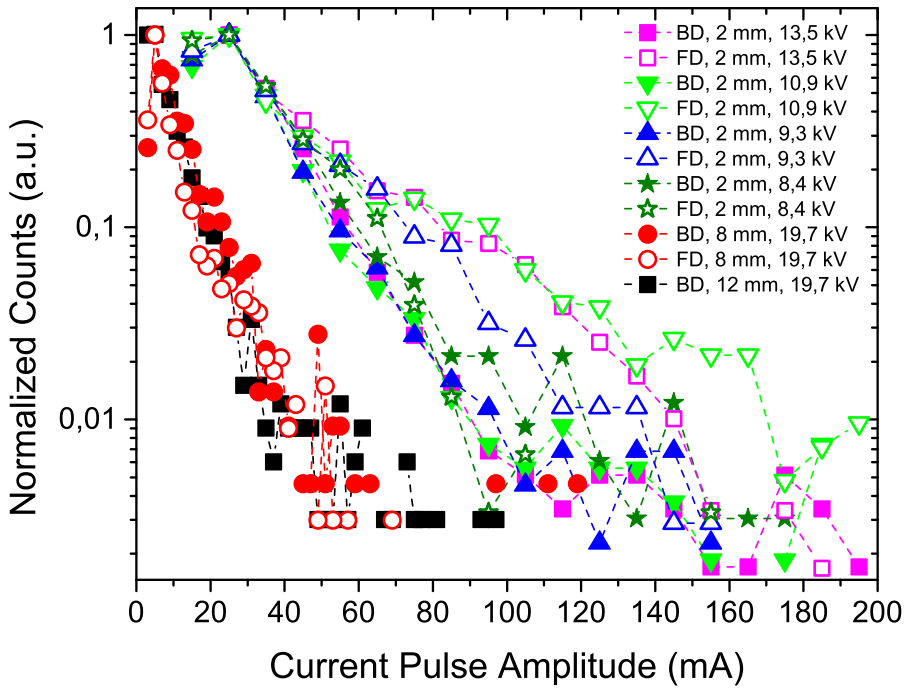

Figure 7.7: Histograms, normalized to the maximum value, of the amplitudes of current microdischarge for the backward (full symbols) and forward (blank symbols) discharges. Results for teflon panels with thickness equal to 2 mm, 8 mm and 12 mm are presented.

tens of mA. Concerning the thickest panels, we found that the number of normalized counts decreases slower with the increase of the voltage amplitude for the BD rather than the FD. An example is shown for the teflon plate with thickness equal to 8 mm, whereas for the 12 mm plate only the BD case is represented, given the small number of pulses detected. When a thickness equal to 2 mm is considered, this evidence is true only to about 9 kV, then the relative number of high amplitude pulses becomes greater for the forward discharge rather then for the backward discharge. On the contrary, the shape of the BD distribution is almost untouched by variations

of the voltage amplitude. These tail events of the FD distribution could be somewhat related to the plasma filaments visible with the unaided eye, which are a limited number, but further investigations are needed. Local measures of the current pulses associated to a plasma filament should be taken, even though it is quite difficult to isolate a filament inside a separated portion of the electrode (small enough for spatially resolved measurements) without influencing the characteristics and the spatial pattern of the discharge.

We found more interesting to previously focus onto the peculiarities of the temporal duration distributions of current pulses , which are shown in Figure 7.8 in both a linear and logarithmic scale. For all the presented curves, two peaks in the distributions are clearly visible, centred around 10 ns and 35 ns. In the logarithmic scale, a tail of longer events is visible for the backward discharge only. For the thickest panels the two peaks have smaller widths and are thus more separated. Three groups of current microdischarges can be identified. The first group is made of microdischarges with the shortest temporal duration (less than 25 ns) and we will refer to it as *Group S*. The second group is made of microdischarges with temporal duration between 25 ns and 45 ns (*Group M*), whereas microdischarges longer than 45 ns belong to the third group (Group L). As already said, the latter is practically absent for the forward stroke. For the whole range of voltage amplitudes investigated, the number of current pulses belonging to Group S that have been detected during a forward half-cycle is larger than the number of FD microdischarges belonging to Group M. For the backward discharge, instead, the relative importance of Group S and Group M depend on the material, frequency and thickness considered.

Let's focus on the 2 mm thick teflon plate, for which the transition from the homogeneous to the filamentary regimes has been clearly observed. First of all, we considered the FD amplitude histograms for Group S and Group M separately, in order to check if the high amplitude events we talked about

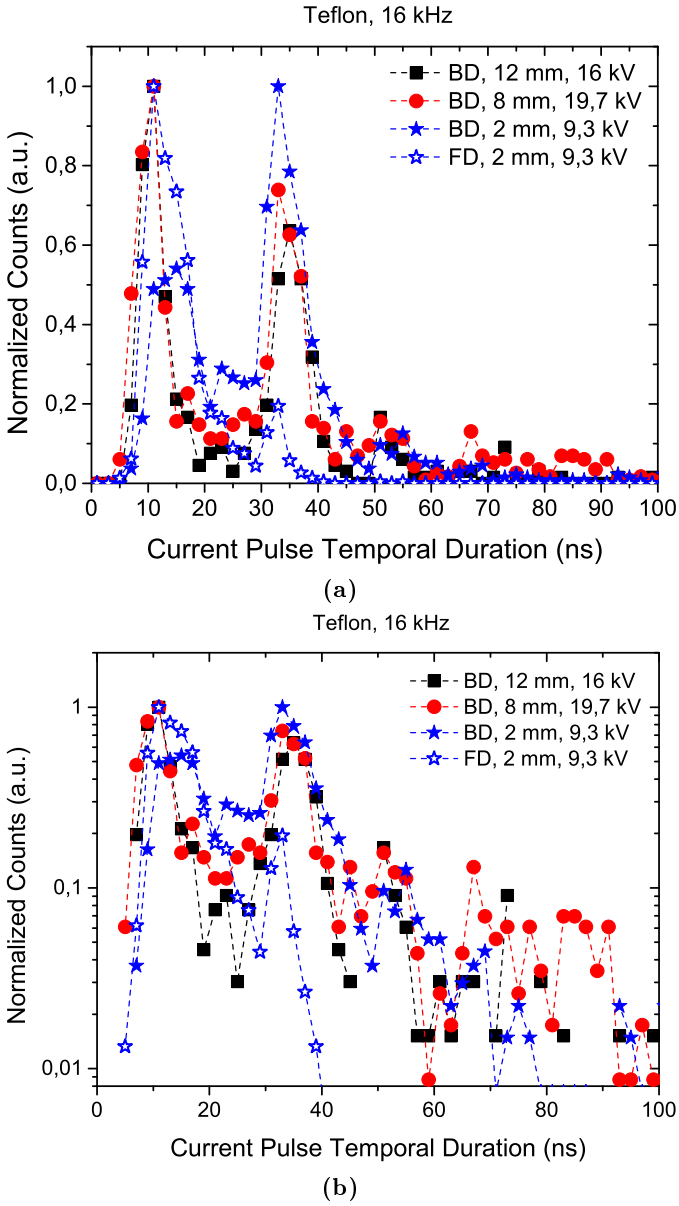

Figure 7.8: Histograms of the temporal duration of current pulses for the BD and FD strokes, for teflon panels with different thickness.

belong to a particular group. We found similar results, so these events are equally distributed between Group S and Group M. We have then calculated the total charge Q_{tot} transported by these three categories, which is presented in Figure 7.9. We notice that for the BD stroke, the contribution of Group S

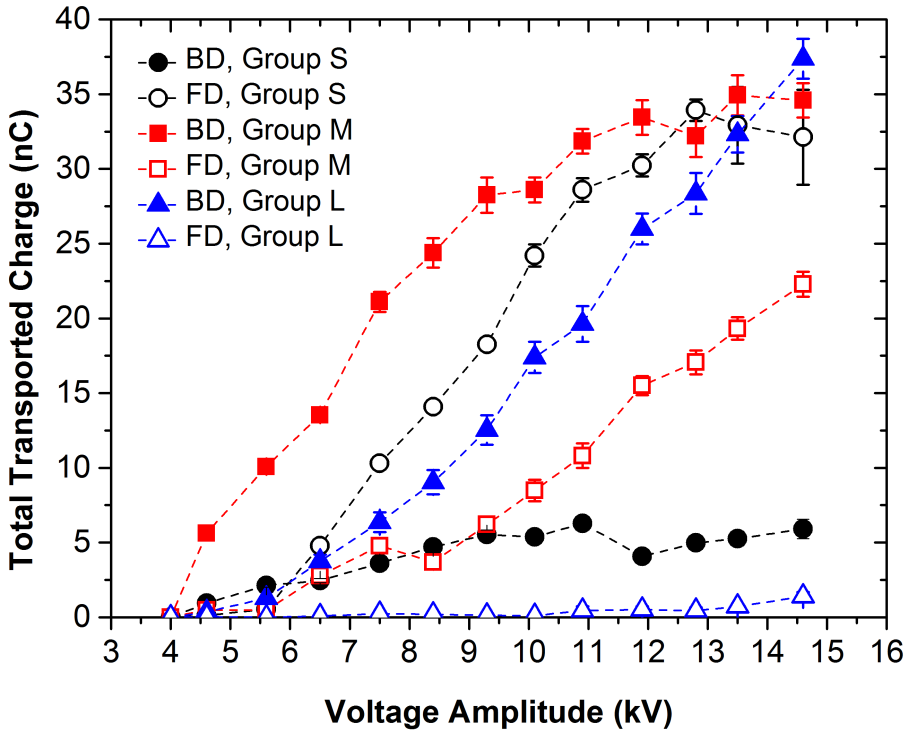

Figure 7.9: Total charge Q_{tot} transported in the course of a BD (full symbols) or FD (blank symbols) by current microdischarges belonging to Group S (circles), Group M (squares) and Group L (triangles). The teflon plate has thickness $d = 2$ mm and the adopted frequency is 16 kHz.

is considerably lower than the contributions of the other groups, because of the different charge associated to a single current pulse. For instance, at 10 kV the number of detected current pulses is 32 ± 5 for Group S, 53 ± 5 for Group M and 12 ± 2 for Group L, and the corresponding values of the mean charge per microdischarge are 0.17 ± 0.11 nC, 0.54 ± 0.04 nC and 1.5 ± 0.3 nC. At low voltages the total charge associated to Group M dominates, but at the highest ones it becomes comparable with Group L, because the latter rises more or less linearly, whereas the increasing rate of the former with the voltage reduces above 9 kV. This is not the case for the forward stroke, for which the contribution of Group M rises linearly and is lower than the total charge transported by Group S, even though the latter saturates at the highest voltages. At 10 kV the number of detected current pulses is about

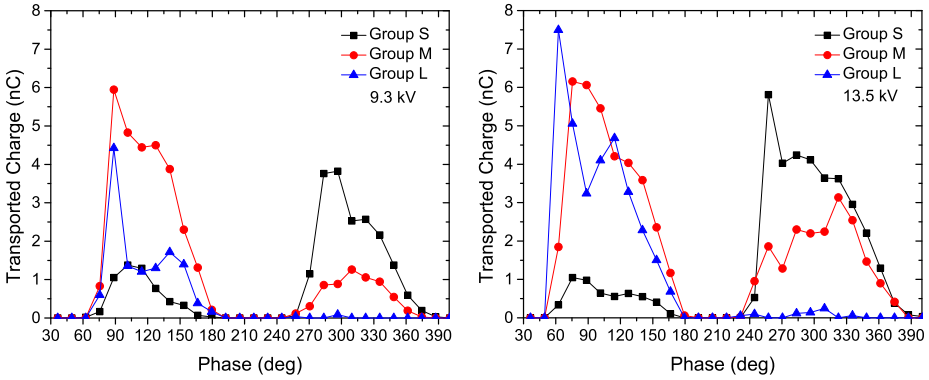

Figure 7.10: Charge transported as a function of the reference phase by current microdishcarges belonging to Group S, Group M and Group L in the course of the BD and FD phase. Two different voltage amplitudes are considered: 9.3 kV (a) and 13.5 kV (b).

91 ± 6 for Group S against 11 ± 3 for Group M. The corresponding values of the mean charge per microdischarge are 0.53 ± 0.03 nC and 1.5 ± 0.3 nC. For all the voltages considered, there are essentially no microdischarges belonging to Group L. A couple of examples of how the transported charge distributes within the plasma phases of the two semi-cycles are shown in Figure 7.10. Concerning Group S and M of the backward discharge as well as Group S of the forward discharge, the relative number of micordischarges (and thus the charge they move) is maximum in the first half of the stroke and decreases at later phases. The presence of BD breakdown micordischarges detected in Section 5.1 is particularly visible from Group L, which have a clear peak at the beginning of the stroke, and a second maximum (though less important) in the second half of the stroke. Group M of the FD is instead more flat with phase.

Another interesting way of analysing how the transported charge evolves in the course of the forward or backward stroke is by considering the total charge that has been moved by current microdischarges already registered during the stroke. At this purpose, for every instant of plasma activity the

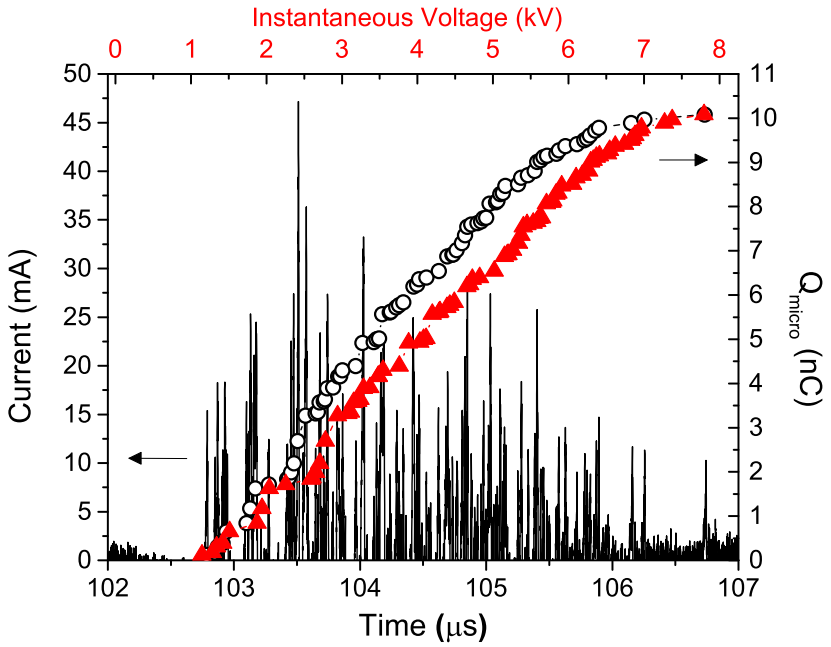

Figure 7.11: An example of Q_{micro} calculation from the temporal signal of the discharge current. The phase of plasma activity begins at about 102.8 μs, when the first current pulse appears. The corresponding evolution of Q_{micro} is plotted as a function of both time (black circles) and instantaneous voltage (red triangles).

charge transported by each microdischarge is added up in a variable that we call Q_{micro}, which is displayed in Figure 7.11. Q_{micro} is equal to zero before the first current pulse of the considered half-cycle, then its value increases each time a plasma microdischarge is created:

$$Q_{micro}(t_i) = Q_{micro}(t_{i-1}) + Q_{pulse}(t_i), \tag{7.1}$$

where $Q_{micro}(t_i)$ denotes the value of Q_{micro} at the time t_i when the $i-th$ current microdischarge is recorded, and $Q_{pulse}(t_i)$ is the charge transported by this microdishcarge, i.e. the area subtended below the considered current pulse. When the last current pulse is detected Q_{micro} becomes equal to Q_{tot}. In Figure 7.11 Q_{micro} is plotted also as a function of the instantaneous voltage. This choice is justified by the fact that these Q_{micro} versus V plots are some sorts of Lissajous figures in which only the voltage intervals of

plasma activity and only the charge transported by current microdischarges are taken into account. A comparison with the corresponding Lissajous figure can thus be drawn, as it will be presented in Section 7.2.

These curves are plotted independently for the three groups of current microdischarges in Figures 7.12 and 7.13. Instead of representing the trend of Q_{micro} versus V for a single voltage semi-cycle, we have averaged Q_{micro} over the voltage cycles recorded in a temporal series (in this case 13). Consequently, rather than considering the instantaneous voltage V at which a single microdischarge happens, we have divided the x-axis in intervals of instantaneous voltages, and we have added up the contributions of all microdischarges recorded at instantaneous voltages falling within an interval. The total values of Q_{micro} obtained in this way for the different voltage intervals have then be divided by the number of cycles, so that these plots refer to the average charge transported during a single voltage cycle. We now can notice that as the voltage amplitude increases, these three groups of plasma microdischarges are favoured or not in different ways. It is evident that for the backward stroke Group S and Group M are penalized in the filament regime rather than in the homogeneous one, since the slope of Q_{micro} versus V associated to these groups is smaller for the blue curves compared to the black ones. This is not the case for Group 3 of the BD, since the increase of Q_{micro} with V is enhanced, especially at the breakdown voltage, meaning that breakdown current microdischarges transport a considerable amount of charges at the highest voltages. Again we can see from Figure 7.12 that these discharge properties saturate at the highest voltages, since the curves associated to 13.5 kV an 14.6 kV look very similar. Analogous considerations can be done for the forward stroke, but in this case Group L is almost absent, Group S is penalized (Figure 7.13a) and Group M is enhanced (Figure 7.13b). These considerations are intriguing and could pave the way for a better understanding of the role played by plasma microdischarges in the

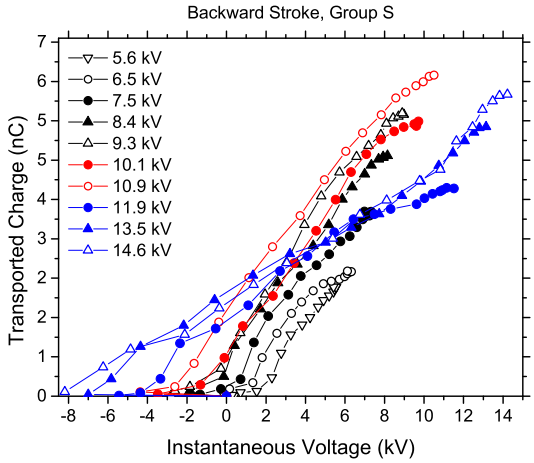

(a)

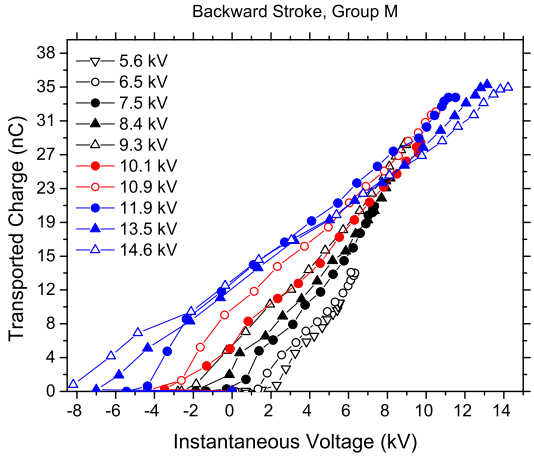

(b)

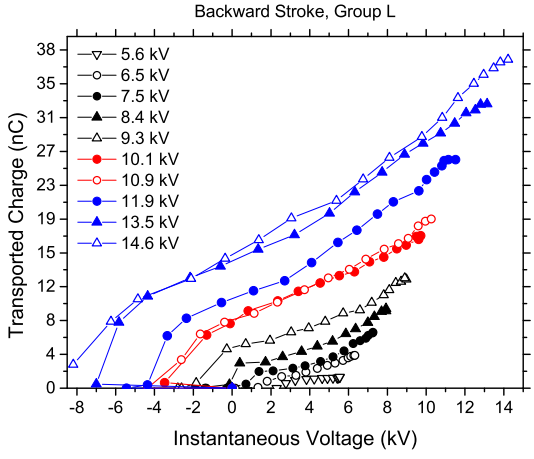

(c)

Figure 7.12: Total charge Q_{micro} that has been moved by BD current microdischarges already registered during the stroke as a function of the voltage V between the electrodes. Figures (a), (b) and (c) refer to microdischarges belonging to Group S, to Group M and to Group L, and the different curves are obtained for different voltage amplitudes. Colours indicate the three plasma regimes: uniform plasma (black), uniform plasma with small plasma filaments (red), uniform plasma with well developed plasma filaments (blue).

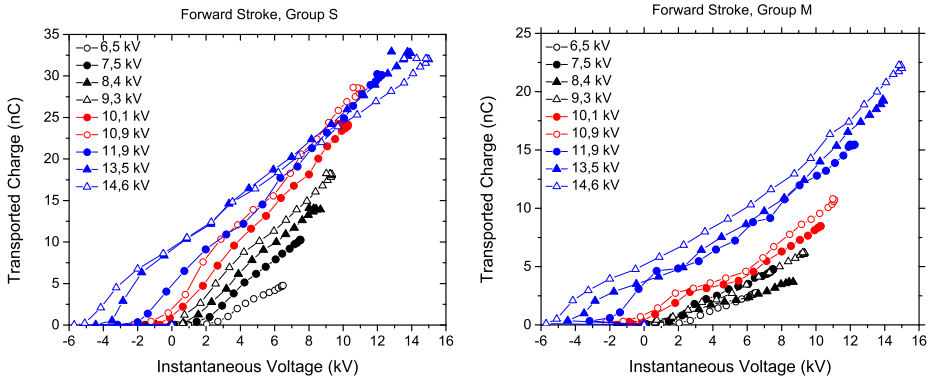

Figure 7.13: Total charge Q_{micro} that has been moved by FD current microdischarges already registered during the stroke as a function of the voltage V between the electrodes. Figures (a) and (b) refer to microdischarges belonging to Group S and to Group M, and the different curves are obtained for different voltage amplitudes. Colours indicate the three plasma regimes: uniform plasma (black), uniform plasma with small plasma filaments (red), uniform plasma with well developed plasma filaments (blue).

creation of the induced airflow. We have thus calculated Q_{tot} and Q_{micro} for the thickest teflon panels. Results are presented in Figures 7.14 and 7.15.

The evident changes of slope of the Q_{micro} versus V found for the teflon with thickness equal to 2 mm are not visible in these cases. All groups of BD microdischarges transport charge even at the lowest voltages (see Figures 7.14d and 7.15d), but again at first the main contribution is associated to Group M. Concerning the forward discharge, instead, Group M is quite negligible for the both 8 mm and 12 mm thick teflon panels, whereas at the highest voltages Group S becomes considerable. No thermal images have been acquired with these plasma actuators, but no filaments were noticeable with unaided eye, so transition to the filamentary regime does not occur within the investigated voltage ranges. Maybe it is possible that some small filaments not appreciable at visual inspection could be present at the highest voltages adopted with the 8 mm thick panel.

Finally, with the aim of understanding if filaments visible with unaided

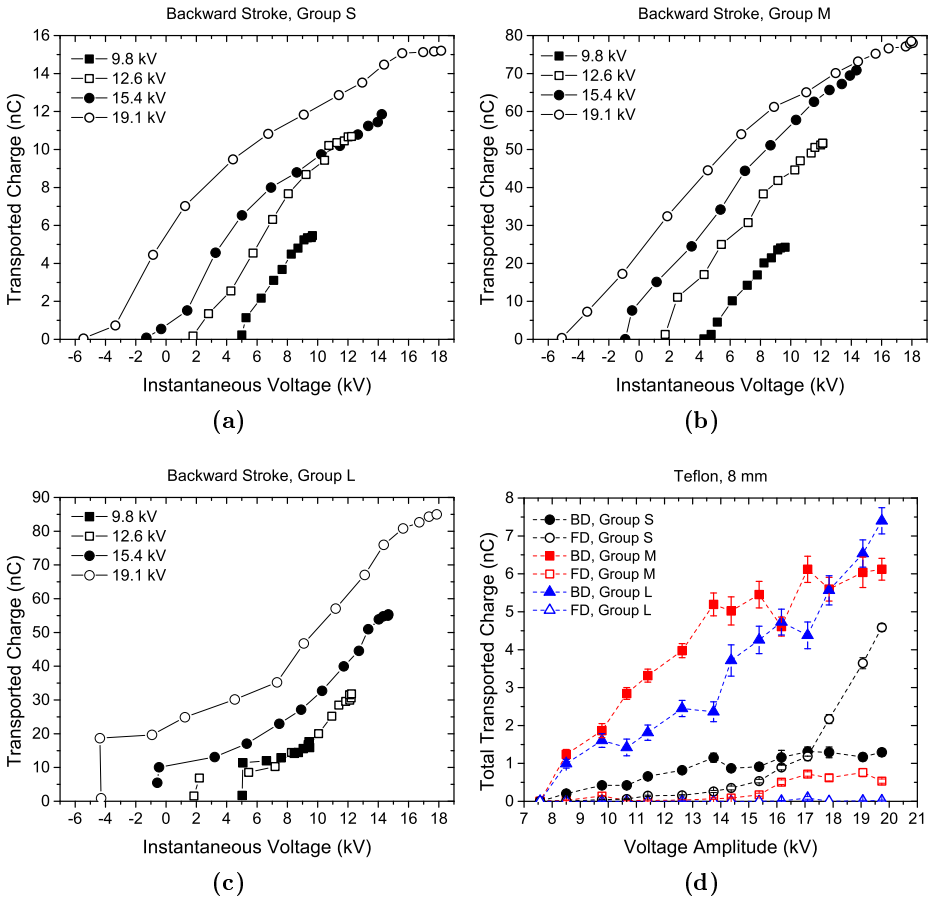

Figure 7.14: Q_{micro} as a function of the instantaneous voltage for microdischarges belonging to Group S (a), Group M (b) and Group L (c). In subfigure (d) the total charge Q_{tot} associated to these microdischarge categories is plotted as a function of the voltage amplitude. The dielectric barrier has thickness equal to 8 mm.

eye are associated to a voltage semi-cycle in particular, we have recorded the light emitted by the discharge, by means of the photomultiplier tube, for a thin teflon plate (1.5 mm) and a voltage sufficiently high so that plasma filaments could be observed. We have thus placed the optical fibre perpendicular to the dielectric surface and close enough to it so that spatially resolved measurements could be made. As described in Section 4.3.1, an alumina tube was adopted for limiting the field of view of the fibre. In this case we were mainly interested in restricting the field of view in the spanwise

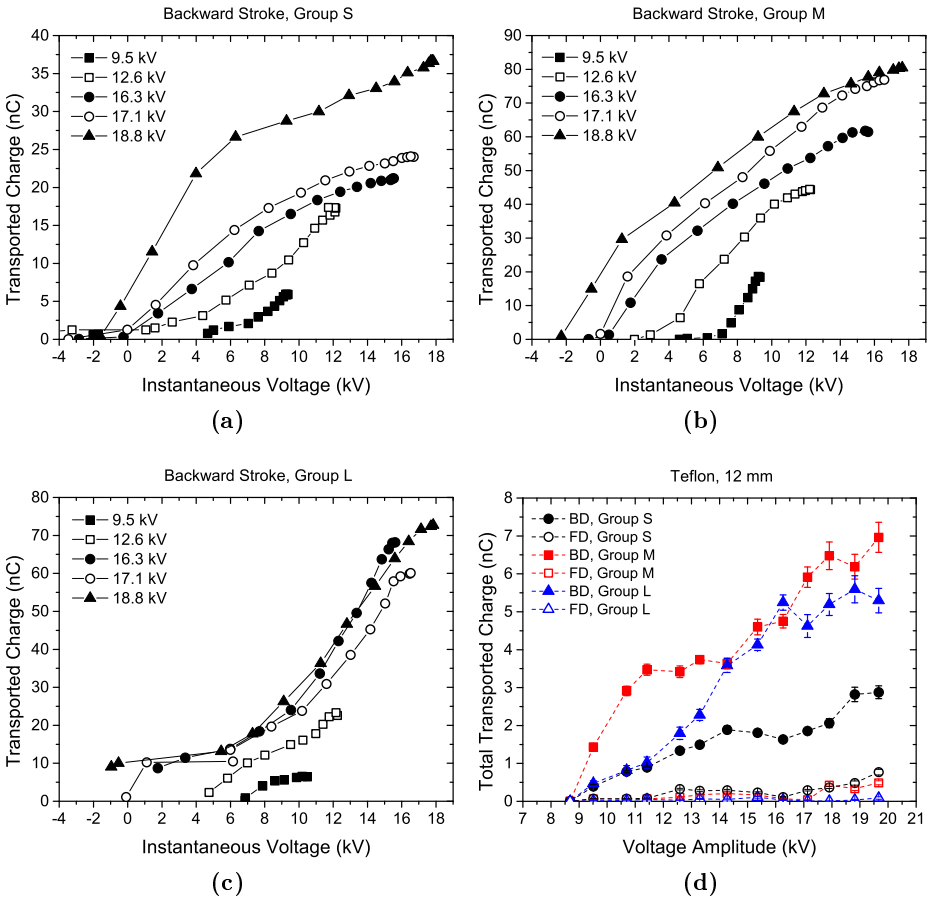

Figure 7.15: Q_{micro} as a function of the instantaneous voltage for microdischarges belonging to Group S (a), Group M (b) and Group L (c). In subfigure (d) the total charge Q_{tot} associated to these microdischarge categories is plotted as a function of the voltage amplitude. The dielectric barrier has thickness equal to 12 mm.

direction, so that we could detect light above a filament or above a region of homogeneous plasma. The light emitted as a function of the reference phase has been considered, as shown in Figure 7.16. No differences in the shapes of these trends could be detected in absence or presence of a plasma filament. However, the number of light pulses was not stable in time and depended on how much the filament was near to the region observed with the optical fibre. For this reason the curves presented in Figure 7.16 have been normalized, and light pulsed detected at different chordwise positions have been treated

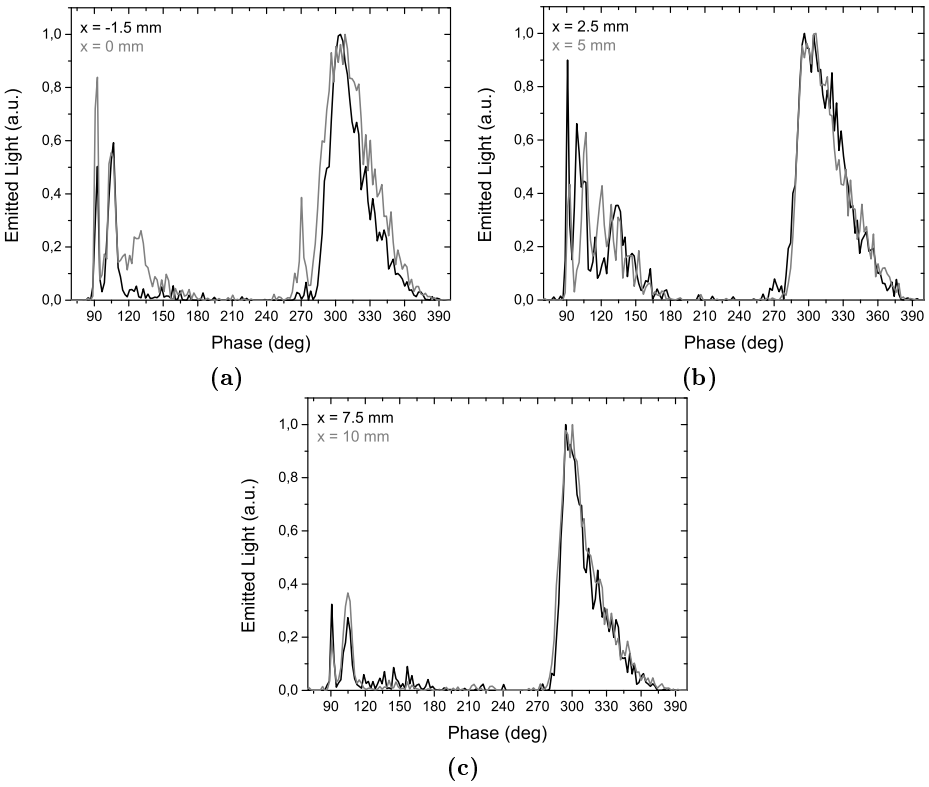

Figure 7.16: Emitted light (expressed in arbitrary units) as a function of the reference phase for different chordwise x positions from the electrode edge ($x = 0$ mm). Negative x indicates the exposed electrode region, whereas positive x stands for the dielectric surface.

separately, instead of drawing a spatio-temporal map of the light emitted as we have done in Section 5.1. It is evident that the relative contribution of the backward and forward strokes to the total emitted light is comparable just up to a few millimetres from the exposed electrode edge. For further chordwise x positions light is associated almost exclusively to the forward discharge. We can thus conclude that the visible plasma filaments are due to the forward half-cycle.

The results presented in this section reveal that for thin dielectric barriers the charge transported by current microdischarges is quite comparable for the two half-cycles, whereas the thicker the insulating plate the larger is the

minimum voltage amplitude required for detecting FD current pulses. This suggests a push-pull mechanism for induced wind formation, in which the two strokes tend to energize air in opposite directions, and the speed observed with the Pitot probe (which is not time resolved) is the net result of a partial cancellation between the backward and forward discharge contributions. However, the induced wind and the transition to the filamentary regime does not occur as soon as the first FD microdischarges appear. These first forward current pulses principally belong to Group S, whereas the charge transported by Group M of the FD becomes considerable at higher voltages. Moreover, we observed that the transition to the filamentary regime enhance Group L of the backward stroke and Group M of the forward discharge, contrary to Group S and Group M of the BD as well as Group S of the FD.

A possible explanation for these observations is that Group L is not particularly effective in generating the electric wind, which is instead ascribable to Group S and Group M. In particular, these results suggest that both Group S of the backward and forward discharges provide a contribution which is not dependent on the voltage polarity, meaning that for these microdischarges a push-push or pull-pull process is involved (or that they are both ineffective). On the contrary, a push-pull mechanism seems more appropriate when microischarges belonging to Group M are considered, meaning that the backward and forward strokes tend to generate a flow directed towards the buried and the exposed electrodes respectively. For example, Group M could be associated to a streamer regime in which positive ions of the microdischarge channel transfer momentum to neutral molecules, thus accelerating them in opposite directions during the two semi-cycles. On the contrary, the discharge nature associated to microdicharges of Group S could be different, such as a Townsend like. We have observed that the plasma filaments emit light mainly in the course of the forward stroke, and they are presumably ascribable to electric field redistribution induced by space charge

effects [170–173].

We will perform dedicated light and current measurements to gain more insights about this topic, in order to understand if the ionization waves detected in the backward stroke (see Section 5.3) are associated only to microdischarges of Group M or not, and we will try to check if a ionizing wave propagates in correspondence of a current pulse of Group M of the forward discharge. This description of the existence of both stremer-like and glow-like microdischarges characterized by a push-pull and a pull-pull mechanism of interaction with neutrals would explain why there are still debates about the discharge nature and the induced airflow direction during the forward half-cycle [32]. The fact that for the FD microdischarges belonging to Group S are more numerous than the ones belonging to Group S would explain why a push mechanism and a glow-like nature is often attributed to this half-cycle. Another possibility is that these two groups of microdischarges are associated to different field lines and thus to different spatial regions of the discharge. Further dedicated measurements are necessary for answering to this question.

7.2 Shapes of the Lissajous Figures

In the previous section we have plotted Q_{micro} versus the instantaneous voltage and we obtained some sorts of Lissajous figures in which only the voltage intervals of plasma activity and only the charge transported by current microdischarges are taken into account. A comparison with the corresponding Lissajous figure can thus be drawn. As already discussed in Chapter 4, this figure is obtained by plotting the charge flowing into the circuit Q as a function of the voltage difference ΔV between the electrodes, which is practically equal to the voltage applied to the DBD if the capacitive probe used for the measure of Q has a sufficiently high capacitance [141]. When the imposed electric field is too small for plasma generation, the Q versus ΔV plot is a

straight line, because the DBD system behaves as a purely capacitive cell and the charge varies proportionally to the voltage, with the constant of proportionality given by the cell capacitance C_{cell}^{off}. Otherwise, if the voltage amplitude is high enough for discharge ignition, during the two phases of plasma activity the charge Q does not vary as $C_{cell}^{off} \cdot \Delta V$ any more, and the Lissajous plot opens and forms a convex figure.

Lissajous figures for planar DBD configurations usually assume the shape of a parallelogram. The discharge cell can be thought as two capacitances in series: the first one (C_{die}) is given by the insulating barrier (or by the two barriers if both electrodes are covered), whereas the second one (C_{gap}) is due to the planar air gap. The value of the latter changes when plasma is created, so the Lissajous figure is delimited by four straight lines with a slope different or equal to C_{cell}^{off}, depending if they correspond or not to a phase of plasma activity [174]. Manley assumed that, during the discharge-on periods, the plasma between the electrodes fills the gap so that the voltage drop in the gap is equal to zero. In this case, the capacitance of the cell, and thus the slope of the the corresponding side of the Lissajous figure, reduces to the capacitance of the dielectric(s): $C_{cell}^{on} = C_{die}$ (see Figure 7.17 (a)) [141, 144]. The instantaneous charge Q represents the total charge and thus captures the charge transported by current microdischarges too. A situation opposite

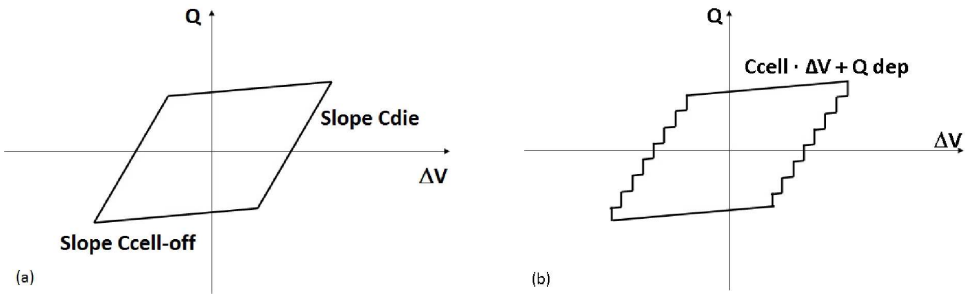

Figure 7.17: Sketch of a Lissajous figure with the hypothesis that during the plasma activity the capacitance of the gap reduces to zero (a), or that it remains equal to the capacitance in absence of discharges (b).

to the one considered by Manley occurs when a DBD is operated just above the minimum voltage amplitude required for plasma ignition, and only few plasma microdischarges are created during a whole sinusoidal voltage cycle. In this case the capacitance of the gap essentially keeps the same, but the Lissajous figure becomes again a sort of parallelogram if the current microdischarges move and deposit charges: the instantaneous charge is given by $Q = C_{cell}^{off} \cdot \Delta V + Q_{dep}$, and even though the capacitance C_{cell}^{off} is constant, Q changes during the phases of plasma activity because the positive or negative deposited charge (Q_{dep}) changes each time a microdischarge crosses the gap. In this case, during the plasma activity, Q varies in steps (Figure 7.17 (b)) [175], whereas during the off-phases, if the deposited charge does not change, the variation of Q with ΔV follows a straight line $Q = C_{cell}^{off} + Q_{dep}$, with intercept Q_{dep} given by the total charge left by microdischarges during the previous plasma activity. Without the assumption that the capacitance or the deposited charge keep constant, the variation of the total charge Q during a voltage cycle thus depends on capacitance changes as well as on the accumulation of charges on the dielectric barriers.

For a SDBD, the situation is complicated by the fact that the discharge does not start and stop with a constant geometrical plasma shape, but the latter can change in the course of the discharge active phase [176], since the accumulation of charges onto the dielectric surface can influence the electric field configuration and thus the development of the following microdischarges. Changes in the shape of the discharge region imply variations in the discharge capacitance, leading to the almond-shaped Lissajous figures often observed for surface discharges [176].

Here we propose to combine the Lissajous figure plot with the detection, by means of a Rogowski coil, of current pulses associated to microdischarges, in order to distinguish the contributions of C_{gap} and Q_{dep} to the variations of the instantaneous total charge Q during a voltage cycle. This method has

been tested for a planar configuration and then applied to a SDBD.

The planar configuration used in these experiments is symmetrical because two identical insulating barriers are used to cover the electrodes. The latter are stainless steel disks (diameter 35 mm and thickness 1.5 mm) that have been inserted into a drilled cylindrical scaffold in Macor (a glass ceramic material by Corning Inc., dielectric constant $\epsilon_r = 6.03$) with diameter equal to 40 mm and external height equal to 3.5 mm. Thus a dielectric barrier of 2 mm separates each electrode surface from the gas gap. The discharge gap was fixed at 0.8 mm. The total cell capacitance without plasma has been calculated using a 2D Laplacian electrostatic field solver (EStat 7.0 by Field precision LLC). It is equal to $C_{cell}^{off} = 8.3$ pF, given by the series of $C_{gap} = 23.5$ pF and $C_{die} = 12.8$ pF (25.7 pF for each dielectric barrier). Calculations show that the electric field is uniform in the gap within 10% and decreases outwards. Concerning the SDBD, the Setup B configuration with a teflon plate with thickness equal to 2 mm has been adopted. The frequency of the sinusoidal voltage signal is equal to 42 kHz for the planar setup and to 16 kHz for the surface DBD.

For the both dielectric barrier discharge configurations studied during this investigation, we have simultaneously acquired the signals corresponding to the three different electrical diagnostics (high-voltage probe, capacitive probe, Rogowski coil). These temporal series have been split into several parts corresponding to different voltage cycles, which have been analysed separately. For the representation of the Lissajous figures, a low-pass filter was previously applied to both the Q and V signals, in order to cut noise at high frequencies, and to reduce the spikes visible in the capacitive probe signals that indicate the plasma activity. A high-pass filter was instead used for the current signals, in order to separate the microdischarge current peaks from the AC current signal, as discussed in the Chapter 4. For each semicycle, the amount of charge transported by current microdischarges Q_{micro}

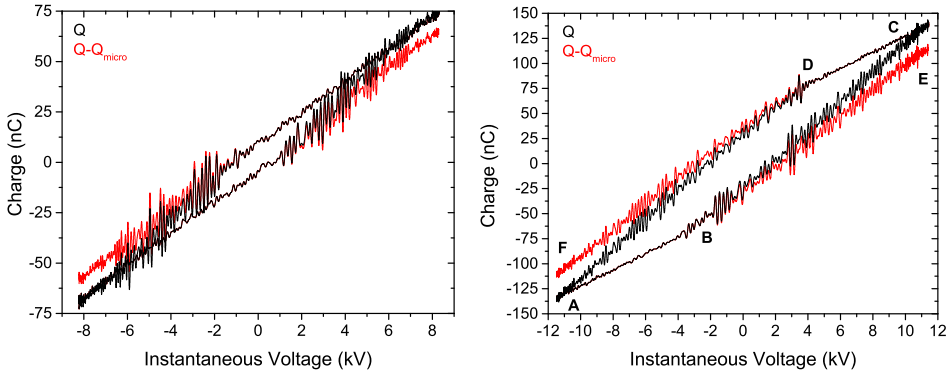

Figure 7.18: Examples of Lissajous figures (shown in black) obtained for two different voltage amplitudes (8.3 kV and 11.4 kV) in a planar configuration. For red curves the charge Q_{micro} transported by current microdischarges have been subtracted from the Q signal of the Lissajous figure.

has been calculated as a function of the applied voltage, as described in Section 7.1.

7.2.1 Planar Configuration

Two Lissajous figures obtained for the planar configuration at two different voltage amplitudes are shown in black in Figure 7.18. Their shape nicely resembles a parallelogram composed of four straight lines with two different slopes. These $Q - V$ plots appear symmetric: as expected there are no evident differences between the two voltage semi-cycles, because of the adopted planar setup with two dielctric barriers. For each semi-cycle, the amount of charge transported by current microdischarges (Q_{micro}) has been calculated as a function of the applied voltage. For the half of the Lissajous figure in which the voltage is rising towards its maximum (sides AC of Figure 7.18 (b)), the current transported by plasma microdischarges is positive and Q_{micro} increases in correspondence of instantaneous voltages at which a current pulse is detected. As discussed in the introduction, we expect that Q is related to the voltage drop between the electrodes as $Q = C_{inst} \cdot \Delta V + Q_{inst}$,

where C_{inst} and Q_{inst} are the instantaneous capacitance of the system and instantaneous amount of charge accumulated inside it. If both these values are constant within a voltage interval, Q varies linearly with ΔV. It is evident that this happens during the two phases of plasma off (sides AB and CD), because no charges are transported by plasma filaments and the capacitance of the system keeps constant. This evidence that Q_{inst} does not change means not only that these are phases of no plasma activity, but also that there is no rearrangement or recombination of the charges left on the insulating barriers or inside the gap. During the plasma active phases, instead, both C_{inst} and Q_{inst} can vary. In order to separate these two contributions affecting the shape of the Lissajous figure, we have supposed that Q_{inst} is completely transported by plasma microdischarges, and we have thus measured $Q_{inst} = Q_{micro}$ with a current probe, and thus with a diagnostic tool independent from the Lissajous figure. At this point we have subtracted Q_{micro} from the Q signal of the Lissajous figure, and we have obtained a sort of new Lissajous micro, shown in red in Figure 7.18, which is no more a closed loop, because the two sides of no plasma activity remains unchanged, whereas BC and DA becomes BE and DF. These ones appear straight at all the considered voltage amplitudes, meaning that the cell capacitance can change at the beginning of the plasma-on or plasma-off phase (becoming equal to C_{on} and C_{off} respectively), because of a sudden change in the C_{gap} value, but that then it keeps the same during each one of these temporal windows. The values of C_{on} and C_{off} obtained for the planar configuration are presented in Figure 7.19 as a function of the applied voltage. We found that the capacitance C_{off} is independent from the voltage amplitude and equal to the C_{cell}^{off} given by the series of the capacitances of two dielectrics and of the gap calculated in absence of discharges. If variations in the C_{off} values were observed this would mean that the gas phase remained perturbed after the stroke quenching, or because of electrode heating at high power levels.

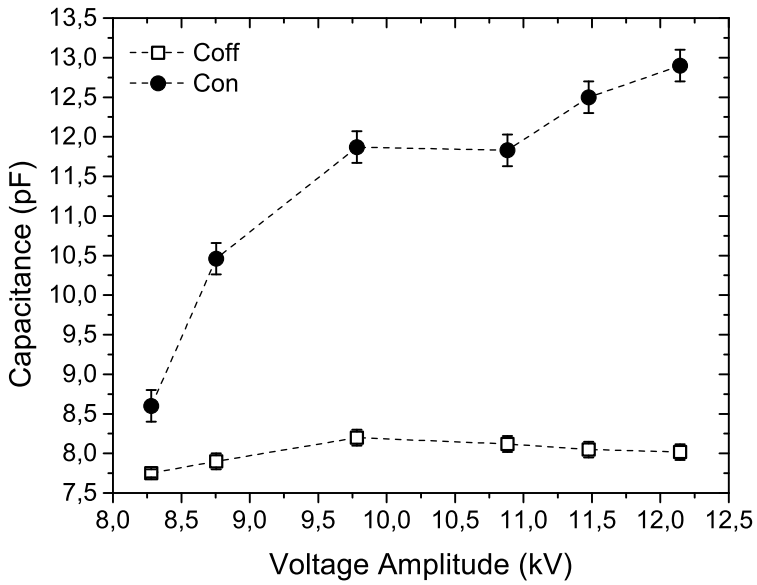

Figure 7.19: Capacitance in the presence (C_{on}) and absence (C_{off}) of plasma, calculated from the Lissajous figures obtained after the subtraction of Q_{micro}, as a function of the voltage amplitude.

In these experiments, however, C_{off} seems to represent just the cold capacitance of the actuator. The capacitance C_{on}, instead, increases with the voltage amplitude, and for sufficiently high values it becomes equal to the capacitance given by the series of the two insulating barriers: $C_{on} = C_{die}$. It is thus clear that Manley's assumption presented in the introduction is adequate only in these conditions. Moreover, it is evident from this discussion that, even though the plasma-off sides AB and CD are straight lines, their intercepts with the Q axis represents the total charge left on the dielectric barriers during the previous plasma activity only if the capacitance C_{on} remains equal to C_{off} (Figure 7.17 (b)), otherwise these intercepts are influenced by capacitance variations too.

7.2.2 SDBD Configuration

The same method for the investigation of Lissajous figures has been adopted for the surface dielectric barrier configuration. In this case a band pass

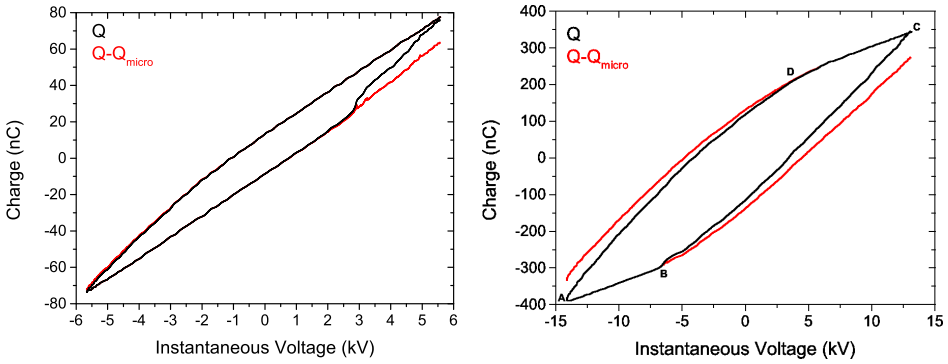

Figure 7.20: Examples of Lissajous figures (shown in black) obtained for two different voltage amplitudes (5.6 kV and 13.5 kV) in a surface configuration. For red curves the charge Q_{micro} transported by current microdischarges have been subtracted from the Q signal of the Lissajous figure.

filter with a lower cut-off frequency was adopted (2 MHz instead of the 15 MHz used for the planar configuration), so that there are no oscillations associated to the plasma presence. This allows to appreciate if asymmetries are present between the two half-cycles of the Lissajous figure. Figures 7.20a and 7.20b show two Lissajous figures (in black) obtained at two different voltage amplitudes (5.6 kV and 13.5 kV). It is clear that in the first case a variation in the Q signal happens abruptly at the beginning of the active phase of the backward semi-cycle (when the voltage is increasing towards its maximum, side AC), whereas the Q variation is more gradual during the forward half-cycle (side CA). At higher voltage amplitudes, instead, the $Q - \Delta V$ plot appears more symmetric, even though the breakdown of the positive plasma phase is always more evident. This is due to the presence of the group of plasma microdischarges that are created at the discharge breakdown (see Section 5.1). The red curves correspond to the Lissajous figures obtained after subtracting Q_{micro} from the original Lissajous plots. Again, it easily to notice that at high voltages the discharge semi-cycles behave quite similarly, whereas at low voltages the two semi-cycles appear considerably different. As a matter of fact, Figure 7.20a reveals that during

the positive half-cycle plasma microdischarges transport a certain amount of charge Q_{micro}, and that after the subtraction of Q_{micro} from the $Q - \Delta V$ plot, the new slope C_{on}^{BD} looks quite similar to the slope C_{off} of the plasma-off phase. On the contrary, during the negative half-period, almost no current microdischarges were detected, and this portion of the Lissajous figure is not affected by the subtraction of Q_{micro}. However, the slope of the curve changes, and this means that there is a capacitance change (due to a charge rearrangement) or a charge transfer happening in a way different from current plasma mirodischarges. Eventually, it is worth to noticing that at high voltages, the transition from C_{off} to C_{on} is not abrupt but gradual (Figure 7.20b). This is probably due to progressive changes in the geometrical shape of the discharge region, which leads to gradual changes in the cell capacitance C_{on} and to the creation of an almond-like Lissajous figure.

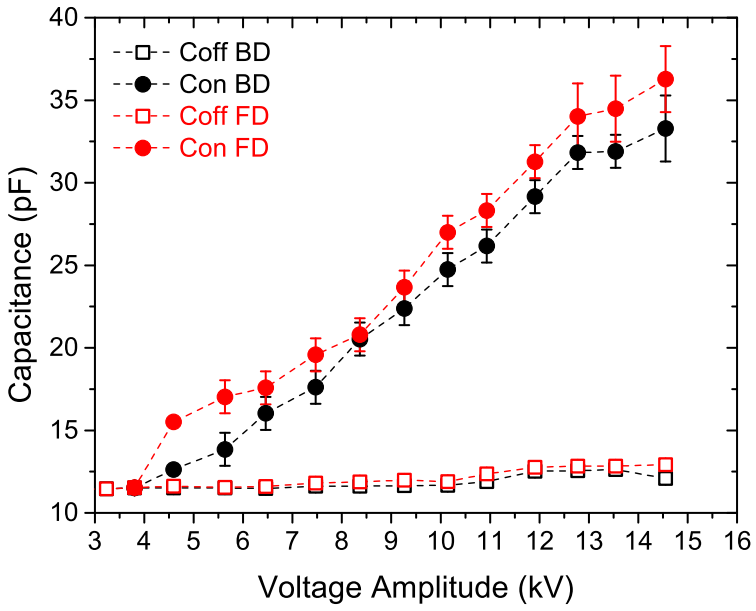

Figure 7.21: Capacitance in the presence (C_{on}) and absence (C_{off}) of plasma, calculated for both the positive and negative half-cycles from the Lissajous figures obtained after the subtraction of Q_{micro}, as a function of the voltage amplitude.

The values of C_{on} and C_{off} obtained for the surface configuration are

presented in Figure 7.21 as a function of the voltage amplitude. These results show that C_{on} is higher for the negative half-cycle. This is probably due to the higher mobility of electrons, which are more easily accumulated on the insulating surface rather than ions. Both C_{on}^{BD} and C_{on}^{FD} tend to increase with the voltage, and this could be associated to a spreading of the discharge region, meaning that the higher the voltage the more the plasma sheet extends to chordwise positions far from the exposed electrode. We will examine in more depth this point in future investigations.

CHAPTER 8

Background Oriented Schlieren Implementation

Background Oriented Schlieren (BOS) has been implemented at University of Milano-Bicocca during the last period of this thesis. BOS is a technique allowing the determination of refractive index gradients without sophisticated optical equipments, recently developed in the fluid imaging community [177,178]. The main characteristics of this diagnostics and of its implementations are presented in this chapter together with an overview of the results obtained up to now. Further details are given in the master's thesis by C. Capone [179].

8.1 Introduction

Understanding a physical process is made easier every time it is possible to reproduce a visual representation of it. This is especially true for fluid dynamics effects, and in particular for boundary layer evolution in space and time. Flow visualization is the oldest method used to study fluid mechanics and it has been used throughout history in a wide range of applications, from aerodynamics to meteorology, medical science, air conditioning and many other fields [180, 181]. Nevertheless, most liquids and gases are transparent medium: their motion cannot always be followed by direct observation neither foreseen because of its complexity. Fluid motion visualization requires non invasive methods to observe and analyse different kinds of flows. Two main techniques are usually adopted, based on direct injection of material or on refractive index changes.

Direct Injection Methods This class includes all methods in which an external material is introduced in the fluid flow [180]. In this case, flow visualization is indirect because it is inferred from that of the foreign particles introduced. These particles should be visible but also small enough to compare their velocity and direction with those of the fluid. Differences between the two flows can be minimized, but not completely removed, by imposing particle density to match the fluid one. Most commonly, dyes are used in water while smoke is applied in air flows. The term smoke is used in a wide sense, not only restricted to combustion products but also including steam, vapour, mist and aerosols [182]. Particle Image Velocimetry (PIV) belongs to these optical methods of flow visualization. It allows velocity measurements within a single plane inside the flow, which are deduced from the displacements of the particles seeded in the flow [183]. A 2-D area in the flow is illuminated twice, within a short time interval, by a laser sheet. Light pulses must be short enough to "froze" the motion of particles during the exposure, in order

to avoid the image blur. Typical dimensions of seeding particles are $10 \div 100$ micrometers, so that they are small enough to move with the local flow speed but at the same time large enough to scatter a significant quantity of the incident light [184].

Methods based on refractive index changes. Index of refraction gradients in transparent inhomogeneous media are due to density, temperature or material changes. Light rays are always refracted towards regions with higher index of refraction and many techniques have been developed to connect these deflections to the structure of the studied object (usually called *phase object*) [181]. Among all optical methods used to investigate fluid flows, they have the advantage of being non invasive. Shadowgraph, Schlieren and Interferometry are the main visualization methods based on the connection between index of refraction gradients and flow density [185].

The great advantage of Shadowgraph lies in the possibility of making large scale flow visualization using a basic setup, consisting in a point light source and a recording plane [186]. A varying density field is placed between them and causes the shadow effect: the individual light rays crossing the test section are refracted and bent out of their original path. The final result is a pattern of light intensity variations on the recording plane, which is related to the second derivative of the fluid refractive index. Therefore, Shadowgraphy is an optical diagnostic technique sensitive to sharp changes of fluid density, and it is commonly used to study compressible gas flows with shock waves and turbulence effects, which can be considered as extremely intense changes of gas density [181]. Shadow images are easy to obtain and can be scaled to large fields of view: these measurements can be even carried out outside a laboratory, using the sun as the light source. Quantitative analysis of shadowgraph images can be obtained by solving the Poisson equation that relates the recorded light intensity variations to the refractive index field

of the physical medium [187, 188]. However, this can be quite difficult, so this method is generally used just to have a quick survey of a flow with density changes. Moreover, Shadowgraphy gives an overall visualization of a complex phenomenon but it's little sensitive to slow density variations, so shadowgrams usually lack of details [189].

The conventional Schlieren system consists of a point-light source, two lenses, a knife-edge and a screen [180, 181]. The beam of light coming from the point source is collimated by the first lens, then crosses the phase object and is finally focused by the second lens onto the screen. The knife-edge is a filter that cuts off light intensity and controls image contrast. Ideally, the knife removes half of the light rays and if the phase object is homogeneous the loss of light is uniform. Instead, if the test region has density gradients, light rays that are deflected can be intercepted by the knife-edge. This effect results in the formation of brighter and darker areas corresponding to the changes of the refractive index in the plane normal to beam propagation [186]. Schlieren produces a real image of the phase object, not only a mere shadow, and its sensitivity can be made higher choosing longer focal lens to widen angular deflection [189]. Where large spaces have to be imaged, off-axis parabolic mirrors are used rather than lenses to collimate and focus the beam (z-type configuration): in this case the light source and the knife edge are placed in the focal plane of the first and second mirror respectively [190]. A drawback of schlieren methods is small flexibility: common setup cannot be easily scaled or moved, and the system geometry is limited from focal length and size of mirrors and lenses [188, 189].

Interferometry is based on the analysis of a pattern of bright and dark fringes, called interferograms. This pattern is the result of a change in the optical path between a *test beam* and a *reference beam*, and it reflects the different phases of the two waves [191, 192]. Interferograms can be interpreted directly by means of index of refraction instead of its derivatives [191]: this fea-

ture makes Interferometry the simplest method in terms of post-processing image analysis and interpretation. Nevertheless, compared with Shadowgraphy or Schlieren, this technique requires a more complex and expensive setup and its more sensitive to alignment and vibration problems. There are many kinds of configurations to produce interference, but the most famous are Michelson, Mach-Zehnder and Fabry-Perot interferometers. Having a higher sensitivity, Interferometry is usually preferred to the other methods when small density gradients are expected. On the other side, interferometers are unreliable when larger angles of refraction are involved because sharp density variations take place.

Being a compromise between the simple analysis of Interferometry and the basic setup of a Shadowgraph, the Schlieren method has emerged as the most popular refractive index based technique [188]. Compared to Interferometry, Schlieren is less sensible to alignment problems because less optical components are used. Some variations of this technique have been developed in the past years. For example, in Colour Schlieren the knife-edge is replaced with a colour band filter, i.e. a coloured circular filter with a radial increasing opacity, providing more information compared to monochromatic knife-edge Schlieren [193, 194]. In Grid-Based Schlieren methods, the knife-edge of the classical set-up is instead replaced by two aligned masks and diffuse light can be used instead of a point source [180]. The digital implementation of these techniques is called Synthetic Schlieren: one of the masks is placed between the light source and the test region while the other one is replaced with the digital image of the first mask without perturbations [195, 196]. Eventually, in Background Oriented Schlieren (BOS), a *background pattern* is placed before the test region and focused by a converging lens onto a high speed digital camera [197]. The visualization process is the result of a comparison between the pattern images recorded in absence and presence of a perturbation introduced in the test region. Many papers refer to BOS as a Synthetic Schlieren

with a more versatile pattern: while Synthetic Schlieren requires an optimized background pattern, in BOS one can even use natural elements like trees branching and leafage [198]. Like other Schlieren-like techniques, BOS provides non intrusive measurements of the first derivative of the refractive index in the test area, but this method has a strong similarity with Shadowgraphy since its equipment doesn't require expensive mirrors or knife-edges and the phase object is not perfectly focused [186]. As a matter of fact, the BOS technique was born with the purpose of minimizing optical alignment problems that affect traditional schlieren systems [189]. Moreover, it is easily scalable on higher dimension [186, 190], and has a quite wide dynamic range, meaning that it can show both large and small perturbations [199]. The quality of the results is mainly due to the technical specifications of the recording camera (e.g. resolution and noise) and to the algorithms used in the post-processing analysis [186]. This feature can be an advantage, since a limitation on technical aspects can be overcome improving data processing or providing higher quality equipments.

8.2 Principles of Operation

A typical BOS set-up is shown in Figure 8.1: a light source illuminates a background pattern, which is focused by a converging lens onto a high speed digital camera; the phase object under study is placed at an optimal distance between the pattern and the lens [200]. BOS is a line-of-sight integrated method, since it is sensitive to the first derivatives perpendicular to the light path of the refractive index [197,201]. The experimental operating procedure for obtaining the refractive index field consists in two main steps:

Image acquisition: a reference image of the unperturbed test area is recorded by the camera, then the phase object is introduced and a second photograph of the background is taken.

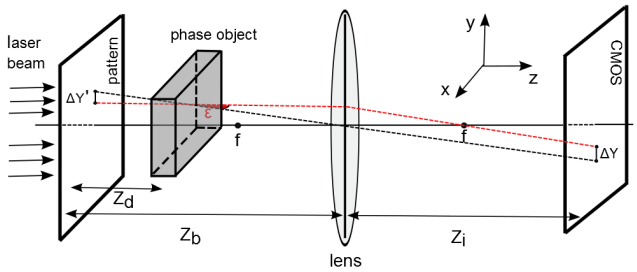

Figure 8.1: Scheme of a typical BOS setup.

Data post processing: the two images are firstly analysed by means of a cross-correlation algorithm and a plot flow of the background shifts is deduced. Index of refraction gradients are proportional to local values of this displacement field and using numerical integration methods one can reproduce a map of the refractive index in the phase object. As we will see in Section 8.4, once the refractive index field is obtained, it becomes easy to deduce the relative density map thanks to the Gladstone-Dale equation [202].

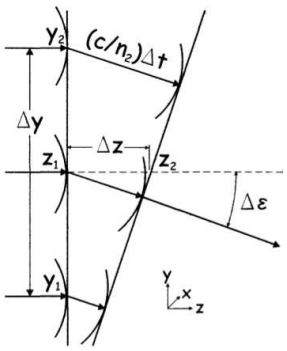

Figure 8.2: Scheme of the angular deflection due to a refractive index gradient.

In optics, the deflection angle expected for a refracted light ray can be deduced from Fermat Principle [203]. The geometric theory of refraction is only an approximation to the more-complete physical optics approach, but is sufficient for the present purposes [181]. Let's consider a negative refractive index gradient along y only (see Figure 8.2): $dn/dy < 0$. A vertical wave front (z_1) is initially perpendicular to the optical axis z. When the wave front propagates in the medium toward z_2, in the path between z_1 and z_2 it covers a differential distance Δz in an infinitesimal time interval Δt and undergoes a differential deflection $\Delta\varepsilon$. Since light rays are always normal to their front waves, one can consider that the initial ray in z_1 is then deflected of an angle $\Delta\varepsilon$ when it

reaches z_2. From the definition of the refractive index $n = v_0/v$ and referring to Figure 8.2, one can deduce that

$$\Delta\varepsilon \approx tg(\Delta\varepsilon) = \frac{\Delta z}{\Delta y} = \frac{v_0/n_2 - v_0/n_1}{\Delta y}\Delta t. \tag{8.1}$$

Furthermore, rewriting Δt as

$$\Delta t = \frac{n}{v_0}\Delta z, \tag{8.2}$$

and combining the two expressions above, it is found that

$$\Delta\varepsilon = \frac{n}{v_0}\frac{v_0/n_2 - v_0/n_1}{\Delta y}\Delta z = \frac{n}{n_1 n_2}\frac{(n_1 - n_2)}{\Delta y}\Delta z. \tag{8.3}$$

When Δy approaches to 0, $\frac{n}{n_1 n_2} \simeq \frac{1}{n}$. In a differential representation

$$\frac{d\varepsilon}{dz} = \frac{1}{n}\frac{dn}{dy}. \tag{8.4}$$

However, since ε is a very small angle, it can be considered approximately as dy/dz. With this substitution the equation that describes the ray deflection is finally found. In particular, this relationship connects the refracted beam curvature with the index of refraction. In the most general case, this equation is expressed in terms of partial derivatives:

$$\frac{\partial\varepsilon_y}{\partial z} = \frac{\partial^2 y}{\partial z^2} = \frac{1}{n}\frac{\partial n}{\partial y}. \tag{8.5}$$

A similar equation is used for deflections on the x-axis

$$\frac{\partial\varepsilon_x}{\partial z} = \frac{\partial^2 x}{\partial^2 z} = \frac{1}{n}\frac{\partial n}{\partial x}. \tag{8.6}$$

From the integration of the previous equations, one obtains

$$\varepsilon_x(x,y) = \frac{dx}{dz} = \int \frac{1}{n}\frac{\partial n(x,y)}{\partial x}dz, \tag{8.7}$$

$$\varepsilon_y(x,y) = \frac{dy}{dz} = \int \frac{1}{n}\frac{\partial n(x,y)}{\partial y}dz, \tag{8.8}$$

where $n(x,y)$ is the local refractive index of the medium. Since a common approximation is $n \approx n_0$, where n_0 is the unperturbed index of refraction, ε_x and ε_y are often treated as:

$$\varepsilon_x(x,y) = \frac{dx}{dz} = \frac{1}{n_0}\int \frac{\partial n(x,y)}{\partial x}dz, \tag{8.9}$$

$$\varepsilon_y(x,y) = \frac{dy}{dz} = \frac{1}{n_0}\int \frac{\partial n(x,y)}{\partial y}dz. \tag{8.10}$$

Moreover, assuming that $\partial n/\partial x$ and $\partial n/\partial y$ are constant within the whole thickness Δz of the phase object that causes the beam deflection:

$$\varepsilon_x(x,y) = \frac{dx}{dz} = \frac{1}{n_0}\frac{\partial n(x,y)}{\partial x}\Delta z, \tag{8.11}$$

$$\varepsilon_y(x,y) = \frac{dy}{dz} = \frac{1}{n_0}\frac{\partial n(x,y)}{\partial y}\Delta z. \tag{8.12}$$

In BOS these deflection angles can be related to the apparent background shift obtained when the phase object is introduced into the system. The converging lens is placed between the background pattern and the recording camera at a distance such that the Law of Conjugate Foci holds (Figure 8.3):

$$\frac{1}{f} = \frac{1}{Z_i} + \frac{1}{Z_B}, \tag{8.13}$$

where f is the focal length, Z_B the distance between the background and the converging lens and Z_i the one between the lens and the camera. In this way, the optical system focuses the background plane, so that all pattern

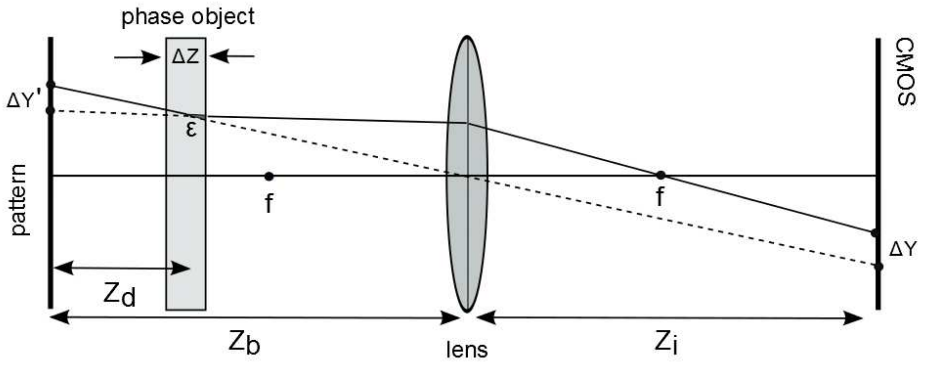

Figure 8.3: Scheme of the pattern shifts induced by the schlieren object.

shifts can be revealed by cross-correlation algorithms. From simple geometric considerations, it is clear that the virtual displacement of the background $\Delta Y'$ in the y direction is connected to the shift ΔY on the recording camera by the distances Z_B and Z_i:

$$\Delta Y = M\Delta Y' = \frac{Z_i \Delta Y'}{Z_B}, \tag{8.14}$$

where M indicates the magnification due to the converging lens.

Introducing the phase object at a distance Z_D from the background (see Figure 8.3) and the small deflection approximation, the deflection angle ε_y can be written as:

$$\varepsilon_y \approx tg\varepsilon_y = \frac{\Delta Y'}{Z_D} = \frac{\Delta Y Z_B}{Z_i Z_D} \qquad Z_B \to \infty \quad \varepsilon_y \approx \frac{\Delta Y Z_B}{f Z_D} \tag{8.15}$$

Therefore, for similar ε_y (i.e. equal index of refraction gradient) and Z_B, the pattern shift ΔY increases with the distance Z_D between the background and the phase object according to

$$\frac{\Delta Y}{\varepsilon_y} = \frac{Z_D Z_i}{Z_B} \approx \frac{Z_D f}{Z_B}. \tag{8.16}$$

Hence, the maximum displacement detectable would appear for $Z_D \to Z_B$ and would be equal to $\Delta Y = Z_i \varepsilon_y \approx f \varepsilon_y$. However, Z_D can't be increased at pleasure, because the larger Z_D the more blurred the phase object will be reproduced [179]. The ideal condition for observing index of refraction gradients would be reached at a distance Z_D satisfying the Law of Conjugate Foci for the schlieren object, and thus for $Z_D = 0$. This is impossible because the pattern is physically located at the distance Z_B from the lens, so Z_D is always greater than 0. In practice, a compromise between sensitivity and resolution has to be reached in choosing the position of the phase object.

After the images with and without perturbation have been recorded, they have to be compared to find the pattern shifts. A fundamental part of the BOS method is thus the post-processing analysis. Several algorithms have been developed to compare undisturbed images with perturbed ones. Some of them had already been used in flow visualization techniques like PIV. The common principle of cross correlation algorithms consists in a comparison among neighbouring pixels for both images. If a matching between two zones is detected, then their relative position defines a two-dimensional displacement vector, representing the refraction due to the local gradients present in the test area [186, 204].

Once the pattern displacements ΔY have been determined, the angular deflection ε_y can be calculated from Equation 8.15. At this point, remembering the relationship between the deflection angle and the first derivative of the refractive index (Equation 8.12) one obtains

$$\frac{\partial n}{\partial y} = \frac{n_0 Z_B \Delta Y}{Z_D Z_i \Delta z} = \frac{n_0 (Z_B - f) \Delta Y}{Z_D f \Delta z}. \tag{8.17}$$

A similar equation stands for the derivative $\partial n / \partial x$ and for the image displacement ΔX along x:

$$\frac{\partial n}{\partial x} = \frac{n_0 Z_B \Delta X}{Z_D Z_i \Delta z} = \frac{n_0 (Z_B - f) \Delta X}{Z_D f \Delta z}. \tag{8.18}$$

These two quantities can be combined into the Poisson equation [202]:

$$\frac{\partial^2 n(x,y)}{\partial x^2} + \frac{\partial^2 n(x,y)}{\partial y^2} = R\left(\frac{\partial \Delta X}{\partial x} + \frac{\partial \Delta Y}{\partial y}\right), \tag{8.19}$$

where $R = \frac{n_0 Z_B}{Z_D Z_i \Delta z}$ is a constant summarizing all the geometrical dimensions of the system involved in the analysis. This equation can be solved with numerical methods, and allows to derive a map for the refractive index of the phase object $n(x,y)$ [177,202].

8.3 Image Acquisition and Post-Processing

The laboratory and computational equipments we have used for the implementation of the Background Oriented Schlieren technique are presented in this section. The experimental apparatus used for image acquisition is made up of a laser, a background pattern, a converging lens and a CMOS camera, all arranged on an optical breadboard (by Newport Corporation, 1.5 m long) in order to favour alignments and to avoid vibrations. Concerning the analysis of images, cross-correlation and the integration algorithms have been used in a Matlab environment.

Laser Source The ideal working condition includes a stable illumination, since during the image post-processing stage the displacements are evaluated from the grey scale of pixels. However, algorithms generally are not so sensible to slightly time-varying brilliance, and in case this disadvantage can be easily overcome with the use of specific light filters of image processing softwares. Different tests with a table lamp, a torch and a laser were carried out [179], and eventually we decided to run experiments with the He-Ne Laser (Newport R-30989), which generates a linearly polarized output beam of 2.0 mW at 633 nm. The laser beam can illuminate just a portion of the background pattern that is smaller than the one imaged by the CMOS cam-

era. This problem can be fixed in two main ways: by using a beam expander or a frosted glass. The former can be build with a couple of converging lens, but, given the lenses at our disposal and the optical table length, this solution requires too much space at the moment, and was thus rejected [179]. The effect of adopting a frosted glass is light diffusion, meaning a loss of the typical laser coherence, which is anyway unnecessary in BOS, and the formation of a speckle background superimposed to the used pattern, which turned out not to be a problem [179].

Background Pattern The most common patterns for BOS are gaussian dot distributions, speckles and wavelet noise. Optical analysis requires non-homogeneous images with high frequency details so that algorithms can be efficiently applied. It's not necessary to realize a different background pattern for each algorithm, but in several cases an optimized pattern improves the results. The optimized condition is reached when pattern and camera resolutions are coupled. Linear grid backgrounds like those used in Synthetic Schlieren experiments [195] are useless for a two-component displacement field evaluation, since their efficiency is restricted to the determination of displacements normal to the pattern lines [205]. When random dot patterns are used, the choice of size and spacing of the pattern elements may cause significant variations in the processed image quality, while no change is observed when different shapes are used. Small dots grouped closely together usually give the algorithm more finely meshed reference points for comparison. The effective optimal dimension for the pattern elements depends on the image sensor [206]. Grey-scale images characterized by random noise functions and with multi-scale patterns are often used as backgrounds. When only random noise characterizes the pattern, it can be difficult to optimize the set-up since for each configuration a different pattern is required. This problem can be avoided by using a *wavelet-noise background*, a multi-scale pattern with high

frequency noise on every scale. Wavelet noise patterns are independent from the set-up configuration and can reduce also computational problems connected to aliasing and loss of details [186]. The essence of wavelet noise creation consists of four steps, which are illustrated in Figure 8.4. An image R filled with random noise is firstly created (a) and subsequently downsampled to create the half-size image $R^{\downarrow}$ (b). Then $R^{\downarrow}$ is upsampled to a full size image $R^{\downarrow\uparrow}$ (c), which is finally subtracted from the original R to create N (d). A complete description of the wavelet noise theory and its practical implementation are discussed in [207].

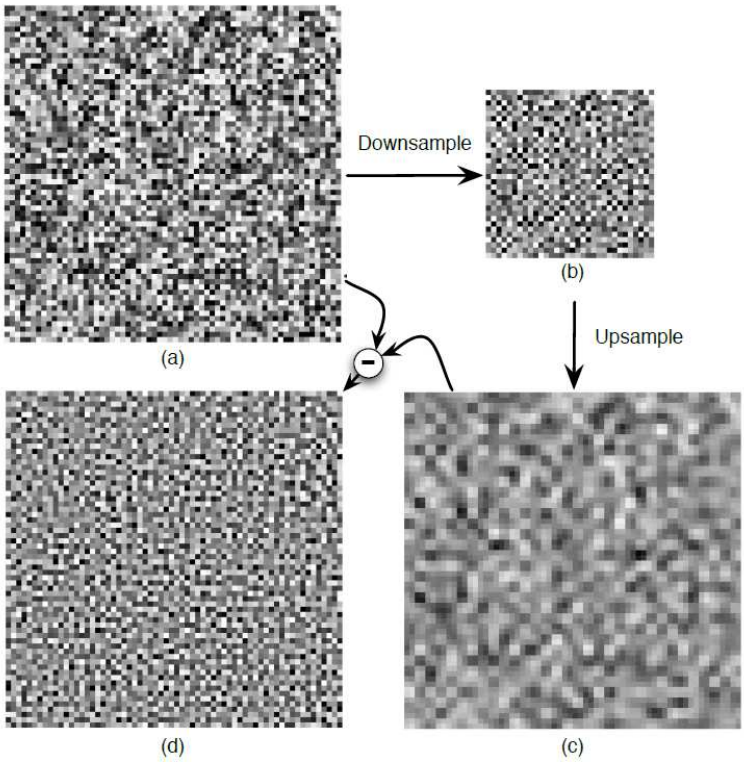

Figure 8.4: (a) Image R of random noise, (b) Half-size image $R^{\downarrow}$, (c) Half-resolution image $R^{\downarrow\uparrow}$, (d) Noise band image $N = R - R^{\downarrow\uparrow}$ [207].

Lens The lenses at disposal have focal lengths of 50, 75, 100, 150, 200 or 300 mm and they all have a diameter of 50 mm. When choosing which lens to adopt, it's necessary to take into account the available distances,

the required magnification and the extension (along the direction of laser beam propagation) of the phase object that has to be placed between the pattern and the lens (with thickness Δz between 0.5 cm and 7 cm in our case). Among all the lenses at disposal, those which provide greater optical magnifications M and larger distances L between the pattern and the camera sensor, have focal lengths f equal to 150 mm and 200 mm [179]. Up to now we have usually made measurements with $f = 200$ mm, $L = 800$ mm, $Z_B = Z_i = 400$ mm and $M = 1$. The main difficulties encountered in decreasing the image magnification lies in pincushion distortions together with the reduction of the laser spot and the consequent darkening of the image borders [179]. On the contrary, before using $M > 1$ we thought it was better to acquire some images with $M = 1$, since the adopted integration algorithm requires the knowledge of a boundary condition for the refractive index n. At this purpose, it is worth to describe the different possibilities in choosing the boundary condition. One of them is to leave the default zero boundary condition and analyse BOS images in order to obtain quantitative information about the refractive index changes Δn inside the image instead of its absolute value n. As an alternative, a magnification low enough for visualising a spatial region including the unperturbed (an thus known) value of n can be adopted. Eventually, another option is to start from an image in which the unperturbed value of n is present, and to concatenate spatially adjacent images, so that it is possible to propagate the boundary condition from one image to another.

CMOS Camera A CMOS Camera (MV-D1024-160-CL-8 by Photonphocus) has been used for acquiring images of the background pattern. All measures recorded up to now were made by using the camera in the free-running mode, meaning that it continuously delivers images with a certain configurable frame rate. When the acquisition of an image needs to be synchronised to

an external event, a trigger can be used. We plan to use this mode in future. The geometrical sensor characteristics are: resolution 1024×1024 pixels, pixel size equal to $10.6\,\mu m \times 10.6\,\mu m$, and sensing area $10.9\,mm \times 10.9\,mm$. The exposure time, indicating the period during which the image sensor integrates the incoming light, can be varied in the range $10\,\mu s \div 0.5\,s$. Actually, the minimum exposure-time we used is 52 μs. This limitation is due to the light source employed, that is not enough intense for shorter time intervals because the background pattern becomes too dark. The maximum frame rate, meaning the minimum temporal interval separating two successive images, for this camera model is 150 frames per second. However, this is valid only when the minimum exposure time is selected. For our purposes, a matrix of about 700×700 pixels was generally scanned, and the lower time interval between two images is equal to several milliseconds (between $15 \div 25$ ms).

Cross-Correlation Algorithms Among cross-correlation algorithms suitable for BOS analysis we remind two categories: *Block-matching algorithms* and *Gradient-based methods*. The former were already used for PIV, so they were the first to be applied to BOS (with adequate changes). The idea behind block matching is to divide the current frame into a matrix of macro blocks each of which is then compared with the corresponding block and its adjacent neighbours in the previous frame. This comparison allows to create a vector that stipulates the movement of a macro block from one location to another (see Figure 8.5). This movement, calculated for all the macro blocks, constitutes the motion estimated for the current frame [208]. In the block based techniques, frame motion is determined from the variations in the pixel intensities. The best matching is considered as the block with less intensity difference between the current frame and the reference frame. In gradient based techniques, instead, the spatio-temporal deriva-

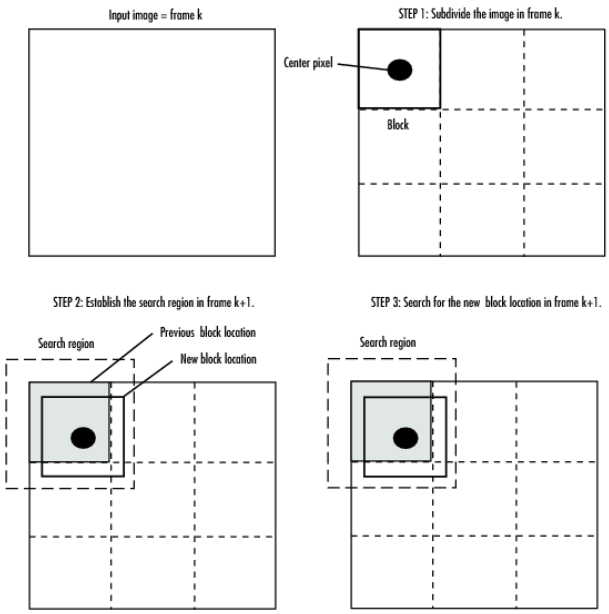

Figure 8.5: . Diagram of block matching operation.

tives of pixel intensities is calculated to determine the frame motion [209]. Gradient-based methods are more sophisticated and give a good equilibrium between good quality results, easy implementation and fast execution. Among gradient-based techniques we have tried the *Horn-Schunck algorithm* (a Matlab function, *HS*) [210] and the *Lucas and Kanade algorithm* (a Matlab script, *LKPR*) [211]. We found that they provide similar results, but they have different advantages and drawbacks. The Horn-Schunck algorithm is quite rapid (only some seconds are required for correlating two images of 700×700 pixels), but its great disadvantage is that a couple $(\Delta X, \Delta Y)$ of displacements is associated to each pixel, which makes the resulting flow field interpretation more difficult. On the contrary, in the Lucas and Kanade case, interrogation windows (like in the block-matching algorithms) and a pyramidal procedure are used. The result is that the Lucas and Kanade algorithm is more accurate and more sensitive to details compared to the Horn-Schunck one, but its elaboration time is higher (an average time of 5 minutes is required for correlating two images of 700×700 pixels), and this

can constitute a problem when the number of images to analyse is large. Detecting displacements that are not integer multiples of pixels requires an interpolation scheme inside the cross-correlation procedure: pixel intensities are recalculated as it happens in image deformation techniques [186]. Both the considered algorithms provide this possibility. Usually, cross-correlation algorithms can detect sub-pixel shifts of the order of $0.01 \div 0.1$ pixels. The accuracy in the pixel shift displacement can be evaluated in terms of bias error and random error. We have considered them both during some tests that we implemented to evaluate the accuracy of each algorithm in detecting shifts. By means of a Matlab function (*ifftshift*) we imposed a known mono-dimensional shift, with amplitude and direction equal for all the image pixels, and we then evaluated this displacement by means of the cross-correlation algorithms. Both integer and fractional shifts were tried. Results show that for integer displacement lower than 5 pixels the Lucas-Kanade algorithm manages to detect the imposed shift with lower statistical and bias errors. For larger shifts the two algorithms provide similar results. It is worth to notice that for sub-pixel displacements the Lucas-Kanade procedure suffers a typical effect associated to the interpolation procedure used to find the sub-pixel displacements, which is called *peak-locking* [179]. Another element that has been considered in the Lucas-Kanade case is the influence of the interrogation window size on the evaluation of the pixel displacement. It turned out that using a window size too large can cause loss of details and that, on the other side, with a too small window the detected shifts are affected by a larger error [179]. The analysis have been carried out with an interrogation window of 9×9, which seemed to be a good compromise.

Integration Algorithm The integration algorithm (a Matlab function called *intgrad2*) generates a two-dimensional surface representing the result of the integration of the gradient map given as input.

8.4 Expected Beam Deflections

In this section the factors that can influence the index of refraction are analysed in order to understand which of them can be observed with our experimental setup. The refractive index is a function of the fluid density: a variation of the latter can be connected to compressibility, temperature variations, or composition in a mixture of fluids. When a plasma is considered, electrons and ions give a contribution to the total refractive index too. For gaseous systems, where the distance among molecules is large, the Gladstone-Dale Equation relates the index of refraction of a fluid to its properties and to the incident radiation frequency ν:

$$n - 1 = \frac{\rho L e^2}{2\pi m_e M} \sum_i [\frac{f_i}{\nu_i^2 - \nu^2}], \tag{8.20}$$

where ν_i are the resonance frequencies (with oscillator strengths f_i) associated to the electron energy levels of molecules [212], e and m_e are the electron charge and mass, M the molar weight of the fluid, ρ its density and L the Loschmidt number, which is the number of particles of an ideal gas per volume at standard conditions. This equation is often expressed as

$$n - 1 = K\rho, \tag{8.21}$$

where K is the Gladstone-Dale constant, which depends from the gas proprieties and at first approximation is independent from frequency. For air at atmospheric pressure (and for $\lambda = 633$ nm) it is equal to $K_{air} = 0.2256\, cm^3/g$. If a gas mixture is considered, the Gladstone-Dale Equation becomes

$$n - 1 = \sum_i K_i \rho_i, \tag{8.22}$$

where ρ_i is the partial density of the single components. In a ionized gas the index of refraction includes the contributes of neutral molecules, ions and

electrons [212]:

$$(n-1) = (n-1)_m + (n-1)_i + (n-1)_e. \tag{8.23}$$

The former is described by the Gladstone-Dale Equation:

$$(n-1)_m = K\rho, \tag{8.24}$$

but can also be expressed as a function of the number of molecules per unit of volume N_m [213] :

$$(n-1)_m = \frac{1}{L}(A + \frac{B}{\lambda^2})N_m. \tag{8.25}$$

For air at atmospheric pressure $A_{air} = 2.83 \cdot 10^{-4}$, $B_{air} = 2.03 \cdot 10^{-6}\,\mu m^2$ and $L = 2.687 \cdot 10^{19}\,cm^{-3}$ The ion contribution is [213]:

$$(n-1)_i = \eta\frac{1}{L}(A + \frac{B}{\lambda^2})N_i, \tag{8.26}$$

where N_i is the number of ions per unit of volume and $\eta_{air} = 0.81 \cdot 10^{-4}$. Eventually, the electron term is [179]:

$$(n-1)_e = -4.4610^{-14}\lambda^2 N_e, \quad (\lambda : cm, N_e : cm^{-3}) \tag{8.27}$$

where N_e is the number of electrons per unit of volume. The electron density effect can thus be observed as a reduction of the refractive index when the gas becomes ionized. For a wavelength equal to 633 nm the refractive index for a plasma of air at atmospheric pressure is thus:

$$(n-1) = 1.0709 \cdot 10^{-23}(N_m + 0.8143N_i) - 1.7859 \cdot 10^{-22}N_e, \tag{8.28}$$

with N_m, N_i and N_e expressed in cm^{-3}.

For an equal number density, the ion contribution is twenty times lower than the term associated to electrons, while the molecule contribution is seventeen times lower [213]. From Equation 8.17 it is possible to estimate the displacement of the pattern image ΔY as a function of the geometrical configuration (Z_D and f), for a phase object with thickness Δz in the laser beam direction and with a refractive index gradient $\partial n/\partial y$ perpendicular to it:

$$\Delta Y = \frac{Z_D f \Delta z}{n_0(Z_B - f)} \frac{\partial n}{\partial y}. \tag{8.29}$$

We have thus considered different phenomena that can produce a variation in the refractive index. An estimate of the pattern shifts determined by these gradients is given and a prediction about the observable variations is made in relation to the specifics of the set up. It is worth noticing that the minimum detectable shift depends on the resolution of the imaging sensor used, since higher resolution implies higher sensitivity [197]. On the basis of some observation made in our experiments and referring to the specifics of the CMOS employed, we came to the conclusion that shifts lower than 0.1 pixel cannot be detected [179].

Deflections expected for generic neutral density changes. We have already said that the dependence of the index of refraction from the gas density in a neutral system is given by the Gladstone-Dale Equation and that in air, for a wavelength of 633 nm, this relation has the form

$$n = 1 + K_{air}\rho = 1 + 0.2256 \cdot \rho, \tag{8.30}$$

where the density ρ is expressed in g/cm^3. In this case the value of $\partial n/\partial y$ to be replaced in Equation 8.29 is thus:

$$\frac{\partial n}{\partial y} = 0.2256 \cdot \frac{\partial \rho}{\partial y}. \tag{8.31}$$

An estimate of the expected shift can thus be given for a particular configuration [179]. In the specific case of $f = 20$ cm, $Z_d = 1$ cm and $\Delta z = 0.5$ cm, the BOS technique implemented allows to observe density changes from the unperturbed value (density of air at standard conditions) larger than 4% within $\Delta y = 1$ cm. In terms of refractive index gradient, this value corresponds to $\frac{\Delta n}{\Delta x} = 1 \cdot 10^{-5} cm^{-1}$. However, changing the working conditions has a great influence on the determination of the minimum detectable gradient: for example, if the integration length is taken as $\Delta z = 7\,cm$ (as done in Section 8.6), density changes larger than 0.8% can be observed within 1 cm.

Deflections expected for density variations due to speed gradients When a gas is considered, density gradients related to velocity variations can be expressed by the following relation [54]:

$$\rho_f - \rho_i = \rho_i (1 - e^{-\frac{1}{2}\frac{(v_f - v_i)^2}{a^2}}), \tag{8.32}$$

where a is the speed of sound, v_i and v_f denote the initial and final gas speeds, and ρ_i and ρ_f are the corresponding densities. Considering a flow initially at rest (v_i=0) and introducing the Mach number $M = v_f/a$, one gets:

$$\rho_f - \rho_i = \rho_i (1 - e^{-\frac{1}{2}M^2}). \tag{8.33}$$

As showed in Figure 8.6, for low subsonic conditions, compressibility can be ignored because density variations are very small. A flow is usually considered incompressible up to $M = 0.3$. The working conditions adopted in this thesis involve speeds arising from zero to a few meters per second in air at atmospheric pressure ($\rho_i = 1.184 \cdot 10^{-3}\, g/cm^3$). Such a velocity variation induces a density change smaller than 0.04%, which is much lower than the minimum detectable value.

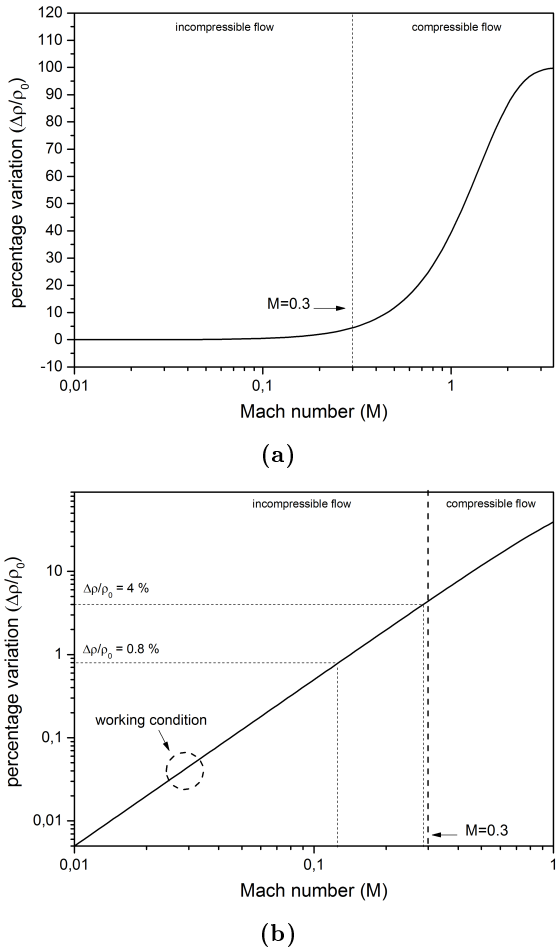

Figure 8.6: Density percentage variation as a function of the Mach number. Subfigure (b) is a zoom of the region of interest of subfigure (a).

Deflections expected from temperature changes. The Gladstone-Dale Equation can be expressed in terms of pressure P and temperature T, instead of gas density:

$$n = 1 + K_{air}\frac{MP}{RT}, \tag{8.34}$$

where $R = 8.31$ J/Kmol is the gas constant. In an isobaric approximation any variation of the refractive index is due to temperature gradients:

$$(n-1) = (n_0 - 1)\frac{T}{T_0}, \tag{8.35}$$

and

$$n = 1 + \frac{8.1 \cdot 10^{-2}}{T}. \tag{8.36}$$

In this case the value of $\partial n/\partial y$ to be replaced in Equation 8.29 is:

$$\frac{\partial n}{\partial y} = 8.1 \cdot 10^{-2} \frac{\partial}{\partial y}\left(\frac{1}{T}\right). \tag{8.37}$$

In the specific case of $f = 20$ cm, $Z_d = 1$ cm and $\Delta z = 0.5$ cm the BOS technique implemented allows to observe temperature changes larger than 10 °C within $1\,cm$. If the integration length is taken as $\Delta z = 7$ cm, temperature changes larger than 2 °C become visible within 1 cm.

Deflections expected for electron density changes. It is easy to see from Equation 8.28 that if the refractive index changes are due to an electron density gradient, the value of $\partial n/\partial y$ to be replaced in Equation 8.29 is:

$$\frac{\partial n}{\partial y} = -1.78594 \cdot 10^{-22} \frac{\partial N_e}{\partial y}. \tag{8.38}$$

Considering the typical dimensions of a single axisymmetric microdischarge ($\Delta z = 0.01$ cm), the minimum electron density change visible within 0.01 cm is $\Delta N_e = 10^{16}$. If the integration length is extended to $\Delta z = 7$ cm, also $\Delta N_e = 10^{14}$ within 0.01 cm should become visible. A further in-depth analysis and improvements in resolution and time response of the imaging sensor used are needed to apply the BOS technique to a plasma discharge, therefore the experimental work up to now is limited to the study of neutral density gradients [179].

8.5 Validation of the Technique

In the first part of the experimental work the BOS method was implemented and tested in different situations to validate the theoretical predictions previously made. In particular, an analysis on stable gradients and a validation of the technique by means of thermocouples were firstly carried out to evaluate the sensitivity and accuracy of the method. Afterwards, some experiments on density changes due to variations of velocity and gas composition were made to verify the versatility of the technique.

Stationary gradients Finding a schlieren object with time stable gradients is very useful to test the optical apparatus and evaluate the results from data post-processing. For this purpose, some authors make use of the so called *calibration lens* [193, 194], which refracts light rays with different deflection angles in function of the radial point (r) of incidence on the lens.

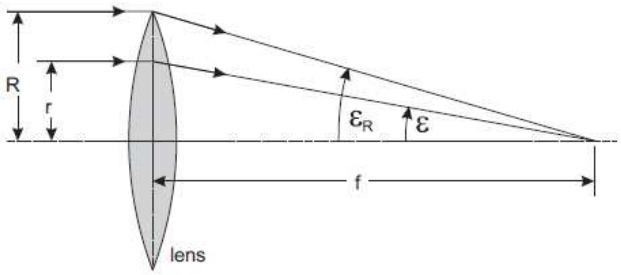

Figure 8.7: Deflection angle scheme for a calibration lens.

This deflection angle ϵ is zero at the centre of the lens and grows monotonically towards the boundaries following the law

$$\epsilon \approx tg(\epsilon) = \frac{r}{f}, \tag{8.39}$$

where f is the focal length. The maximum deflection angle is reached in correspondence of the radius R of the lens. This feature permits to consider the lens as a schlieren object with a radial gradient of the refractive index,

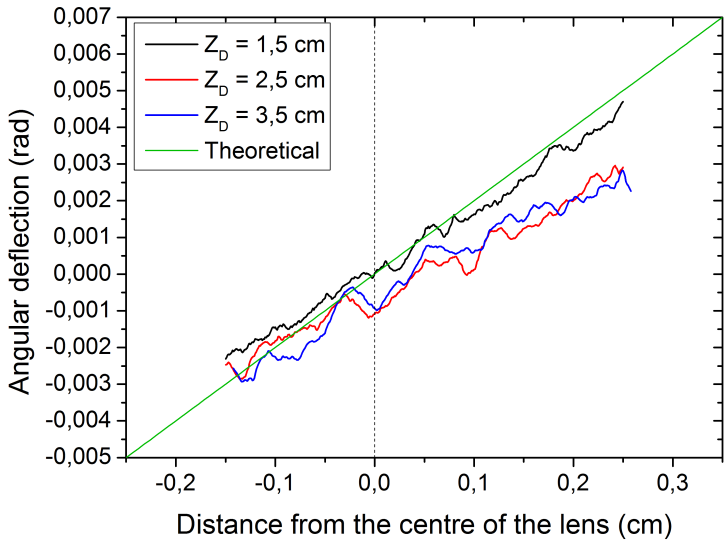

Figure 8.8: Comparison between the deflection angles predicted from theory and the BOS results. Deflection angles are expressed in radiants.

which doesn't vary in time. The calibration lens should be a lens with a large focal length ($R << f$), so that the small angle approximation could be satisfied. In the present experiment a calibration lens with a focal length of $f = 50$ cm was employed. In many Schlieren systems, these lenses are employed to calibrate the apparatus with a quantifiable relation between deflection angles and pixel intensities of the acquired image. In the specific case of a BOS, this kind of calibration is not necessary, but these lenses can be used to analyse the influence of the setup geometry on sensitivity and accuracy of the technique.

The sensitivity of a BOS system is a function of the optical geometry and of the specifics of the image acquisition sensor. In general, to obtain the highest sensitivity, the distance between the optical sensor and the background (Z_{tot}) should be maximized and the ratio Z_a/Z_{tot} should be minimized (Z_a is the distance between the phase object and the lens). However, there are some limitations connected to the field of view: it is fundamental to maintain reasonably in focus both the background pattern and the phase object in

order to apply the BOS technique successfully. The pixel shifts (ΔY) due to the introduction of the schlieren object are related to the deflection angle by the trigonometric law:

$$\epsilon \approx tg(\epsilon) = \frac{\Delta Y}{f}. \tag{8.40}$$

This theoretical prevision was compared with the deflections obtained by the background displacements, for a $f = 50$ cm calibration lens placed at three different Z_D distances from the background, as shown in Figure 8.8. A loss of accuracy and a consistent difference from theoretical predictions is shown when Z_D increases. This behaviour can be explained as follows, in relation to the increase of ΔY for larger Z_D. On one side, when pixel displacements are too large, cross correlation algorithms are less accurate. Moreover, when Z_D is increased, light rays may cross the schlieren object in a different area with respect to smaller Z_D [179]. The complete analysis of the detected shifts and displacements is described in [179].

BOS validation by means of thermocouples Referring to some experiments reported in literature [197, 214] a validation of the BOS system by means thermocouples was made. The differential equations governing convective heat transfer belong to the most difficult class of theoretical physics and have been solved analytically for only a few simple cases. A Schlieren-like method for the evaluation of temperature distributions (previously checked with comparison to thermocouples) provides a means of circumventing the mathematical problem for many conditions. A quantitative investigation of free-convection boundary layer temperature profiles generated by a heated metal plate and by a cold plate was carried out to verify how the BOS system reacted to gradients of different sign and intensity. Since similar results were obtained, only the hot plate case will be discussed. Further details on the adopted procedure can be found in [179]. The heated plate shown in Figure

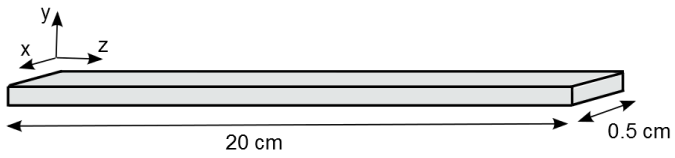

Figure 8.9: Scheme of the heated metal plate used in the procedure of comparison between BOS and thermocouples.

8.9 was used. Remembering that the CMOS sensor is 1 cm ×1 cm wide, this schlieren object can be considered as bi-dimensional, has negligible lateral boundary effects, and can be kept at a fixed temperature (140 °C). A first study of the hot air above the plate was carried out in terms of time averaged temperature values: once the steady-state condition was reached, the temperature above the plate was monitored with some thermocouples placed at different distances from the plate surface (see Figure 8.10). At the same time, BOS measurements were acquired.

The two cross-correlation and the integration algorithms previously introduced were used to extrapolate the temperature maps showed in Figure

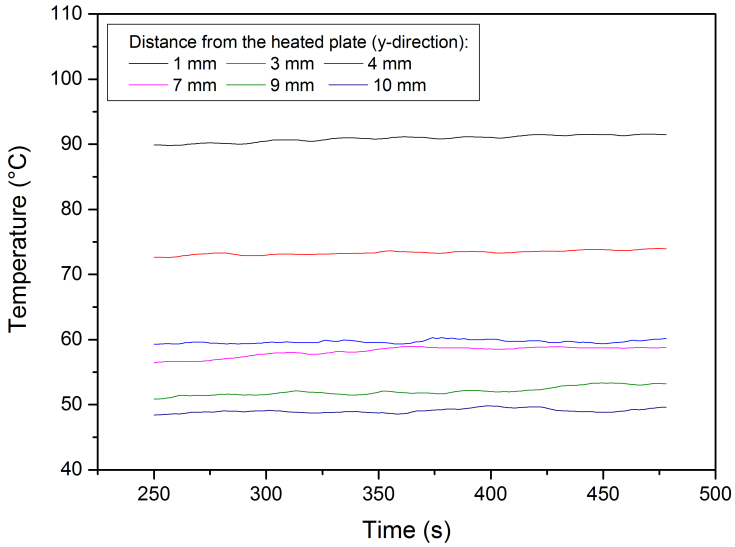

Figure 8.10: Thermocouple measures of temperature at different distances above the metal plate, in a steady condition.

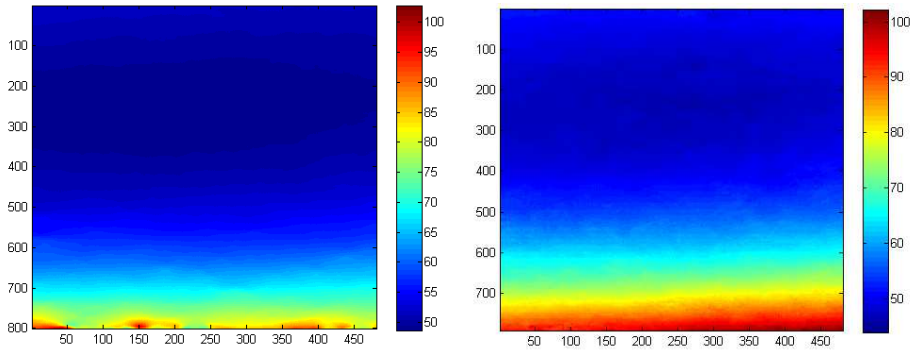

(a) Lucas-Kanade **(b)** Horn-Schunck

Figure 8.11: BOS temperature maps obtained using the two cross correlation algorithms.

8.11. From these maps the curves drawn in Figure 8.12 were determined, so that a comparison with the average temperature measured by means of thermocouples becomes possible. Thermocouple and BOS measures seem to agree within the uncertainty due to the experimental and computer processing procedures. On one side, thermocouples are not particularly suitable for measuring gas temperatures and the error associated to this diagnostics is higher than the $0.1°C$ uncertainty given in the datasheet, which is valid for contact measurements on a solid surface. For this reason, the error affecting

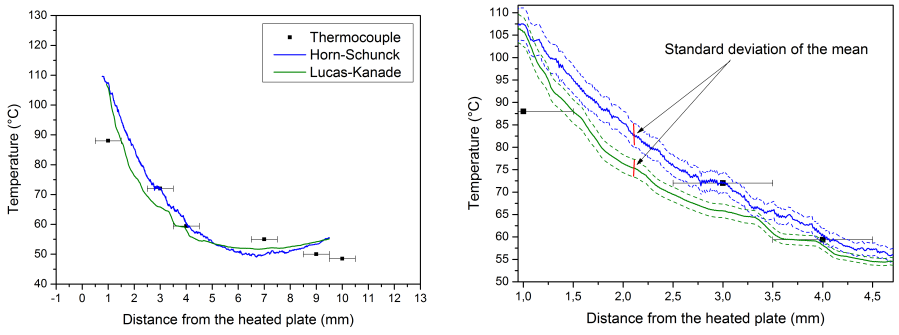

(a) **(b)**

Figure 8.12: (a): comparison between BOS measures obtained with the two cross correlation algorithms and thermocouple measurements. The uncertainty associated to thermocouples is relative to their positioning. Schlieren measures are averaged on several x positions: a focus on the standard deviation of the mean associated to those measures is given in graph (b).

Distance	Temperature	Statistical error
mm	°C	°C
1	88	0.2
3	72	0.1
4	59	0.02
7	55	0.2
9	50	0.1
10	49	0.04

Figure 8.13: Statistical values associated to thermocouples measurements at different distances from the heated plate in a steady state condition.

thermocouples data was evaluated as the standard deviation of the mean for the temperature values obtained, in the steady state condition. These values are summarized in Table 8.13. However, the highest error related to these measures is the one related to the vertical positioning of the thermocouples, because temperature gradients are very sharp near the heated surface. The distance between the thermocouples and the metal plate was measured with an uncertainty of 0.5 mm. Another aspect to be considered is the error associated to the Schlieren measurements: as already outlined, each step

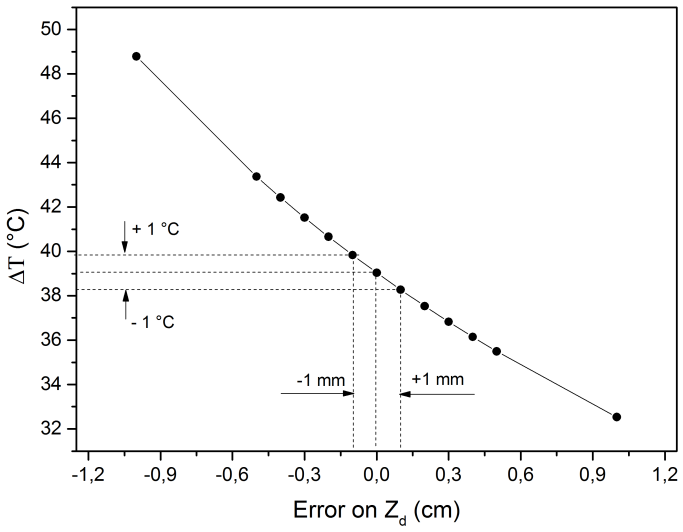

Figure 8.14: Evaluation of the error committed on the overall ΔT in function of the uncertainty in the Z_D determination.

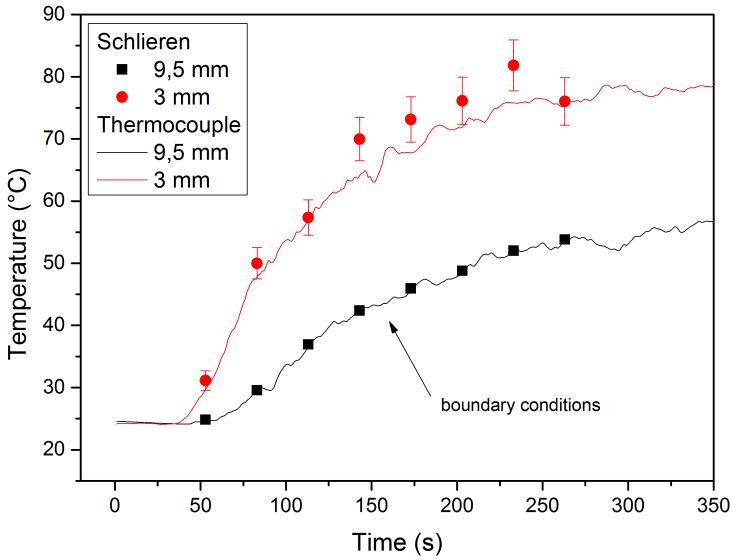

Figure 8.15: Comparison between BOS (scatter) and thermocouples (lines) measures of the hot plate heating.

of the BOS procedure contains intrinsic errors which affect the accuracy of the diagnostics. By considering that in Figure 8.15 error bars associated to Schlieren results are shown but not those relative to thermocouple positioning, we can conclude that the agreement is quite good for both the steady state and transient cases that have been studied. An influential uncertainty on the final result is the one connected to the positioning of the phase object (i.e. the measure of the Z_D distance), since it is not two-dimensional but has a spatial extension along the z-direction. Hence, it is worth to understand how an error in measuring Z_D reflects upon temperature determination. At this purpose, we considered different uncertainties included between ± 1 mm and ± 10 mm in the measure of Z_D and we found the results shown in Figure 8.14. We can reasonably think that our real uncertainty in measuring the placement of the heated plate is included between 1 and $2\,mm$, which means an error of $\pm 1°C$ on the determination of ΔT (corresponding to a 5% percentage error).

Time resolved measurements were then made during the heating of the

metal plate, before the steady state was reached. Two thermocouples monitored the temperature of air at 3 mm and 9.5 mm above the heated surface. At the same time, a sequence of Schlieren images of the same area were acquired. As pointed out in Figure 8.15, measures obtained with the thermocouple at 9.5 mm from the plate were used as boundary conditions for the BOS analysis. Schlieren data at 3 mm from the heated surface were compared with those taken by the thermocouple placed at the same distance.

Density gradient visualization At this point we verified that the visualization of a gas different from air is strictly connected to the degree of perturbation introduced into the system. More specifically, two different flows of Argon and Helium in air at $25\,°C$ were analysed (see Figure 8.16). The gas flow was

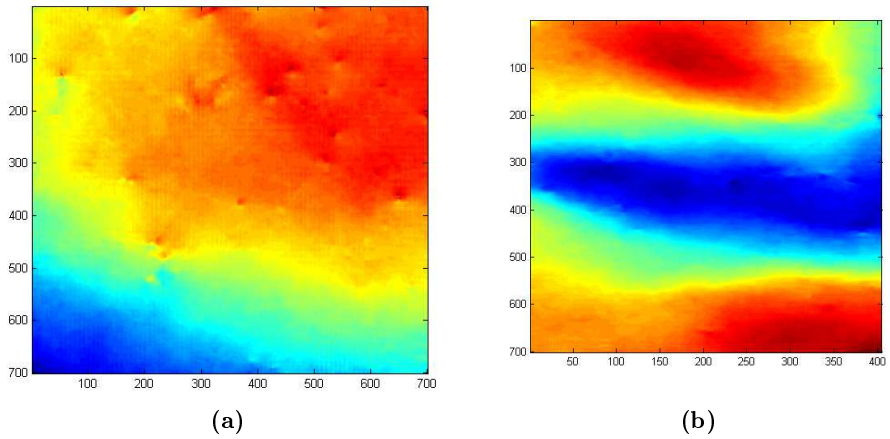

(a) **(b)**

Figure 8.16: Gas flows of Argon (a) and Helium (b) in quiescent air at 25°C.

released from a nozzle placed at the top-centre (a) and at the left-centre (b) area of the schlieren image, but while the Helium flow could be observed, in the Argon case no clear trend were detected. A quantitative explanation of these results can be described, since the index of refraction for noble gases at standard condition ($T_0 = 0$ °C, $p_0 = 1$ atm) for a wavelength of 633 nm is known:

$$n_{0,He} = 1.0000349,$$

$$n_{0,Ar} = 1.0002811.$$

To find the indexes of refraction at the desired temperature (T), the following equation can be used in the isobaric approximation:

$$n = 1 + (n_0 - 1)\frac{T_0}{T}, \tag{8.41}$$

and from this equation the values for Helium and Argon were obtained at a temperature $T = 25$ °C:

$$n_{He} = 1.000032,$$

$$n_{Ar} = 1.000257.$$

Once the refractive indexes are known, we can evaluate the order of magnitude of the gradients for the two noble gas flows:

$$\frac{\Delta n}{\Delta x} = \frac{n_{air} - n_{He,Ar}}{\Delta x}. \tag{8.42}$$

Remembering that

$$n_{air} = 1.0002671$$

at $25\,°C$ the resulting gradient is:

- Helium: $\frac{\Delta n}{\Delta x} \approx 2 \cdot 10^{-4}\, cm^{-1}$,
- Argon: $\frac{\Delta n}{\Delta x} \approx 9 \cdot 10^{-6}\, cm^{-1}$.

In both cases the nozzle was placed at a distance $Z_D = 1$ cm from the pattern and the integration length was taken as the nozzle diameter ($\Delta z = 0.5$ cm). The flow is considered axisymmetric so $\Delta x = \Delta z = 0.5$ cm. Remembering the considerations made in the section dedicated to preliminary calculations, the pixel shift associated to each case can be evaluated as

$$\Delta Y = 20 \cdot \frac{\Delta z}{Z_d}\frac{\Delta n}{\Delta x}, \tag{8.43}$$

obtaining the following values

- Helium: $\Delta Y \approx 2 \cdot 10^{-3}\, cm = 20\, \mu m$,
- Argon: $\Delta Y \approx 1 \cdot 10^{-4}\, cm = 1\, \mu m$.

These values explain the results showed in Figure 8.16: the flow of Helium causes a deflection around 2 pixel (which can be detected) while the Argon flow cannot be observed in the same operative conditions since the correspondent shifts are lower than 0.1 pixel. Moreover, this experiment confirms the predictions about the observable gradients made in Section 8.4, where the minimum detectable gradient was estimated to be of $\frac{\Delta n}{\Delta x} = 1 \cdot 10^{-5}\, cm^{-1}$. It is worth to notice that this comparison cannot be expressed in terms of density percentage variations, since in the preliminary calculations we deduced it from the relation:

$$\frac{\Delta n_{air}}{\Delta x} = K_{air} \frac{\Delta \rho_{air}}{\Delta x}, \tag{8.44}$$

while in presence of other gases, we must consider

$$\frac{\Delta n}{\Delta x} = \frac{n_{air} - n_i}{\Delta x} = \frac{K_{air}\rho_{air} - K_i \rho_i}{\Delta x}, \tag{8.45}$$

where the index i stands for the gas considered (in this case Helium or Argon) and is characterized by a specific Gladstone-Dale constant.

8.6 Application to Plasma Actuators

The BOS diagnostics implemented was finally applied to a plasma actuator device fed by an ac power supply. This choice was given by the need to have a deeper insight into the aerodynamic performance of plasma actuators and the parameters affecting flow control. A Schlieren-like technique is non invasive and gives instantaneous two-dimensional maps of the perturbation above the surface. This is a great advantage if compared with other punctual flow

diagnostics like the Pitot tube, which requires long sets of measurements to investigate a similar area and that in some circumstances can interfere with the discharge. Most of the flow control experiments found in literature [64, 65,215–217] that make use of refractive index based diagnostics are referred to ns-impulsed discharges, which induce strong pressure and temperature gradients during both the rising and dropping times of the applied voltage. These changes are visible in terms of shock waves and vortices, which are considered to be the mechanisms that allow the control of flow separation and other behaviours of an airflow passing by the discharge region. Few authors made use of shadowgraphy to obtain a fast imaging of the modifications of the surrounding medium caused by plasma propagation [65,218]. Interferometry is usually avoided, because of its lack of accuracy in detecting the sharp gradients involved in ns actuation processes. An example of interferometric measures of the shock wave generated by a unique nanosecond ramp is given in [216]. Most authors adopt Schlieren-like techniques to investigate the topology of thermal perturbations related to the actuation mechanism [215] and to make parametric studies of vortices [219] or shock waves [64,217] at different bias voltages and pulse repetition rates.

A few studies about the interaction of aerodynamic plasma actuators with the surrounding atmosphere were also carried out for ac power supplies [220–222]. In this type of actuators no strong pressure gradients are present but thermal effects can still be monitored and allow to visualize the induced airflow and to estimate its orientation. To favour the visualization of the electric wind effect, in [156] two vertical jets of helium were injected and their lateral deflection was analysed. A classical Schlieren technique was used by [162] to visualize the plasma boundary layer during the steady state regime, making a comparison between the resulting intensity profiles and the Pitot tube velocity measurements. The same authors also acquired Schlieren images during the discharge ignition phase and showed that vortex

phenomena can be also observed in plasma actuators fed by an ac voltage. Schlieren imaging was employed by [221] to characterize the propagation behaviour of vortices created by a plasma aerodynamic actuator array. Until now, no extensive literature has been found about neutral density changes in the induced flow: time resolved measurements of neutral air density near the electrodes were made by [222] using a laser deflection technique. No evidences of the application of a BOS schlieren technique on plasma actuators has been found during the development of the present work.

The configuration used in all the following experiments is shown in Figure 8.17: The electrodes are placed at the opposite sides of a rectangular 10 ×

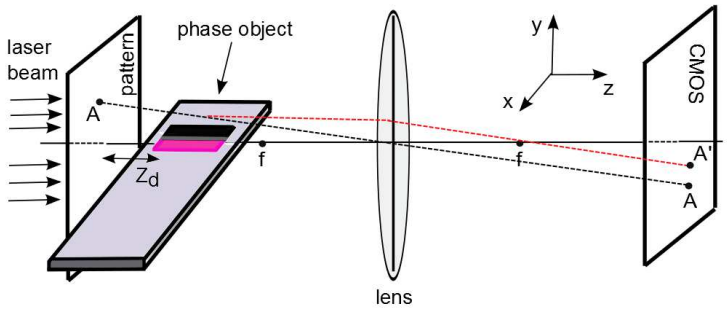

Figure 8.17: Scheme of the BOS configuration used to study the air above the plasma actuator.

15 cm dielectric panel (teflon, 1.5 mm thick), without overlap along the chordwise x-coordinate. The lower electrode (tinned copper adhesive tapes, 60 μm thick, 10 mm wide, 7 mm long) is grounded and buried by insulating adhesive tapes, whereas the upper electrode (tinned copper adhesive tapes, 60 μm thick, 5 mm wide - of which 3 mm are exposed and 2 mm are buried - 7 mm long) is glued onto the top of the dielectric panel and is connected through a HV cable to the tunable power generator of University of Milano-Bicocca. Our experiments were conducted at two different voltage amplitudes equal to 5.9 ± 0.1 kV and 7.1 ± 0.3 kV, with frequency changing from 43.72 ± 0.02 kHz to 42.68 ± 0.04 kHz.

Temperature and density changes In order to investigate the interaction between the discharge and the surrounding air in the boundary layer, we performed an optical scanning in the chordwise direction of the area above the actuator (y between 0.5 mm and 8 mm) for the two different voltage amplitudes, in quiescent flow conditions. We chosed the amplitudes so that the plasma discharge had different features [179]: in the $5.9\,kV$ configuration the plasma was about 3 mm long and appeared homogeneous, while in the 7.1 kV case streamers became visible and the discharge was 5 cm long. In the previous section we verified that density changes due to speed variations are not detectable with a schlieren technique, however we expected a rise in temperature of the moving air contained within the discharge volume, allowing the visualization of the induced wall jet [215, 219]. From these premises, we first expressed the perturbation above the actuator surface in terms of temperature changes. In Figure 8.18 the maps of the perturbation taken at different distances from the exposed electrode edge ($x = 0$ mm) were joined together. To do that we started from an image sufficiently upstream from the upper electrode and we imposed the boundary condition in the lowest left corner of that image (not shown here), corresponding to $x = -23$ mm and $z = 8$ mm in our coordinate system. The boundary condition of the other images was always imposed in the bottom left pixel and was chosen so that a good matching with the adjacent upper image was achieved. In this way consecutive images are consistent. For the images from 1 to 5 similar results were found by imposing the unperturbed index of refraction of air as boundary condition for each image, but at larger distances from the electrode edge this method failed, since the perturbed area exceeds the recorded image size in the y direction. This procedure was carried out for both the two voltage amplitudes: the reconstructed flow on the left side of Figure 8.18 is referred to the higher voltage, while the other corresponds to the lower one. At first sight, a comparison between the two experiments may appear consistent,

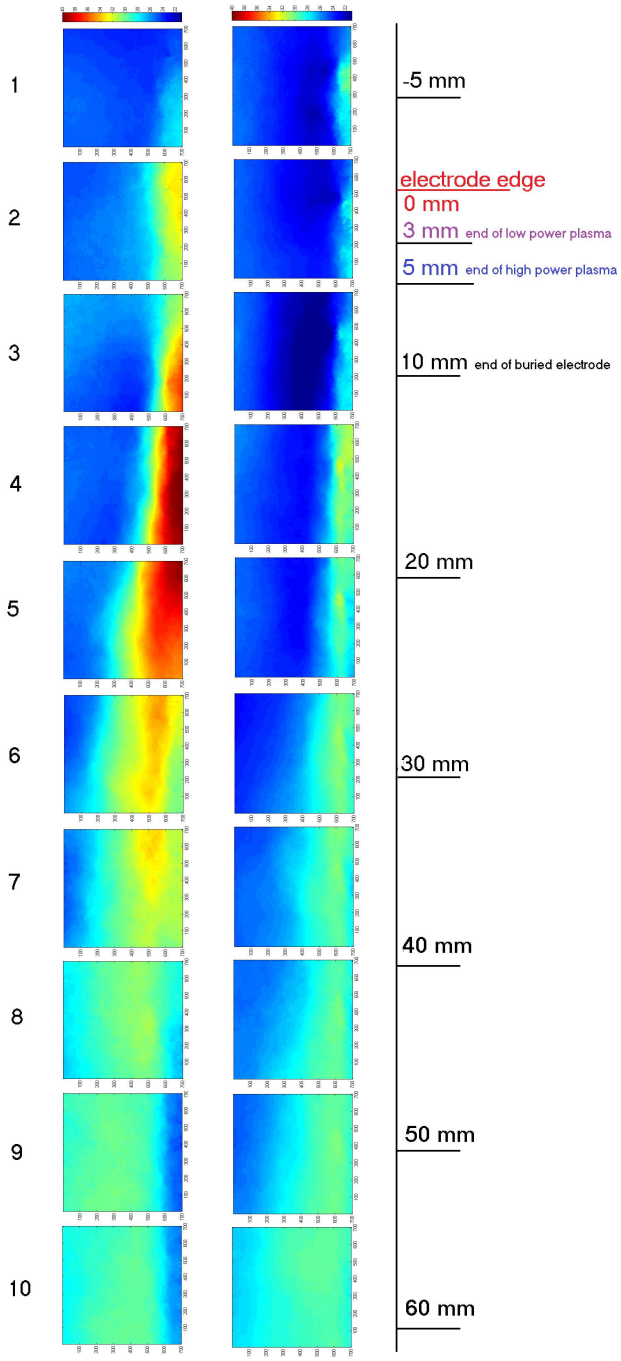

Figure 8.18: Temperature change in the chordwise x and in the y directions in presence of plasma. Images on the left and right sides are referred to the high and low adopted voltages, respectively. The colour map is the same for both cases, and ranges from 21 °C (blue) to 40 °C (red).

since the temperatures involved in the higher voltage case are much higher. However, taking a closer look to the maps, we can observe some effects that can't be explained in terms of mere temperature changes. In particular, the maximum temperature is reached after the end of the plasma discharge, and some areas have a temperature lower than the room one.

In order to understand if these phenomena are related to the development of the discharge, we observed more in detail the maps of the area above the upper electrode plasma region, comparing temperatures when the actuator is on (Figure 8.19) and some seconds after it has been turned off (Figure 8.20). In all the following temperature maps the unperturbed boundary condition was imposed in the upper left corner. In all the three areas the ΔT is higher when plasma is off: this trend can be easily observed also looking at the graphs in Figures 8.21 and 8.22, where data extracted from these temperature maps are compared for two different distances y

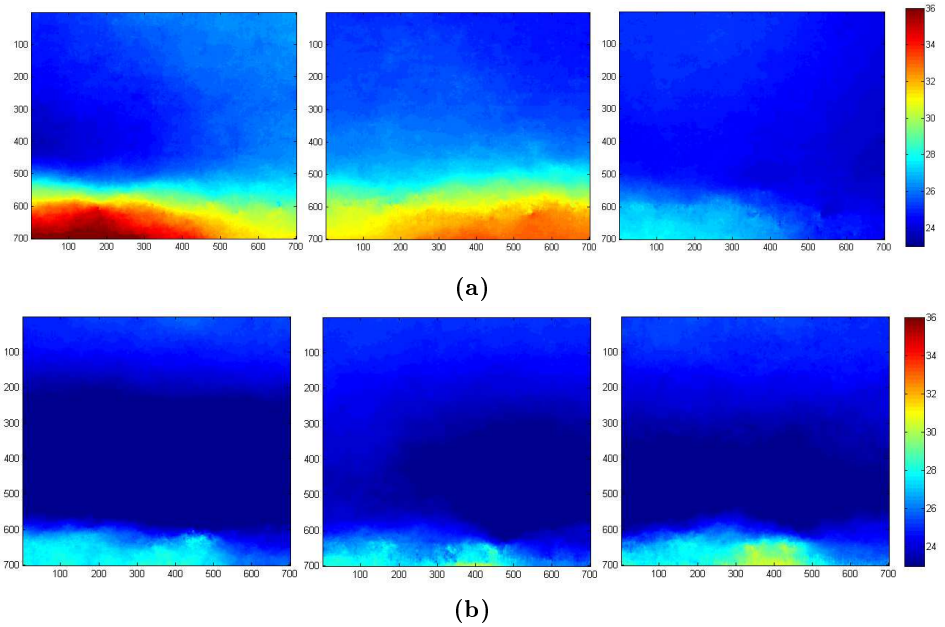

Figure 8.19: Temperature change above the electrodes, in presence of plasma, for the high voltage (a) and low voltage (b) cases. Image 3 (on the left), image 2 (in the middle) and image 1 (on the right) are shown.

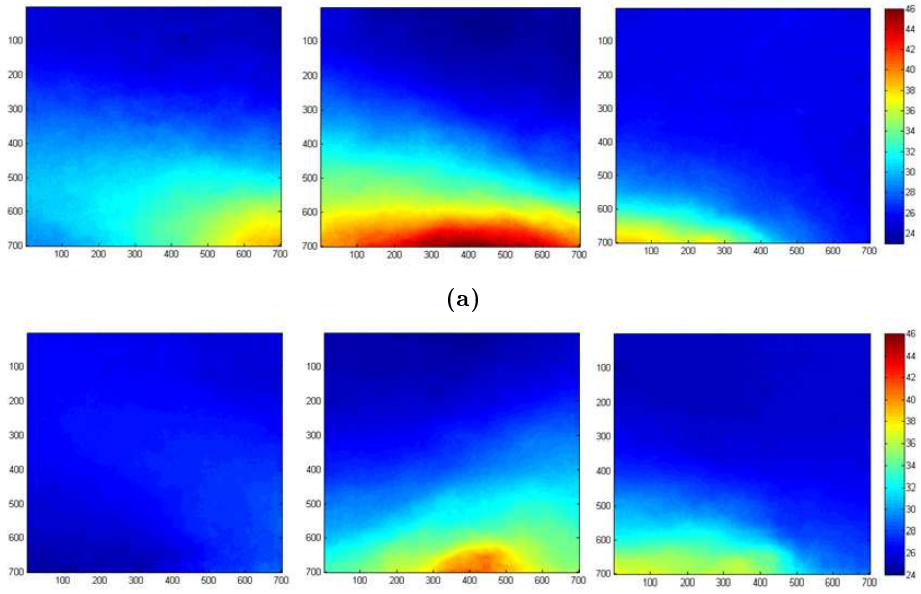

(a)

(b)

Figure 8.20: Temperature change above the electrodes, in absence of plasma, for the high voltage (a) and low voltage (b) cases. Image 3 (on the left), image 2 (in the middle) and image 1 (on the right) are shown.

above the actuator (respectively, at 0.5 mm and 7.5 mm). Far from the surface, where air was supposed to be unperturbed, the detected temperature is the same when plasma is on and when it has been turned off, whereas close to the actuator, a different trend becomes visible. In the high voltage case, the off-temperature gradually increases above the exposed electrode and moving towards the discharge, but then experiences a sharp change in correspondence of the discharge area and reaches its maximum of 52 °C at x between 1 and 2 mm. After the discharge zone, the off-temperature decreases gradually down to 30 °C at a chordwise distance of 12 mm from the electrode edge. On the contrary, the on-temperature remains approximately the same over the exposed electrode and the plasma discharge, while it starts to increase slightly only after the end of the discharge area. The latter behaviour has thus an opposite trend with respect to the off condition. The difference in the two temperatures is maximum above the plasma discharge

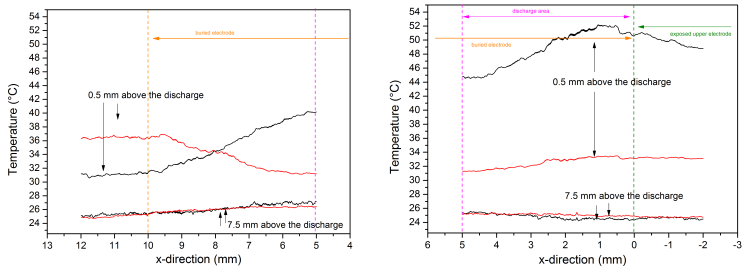

(a) (b)

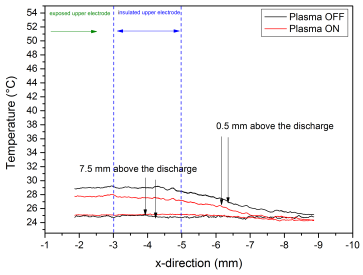

(c)

Figure 8.21: Temperature change above the electrodes (high voltage). Images number 3 (a), 2 (b), and 1 (c) are shown.

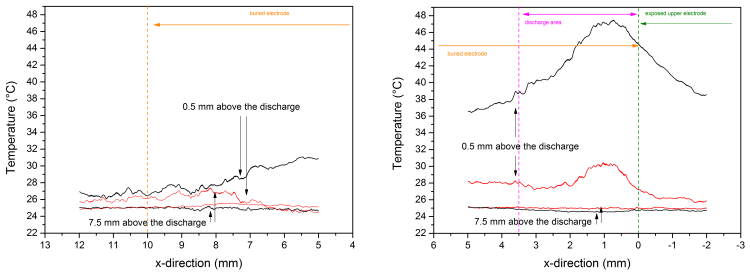

(a) (b)

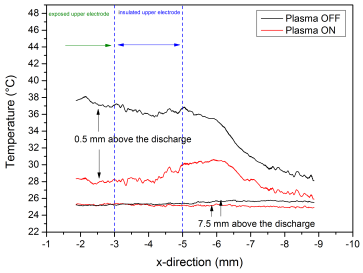

(c)

Figure 8.22: Temperature change above the electrodes (low voltage). Images number 3 (a), 2 (b), and 1 (c) are shown.

and reaches a value around $\Delta T \approx 20\,°C$.

In the low power case, the off-temperature has a trend similar to the one described above, reaching its highest value of 47 °C in 1 mm after the upper electrode edge and then decreasing to its initial value after 12 mm. The on-temperature keeps similar values along all the considered positions: it experiences a small increase at 1 mm, then a successive reduction after the discharge area and finally reaches the same value of the off-temperature. The highest temperature difference between off and on values is around $\Delta T \approx 15\,°C$.

From these curves, we must deduce that there is an other effect - overlapping the temperature one - which influences mostly the area above the electrodes and that appears when the actuator is turned on. In particular, since an increase in temperature means a density reduction, this effect should have the opposite result (i.e. tend to increase density above the electrodes). A possible explanation could be ozone production: dielectric barrier discharges in air are well known sources of ozone, allowing efficient oxygen dissociation by electron impact [223]. In some experiments found in literature on plasma actuators [223,224], it was observed that ozone concentration initially grows with the voltage amplitude: for a given electrode configuration, the reduced electric field increases with the magnitude of the voltage. Ionization is therefore more effective and the electron density is greater. This implies a higher oxygen atom density and therefore a higher ozone production [224]. However, authors in [223] also suggests to take into account that, at high operative temperatures, ozone may be thermally destructed. We had already demonstrated that our BOS analysis is sensible to the presence of some gases different from air, so we believe that the effect previously observed could be related to ozone production. In the present experiments the increase in density appears more intense in the low voltage case. This would mean that with the lower voltage ozone production has an effect on density

higher than the temperature one, while with the higher voltage temperature effects hang over chemical variations. However, a further investigation on ozone concentration and distribution above the actuator is needed. Future experiments with discharge in gases different from air (which don't produce ozone) should be carried out in order to get a better understanding of the phenomenon. Since we don't have a way to discriminate these two effects yet, it is more meaningful to express our measures in terms of percentage density changes with respect to the unperturbed condition of air at $25\,^{\circ}C$. A comparison between the situations at different voltages is shown in Figure 8.23. In these graphs the density percentage variations in the chordwise direction are shown for different distances above the surface. The most interesting trends are those at 8 and 0.5 mm above the dielectric surface, since all the others have an intermediate behaviour:

at a height of 8 mm, air seems to be unperturbed before $x = 40$ mm, where the density decreases up to 2% of its initial value;

at a height of 0.5 mm, density falls to a value of 2.5% lower than the unperturbed situation above the exposed electrode, then slightly increases between the electrode edge and the end of the plasma. Another decrease is observed after the end of plasma, and the minimum value of -5% is detected. After this point, density gradually rises up to $x = 40$ mm, where a more sharp growth happens (just in correspondence of the density reduction observed at 8 mm above the surface).

A possible interpretation of this behaviour is that before $x = 40$ mm the air at 8 mm above the actuator is unperturbed, while the density reduction observed at 0.5 mm between $x = 5$ mm and $x = 20$ mm can be ascribed to the induced wind that has been accelerated and heated in the discharge region. This induced flow propagates downstream away from the electrode edge and gradually cools down. The sharp change seen at $x = 40$ mm

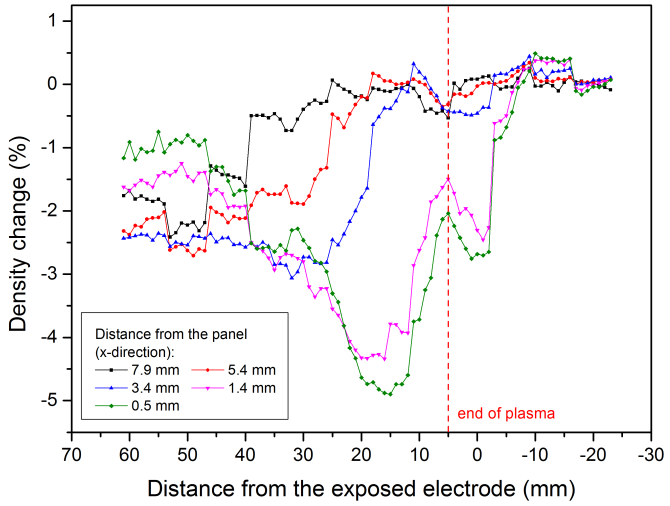

(a)

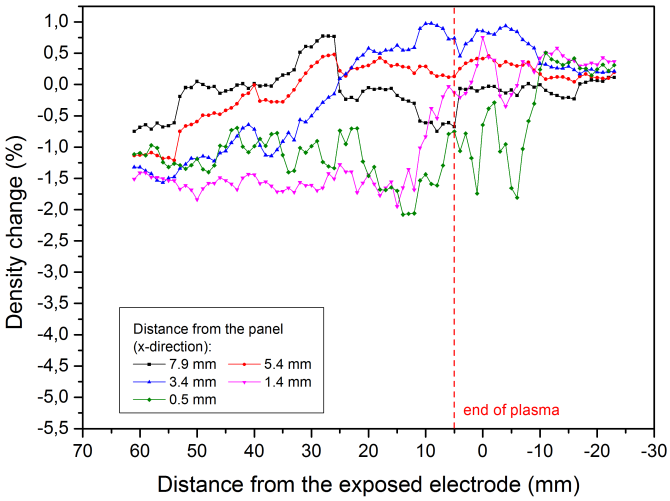

(b)

Figure 8.23: Density changes in the chordwise direction in presence of plasma for the high voltage (a) and low voltsge (b).

presumably reveals that a flow separation from the surface is happening in that point: the density value at 8 mm for $x > 40$ mm is in fact comparable to the one at 0.5 mm before separation. When the hot airflow has a detachment from the surface, the air around the electric wind (which is cooler) tends to insinuate between the induced airflow and the dielectric surface. This phenomenon can be easily observed in the left map of Figure 8.18: a hot

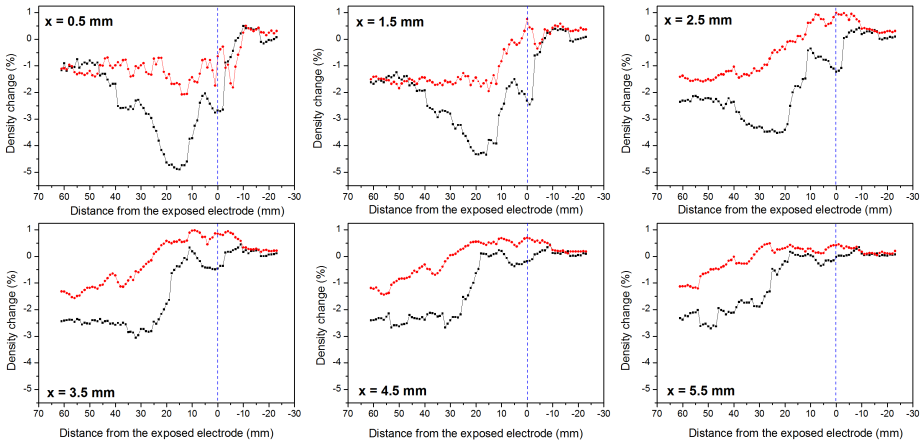

Figure 8.24: Density change in the chordwise direction at different distances above the dielectric layer. The red line stays for the low voltage measurements, while the black line represents the high voltage data.

airflow is generated in the plasma discharge area and propagates downstream, broadening in the y-direction. At a chordwise distance of $x = 40$ mm from the upper electrode edge the flow detachment described before is clearly visible and the flux appears quite uniform between $y = 1$ mm and $y = 8$ mm above the surface.

As we can see by comparing Figure 8.19a and Figure 8.20a, the maximum heating of 52 °C is reached at $x \approx 1 - 2$ mm from the electrode edge and seems to happen when plasma is turned off. Actually, we expect that during the discharge the density would reach its minimum value at about $x \approx 1 - 2$ mm and that it would be equal to -8% its unperturbed value or less, because this is the value corresponding to 52 °C. In conclusion, we think that between $x = -5$ mm and $x = 15$ mm our density measures at 0.5 mm above the dielectric surface are influenced from the physical factors previously discussed and presumably connected to ozone production or more generally to the composition of the air above the electrodes.

In the low voltage case, only smooth changes are observed. A possible explanation for these trends is that between $x = -5$ mm and $x = 10$ mm the changes in air composition may dominate above temperature effects, since

a density reduction becomes visible only after $x = 5$ mm in the chordwise direction. Finally, to have a better insight into the different behaviours for the two discharge powers, in Figure 8.24 a comparison between them is shown for different distances above the actuator surface.

Pitot measurements It was already told and demonstrated that the implemented optical diagnostics cannot reveal velocity variations. However, an interesting issue to be investigated is related the comparison between electric wind speed changes and density variations in the boundary layer. For this purpose, some measurements with the Pitot tube were made in order to understand if the thermal perturbed area and the dynamic boundary layer have the same extension in the x and y direction. A confirm of such similar behaviour would mean that BOS measurements contain further useful information for the investigation of the induced flow. A comparison between the measures acquired with the Schlieren method and the Pitot diagnostics was made for the high voltage configuration, where density variations are more

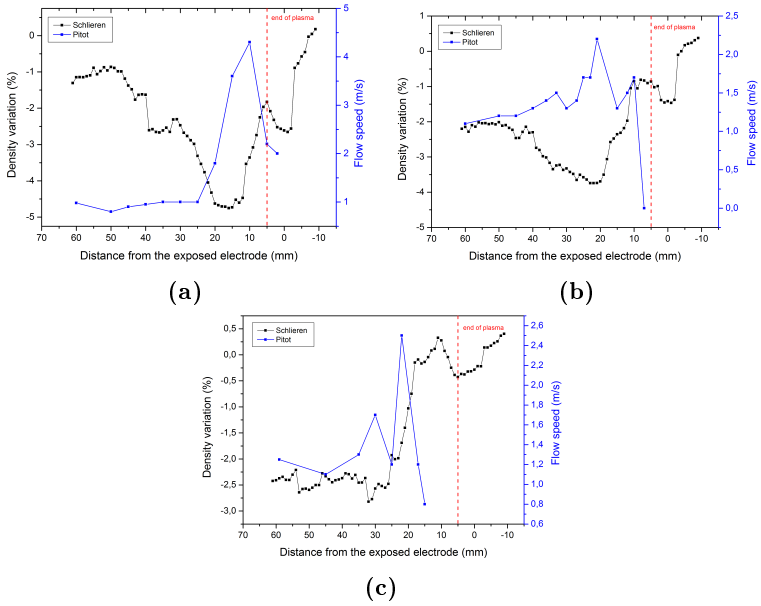

Figure 8.25: Comparison between Pitot and Schlieren measurements for three y distances above the actuator surface: 0.8 mm (a), 2,2 mm (b), 4.0 mm (c).

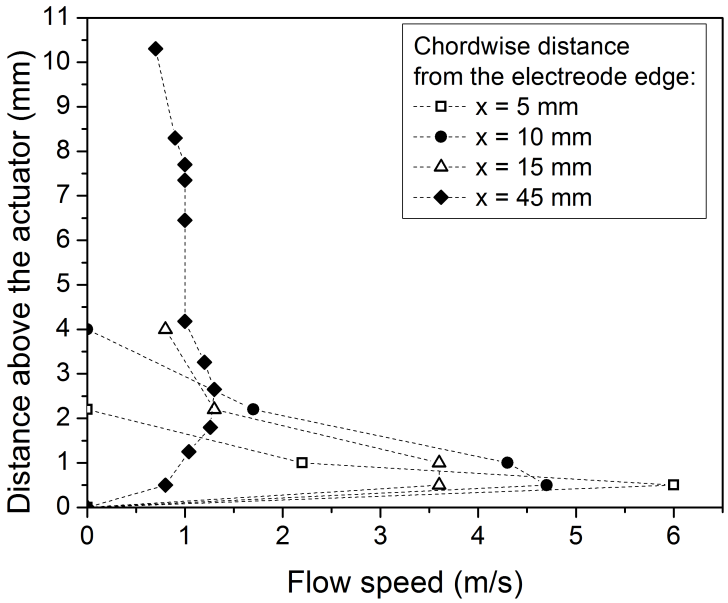

Figure 8.26: Vertical profiles of the flow speed relative to four distances from the upper electrode edge.

visible. The three graphs in Figure 8.25 show how density and speed vary with the distance from the electrode edge for three different heights above the dielectric surface. From the data acquired, the area interested by the major changes seems to be the same for both the two measured quantities. In the first millimetres after the end of the exposed electrode, Pitot values are non-zero only for $y = 0.8$ mm, which is consistent with the confinement of the induced flow near the dielectric surface. After some centimetres from the edge of the upper electrode, speed is lower than 2 m/s, but the velocity field is more uniform along the x and y directions. The same trend is also visible in Figure 8.26, where four vertical profiles of the flow speed are shown for different chordwise positions. At 11 mm from the electrode edge, an homogeneity in y similar to the Schlieren results is clearly observable, while getting closer to the discharge the flow is more confined in proximity of the dielectric surface.

In conclusion, although it doesn't have the sensitivity required to observe

speed variations of few m/s, our Schlieren technique allows the visualization of the area perturbed by the induced flow.

Vortices creation and time evolution of the boundary layer Vortices creation is a peculiar feature of plasma actuators which has been visualized by means of different techniques like smoke flow visualization [225], PIV [226] and schlieren methods [162, 219]. Numerical simulations of this phenomenon have also been carried out [219,227]. Experiments on actuators in quiescent air showed that, during the initiation phase, the interaction between the air accelerated by the discharge and the surrounding environment results in the formation of a starting vortex [225]. This vortex rolls up and convects along the wall, leading to the formation of a laminar wall jet [228]. When the vortex moves downstream, away from the electrode edge, it increases in size and weakens until extinguishing. This vortex is observable by means of Schlieren techniques because it involves flow that has been heated by the discharge. Other eventual swirling structures that don't swallow airflows at different temperature cannot be detected with these diagnostics [219].

With BOS, images of vortices were taken with a time interval of 20 ms and an exposure time of 0.052 ms. Two examples of the temporal evolution and stabilization of the induced airflow at two different distances from the electrode edge (respectively $5 \div 12$ mm and $12 \div 19$ mm) are shown in Figures 8.27 and 8.28. The voltage used is of 5.9 kV. All images are expressed in the same scale ($\Delta T = 8$ °C): the vortex observed in Figure 8.27 revels a $\Delta T = 4$ °C which increases up to $\Delta T = 8$ °C for the wall jet after about 40 ms. In Figure 8.28 ΔT varies from 2 °C in the vortex to 8 °C of the stationary jet. In literature it has been estimated that the vortex speed is of the order of 1 m/s and that the steady state condition is reached in less than 100 ms from ignition [162]. Therefore, we expect the vortex to be shifted of 2 cm away from its position after 20 ms and that's why we clearly see

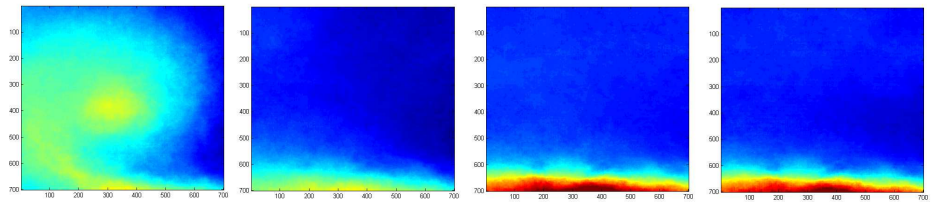

Figure 8.27: Vortex formation and stabilization of the induced flow at a distance between 5 and 12 mm from the electrode edge. Images are expressed in the same scale ($\Delta T = 8$ °C) and refer to different temporal moments (starting from left and moving to right).

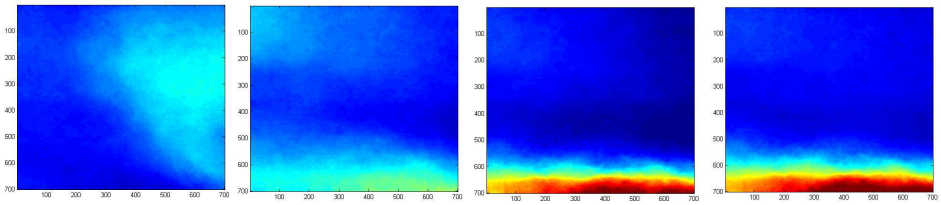

Figure 8.28: Vortex formation and stabilization of the induced flow at a distance between 12 and 19 mm from the electrode edge. Images are expressed in the same scale ($\Delta T = 8$ °C) and refer to different temporal moments (starting from left and moving to right).

the vortex structure in the first image. The achievement of the steady state condition seems to be established within 40 ms from the vortex passage.

In Figure 8.29 images of vortices acquired (at different moments) in adjacent positions (between 5 mm and 33 mm from the electrode edge) and at the same voltage (5.9 kV) are shown: near the electrode the vortex can be photographed entirely thanks to its small dimension, while moving away from the discharge, the vortex widens and only a small portion of it can be observed.

Finally, four vortices observed when the actuator is fed by different voltages are shown in Figure 8.30: at 5.8 kV the vortex has a chordwise dimension lower than 7 mm and can thus be detected in its entire shape, but at higher powers its size increases and at voltages over 6.6 kV we can observe only its lower edge.

Some authors [229] describe the physics of vortex creation and development

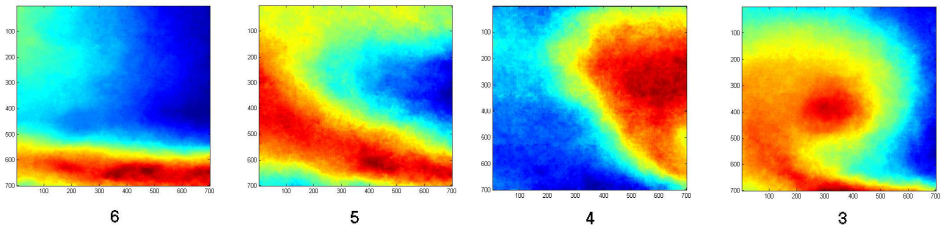

Figure 8.29: Vortices observed between 5 mm and 33 mm from the electrode edge. All images are expressed in their automatic scale. The number of images are referred to Figure 8.18

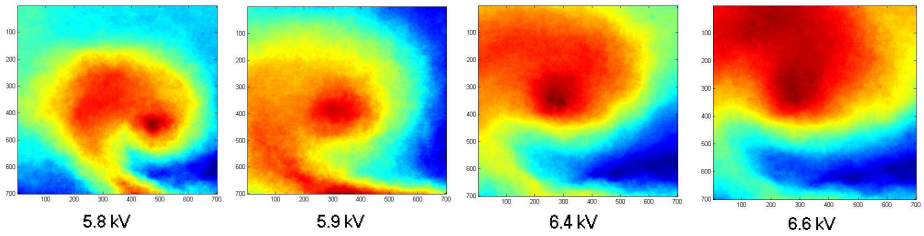

Figure 8.30: Vortices observed between 5 mm and 12 mm from the electrode edge at four different voltages. All images are expressed in their automatic scale.

by means of convective velocity of the vortex core (evaluated from vortex core trajectory), as well as the vortex equivalent radius and circulation. In the present study, such a deep analysis on the vortex dynamics cannot be developed because of the fast evolution of the phenomena and of the small area that can be investigated by means of the BOS system used. With a future improving of the experimental equipment, we could follow the vortex evolution in space and time, and parametric studies of the phenomenon in relation to the discharge properties will become possible. In this way, the Schlieren technique could be used to determine the vortex propagation speed, i.e. its convective velocity, which is expected to be similar to that of the induced flow near the discharge.

CHAPTER 9

Conclusions

This Ph.D. thesis deals with the characterization of Surface Dielectric Barrier Discharges (SDBDs) in an asymmetrical configuration in which one electrode is buried into an insulating material and the other one is exposed to air, so that plasma is created in correspondence of just one side of the dielectric barrier that separates the electrodes. This configuration is particularly suitable for aerodynamics, since a weakly ionized plasma is created in proximity of the insulating barrier, and can effectively influence the local properties of the boundary layer associated to an external flow. When plasma is generated in quiescent air conditions, an airflow induced by the discharge is observed, which is usually called electric wind, ionic wind, induced airflow, or wall jet.

Interesting results dealing with flow control applications such as lift enhancement, drag reduction and stall delay raised the attention of the worldwide aerospace community for plasma actuators, which are appealing because of their fast temporal response and the absence of moving mechanical parts. However, the electric wind they produce has velocities generally equal to a few metres per second and this limits the present usefulness of these devices to low speed applications. Moreover, despite the large number of publications on this topic, there still remain some very basic questions regarding performance and efficiency of these actuators, as well as about the discharge mechanisms and peculiarities. This thesis comes from a scientific collaboration between the Centre of Excellence PlasmaPrometeo of University of Milano-Bicocca and the Aerodynamics and Wind Tunnel Department of the aerospace company Alenia Aermacchi, and it is thus motivated by the fact that new studies focusing on plasma properties and dynamics are required.

During these years I have studied the properties of these discharges by means of electrical and optical diagnostics. With some of them a temporal resolution high enough for studying several characteristics of plasma has been achieved. This is important because these strokes are made up of plasma microdischarges that manifest as series of current and light pulses, lasting tens of nanoseconds and a few nanoseconds respectively. Rogowski coils, photomultiplier tubes and capacitive probes are often adopted when dealing with plasma actuators. In this thesis, I have tried to exploit their potentialities in order to get new insights about these discharges.

Concerning capacitive probes, they are usually used in combination with high-voltage probes for drawing the Lissajous figures, which are used for calculating the energy consumed by plasma actuators in the course of a sine voltage cycle and for detecting how much the DBD system capacitance changes when plasma is created and the air gap thus becomes conductive. In this work I have proposed to combine capacitive and Rogowski probes for

the system capacitance evaluation, so that the when analysing the Lissajous figure shape one can separate the effect of charge brought on the dielectric barrier (by current microdischarges) from that associated to the capacitance value.

Statistical analysis of current and light microdischarges (recorded with Rogowski coils and photmultiplier tubes) have been done in order to carry out a detailed investigation of the properties of these events and of their evolution in space and time in the course of the two voltage half-cycles, which are called Backward Stroke (BD) and Forward Stroke (FD). It has been pointed out that there are several analogies between the BD and FD, but that not all plasma properties are identical for the two semi-cycles, because of the asymmetrical configuration adopted. A group of breakdown microdischarges was observed at the beginning of each backward discharge, probably initiated by free electrons left on the dielectric surface during the previous forward half-cycle.

These investigations let think that light and current signals give insights about different microdischarge properties. Light is presumably ascribable to electrons that excite nitrogen immediately after the creation of a microdischarge. In contrast, the current signal is due to the movement of charges into the plasma channel and thus reflects the microdischarge temporal evolution, rather than its formation. The propagation of an ionizing wave has been observed during the backward stroke, by recording the light emitted at different positions of the discharge. From these measurements the velocity of propagation has been calculated.

Since the main mechanism responsible for the generation of the electric wind is believed to be momentum transfer from the plasma charged particles to the surrounding fluid by particle-particle collisions, in the following experiments I have focused mainly on the electrical properties of plasma microdicharges, with the aim of better understanding which plasma charac-

teristics are responsible for the induced airflow generation.

By means of a Pitot probe, local measurements of the electric wind have been done. At first the speed of the induced wind increases with the voltage amplitude, but later this growth flattens, if panels with thickness equal to few millimetres are adopted as dielectric barriers. It has been noticed that this saturation of the electric wind speed is accompanied by a change of the appearance of the plasma, because a pattern of filaments visible with the unaided eye becomes evident. The light emitted by these filaments was found to be ascribable to the forward stroke. Results showed that the velocity is higher in correspondence of these plasma filaments, but that saturation occurs as well.

Three groups of microdischarges have been identified, depending on the temporal duration of the current pulses (that I have called Gruop S, Group M and Group L). The contributions of these categories of microdischarges to the total charge of the backward and forward strokes was analysed for three dielectric panels with different thickness, such that the saturation of the induced airflow velocity was visible for only the thinnest one. Results let think that these three groups don't contribute equally to the electric wind generation. A possible explanation for our observations is that a push-push mechanism is attributable to Group S, meaning that the backward and forward strokes tend to energize the surrounding air in the same direction. On the contrary, a push-pull process could be associated to Group M, so that the backward microdishcarges of this category tend to push the air towards the buried electrode, whereas the forward microdischarges pull it towards the exposed one.

Eventually, I proposed to implement the Background Oriented Schlieren (BOS) technique for the visualization and characterization of the airflow induced by the discharge, and thus for future investigations concerning the interaction between plasma and background air. The potentialities of this

technique have been evaluated in relation to the specifics of the available scientific equipment. The technique has then been proved to be able to visualize density changes induced by plasma. A spatial characterization of the air near the discharge was made in stationary wall jet conditions as well as in the transient period following the discharge ignition when a starting vortex is generated.

Bibliography

[1] A. Bogaerts, E. Neyts, R. Gijbels, and J. van der Mullen, "Gas discharge plasmas and their applications", *Spectrochimica Acta Part B*, vol. 57, pp. 609-658, 2002.

[2] M. Moreau, N. Orange, and M.G.J. Feuilloley, "Non-thermal plasma technologies: New tools for bio-decontamination", *Biotechnology Advances*, vol. 26, pp. 610-617, 2008.

[3] V. Nehra, A. Kumar, and H.K. Dwivedi, "Atmospheric non-thermal plasma sources", *International Journal of Engineering*, vol. 2, issue 1, pp. 53-68, 2008.

[4] K. Urashima and J-S. Chang, "Removal of volatile organic compounds from air strams and industrial flue gases by non-thermal plasma technology", *IEEE Transactions on Dielectrics and Electrical Insulation*, vol. 7, no. 5, pp. 602-614, 2000.

[5] A. Fridman, A. Chirokov, and A. Gutsol, "Non-thermal atmospheric pressure discharges", *Journal of Physics D: Applied Physics*, vol. 38, pp. R1-R24, 2005.

[6] G. Fridman, A.D. Brooks, M. Balasubramanian, A. Fridman, A. Gustol, V.N. Vasilets, H.Ayan, and G. Friedman "Comparison of direct and indirect effects of non-thermal atmospheric-pressure plasma on bacteria", *Plasma Processes and Polymers*, vol. 4, pp. 370-375, 2007.

[7] R. Foest, E. Kindel, A. Ohl, M. Stieber, and K-D. Weltmann, "Non-thermal atmospheric pressure discharges for surface modification", *Plasma Physics and Controlled Fusion*, vol. 47, pp. B525-B536, 2005.

[8] U. Kogelschatz, "Dielectric barrier discharges: their history, discharge physics, and industrial applications", *Plasma Chemistry and Plasma Processing*, vol. 23, no. 1, pp. 1-46, 2003.

[9] A.P. Napartovich, "Overview of atmospheric pressure discharges producing nonthermal plasma", *Plasma and Polymers*, vol. 6, issue 1, pp. 1-14, 2001.

[10] V.I. Kolobov, "Advances in electron kinetics and theory of gas discharges", *Physics of Plasmas*, vol. 20, no. 101610-46, pp. 1-14, 2013.

[11] N.St.J. Braithwaite, "Introduction to gas discharges", *Plasma Sources Science and Technology*, vol. 9, pp. 517-527, 2000.

[12] A. Piel, *Plasma physics: an introduction to laboratory, space, and fusion plasmas*, Springer, 2010, ISBN: 978-3-642-10490-9.

[13] Y.P. Raizer, *Gas discharge physics*, Springer-Verlag Berlin Heidelberg, 1991, ISBN: 3-540-19462-2.

[14] R. Morrow, "Streamer propagation in air", *Journal of Physics D: Applied Physics*, vol. 30, pp. 614-627, 1997.

[15] R.N. Varney, "Drift velocity of ions in oxygen, nitrogen, and carbon monoxide", *Physical Review*, vol. 89, no. 4, pp. 708-711, 1953.

[16] L.E. Kline and J. G. Siambis, "Computer simulation of electrica breakdown in gases; avalanche and streamer formation", *Physical Review A*, vol. 5, no. 2, pp. 794-805, 1972.

[17] L.B. Loeb and J.M. Meek, "The mechanism of spark discharge in air at atmospheric pressure. I", *Journal of Applied Physics*, vol. 11, pp. 438-447, 1940.

[18] L.B. Loeb and A.F. Kip, "Electrical discharges in air at atmospheric pressure: the nature of the positive and negative point-to-plane coronas and the mechanism of spark propagation", *Journal of Applied Physics*, vol. 10, pp. 142-460, 1939.

[19] J.M. Meek, "A theory of spark discharge", *Physical Review*, vol. 57, pp. 722-728, 1940.

[20] U. Kogelschatz, B. Eliasson, and W. Egli, "Dielectric barrier discharges. principles and applications", *Journal de Physique IV*, vol. 7, no. C4, pp. 47-66, 1997.

[21] B. Eliasson, and U. Kogelschatz, "Modeling and applications of silent discharge plasmas", *IEEE Transactions on Plasma Science*, vol. 19, no. 2, pp. 309-323, 1991.

[22] I. Biganzoli, R. Barni and C. Riccardi, "Temporal evolution of a surface dielectric barrier discharge for different groups of plasma microdischarges", *Journal of Physics D: Applied Physics*, vol. 46, issue. 2, pp. 025201 1-11, 2013.

[23] B. Eliasson, M- Hirth, and U. Kogelschatz, "Ozone synthesis from oxygen in dilectric barrier discharges", *Journal of Physics D: Applied Physics*, vol. 20, pp. 1421-1437, 1987.

[24] B. Eliasson and U. Kogelschatz, "Nonequilibrium volume plasma chemical processing", *IEEE Transactions on Plasma Science*, vol. 19, no. 6, pp. 1063-1077, 1991.

[25] S. Meiners, J.G.H. Salge, E. Prinz, and F. Főrster, "Surface modification of polymer materials by transient gas discharges at atmospheric pressure", *Surface and Coatings Technology*, vol. 98, pp. 1121-1127, 1998.

[26] R. Siliprandi *Atmospheric pressure plasmas for surface modification*, PhD Thesis, Università degli Studi di Milano-Bicocca, 2007.

[27] R. Hackam and H. Akiyama, "Air pollution control by electrical discharges", *IEEE Transactions on Dielectrics and Electrical Insultaion*, vol. 7, no. 5, pp. 654-683, 2000.

[28] M.G. Kong, G. Kroesen, G. Morfill, T. Nosenko, T. Shimizu, J. van Dijk, and J.L. Zimmermann, "Plasma medicine: an introductory review", *New Journal of Physics*, vol. 11, 115012, pp. 1-35, 2009.

[29] K.D. Weltmann, E. Kindel, T. von Woedtke, M. Hähnel, M. Stieber, and R. Brandenburg, "Atmospheric pressure plasma sources: prospective tools for plasma medicine", *Pure and Applied Chemistry*, vol. 82, no. 6, pp. 1223-1237, 2010.

[30] A. Starikovskiy and N. Aleksandrov, "Plasma-assisted ignition and combustion", *Progress in Energy and Combustion Science*, vol. 39, pp. 61-110, 2013.

[31] E. Moreau, "Airflow control by non-thermal plasma actuators", *Journal of Physics D: Applied Physics*, vol. 40, pp. 605-636, 2007.

[32] T.C. Corke, C.L. Enloe, and S.P. Wilkinson, "Dielectric barrier discharge plasma actuators for flow control", *Annual Review of Fluid Mechanics*, vol. 42, pp. 505-529, 2010.

[33] V.I. Gibalov and G.J. Pietsch, "The development of dielectric barrier discharges", *Journal of Physics D: Applied Physics*, vol. 33, pp. 2618-2636, 2000.

[34] U. Kogelschatz, "Filamentary, patterned and diffuse barrier discharges", *IEEE Transactions on Plasma Science*, vol. 30, no. 4, pp. 1400-1408, 2002.

[35] S. Műller, R-J. Zahn, J. Grundmann, "Extraction of ions from dielectric barrier discharge configurations", *Plasma Processes and Polymers*, vol. 4, pp. S1004-S1008, 2007.

[36] R. Bartnikas, "Note on discharges in helium under a.c. conditions", *British Journal of Applied Physics*, vol. 1, pp. 659-661, 1968.

[37] S. Kanazawa, M. Kogoma, T. Moriwaki, and S. Okazaki, "Stable glow plasma at atmospheric pressure", *Journal of Physics D: Applied Physics*, vol. 21, pp. 838-840, 1988.

[38] S. Okazaki, M. Kogoma, M. Uehara, and Y. Kimura, "Appearence of stable glow discharge in air, oxygen and nitrogen at atmospheric pressure using a 50 Hz source", *Journal of Physics D: Applied Physics*, vol. 26, pp. 889-892, 1993.

[39] F. Massines, N. Gherardi, N. Naudé, and P. Ségur, "Glow and Townsend dielectric barrier discharge in various atmosphere", *Plasma Physics and Controlled Fusion*, vol. 47, pp. B577-B588, 2005.

[40] M.J. Druyvesteyn, and F.M. Penning, "The mechanism of electrical discharges in gases of low pressure", *Reviews of Modern Physics*, vol. 12, no. 2, pp. 87-176, 1940.

[41] N. Gherardi, G. Gouda, E. Gat, A. Ricard, and F. Massines, "Transition from glow silent discharge to micro-discharges in nitrogen gas", *Plasma Sources Science and Technology*, vol. 9, pp. 340-346, 2000.

[42] K.V. Kozlov, R. Brandenburg, H-E. Wagner, A.M. Morozov and P. Michel, "Investigation of the filamentary and diffuse mode of barrier discharges in N_2/O_2 mixtures at atmospheric pressure by cross-correlation spectroscopy", *Journal of Physics D: Applied Physics*, vol. 38, pp. 518-529, 2005.

[43] Y.B. Golubovskii, V.A. Maiorov, J. Behnke, and J.F.Behnke "Influence of interaction between charged particles and dielectric surface over a homogeneous barrier discharge in nitrogen", *Journal of Physics D: Applied Physics*, vol. 35, pp. 751-761, 2002.

[44] A. Meiners, M. Leck, and B. Abel, "Multiple parameter optimization and spectroscopic characterization of a dielectric barrier discharge in N_2", *Plasma Sources Science and Technology*, vol. 18, 045015, pp. 1-10, 2009.

[45] K.V. Kozlov, H-E. Wagner, R. Brandenburg and P. Michel, "Spatio-temporally resolved spectroscopic diagnostics of the barrier discharge in air at atmospheric pressure", *Journal of Physics D: Applied Physics*, vol. 34, pp. 3164-3176, 2001.

[46] A. Kossyi, A.Y. Kostinsky, A.A. Matveyev, and V.P. Silakov, "Kinetic scheme of the non-equilibrium discharge in nitrogen-oxygen mixtures", *Plasma Sources Science and Technology*, vol. 1, pp. 207-220, 1992.

[47] T. Hoder, R. Brandenburg, R. Basner, K-D. Weltmann, K.V. Kozlov and H-E. Wagner, "A comparative study of three different types of barrier discharges in air at atmospheric pressure by cross-correlation spectroscopy", *Journal of Physics D: Applied Physics*, vol. 43, 124009, pp. 1-8, 2010.

[48] Y.V. Yurgelenas and H-E. Wagner, "A computational model of a barrier discharge in air at atmospheric pressure: the role of residual surface charges in microdischarge formation", *Journal of Physics D: Applied Physics*, vol. 39, pp. 4031-4043, 2006.

[49] H. Grosch, T. Hoder, K-D. Weltmann, and R. Brandenburg, "Spatio-temporal development of microdischarges in a surface barrier discharge arrangement in air at atmospheric pressure", *The European Physical Journal D*, vol. 60, pp. 547-553, 2010.

[50] L. Niemeyer, "A generalized approach to partial discharge modeling", *IEEE Transactions on Dielectrics and Electrical Insulation*, vol. 2, no. 4, pp. 510-528, 1995.

[51] J.P. Boeuf, Y. Lagmich, and L.C. Pitchford, "Contribution of positive and negative ions to the electrohydrodynamic force in a dielectric barrier discharge plasma actuator operating in air", *Journal of Applied Physics*, vol. 106, 023115, pp. 1-9, 2009.

[52] R. Brandenburg, H. Grosch, T. Hoder, and K-D. Weltmann, "Phase resolved cross-correlation spectroscopy on surface barrier discharges in air at atmospheric pressure", *The European Physical Journal - Applied Physics*, vol. 55, issue 1, 13813, pp. 1-6, 2011.

[53] M. Gad-el-Hak, "Flow control: passive, active and reactive flow management", Cambridge University Press, 2000.

[54] J.D. Anderson, "Fundamentals of aerodynamics", *The European Physical Journal - Applied Physics*, vol. 55, issue 1, 13813, pp. 1-6, 2011.

[55] L.N. Cattafesta and M. Sheplak, "Actuators for active flow control", *Annual Review of Fluid Mechanics*, vol. 43, pp. 247-272, 2011.

[56] A. Glezer and M. Amitay, "Synthetic jets", *Annual Review of Fluid Mechanics*, vol. 34, pp. 503-529, 2002.

[57] M. Goodarzi, R. Fereidouni, and M. Rahimi, "Investigation of flow control over a NACA 0012 airfoil by suction effect on aerodynamic characteristics", *Canadian Journal on Mechanical Sciences & Engineering*, vol. 3, no. 3, pp. 102-109, 2012.

[58] A. Bar-Sever, "Separation control on an airfoil by periodic forcing", *AIAA Journal*, vol. 27, no. 6, pp.820-821, 1989.

[59] R.L. Kimmel, J.R. Hayes, J.A. Menart, and J. Shang, "Effect of magnetic fields on surface plasma discharges at Mach 5", *Journal of Spacecraft and Rockets*, vol. 43, no. 6, pp. 1340-1346, 2006.

[60] S. Merriman, E. Ploenjes, and I.V. Adamovich, "Shock wave control by nonequilibrium plasmas in cold supersonic gas flows", *AIAA Journal*, vol. 39, no. 8, pp. 1547-1552, 2001.

[61] T.C. Corke and M.L. Post, "Overview of plasma flow control: concepts, optimization, and applications", *43rd AIAA Aerospace Science Meeting and Exhibit*, no. 563, pp. 1-15, 2005.

[62] M. Samimy, I. Adamovich, B. Webb, J. Kastner, J. Hileman, S. Keshav, and P. Palm, "Development and characterization of plasma actuators for high-speed jet control", *Experiments in Fluids*, no. 37, pp. 577-588, 2004.

[63] S. Pavón, P. Ott, P. Leyland, J.-L. Dorier, and Ch. Hollenstein, "Effects of a surface dielectric barrier discharge on transonic flows around an airfoil", *47th AIAA Aerospace Science Meeting*, no. 649, pp. 1-25, 2009.

[64] K. Takashima, Y. Zuzeek, W.R. Lempert, and I.V. Adamovich, "Characterization of a surface dielectric barrier discharge plasma sustained by repetitive nanosecond pulses", *Plasma Sources Science and Technology*, vol. 20, no. 055009, pp. 1-10, 2011.

[65] N. Benard, N. Zouzou, A. Claverie, J. Sotton, and E. Moreau, "Optical visualization and electrical characterization of fast-rising pulsed dielectric barrier discharge for airflow control applications", *Journal of Applied Physics*, vol. 111, no. 033303, pp. 1-13, 2012.

[66] C.L. Enloe, M.G. McHarg, and T.E. McLaughlin, "Time-correlated force production measurements of the dielectric barrier discharge plasma aerodynamic actuator", *Journal of Applied Physics*, vol. 103, no. 073302, pp. 1-7, 2008.

[67] R. Sosa, E. Arnaud, E. Memin, and G. Artana, "Study of the flow induced by a sliding discharge", *IEEE Transactions on Dilectrics and Electrical Insultation*, vol. 16, no. 2, pp. 305-311, 2009.

[68] G.I. Font, and W.L. Morgan, "Plasma discharges in atmospheric pressure oxygen for boundary layer separation control", *35th AIAA Fluid Dynamics Conference and Exhibit*, Toronto, Ontario, Canada, no. 4632, 2005.

[69] C.O. Porter, J.W. Baughn, T.E. McLaughlin, C.L. Enloe and G.I. Font, "Plasma actuator force measurements", *AIAA Journal*, vol. 45, no. 7, pp. 1562-1570, 2007.

[70] G.I. Font, C.L.Enloe, and T.E. McLaughlin, "Plasma volumetric effects on the force production of a plasma actuator", *AIAA Journal*, vol. 48, no. 9, 2010.

[71] J.P. Boeuf, Y. Lagmich, Th. Unfer, Th Callegari, and L.C. Pitchford, "Electrohydrodynamic force in dielectrc barrier discharge plasma actuators", *Journal of Physics D: Applied Physics*, vol. 40, pp. 652-662, 2007.

[72] H. Velkoff and J. Ketchman, "Effect of an electrostatic field on boundary layer transition", *AIAA Journal*, vol. 16, pp. 1381-1383, 1968.

[73] A. Yabe, Y. Mori, and K. Hijikata, "EHD study of the corona wind between wire and plate electrodes", *AIAA Journal*, vol. 16, pp. 340-345, 1978.

[74] D. Bushnell, "Turbulent drag reduction for external flows", *21st Aerospace Sciences Meeting*, Reno, USA, no. 0231, 1983.

[75] S. El-Khabiry and G.M. Colver, "Drag reduction by DC corona discharge along an electrically conductive flat plate for small Reynolds number flow", *Physics of Fluids*, vol. 9, no. 3, pp. 587-599, 1997.

[76] A. Soldati and S. Banerjee, "Turbulence modification by large-scale organized electrohydrodynamic flows", *Physics of Fluids*, vol. 10, no. 7, pp. 1742-1756, 1998.

[77] G. Artana, G. DiPrimio, E. Moreau, and G. Touchard, "Electrohydrodynamic actuators on a subsonic air flow around a circular cylinder", *Proc. 4th AIAA Weakly Ionized Gases International Conference* Anaheim, USA, no. 3056, 2001.

[78] L. Léger, E. Moreau, and G.G. Touchard, "Effect of a DC corona electrical discharge on the airflow around a flat plate", *IEEE Transactions on Industry Applications*, vol. 38, no. 6, pp. 1478-1485, 2002.

[79] J.R. Roth, P.P. Tsai and C. Liu, *US Patent*, no. 5387842, 1995.

[80] J.R. Roth and D.M. Sherman, "Boundary layer flow control with a one atmosphere uniform glow discharge surface plasma", *36th Aerospace Sciences Meeting & Exhibit* Reno, USA, no. 0328, 1998.

[81] J.R. Roth, "Electrohydrodynamically induced airflow in a one atmosphere uniform glow discharge surface plasma", *25th IEEE International Conference on Plasma Science* Raleigh, USA, no. 6P67, 1998.

[82] M. Forte, L. Leger, J. Pons, E. Moreau, and G. Touchard, "Plasma actuators for airflow control: measurement of the non-stationary induced flow velocity", *Journal of Electrostatics*, vol. 63, pp. 929-936, 2005.

[83] H. Do, W. Kim, M.G. Mungal, and M.A. Cappelli, "Bluff Body Flow Separation Control Using Surface Dielectric Barrier Discharges", *Proceedings of the 45th AIAA Aerospace Science Meeting and Exhibit*, Reno, USA, no. 939, 2007.

[84] M.L. Post and T.C. Corke, "Separation Control on High Angle of Attack Airfoil Using Plasma Actuators", *AIAA Journal*, vol. 42, no. 11, pp. 2177-2184, 2004.

[85] J. Huang, T.C. Corke, and F.O. Thomas "Plasma Actuators for Separation Control of Low-Pressure Turbine Blades", *AIAA Journal*, vol. 44, no. 1, pp. 51-57, 2006.

[86] Y. Sung, W. Kim, M.G. Mungal, and M.A. Cappelli, "Aerodynamic modification of flow over bluff objects by plasma actuation", *Experiments in Fluids*, vol. 41, pp. 479-486, 2006.

[87] C. He, T.C. Corke, and M.P. Patel, "Numerical and Experimental Analysis of Plasma Flow Control Over a Hump Model", *Proceedings of the 45th AIAA Aerospace Science Meeting and Exhibit*, Reno, USA, no. 0935, 2007.

[88] S. Grundmann and C. Tropea, "Experimental transition delay using glow-discharge plasma actuators", *Experiments in Fluids*, vol. 42, pp. 653-657, 2007.

[89] D. Schatzman and F. Thomas, "Turbulent Boundary Layer Separation Control Using Plasma Actuators", *Proceedings of the 4th Flow Control Conference*, Seattle, USA, no. 4199, 2008.

[90] A. Santhanakrishnan and J.D. Jacob, "Flow control with plasma synthetic jet actuators", *Journal of Physics D: Applied Physics*, vol. 40, pp. 637-651, 2007.

[91] N. Benard, J. Jolibois, G. Touchard, and E. Moreau, "A Directional Plasma-Jet Device Generated by Double DBD Actuators: An Active Vortex Generator for Aerodynamic Flow Control", *Proceedings of the 4th Flow Control Conference*, Seattle, USA, no. 3763, pp. 1-26, 2008.

[92] J. Jolibois, M. Forte, and E. Moreau, "Application of an AC barrier discharge actuator to control airflow separation above a NACA 0015 airfoil: Optimization of the actuation location along the chord", *Journal of Electrostatics*, vol. 66, no. 9-10, pp. 496-503, 2008.

[93] R. Sosa, G. Artana, E. Moreau, and G. Touchard, "Stall control at high angle of attack with plasma sheet actuators", *Experiments in Fluids*, no. 42, pp. 143-167, 2007.

[94] A.N. Vorobiev, R.M. Rennie, E.J. Jumper, and T.E. McLaughlin, "Experimental Investigation of Lift Enhancement and Roll Control Using Plasma Actuators", *Journal of Aircraft*, vol. 45, no. 4, pp. 1315-1321, 2008.

[95] C. He, T.C. Corke, and M.P. Patel, "Plasma Flaps and Slats: An Application of Weakly Ionized Plasma Actuators", *Journal of Aircraft*, vol. 46, no. 3, pp. 864-873, 2009.

[96] D. Roupassov, I. Zavialov, and A. Starikovskii, "Boundary Layer Separation Plasma Control Using Low-Temperature Non-Equilibrium Plasma of Gas Discharge", *44th Aerospace Sciences Meeting and Exhibit*, Reno, USA, no. 373, 2006.

[97] J. Little, M. Nishihara, I. Adamovich, and M. Samimy "High-lift airfoil trailing edge separation control using a single dielectric barrier discharge plasma", *Experiments in Fluids*, no. 48, pp. 521-537, 2010.

[98] T.C. Corke, M.L. Post, and D.M. Orlov, "SDBD plasma enhanced aerodynamics: concepts, optimization and applications", *Progress in Aerospace Sciences*, vol. 43, pp. 193-217, 2007.

[99] T. Jukes, K.S. Choi, G. Johnson, and S. Scott, "Turbulent Boundary-Layer Control for Drag Reduction Using Surface Plasma", *2nd AIAA Flow Control Conference*, Portland, USA, no. 2216, 2004.

[100] J.R. Roth, D.M. Sherman, and S.P. Wilkinson "Electrohydrodynamic Flow Control with a Glow-Discharge Surface Plasma", *AIAA Journal*, vol. 38, no. 7, pp. 1166-1172, 2000.

[101] A. Asghar, E. Jumper, and T. Corke, "On the Use of Reynolds Number as the Scaling Parameter for the Performance of Plasma Actuator in a Weakly Compressible Flow", *44th AIAA Aerospace Sciences Meeting and Exhibit*, Reno, USA, no. 170, 2006.

[102] T.N. Jukes and K.S. Choi "Flow control around a circular cylinder using pulsed dielectric barrier discharge surface plasma", *Physics of Fluids*, vol. 21, no. 084103, pp. 1-12, 2009.

[103] N. Benard, P. Braud, G. Touchard, and E. Moreau, "Detachment and attachment of an axisymmetric non-reactive jet with turbulent shear layer: Control by plasma actuator", *Experimental Thermal and Fluid Science*, vol. 32, no. 6, pp. 1193-1203, 2008.

[104] N. Benard, E. Moreau, J. Griffin, and L.N. Cattafesta "Slope seeking for autonomous lift improvement by plasma surface discharge", *Experiments in Fluids*, vol. 48, pp. 791-808, 2010.

[105] J.R. Roth, "Aerodynamic flow acceleration using paraelectric and peristaltic electrohydrodynamic effects of a One Atmosphere Uniform Glow Discharge Plasma", *Physics of Plasmas*, vol. 10, no. 5, pp. 2117-2126, 2003.

[106] F.O. Thomas, A. Kozlov, and T.C. Corke "Plasma actuators for bluff body flow control", *3rd AIAA Flow Control Conference*, San Francisco, USA, no. 2845, 2006.

[107] G. Artana, R. Sosa, E. Moreau, and G. Touchard, "Control of the near-wake flow around a circular cylinder with electrohydrodynamic actuators", *Experiments in Fluids*, no. 35, pp. 580-588, 2003.

[108] N. Benard, N. Balcon, G. Touchard, and E. Moreau, "Control of diffuser jet flow: turbulent kinetic energy and jet spreading enhancements assisted by a non-thermal plasma discharge", *Experiments in Fluids*, no. 45, pp. 333-355, 2008.

[109] N. Benard, J.P. Bonnet, G. Touchard, and E. Moreau, "Flow Control by Dielectric Barrier Discharge Actuators: Jet Mixing Enhancement", *AIAA Journal*, vol. 46, no. 9, pp. 2293-2305, 2008.

[110] F.O. Thomas, A. Kozlov, and T.C. Corke, "Plasma Actuators for Landing Gear Noise Reduction", *11th AIAA/CEAS Aeroacoustics Conference*, Monterey, USA, no. 3010, 2005.

[111] X. Huang and X. Zhang, "Streamwise and spanwise plasma actuators for flow-induced cavity noise control", *Physics of Fluids*, vol. 20, no. 037101, pp. 1-10, 2008.

[112] S. Chan, X. Zhang, and S. Gabriel "Attenuation of Low-Speed Flow-Induced Cavity Tones Using Plasma Actuators", *AIAA Journal*, vol. 45, no. 7, pp. 1525-1538, 2007.

[113] D. Greenblatt, B. Gőksel, I. Rechenberg, C.Y. SchÃ$\frac{1}{4}$le, D. Romann, and C.O. Paschereit, "Dielectric Barrier Discharge Flow Control at Very Low Flight Reynolds Numbers", *AIAA Journal*, vol. 46, no. 6, pp. 1528-1541, 2008.

[114] M.P. Patel, T.T. Ng, S. Vasudevan, T.C. Corke, M.L. Post, T.E. McLaughlin, and C.F. Suchomel, "Scaling Effects of an Aerodynamic Plasma Actuator", *Journal of Aircraft*, vol. 45, no. 1, pp. 223-236, 2008.

[115] N. Benard, J. Jolibois, and E. Moreau, "Lift and drag performances of an axisymmetric airfoil controlled by plasma actuator", *Journal of Electrostatics*, vol. 67, no. 2-3, pp. 133-139, 2009.

[116] V. Boucinha, P. Magnier, R. Weber, A. Leroy-Chesneau, B. Dong, D. Hong, and R. Joussot, "Characterization of the Ionic Wind Induced by a Sine DBD Actuator Used for Laminar-to-Turbulent Transition Delay", *4th Flow Control Conference*, Seattle, USA, no. 4210, 2008.

[117] W. Kim, H. Do, M.G. Mungal, and M.A. Cappelli, "On the role of oxygen in dielectric barrier discharge actuation of aerodynamic

flows", *Applied Physics Letters*, vol. 91, no. 18, pp. 181501-181503, 2007.

[118] T. Abe, Y. Takizawa, S. Sato, and N. Kimura, "Experimental Study for Momentum Transfer in a Dielectric Barrier Discharge Plasma Actuator", *AIAA Journal*, vol. 46, no. 9, pp. 2248-2256, 2008.

[119] J.H. Mabe, F.T. Calkins, B. Wesley, R. Woszidlo, L.Taubert, and I. Wygnanski, "Single dielectric barrier discharge plasma actuators for improved airfoil performance", *Journal of Aircraft*, vol. 46, no. 3, pp. 847-855, 2009.

[120] S. Im, H. Do, and M.A. Capelli, "Dielectric barrier discharge control of a turbulent boundary layer in a supersonic flow", *Applied Physics Letters*, vol. 97, no. 041503, pp. 1-3, 2010.

[121] P. Bletzinger and B.N. Ganguly, "Local acoustic shock velocity and shock structure recovery measurements in glow discharges", *Physics Letters*, vol. 258, pp. 342-348, 1999.

[122] D. Bivolaru and S.P. Kuo, "Aerodynamic Modification of Supersonic Flow Around Truncated Cone Using a Pulsed Electrical Discharges", *AIAA Journal*, vol. 43, no. 7, pp. 1482-1489, 2005.

[123] V. Narayanaswamy, L.L. Raja, and N.T. Clemens, "Characterization of a high-frequency pulsed-plasma jet actuator for supersonic flow control", *AIAA Journal*, vol. 48, no. 2, pp. 297-305, 2010.

[124] E. Menier, L. Leger, E. Depussay, V. Lago, and G. Artana, "Effect of a dc discharge on the supersonic rarefied air flow over a flat plate", *Journal of Physics D: Applied Physics*, vol. 40, pp. 695-701, 2007.

[125] A.V. Likhanskii, M.N. Shneider, S.O. Macheret, and R.B. Miles, "Optimization of Dielectric Barrier Discharge Plasma Actuators

Driven By Repetitive Nanosecond Pulses", *45th AIAA Aerospace Sciences Meeting and Exhibit*, Reno, USA, no. 633, 2007.

[126] D.F. Opaits, G. Neretti, A.V. Likhanskii, S. Zaidi, Mi.N. Shneider, R.B. Miles, and S.O. Macheret, "Experimental Investigation of DBD Plasma Actuators Driven by Repetitive High Voltage Nanosecond Pulses with DC or Low-Frequency Sinusoidal Bias", *38th AIAA Plasmadynamics and Lasers Conference*, Miami, USA, no. 4532, 2007.

[127] D.V. Roupassov, A.A. Nikipelov, M.M. Nudnova, A.Y. Starikovskii, "Flow Separation Control by Plasma Actuator with Nanosecond Pulsed-Periodic Discharge", *AIAA Journal*, vol. 47, no. 1, pp. 168-185, 2009.

[128] A.Y. Starikovskiy, A.A. Nikipelov, M.M. Nudnova, and D.V. Roupassov, "SDBD plasma actuator with nanosecond pulse-periodic discharge", *Plasma Sources Science and Technology*, vol. 18, no. 034015, pp. 1-17, 2009.

[129] N.L. Aleksandrov, S.V. Kindysheva, M.M. Nudnova, and A.Y. Starikovskiy, "Mechanisms of ultra-fast heating in a non-equilibrium weakly ionized air discharge plasma in high electric fields", *Journal of Physics D: Applied Physics*, vol. 43, no. 255201, pp. 1-19, 2010.

[130] M. Samimy, J.H. Kim, J. Kastner, I. Adamovich, and Y. Utkin, "Active control of high-speed and high-Reynolds-number jets using plasma actuators", *Journal of Fluid Mechanics*, vol. 578, pp. 305-330, 2007.

[131] R.A. Siliprandi, H.E. Roman, R. Barni, and C. Riccardi, "Characterization of the streamer regime in dielectric barrier discharges", *Journal of Applied Physics*, vol. 104, no. 063309, pp. 1-9, 2008.

[132] C.L. Enloe, T.E. McLaughlin, R.D. VanDyken, K.D. Kachner, E.J. Jumper, and T.C. Corke, "Mechanisms and responses of a single dielectric barrier plasma actuator: plasma morphology", *AIAA Journal*, vol. 42, no. 3, pp. 589-594, 2004.

[133] R.W.B. Pearse and A.G. Gaydon, "The identification of molecular spectra", *New York: Wiley*, 1976.

[134] W. Rogowki and W. Steinhaus, "Die messung der magnetische spannung", *Archiv fűr Elektrotechnik*, vol. 1, no. 4, pp. 141-150, 1912.

[135] W.F. Ray and C.R. Hewson, "High performance Rogowski current transducer", *Industry Applications Conference. Conference Record of the 2000 IEEE*, Rome, Italy, vol. 5, pp. 3083-3090, 2000.

[136] D.G. Pellinen, M.S. Di Capua, S.E. Sampayan, H. Gerbracht, and M. Wang, "Rogowski coil for measuring fast, high-level pulsed currents", *Review of Scientific Instruments*, vol. 51, no. 11, pp. 1535-1540, 1980.

[137] Q. Zhang, J. Zhu, J. Jia, F. Tao, and L. Yang, "Design of a current transducer with a magnetic core for use in measurements of nanosecond current pulses", *Measurement Scince and Technology*, vol. 17, pp. 895-900, 2006.

[138] M. Argűeso, G. Robles, and J. Sanz, "Implementation of a Rogowski coil for the measurement of partial discharges", *Review of Scientific Instruments*, vol. 76, no. 065107, pp. 1-7, 2005.

[139] I. Biganzoli, R. Barni, and C. Riccardi, "Note: On the use of Rogowski coils as current probes for atmospheric pressure dielectric barrier discharges", *Review of Scientific Instruments*, vol. 84, no. 016101, pp. 1-3, 2013.

[140] R. Barni, I. Biganzoli, and C. Riccardi, "Experimental characterization of plasmas for aerodynamical applications", *Proceeding to the 30th International Conference on Phenomena of Ionized Gases (ICPIG)*, Belfast: Queen's University, North Ireland, no. D-16, pp. 1-4, 2011.

[141] Z. Falkestein, and J.J. Coogan, "Microdischarge behaviour in the silent discharge of nitrogen-oxygen and water-air mixtures", *Journal of Physics D: Applied Physics*, vol. 30, pp. 817-825, 1997.

[142] S. Grundmann, and C. Tropea, "Experimental damping of boundary-layer oscillations using DBD plasma actuators", *International Journal of Heat and Fluid Flow*, vol. 30, pp. 394-402, 2009.

[143] G. Borcia, C.A. Anderson, and N.M.D. Brown, "Dielectric barrier discharge for surface treatment: application to selected polymers in film and fibre form.", *Plasma Sources Science and Technology*, vol. 12, no. 3, pp. 335-344, 2003.

[144] T.C. Manley, "The electric characteristics of the ozonator discharge", *Journal of the Electrochemical Society*, vol. 84, no. 1, pp. 83-96, 1943.

[145] J. Pons, E. Moreau, and G. Touchard, "Asymmetric surface dielectric barrier discharge in air at atmospheric pressure: electrical properties and induced airflow characteristics", *Journal of Physics D: Applied Physics*, vol. 38, pp. 3635-3642, 2005.

[146] C.A. Borghi, A. Cristofolini, C. Latini, G. Neretti, A. Gurioli, and R. Pertile, "Experimental results in DBD plasma actuators for airflow control", *41st Plasmadynamics and Laser Conference*, Chicago, USA, no. 4763, pp. 1-13, 2010.

[147] D.M. Orlov, G.I. Font, and D. Edelstein, "Characterization of discharge modes of plasma actuators", *AIAA Journal*, vol. 46, no. 12, pp. 3142-3148, 2008.

[148] M. Šimec, V. Babický, M. Člupek, S. DeBenedictis, G. Dilecce, and P. Šunka, "Excitation of $N_2(C^3\Pi_u)$ and $NO(A^2\Sigma^+)$ states in a pulsed positive corona discharge in N_2, $N_2 - O_2$ and $N_2 - NO$ mixtures", *Journal of Physics D: Applied Physics*, vol. 31, no. 19, pp. 2591-2602, 1998.

[149] R. Barni, P. Esena, and C. Riccardi, "Chemical kinetics simulation for atmospheric pressure air plasmas in a streamer regime", *Journal of Applied Physics*, vol. 97, no. 073301, pp. 1-7, 2005.

[150] S.M. Starikovskaia, K. Allegraud, O. Guaitella, and A. Rousseau, "On electric field measurements in surface dielectric barrier discharge", *Journal of Physics D: Applied Physics*, vol. 43, no. 124007, pp. 1-5, 2010.

[151] N. Takeuchi, T. Hamasaki, K. Yasuoka, and T. Sakurai, "Surface charge measurement in surface dielectric barrier discharge by laser polarimetry", *Journal of Electrostatics*, vol. 69, pp. 87-91, 2011.

[152] J. Kriegseis *Performance characterization and quantification of dielectric barrier discharge plasma actuators*, PhD Thesis, Technischen Universität Darmstadt, 2011.

[153] S. Grundmann, M. Frey, and C. Tropea, "Unmanned Aerial Vehicle (UAV) with plasma actuators for separation control", *47th AIAA Aerospace Sciences Meeting*, Orlando, USA, no. 698, 2009.

[154] R. Erfani, H. Zare-Behtash, and K. Kontis, "Plasma actuator: influence of the dielectric surface temperature", *Experimental Thermal and Fluid Science*, vol. 42, pp. 258-264, 2012.

[155] M. Forte, J. Jolibois, J. Pons, E. Moreau, G. Touchard, and M. Cazalens, "Optimization of a dielectric barrier discharge actuator by stationary and non-stationary measurements of the induced flow velocity: application to airflow control", *Experiments in Fluids*, vol. 43, pp. 917-928, 2007.

[156] E. Moreau, R. Sosa, and G. Artana, "Electric wind produced by surface plasma actuators: a new dielectric barrier discharge based on a three-electrode geometry", *Journal of Physics D: Applied Physics*, vol. 41, no. 115204, pp. 1-12, 2008.

[157] F.O. Thomas, T.C. Corke, M. Iqbal, A. Kozlov, and D. Schatzman "Optimization of dielectric barrier discharge plasma actuators for active aerodynamic flow control", *AIAA Journal*, vol. 47, no. 9, pp. 2169-2178, 2009.

[158] G. Neretti, A. Cristofolini, and C.A. Borghi, "Experimental results in DBD plasma actuators for air flow control", *IEEE Transactions on Plasma Science*, vol. 40, no. 6, pp. 1678-1687, 2012.

[159] R. Durscher, S. Stanfield, and S. Roy, "Characterization and manipulation of the "saturation" effect by changing the surface temperature of a dielectric barrier discharge actuator", *Applied Physics Letters*, vol. 101, no. 252902, pp. 1-4, 2012.

[160] H. Nishiyama, and M. Nakamura, "Capacitance of disk capacitors", *IEEE Transactions on Components, Hybrids, and Manufacturing Technology*, vol. 16, no. 3, pp. 360-366, 1993.

[161] E. Legnani *Studio e simulazione di plasmi atmosferici per applicazioni aerospaziali*, Master's Thesis, Università degli Studi di Milano-Bicocca, 2012.

[162] A. Cristofolini, C.A. Borghi, and G. Neretti, "Charge distribution on the surface of a dielectric barrier discharge actuator for the fluid-dynamic control", *Journal of Applied Physics*, vol. 113, no. 143307, pp. 1-11, 2013.

[163] J.D. Jacob, K. Ramakumar, R. Anthony, and R.B. Rivir, "Control of laminar and turbulent shear flows using plasma actuators", *4th International Symposium on Turbulence and Shear Flow Phenomena*, Williamsburg, 2005.

[164] D.F. Opaits, D.V. Roupassov, S.M. Starikovskaia, A.Y. Starikovskii, I.N. Zavialov, and S.G. Saddoughi, "Plasma control of boundary layer using low-temperature non-equilibrium plasma of gas discharge", *43rd AIAA Aerospace Sciences Meeting & Exhibit*, Reno, USA, no. 1180, 2005.

[165] H.E. Wagner, R. Brandenburg, K.V. Kozlov, A. Sonnenfeld, P. Michel, and J.F. Behnke, "The barrier discharge: basic properties and applications to surface treatment", *Vacuum*, vol. 71, pp. 417-436, 2003.

[166] B. Dong, J.M. Bauchire, J.M. Pouvesle, P.Magnier, and D. Hong, "Experimental study of a DBD surface discharge for the active control of subsonic airflow", *Journal of Physics D: Applied Physics*, vol. 41, no. 155201, pp. 1-9, 2008.

[167] C.O. Porter, J.W. Baughn, T.E. McLaughlin, C.L. Enloe and G.I. Font, "Temporal force measurements on an aerodynamic plasma actuator", *44th AIAA Aerospace Science Meeting and Exhibit*, Reno, USA, no. 104, 2006.

[168] R.H.M. Giepman, and M. Kotsonis, "On the mechanical efficiency of dielectric barrier discharge plasma actuators", *Applied Physics Letters*, vol. 98, no. 221504, pp. 1-3, 2011.

[169] O.T. Flint, T.C. Corke, M. Iqbal, A. Kozlov, and D. Schatzman, "Optimization of dielectric barrier discharge plasma actuators for active aerodynamic flow control", *AIAA Journal*, vol. 47, no. 9, pp. 2169-2178, 2009.

[170] Y.P. Raizer, and M.S. Mokrov, "Physical mechanisms of self-organization and formation of current patterns in gas discharges of the Townsend and glow types", *Physics of Plasmas*, vol. 20, no. 101604, pp. 1-14, 2013.

[171] I. Műller, C. Punset, E. Ammelt, H.G. Purwins, and J.P. Boeuf, "Self-Organized Filaments in Dielectric Barrier Glow Discharges", *IEEE Transactions on Plasma Science*, vol. 27, no. 1, pp. 20-21, 1999.

[172] I. Brauer, C. Punset, H.G. Purwins, and J.P. Boeuf, "Simulations of self-organized filaments in a dielectric barrier glow discharge plasma", *Journal of Applied Physics*, vol. 85, no. 11, pp. 7569-7572, 1999.

[173] H. Akashi, A. Oda, and Y. Sakai, "Modeling of multifilaments formation in dielectric barrier discharge excimer lamp", *IEEE Transactions on Plasma Science*, vol. 33, no. 2, pp. 308-309, 2005.

[174] G.H. Kim, S.Y. Jeong, and H.C. Kwon, "Capacitance between an atmospheric discharge plasma and the dielectric electrode in the parallel cell reactor", *Journal of the Korean Physical Society*, vol. 49, no. 3, pp. 1307-1311, 2006.

[175] Z. Buntat, J.E. Harry, and I.R. Smith, "Generation of a homogeneous glow discharge in air at atmospheric pressure", *Elektrika*, vol. 9, no. 2, pp. 60-65, 2007.

[176] J. Kriegseis, B. Mőller, and C. Tropea, "Capacitance and power consumption quantification of dielectric barrier discharge (DBD) plasma actuators", *Journal of Electrostatics*, vol. 69, no. 4, pp. 302-312, 2011.

[177] H. Richard, and M. Raffel, "Principle and applications of the background oriented schlieren (BOS) method", *Measurement Science and Technology*, vol. 12, pp. 1576-1585, 2001.

[178] G.E.A. Meier, "Computerized background-oriented schlieren", *Experiments in Fluids*, vol. 33, pp. 181-187, 2002.

[179] C. Capone, *Development of a schlieren technique for atmospheric plasma characterization*, Master's Thesis, Università degli Studi di Milano-Bicocca, 2014.

[180] W. Merzkirch, "Techniques of Flow Visualization" Universität Essen, 1987.

[181] G. S. Settles, "Schlieren and Shadowgraph Techniques", *Springer*, 2006.

[182] R. Goldstein, "Fluid Mechanics Measurements", *Goldstein*, 1996.

[183] M. Jahanmiri, "Particle Image Velocimetry: Fundamentals and Its Applications", Research report 2011:03, Chalmers University of Technology, 2011.

[184] A. Melling, "Tracer particles and seeding for particle image velocimetry", *Measurement Science and Technology*, vol. 8, pp. 1406-1416, 1997.

[185] J.M. Desse, and R. Deron, "Shadow, Schlieren and Color Interferometry", *Journal Aerospace Lab*, vol. 1, pp. 1-10, 2009.

[186] B. Atcheson, *Schlieren-Based Flow Imaging*, Master's Thesis, University of Witwatersrand, 2004.

[187] G. Izarra, and C. Izarra, "Quantitative shadowgraphy made easy", textitEuropean Journal of Physics, vol. 33, pp. 1821-1842, 2012.

[188] P. K. Panigrahi, and K. Muralidhar, "Schlieren and Shadowgraph Methods in Heat and Mass Transfer", *Springer*, 2012.

[189] A. Mazumdar, *Principles and Techniques of Schlieren Imaging Systems*, Columbia University, 2013.

[190] Q.Wang, *Advanced Optical and 3D Reconstruction Diagnostics for Combustion and Fluids Research*, PhD thesis, University of Sheffield.

[191] A. H. Ali, "Measurement of Air Temperature using Laser Interferometry", *Journal of Applied Scienced*, vol. 11, pp. 1431-1435, 2011.

[192] M. E. Russo, "Optical Interferometers: Principles and Applictions in Transport Phenomena", *Nova Science Publishers*, 2011.

[193] D. Stevenson, *Quantitative Colour Schlieren Techniques*, Master's Thesis, University of the Witwatersrand, 2011.

[194] M. J. Hargather, and G.S.Settles, "A comparison of three quantitative schlieren techniques", *Optics and Lasers in Engineering*, vol. 50, pp. 8-17, 2012.

[195] S. B. Dalziel, G. O. Hughes, and B. R. Sutherland, "Whole-field density measurements by synthetic schlieren", textitExperiments in Fluids, vol. 28, pp. 322-335, 2000.

[196] S. B. Dalziel, G. O. Hughes, and B. R. Sutherland, "Synthetic Schlieren", *8th International Symposium On Flow Visualization*, Sorrento, 1998.

[197] E. Goldhahn, and J. Seume, "The background oriented schlieren technique: sensitivity, accuracy, resolution and application to a three-dimensional density field", *Experiments in Fluids*, vol. 43, pp. 241-249, 2007.

[198] M. J. Hargather, and G.S.Settles "Natural-background-oriented schlieren imaging", textitExperiments in Fluids, vol. 48, no. 1, pp. 59-68, 2010.

[199] G. Elsinga, *Density measurements by means of schlieren methods*, Master's Thesis, Delft University of Technology, 2003.

[200] L. Venkatakrishnan, and G. E. A. Meier, "Density measurements using the Background Oriented Schlieren technique", *Experiments in Fluids*, vol.37, pp. 237-247, 2004.

[201] W. Nitsche, and C.Dobriloff, "Imaging Measurement Methods for Flow Analysis", *Springer*, 2009.

[202] G.Vasudeva, D.R. Honnrey,and J.Soria, "Non-intrusive measurement of a density field using the background oriented schlieren (BOS) method", *4th Australian Conference on Laser Diagnostics*, Adelaide, 2005.

[203] D. Mescheded, "Optics, Light and Lasers: The Practical Approach to Modern Aspects of Photonics and Laser Physics", *Wiley*, 2007.

[204] B. Atcheson, W. Heidrich, and I. Ihrke, "An evaluation of optical flow algorithms for background oriented schlieren imaging", *Experiments in Fluids*, vol.46, no. 3, pp. 467-476, 2009.

[205] N. A. Vinnichenko, I.A. Znamenskaya, F. N. Glazyrin,and A. V. Uvarov, "Study of Backround Oriented Schlieren Method Accuracy by means of Sinthetic Images Analysis", *22nd International Symposium on Transport Phenomena*, Delft, 2011.

[206] J. E. Hartberger, *Background-Oriented Schlieren pattern optimization*, Master's thesis, Air Force Institute of Technology, 2011.

[207] R. L. Cook, and T. DeRose, "Wavelet Noise", *ACM Transactions on Graphics*, vol. 24, no. 3, pp. 803-811, 2005.

[208] A. Barjatya, "Block matching algorithms for motion estimation.", *IEEE Transactions Evolution Computation*, vol. 8, no. 3, pp. 225-239, 2004.

[209] D.M. Thomas, "A Study on Block Matching Algorithms and Gradient Based Method for Motion Estimation in Video Compression", *Communications in Computer and Information Science*, vol. 205, pp. 136-145, 2011.

[210] B. K.P. Horn, and B. G. Shunck, "Determining Optical Flow", *Artificial Intelligence*, vol. 17 , pp. 185-203, 1981.

[211] J.Y. Bouguet, "Pyramidal implementation of the affine Lucas Kanade feature tracker description of the algorithm", *Intel Corporation*, 2001.

[212] W. Merzkirch, "Flow Visualization", *Academic Press*, 1987.

[213] F. S. Meidanshahi, K. Madanipour, and B. Shokri, "Investigation of first and second ionization on optical properties of atmospheric plasmas", *Optics Communications*, vol. 285, pp. 453-458, 2012.

[214] O. S. Jensen, J. P. Kunsch, and T. Rosgen, "Optical density and velocity measurements in cryogenic gas flows", *Experiments in Fluids*, vol. 39 , pp. 48-55, 2005 .

[215] G. Correale, T. Michelis, D. Ragni, M. Kotsonis, and F. Scarano, "Nanosecond-pulsed plasma actuation in quiescent air and laminar boundary layer", *Journal of Physics D: Applied Physics*, vol. 47, pp. 1-11, 2014.

[216] J. Pons, H. Rabat, A. Leroy, and D. Hong, "Experimental Study of a Surface DBD Actuator Supplied by an Atypical Nanosecond Rising High-Voltage Pulse", *IEE Transaction on Plasma Science*, vol. 42, no. 6, pp. 1661-1668, 2014.

[217] R. Dawson, and J. Little, "Characterization of nanosecond pulse driven dielectric barrier discharge plasma actuators for aerodynamic flow control", *Journal of Applied Physics*, vol. 113, pp. 1-10, 2013.

[218] P. P. Khramtsov, O. G. Penyazkov, V. M. Grishchenko, M. V. Doroshko, M. Yu. Chernik, and I. A. Shikh, "Diagnostics Of Average Temperature Fields and Electron Densities in a Barrier Discharge Plasma in the Presence of Air Flow", *Journal of Engineering Physics and Thermophysics*, vol. 82 , no. 6, pp. 1146-1152, 2009.

[219] D. F. Opaits, A. V. Likhanskii, G. Neretti, S. Zaidi, M. N. Shneider, R. B. Miles, and S. O. Macheret, "Experimental investigation of dielectric barrier discharge plasma actuators driven by repetitive high-voltage nanosecond pulses with dc or low frequency sinusoidal bias", *Journal of Applied Physics*, vol. 104, pp. 1-15, 2008.

[220] A. Cristofolini, G. Neretti, F. Roveda, and C. A. Borghi, "Schlieren imaging in a dielectric barrier discharge actuator for airflow control", *Journal of Applied Physics*, vol. 111 , pp. 1-6, 2012.

[221] G. Neretti, A. Cristofolini, and C. A. Borghi, "Experimental investigation on a vectorized aerodynamic dielectric barrier discharge plasma actuator array", *Journal of Applied Physics*, vol. 115 , pp. 1-12, 2014.

[222] C. L Enloe, T. E. McLaughlin, G. I. Font,J. W. Baughn "Parameterization of Temporal Structure in the Single Dielectric Barrier Aerodynamic Plasma Actuator", *43rd AIAA Aerospace Sciences Meeting and Exhibit*, Reno, USA, no. 564, 2005.

[223] D. F. Opaits, "Dielectric Barrier Discharge Plasma Actuator for Flow Control", *Final Report*, Princeton University, 2012.

[224] , "Measurement of Ozone Production in Non-thermal Plasma Actuator Using Surface Dielectric Barrier Discharge", *Plasma Chemistry and Plasma Processing*, vol. 34, pp. 887-897, 2014.

[225] R. Whalley, and K. S. Choi , "Starting, traveling, and colliding vortices: Dielectric-barrier-discharge plasma in quiescent air", *Physics Of Fluids*, vol. 22 , pp. 091105, 2010.

[226] R. Whalley, and K. S. Choi, "The starting vortex in quiescent air induced by dielectric-barrier-discharge plasma", *Journal of Fluid Mechanics*, vol. 703, pp. 192-203, 2013.

[227] G. I. Font, S. Jung, C. L. Enloe, T.E. McLaughlin, W. L. Morgan, and J. W. Baughn, "Simulation of the Effects of Force and Heat Produced by a Plasma Actuator on Neutral Flow Evolution", *44th AIAA Aerospace Sciences Meeting*, Reno, USA, no.167, 2006.

[228] T. N. Jukes, and K. S. Choi, "On the formation of streamwise vortices by plasma vortex generators", *Journal of Fluid Mechanics*, vol. 733, pp. 370-393, 2013.

[229] P. Prochàzka, and V. Uruba, "Physical principle dealing with development of vortices formed by DBD actuator", *EPJ Web of Conferences*, vol. 67 , pp. 1-5, 2014 .